

INVESTIGATION AND CHARACTERIZATION OF RARE-EARTH Pnictide  
SUBOXIDES FOR THERMOELECTRIC APPLICATIONS

INVESTIGATION AND CHARACTERIZATION OF RARE-EARTH Pnictide  
SUBOXIDES FOR THERMOELECTRIC APPLICATIONS

By

SCOTT HARRY FORBES, B. Sc.

A Thesis

Submitted to the School of Graduate Studies

in Partial Fulfillment of the Requirements

For the Degree

Doctor of Philosophy

McMaster University

© Copyright by Scott Forbes, September 2015

Doctor of Philosophy (2015)  
(Chemistry)

McMaster University  
Hamilton, Ontario

TITLE: Investigation and Characterization of Rare-earth Pnictide Suboxides  
for Thermoelectric Applications

AUTHOR: Scott Harry Forbes

SUPERVISOR: Dr. Yuriy Mozharivskyj

NUMBER OF PAGES: xxiv, 219

## Abstract

Several rare-earth pnictide suboxides were investigated for their structures, chemistry, and physical properties. The goal of this research was to develop a highly stable material that could combine the thermally insulating properties of a rare-earth oxide framework with the electrically conductive properties of a rare-earth pnictide framework. These materials were synthesized by solid state reactions at high temperatures, producing highly pure products for measurement. All phases were subjected to several different forms of analysis, including X-ray powder and single crystal diffraction, energy dispersive X-ray spectroscopy (EDS), electron microprobe analysis (EPMA), magnetization, and hall resistivity measurements. Sufficiently pure bulk samples were then measured for thermoelectric properties in terms of electrical resistivity, Seebeck coefficient, and thermal conductivity, where applicable. The roles of structure and chemistry for each phase were then discussed with respect to the obtained physical properties and calculated electronic structures.

Seven distinct classes of rare-earth pnictide suboxides were investigated in this dissertation: the tetragonal  $(RE^I RE^{II})_3SbO_3$  phases (space group  $C2/m$ ), the  $CaRE_3SbO_4$  phases (space group  $I4/m$ ), the  $Ca_2RE_8Sb_3O_{10}$  phases (space group  $C2/m$ ), the  $Gd_3BiO_3$  phase and  $Gd_8Bi_3O_8$  phases (space groups  $C2/m$ ), and the  $Ca_2RE_7Sb_5O_5$  phase and  $Ca_2RE_7Bi_5O_5$  phases (space groups  $P4/n$ ). All of these phases share many common structural features, and can be related by different  $RE_4O$  tetrahedral building block stacking sequences and locations of the pnictide atoms.

Structurally speaking, the simplest possible arrangement of the  $RE$ -O and  $RE$ -Pn frameworks we investigated are found in the  $CaRE_3SbO_4$  phase. This phase contains the smallest unit cell of all known rare-earth pnictide suboxides with only a two unit  $RE_4O$  tetrahedral building block and ordered antimony atoms. Extended heat treatments gradually convert this phase into the corresponding  $Ca_2RE_8Sb_3O_{10}$  phase, with a significantly more complicated arrangement of  $RE_4O$  building blocks. By controlling the loading composition and reaction conditions, the  $CaRE_3SbO_4$  phase can be prepared as a kinetic product, while the  $Ca_2RE_8Sb_3O_{10}$  phase forms as the thermodynamic product. Likewise, the tetragonal  $(RE^I RE^{II})_3SbO_3$  phases can also be prepared through high temperature reactions. This phase contains a unique three  $RE_4O$  unit ( $RE_8O_3$ ) building block in its structure, which creates two rare-earth sites with a large difference in site volume. Thus, this phase can only be prepared when two rare-earth atoms of sufficiently different size are present.

Despite similar structures, the physical properties of the studied rare-earth pnictide suboxide phases can display quite different behavior. For the  $CaRE_3SbO_4$ ,  $Ca_2RE_7Sb_5O_5$ ,  $Ca_2RE_7Bi_5O_5$ , and tetragonal  $(RE^I RE^{II})_3SbO_3$  phases, the electrical resistivity remains fairly constant throughout the series, which can be traced to their highly ordered structures, as well as the physical and chemical similarities between rare-earths. Conversely, the more structurally disordered  $Ca_2RE_8Sb_3O_{10}$  and  $Gd_8Bi_3O_8$  phases behave as semiconductors despite the fact they are not charge balanced. This anomalous behavior arises from the disorder of Sb and Bi atoms, which are responsible for electrical conduction in the phase. Interestingly, the level of disorder and thus, the magnitude of the

electrical resistivity, can be greatly influenced by the rare-earth atom that is present, despite maintaining similar structures and charge carrier concentrations. Smaller rare earth atoms introduce a larger chemical pressure on the disordered antimony/bismuth atoms which lowers the range of Anderson localized states, pushing the system closer to metallic-type conduction.

## Preface

Chapter 1 of this dissertation begins with the history of thermoelectricity, including the scientists responsible for discovering and characterizing each of its individual phenomena. The applications and limitations of devices constructed with thermoelectric materials are then presented, along with the design philosophies of improving efficiency. The materials in focus, rare-earth pnictide suboxides, are then presented, and their merits as potential thermoelectric material candidates are discussed. Chapter 2 focuses on the experimental techniques used to study these materials, illustrating the manner of operation and role of material characterization for each method. The significance of each technique for the phases studied in this dissertation will be presented in the subsequent chapters.

Although some of the phases included in the author's work were the discovered as the result of exploratory synthesis, all phases discussed herein were designed under the premise of chemical fusion of rare-earth pnictides and rare-earth oxides, with the aim of preserving the ideal physical properties of each. As such, each phase retains the anionic pnictide found in the rare-earth pnictide precursor, albeit with some disorder in the case of  $\text{Ca}_2\text{RE}_8\text{Sb}_3\text{O}_{10}$  and  $\text{Gd}_8\text{Bi}_3\text{O}_8$ . For each of the following chapters, where possible, bulk samples of the phases discussed therein were prepared and measured. The data acquired from these experiments was used to establish the relation of crystal structure to physical properties. Thermoelectric efficiency, where applicable, was then evaluated for each material.

The tetragonal  $(RE^I RE^{II})_3SbO_3$  phases presented and discussed in Chapter 3 were discovered while exploring the effects of secondary atom substitution in the  $RE$ -Sb-O system. Indeed, it was discovered that this phase necessitates the presence of two rare-earth atoms for formation due to large differences in rare-earth site volume. Much like the monoclinic  $RE_3SbO_3$  phases, the tetragonal  $(RE^I RE^{II})_3SbO_3$  phases adopt a similar framework including  $RE_4O$  tetrahedra and empty channels occupied by  $Sb^{3-}$  atoms, although the connectivities of the  $RE$ -O building blocks are different between the two. Although the temperatures required to form the tetragonal  $(RE^I RE^{II})_3SbO_3$  phases are the highest of all the  $RE$ -Sb-O phases studied by our group, there is no obvious pathway of structural conversion from one phase into the other, eliminating the possibility of the tetragonal phase simply being a high temperature form of the monoclinic phase. Due to the relative ease of tetragonal  $(RE^I RE^{II})_3SbO_3$  sample preparation, as well as its structural simplicity, the work presented in Chapter 3 offers an excellent perspective of the steps required to properly investigate and analyze  $RE$ -Sb-O phases.

Our success with the preparation and discovery of the tetragonal  $(RE^I RE^{II})_3SbO_3$  phases motivated us to explore other atoms to substitute into the  $RE$ -Sb-O framework. The  $CaRE_3SbO_4$  and  $Ca_2RE_8Sb_3O_{10}$  phases presented in Chapter 4 represent yet another case of a  $RE$ -Sb-O framework phase that cannot be made with rare-earth alone. This is due to a certain electron count being required, which can only be accomplished with the presence of  $Ca^{2+}$ . The  $CaRE_3SbO_4$  and  $Ca_2RE_8Sb_3O_{10}$  phases were found to be analogous to the  $RE_3SbO_3$  and  $RE_8Sb_3O_8$  phases in several ways, including structure, chemistry, and to an extent, physical properties. In particular, the electrical resistivity of the

$\text{Ca}_2\text{RE}_8\text{Sb}_3\text{O}_{10}$  phases proved to be highly dependent on the rare-earth atom used; a feature that is similar to that seen in the  $\text{RE}_2(\text{Sb/Bi})\text{O}_2$  phases. As such, the nature of the semiconducting behavior observed in  $\text{Ca}_2\text{RE}_8\text{Sb}_3\text{O}_{10}$  could be traced to Anderson localization, a common theme amongst  $\text{RE-Sb-O}$  phases with pnictide site disorder. While the  $\text{Ca}_2\text{RE}_8\text{Sb}_3\text{O}_{10}$  phases do not share the same degree of chemical flexibility as  $\text{RE}_2(\text{Sb/Bi})\text{O}_2$ , they do serve as an important example of the ability to manipulate physical properties without changing the structure of the phase. The importance of this quality cannot be overemphasized, as it may serve as one of the foundations of future improvement of existing thermoelectrics.

The discovery of several new  $\text{RE-Sb-O}$  phases by our group had also motivated us to synthesize the corresponding  $\text{RE-Bi-O}$  phases. These two phases were initially investigated as a means to improve the electrical properties of the rare-earth pnictide sublattice without compromising the overall structure. Unfortunately, the rare-earth oxide frameworks contained in most of these phases render them unable to accommodate bismuth, due to its large atomic radius. Nevertheless, the  $\text{Gd}_3\text{BiO}_3$  and  $\text{Gd}_8\text{Bi}_3\text{O}_8$  phases were successfully prepared, and are discussed in Chapter 5. While  $\text{Gd}_3\text{BiO}_3$  could not be made pure by our synthetic approach, we were able to obtain pure phases of  $\text{Gd}_8\text{Bi}_3\text{O}_8$  by carefully controlling the heat treatment used. Similar to other  $\text{RE-Pn-O}$  phases,  $\text{Gd}_8\text{Bi}_3\text{O}_8$  contains disorder bismuth atoms that can be traced as the origin of its semiconducting behavior. However, our inability to form other members of the  $\text{RE}_8\text{Bi}_3\text{O}_8$  series prevented us from further exploring the role of bismuth disorder with respect to physical properties.

The synthetic challenges of preparing each of these phases are discussed in this chapter, as well as our means of characterization.

Much like our work discussed in Chapter 5, the  $\text{Ca}_2\text{RE}_7\text{Pn}_5\text{O}_5$  phases were studied as a means to improve upon the physical properties of a known phase. Upon successful preparation and study of  $\text{CaRE}_3\text{SbO}_4$ ,  $\text{Ca}_2\text{RE}_8\text{Sb}_3\text{O}_{10}$ , and  $\text{Gd}_8\text{Bi}_3\text{O}_8$ , we then turned our attention to the  $\text{RE}_9\text{Sb}_5\text{O}_5$  phases. Unlike the other phases discussed above,  $\text{RE}_9\text{Sb}_5\text{O}_5$  adopts a natural superlattice type structure; a feature which may yield good thermoelectric properties by virtue of separating electrical transport and phonon mitigation properties into different regions of the crystal lattice. The goal of the research presented in Chapter 6 was to partially substitute calcium for rare-earth, yielding an electron balanced  $\text{Ca}_2\text{RE}_7\text{Pn}_5\text{O}_5$  phase. By this method, we had hoped to simultaneously improve the stability and physical properties of the  $\text{RE}_9\text{Sb}_5\text{O}_5$  parent phase. Our hypothesis proved to be true, as we managed to obtain pure, bulk  $\text{Ca}_2\text{RE}_7\text{Sb}_5\text{O}_5$  and  $\text{Ca}_2\text{RE}_7\text{Bi}_5\text{O}_5$  phases. While the work contained in this chapter yet remains unpublished, the crystal structures, electronic structures, and physical properties of each phase are presented.

Finally, Chapter 7 summarizes the important qualities of each of the rare-earth pnictide suboxide phases discussed in this dissertation in terms of structure, chemistry, and physical properties. Potential areas for improvement, as well as the existence of new and unstudied rare-earth pnictide suboxide phases, are also presented.

## **Acknowledgement**

Firstly, I would like to thank my supervisor, Dr. Yuriy Mozharivskyj, for giving me a chance and allowing me to work in his group. I greatly appreciate his patience with me in the first year and a half of my studies when results were not being produced, and I offer thanks for all the years of suggestions and guidance that he has given me. I also thank my supervisory committee members, Dr. John Greedan and Dr. Gillian Goward, for their insight and guidance throughout my graduate studies.

I thank all members of the Mozharivskyj group, past and present, for their assistance with my studies, especially Dr. Volodymyr Svitlyk, Dr. Peng Wang, and Dr. Jinlei Yao; I could not have succeeded in my research without your tutelage and training. I thank the members of the BIMR, including Dr. Hanna Dabkowska, Dr. Anton Dabkowski, and Mr. Jim Garrett for their vital assistance with the equipment I needed throughout my studies. I would also thank our collaborators, Dr. Taras Kolodiazhyni and Dr. Athena Safa Sefat, for assisting us with data collection for numerous samples. Additionally, I would like to thank all the people at McMaster who helped me along the way to achieve my goals, be it through teaching, scheduling, craftsmanship, or otherwise.

Finally, I would like to give a special thanks to my friends and family for their support and companionship over the years. I thank my cat, Gandalf, for being the best friend I could have asked for. Thanks are also in order for my Sun Tzu and Enixx friends for being there after work and helping me relax and unwind. And of course, I thank my family: Harry, Auntie Heather, Sarah, and my Dad, for helping me get here today.

# Table of Contents

Chapter 1. Introduction .....	1
1.1 Discovery of Thermoelectricity .....	1
1.2 Applications of Thermoelectric Materials .....	6
1.3 Thermoelectric Efficiency.....	10
1.3.1 Carnot Efficiency.....	10
1.3.2 Optimization of the Power Factor .....	12
1.3.3 Reduction in Thermal Conductivity .....	16
1.4 Benchmark Thermoelectric Materials.....	21
1.4.1 Advancements in Thermoelectric Efficiency .....	21
1.4.2 Bi <sub>2</sub> Te <sub>3</sub> .....	24
1.4.3 Solid solutions of PbTe.....	25
1.4.4 Half-Heusler Phases .....	26
1.4.5 Zintl Compounds .....	27
1.4.6 Clathrates .....	29
1.4.7 Natural Superlattices.....	30
1.5 Materials in focus: Rare-earth pnictide oxides ( <i>RE-Pn-O</i> ) ( <i>Pn</i> = Sb, Bi) .....	34
1.5.1 Tetragonal ( <i>RE<sup>I</sup>RE<sup>II</sup></i> ) <sub>3</sub> SbO <sub>3</sub> Phases .....	37
1.5.2 CaRE <sub>3</sub> SbO <sub>4</sub> and Ca <sub>2</sub> RE <sub>8</sub> Sb <sub>3</sub> O <sub>10</sub> phases .....	38
1.5.3 RE <sub>3</sub> BiO <sub>3</sub> and RE <sub>8</sub> Bi <sub>3</sub> O <sub>8</sub> .....	40
1.5.4 Ca <sub>2</sub> RE <sub>7</sub> Pn <sub>5</sub> O <sub>5</sub> Phases .....	42
Chapter 2. Methodology and Experimentation .....	44
2.1 Synthetic Approach.....	44
2.2 X-ray Diffraction Analysis .....	47
2.2.1 Basic Theory .....	47
2.2.2 X-ray Single Crystal Diffraction .....	54
2.2.3 X-ray Powder Diffraction .....	56
2.3 Energy-dispersive X-ray Spectroscopy and Electron Microprobe Analysis .....	57

2.4 Physical Property Measurements .....	60
2.5 Electronic Structure Calculations .....	62
Chapter 3. Synthesis, Crystal Structure, and Electronic Properties of the Tetragonal ( $RE^I RE^{II}$ ) <sub>3</sub> SbO <sub>3</sub> Phases ( $RE^I = \text{La, Ce}$ ; $RE^{II} = \text{Dy, Ho}$ ).....	65
3.1 Introduction.....	66
3.2 Experimental.....	68
3.2.1 Synthesis .....	68
3.2.2 X-ray Single Crystal Diffraction .....	70
3.2.3 X-Ray Powder Diffraction .....	74
3.2.4 Coordination Polyhedra Analysis .....	74
3.2.5 Microprobe Measurements .....	74
3.2.6 Electrical Resistivity Measurements .....	75
3.2.7 Electronic Band Structure Calculations .....	75
3.3 Results and Discussion .....	76
3.3.1 Composition and Formation of ( $RE^I RE^{II}$ ) <sub>3</sub> SbO <sub>3</sub> .....	76
3.3.2 Structures and Preferential Site Occupancy .....	79
3.3.3 Electrical Resistivity and Electronic Structure .....	86
3.4 Conclusions.....	89
Chapter 4. Synthesis, Crystal Structure, and Electronic Properties of the CaRE <sub>3</sub> SbO <sub>4</sub> and Ca <sub>2</sub> RE <sub>8</sub> Sb <sub>3</sub> O <sub>10</sub> Phases ( $RE$ is a rare-earth metal) .....	91
4.1 Introduction.....	93
4.2 Experimental.....	95
4.2.1 Synthesis .....	95
4.2.2 X-ray Single Crystal Diffraction .....	98
4.2.3 X-Ray Powder Diffraction .....	104
4.2.4 Electron Microprobe Analysis (EPMA) .....	105
4.2.5 Hall Resistivity Measurements .....	105
4.2.6 Electrical Resistivity Measurements .....	106
4.2.7 Electronic Band Structure Calculations .....	106

4.3 Results and Discussion .....	107
4.3.1 Composition of $\text{CaRE}_3\text{SbO}_4$ and $\text{Ca}_2\text{RE}_8\text{Sb}_3\text{O}_{10}$ .....	107
4.3.2 Formation and Stability of $\text{CaRE}_3\text{SbO}_4$ .....	110
4.3.3 Formation and Stability of $\text{Ca}_2\text{RE}_8\text{Sb}_3\text{O}_{10}$ .....	112
4.3.4 Structural Features of $\text{CaRE}_3\text{SbO}_4$ .....	113
4.3.5 Structural Features of $\text{Ca}_2\text{RE}_8\text{Sb}_3\text{O}_{10}$ .....	115
4.3.6 Electrical and Hall Resistivity .....	118
4.3.7 Electronic Structure of $\text{CaRE}_3\text{SbO}_4$ .....	124
4.3.8 Electronic Structure of $\text{Ca}_2\text{RE}_8\text{Sb}_3\text{O}_{10}$ .....	125
4.4 Conclusions.....	127
 Chapter 5. Synthesis, Crystal Structure, and Physical Properties of the $\text{Gd}_3\text{BiO}_3$ and $\text{Gd}_8\text{Bi}_3\text{O}_8$ phases .....	129
5.1 Introduction.....	130
5.2 Experimental .....	133
5.2.1 Synthesis .....	133
5.2.2 X-ray Single Crystal Diffraction .....	135
5.2.3 X-Ray Powder Diffraction .....	138
5.2.4 Energy-Dispersive X-ray Spectroscopy .....	138
5.2.5 Electron Microprobe Analysis (EPMA) .....	138
5.2.6 Coordination Polyhedra Analysis .....	139
5.2.7 Thermoelectric Measurements .....	139
5.2.8 Magnetic Measurements .....	140
5.2.9 Electronic Band Structure Calculations .....	141
5.3 Results and Discussion .....	142
5.3.1 Structures .....	142
5.3.2 Formation of $\text{Gd}_3\text{BiO}_3$ and $\text{Gd}_8\text{Bi}_3\text{O}_8$ .....	143
5.3.3 Physical Properties .....	148
5.3.4 Electronic Structures .....	149
5.4 Conclusions.....	151

Chapter 6. Investigation of the physical properties and compositions of the $\text{Ca}_2\text{RE}_7\text{Pn}_5\text{O}_5$ series ( $\text{RE}$ is a rare-earth metal, $\text{Pn} = \text{Sb, Bi}$ ) .....	153
6.1 Introduction.....	154
6.2 Experimental .....	157
6.2.1 Synthesis.....	157
6.2.2 X-ray Single Crystal Diffraction .....	159
6.2.3 X-Ray Powder Diffraction .....	163
6.2.4 Electron Microprobe Analysis (EPMA).....	164
6.2.5 Electrical Resistivity Measurements .....	164
6.2.6 Electronic Band Structure Calculations.....	165
6.3 Results and Discussion .....	166
6.3.1 Phase Formation and Stability.....	166
6.3.2 Structural Determination and Analysis.....	167
6.3.3 Compositional Analysis.....	169
6.3.4 Electrical Properties and Electronic Structure.....	171
6.4 Conclusions.....	175
Chapter 7. Conclusions and Future Work.....	176
7.1 Structural Features .....	176
7.2 Chemistry and Structural Modification .....	177
7.3 Physical Properties.....	179
7.4 Further Exploration of the $\text{RE-Pn-O}$ System .....	182
Appendix.....	185
A1. X-ray Powder Diffraction Data .....	185
A1.1 Tetragonal $(\text{RE}^{\text{I}}\text{RE}^{\text{II}})_3\text{SbO}_3$ .....	186
A1.2 $\text{CaRE}_3\text{SbO}_4$ and $\text{Ca}_2\text{RE}_8\text{Sb}_3\text{O}_{10}$ .....	188
A1.3 $\text{Gd}_8\text{Bi}_3\text{O}_8$ .....	193
A1.4 $\text{Ca}_2\text{RE}_7\text{Pn}_5\text{O}_5$ .....	193
A2. Additional X-ray Single Crystal Data .....	197

A3. Additional Electronic Structures .....	205
A4. Additional Physical Property Data .....	211
References .....	214

## List of Figures

Figure	Description	Page
1.1	The Seebeck effect produced from a junction of two dissimilar metals	2
1.2	A basic thermoelectric device constructed from p- and n-type components	7
1.3	Schematic diagram of a radioisotope thermoelectric generator (RTG)	9
1.4	Thermoelectric device efficiency as a function of the temperature gradient and the figure of merit ( $T_C = 300$ K)	12
1.5	The combination of momentum wavevectors in the Brillouin zone resulting in harmonic (normal) and anharmonic (Umklapp) vibrations	19
1.6	Structure of $\text{Bi}_2\text{Te}_3$ , viewed in the (111) direction. $\text{BiTe}_6$ polyhedra are shown in blue	24
1.7	Structure of $\text{Yb}_{14}\text{MnSb}_{11}$ , viewed along the c- and b-directions (left and right, respectively). Hypervalent $\text{Sb}_3^{7-}$ bonds (blue atoms linked together), $\text{MnSb}_4^{10-}$ tetrahedra (purple) and $\text{Yb}^{2+}$ atoms (black) are shown	28
1.8	Clathrate cage structures displaying the different guest atom arrangements for the type I (left) and type II (right) clathrates	29
1.9	Schematic diagram of a natural superlattice structure combining two distinct building blocks into one phase	31
1.10	Structure of $\text{Na}_x\text{Co}_2\text{O}_4$ , viewed along the (111) direction. $\text{CoO}_6$ octahedra are shown in blue	33
1.11	Rare-earth antimonate and bismuthate crystal structures. (a) $\text{RESb}_5\text{O}_{12}$ , (b) $\text{RE}_3\text{Sb}_5\text{O}_{12}$ , (c) $\text{RE}_3\text{SbO}_7$ , (d) $\text{RESbO}_4$ , (e) $\text{RE}_{10}\text{Bi}_8\text{O}_{27}$	36
1.12	The $(\text{RE}^{\text{I}}\text{RE}^{\text{II}})_3\text{SbO}_3$ phase shown with the RE1 and RE2 sites (light gray and dark gray, respectively)	38
1.13	Conversion of $\text{CaRE}_3\text{SbO}_4$ into $\text{Ca}_2\text{RE}_8\text{Sb}_3\text{O}_{10}$ . A portion of the	39

	CaRE <sub>3</sub> SbO <sub>4</sub> framework is preserved in Ca <sub>2</sub> RE <sub>8</sub> Sb <sub>3</sub> O <sub>10</sub> (gray background)	
1.14	Reaction pathway of GdBi and Gd <sub>2</sub> O <sub>3</sub> to Gd <sub>8</sub> Bi <sub>3</sub> O <sub>8</sub> and ultimately Gd <sub>2</sub> BiO <sub>2</sub>	41
1.15	Structure of Ca <sub>2</sub> RE <sub>7</sub> Sb <sub>5</sub> O <sub>5</sub> , viewed along the c- and b-directions, respectively	43
2.1	A sample of PrSb before (top) and after (bottom) reaction at high temperature	45
2.2	Radio Frequency Induction Furnace used for high temperature synthesis. The molybdenum susceptor containing samples sealed in tantalum ampoules (a) is heated in the apparatus shown in (b). A schematic diagram of the equipment is shown in (c)	47
2.3	Diffraction of X-rays in a periodic lattice. When the path difference (bolded lines) between adjacent beams, $2d_{hkl}\sin\theta$ , is equal to a multiple of the incident wavelength $\lambda$ , constructive interference occurs and a signal is detected	49
2.4	Schematic diagram of Ewald's sphere, displaying the relationship between the incident wavelength, reciprocal space, and real space	51
2.5	Scattering of X-rays by an atom with a diffraction angle of $\theta$ equal to $0^\circ$ (left) and $\theta$ greater than $0^\circ$ (right)	52
2.6	Generalized X-ray single crystal diffraction instrument diagram	56
2.7	A sample holder (a) containing bulk samples and single crystals for energy dispersive X-ray spectroscopy (EDS) measurements. A scanning electron microscope (SEM) image of a crystal is shown in (b), while an example EDS spectrum is shown in (c).	59
2.8	Illustration of the Hall effect. A current $I$ is passed through a material with a magnetic field $B$ applied at a 90 degree angle. The result is a voltage $V$ perpendicular to both the current and the magnetic field	62
3.1	The tetragonal $(RE^I RE^{II})_3SbO_3$ structure and its building block type composed of $RE_4O$ tetrahedra	81

3.2	Comparison of the tetragonal ( $RE^I RE^{II}$ ) <sub>3</sub> SbO <sub>3</sub> (left), monoclinic $RE_3$ SbO <sub>3</sub> (middle), and monoclinic $RE_8$ Sb <sub>3-8</sub> O <sub>8</sub> (right) phases. Different building block types are highlighted with different colours	82
3.3	Coordination polyhedra of the $RE1$ site (left) and the $RE2$ site (right) in the tetragonal ( $RE^I RE^{II}$ ) <sub>3</sub> SbO <sub>3</sub> phases	83
3.4	Electrical resistivities of the Ce <sub>1.5</sub> Ho <sub>1.5</sub> SbO <sub>3</sub> , La <sub>1.5</sub> Dy <sub>1.5</sub> SbO <sub>3</sub> , and La <sub>1.5</sub> Ho <sub>1.5</sub> SbO <sub>3</sub> samples	87
3.5	Contribution of orbitals to bands near the Fermi levels in the electronic band structure of LaDy <sub>2</sub> SbO <sub>3</sub>	89
4.1	X-ray powder diffraction patterns showing the conversion of CaGd <sub>3</sub> SbO <sub>4</sub> into Ca <sub>2</sub> Gd <sub>8</sub> Sb <sub>3</sub> O <sub>10</sub> after heat treatments at 1300°C. The dashed lines correspond to the positions of the Ca <sub>2</sub> Gd <sub>8</sub> Sb <sub>3</sub> O <sub>10</sub> diffraction peaks only, while the solid lines correspond to a set of overlapping peaks of both CaGd <sub>3</sub> SbO <sub>4</sub> and Ca <sub>2</sub> Gd <sub>8</sub> Sb <sub>3</sub> O <sub>10</sub>	112
4.2	The CaRE <sub>3</sub> SbO <sub>4</sub> (left) and Ca <sub>2</sub> RE <sub>8</sub> Sb <sub>3</sub> O <sub>10</sub> (right) structures viewed along the $c$ and $b$ directions, respectively. The 2D slabs in each structure are composed of RE <sub>4</sub> O tetrahedra. The CaRE <sub>3</sub> SbO <sub>4</sub> structure contains only one type of building block while the Ca <sub>2</sub> RE <sub>8</sub> Sb <sub>3</sub> O <sub>10</sub> structure contains two types. Only the RE sites are shown for Ca <sub>2</sub> RE <sub>8</sub> Sb <sub>3</sub> O <sub>10</sub>	115
4.3	Electron density maps of the Ca <sub>2</sub> Sm <sub>8</sub> Sb <sub>3</sub> O <sub>10</sub> structure displaying the Sb1 atoms (upper map, $z = 0$ ) and the Sb2 atoms (lower map, $z = 0.389$ ). The oblong shape of the electron density for the Sb2 atoms suggests split positions	118
4.4	Electrical resistivities of the phase pure CaRE <sub>3</sub> SbO <sub>4</sub> samples	122
4.5	Electrical resistivities of the phase pure Ca <sub>2</sub> RE <sub>8</sub> Sb <sub>3</sub> O <sub>10</sub> and Ca <sub>2</sub> RE <sup>I</sup> <sub>4</sub> RE <sup>II</sup> <sub>4</sub> Sb <sub>3</sub> O <sub>10</sub> samples	122
4.6	Calculated total and partial densities of states (DOS) for the Sm <sub>4</sub> SbO <sub>4</sub> structure. The Fermi level is placed at the energy corresponding to the electron count of the CaSm <sub>3</sub> SbO <sub>4</sub> composition	125

4.7	Calculated electronic band structure of the $\text{Sm}_{10}\text{Sb}_3\text{O}_{10}$ structure, including the total and partial densities of states. The Fermi level is placed at the energy level corresponding to the $\text{Ca}_2\text{Sm}_8\text{Sb}_3\text{O}_{10}$ composition	126
5.1	The $\text{Gd}_3\text{BiO}_3$ (left) and $\text{Gd}_8\text{Bi}_3\text{O}_8$ (right) structures viewed along the $b$ directions of each unit cell. Both structures are defined by a framework of $\text{Gd}_4\text{O}$ tetrahedra which stack together to form building blocks of composed of two, four, or six units (green, orange, and blue ellipses, respectively)	143
5.2	The surface of a tantalum ampoule containing the reaction of $\text{Gd}_3\text{BiO}_3$ . Only Gd and O signals are observed from the EDS data, indicating that $\text{Gd}_2\text{O}_3$ and/or Gd may have been expelled during the reaction and deposited on the ampoule	145
5.3	Electrical resistivity data (left) and Seebeck coefficient data (right) of a sample of $\text{Gd}_8\text{Bi}_3\text{O}_8$	148
5.4	Thermal conductivity data (left) and Magnetization data (right) of a sample of $\text{Gd}_8\text{Bi}_3\text{O}_8$	149
5.5	Contribution of orbitals to bands near the Fermi level in the electronic band structure of $\text{Gd}_3\text{BiO}_3$ (left) and $\text{Gd}_8\text{Bi}_3\text{O}_8$ (right)	151
6.1	Structural comparison of the $P4/nmm$ and $P4/n$ structures. The normally vacant sites in the $P4/n$ structure are hereto assigned to be occupied by calcium in $\text{Ca}_2\text{RE}_7\text{Pn}_5\text{O}_5$ (yellow atoms).	169
6.2	Electrical resistivity data for the $\text{Ca}_2\text{RE}_7\text{Pn}_5\text{O}_5$ samples: a) $\text{Ca}_2\text{Pr}_7\text{Sb}_5\text{O}_5$ , b) $\text{Ca}_2\text{Sm}_7\text{Sb}_5\text{O}_5$ , c) $\text{Ca}_2\text{Gd}_7\text{Sb}_5\text{O}_5$ , d) $\text{Ca}_2\text{Dy}_7\text{Sb}_5\text{O}_5$ , e) $\text{Ca}_2\text{Gd}_7\text{Bi}_5\text{O}_5$ , and f) $\text{Ca}_2\text{Dy}_7\text{Bi}_5\text{O}_5$ .	172
6.3	Seebeck coefficient data for the $\text{Ca}_2\text{RE}_7\text{Pn}_5\text{O}_5$ samples: a) $\text{Ca}_2\text{Pr}_7\text{Sb}_5\text{O}_5$ , b) $\text{Ca}_2\text{Sm}_7\text{Sb}_5\text{O}_5$ , c) $\text{Ca}_2\text{Gd}_7\text{Sb}_5\text{O}_5$ , d) $\text{Ca}_2\text{Dy}_7\text{Sb}_5\text{O}_5$ , e) $\text{Ca}_2\text{Gd}_7\text{Bi}_5\text{O}_5$ , and f) $\text{Ca}_2\text{Dy}_7\text{Bi}_5\text{O}_5$ .	173
6.4	Calculated electronic band structures for the $\text{Ca}_2\text{Gd}_7\text{Sb}_5\text{O}_5$ structure (left) and $\text{Ca}_2\text{Gd}_7\text{Bi}_5\text{O}_5$ structure (right).	174

7.1	The $\text{Ca}_4\text{REBi}_3\text{O}$ structure, viewed along the c-direction. This structure features isolated $(\text{Ca},\text{RE})_4\text{O}$ tetrahedra and a three dimensional <i>RE</i> -Bi framework	183
A1-1	Rietveld refinement of the X-ray powder data collected for a $\text{La}_{1.5}\text{Dy}_{1.5}\text{SbO}_3$ sample	186
A1-2	Rietveld refinement of the X-ray powder data collected for a $\text{La}_{1.5}\text{Ho}_{1.5}\text{SbO}_3$ sample	186
A1-3	Rietveld refinement of the X-ray powder data collected for a $\text{Ce}_{1.5}\text{Dy}_{1.5}\text{SbO}_3$ sample. This sample was not measured for physical properties, but can confirm the existence of the $\text{Ce}_{1.5}\text{Dy}_{1.5}\text{SbO}_3$ phase	187
A1-4	Rietveld refinement of the X-ray powder data collected for a $\text{Ce}_{1.5}\text{Ho}_{1.5}\text{SbO}_3$ sample	187
A1-5	Rietveld refinement of the X-ray powder data collected for a $\text{CaCe}_3\text{SbO}_4$ sample	188
A1-6	Rietveld refinement of the X-ray powder data collected for a $\text{CaPr}_3\text{SbO}_4$ sample	188
A1-7	Rietveld refinement of the X-ray powder data collected for a $\text{CaNd}_3\text{SbO}_4$ sample	189
A1-8	Rietveld refinement of the X-ray powder data collected for a $\text{CaSm}_3\text{SbO}_4$ sample	189
A1-9	Rietveld refinement of the X-ray powder data collected for a $\text{CaGd}_3\text{SbO}_4$ sample	190
A1-10	Rietveld refinement of the X-ray powder data collected for a $\text{CaDy}_3\text{SbO}_4$ sample. This sample was not measured for physical properties, but can confirm the existence of the $\text{CaDy}_3\text{SbO}_4$ phase	190
A1-11	Rietveld refinement of the X-ray powder data collected for a $\text{Ca}_2\text{Nd}_8\text{Sb}_3\text{O}_{10}$ sample	191
A1-12	Rietveld refinement of the X-ray powder data collected for a $\text{Ca}_2\text{Nd}_4\text{Sm}_4\text{Sb}_3\text{O}_{10}$ sample	191

A1-13	Rietveld refinement of the X-ray powder data collected for a $\text{Ca}_2\text{Sm}_8\text{Sb}_3\text{O}_{10}$ sample	192
A1-14	Rietveld refinement of the X-ray powder data collected for a $\text{Ca}_2\text{Sm}_4\text{Gd}_4\text{Sb}_3\text{O}_{10}$ sample	192
A1-15	Rietveld refinement of the X-ray powder data collected for a $\text{Gd}_8\text{Bi}_3\text{O}_8$ sample	193
A1-16	Rietveld refinement of the X-ray powder data collected for a $\text{Ca}_2\text{Ce}_7\text{Sb}_5\text{O}_5$ sample	193
A1-17	Rietveld refinement of the X-ray powder data collected for a $\text{Ca}_2\text{Pr}_7\text{Sb}_5\text{O}_5$ sample	194
A1-18	Rietveld refinement of the X-ray powder data collected for a $\text{Ca}_2\text{Sm}_7\text{Sb}_5\text{O}_5$ sample	194
A1-19	Rietveld refinement of the X-ray powder data collected for a $\text{Ca}_2\text{Gd}_7\text{Sb}_5\text{O}_5$ sample	195
A1-20	Rietveld refinement of the X-ray powder data collected for a $\text{Ca}_2\text{Gd}_7\text{Bi}_5\text{O}_5$ sample	195
A1-21	Rietveld refinement of the X-ray powder data collected for a $\text{Ca}_2\text{Dy}_7\text{Sb}_5\text{O}_5$ sample	196
A1-22	Rietveld refinement of the X-ray powder data collected for a $\text{Ca}_2\text{Dy}_7\text{Bi}_5\text{O}_5$ sample	196
A3-1	Calculated electronic structure of $\text{La}_{1.5}\text{Dy}_{1.5}\text{SbO}_3$	205
A3-2	Calculated electronic structure of $\text{La}_{1.5}\text{Ho}_{1.5}\text{SbO}_3$	206
A3-3	Calculated electronic structure of $\text{Ce}_{1.5}\text{Ho}_{1.5}\text{SbO}_3$	206
A3-4	Calculated total and partial densities of states (DOS) for $\text{Ce}_4\text{SbO}_4$ (top left), $\text{Pr}_4\text{SbO}_4$ (top right), $\text{Nd}_4\text{SbO}_4$ (bottom left), and $\text{Gd}_4\text{SbO}_4$ (bottom right). The Ca/ <i>RE</i> site is assumed to be occupied by <i>RE</i> atoms. The Fermi levels are placed at the energies corresponding to the electron count of the $\text{CaRE}_3\text{SbO}_4$ composition	207

A3-5	Calculated total and partial densities of states (DOS) for $\text{Pr}_{10}\text{Sb}_3\text{O}_{10}$ (top left), $\text{Nd}_{10}\text{Sb}_3\text{O}_{10}$ (top right), $\text{Gd}_{10}\text{Sb}_3\text{O}_{10}$ (bottom left), and $\text{Tb}_{10}\text{Sb}_3\text{O}_{10}$ (bottom right). All Ca/ <i>RE</i> sites are assumed to be occupied by <i>RE</i> atoms only. The Fermi levels are placed at the energies corresponding to the electron count of the $\text{Ca}_2\text{RE}_8\text{Sb}_3\text{O}_{10}$ composition	208
A3-6	Calculated total and partial densities of states (DOS) for $\text{Sm}_{10}\text{Sb}_3\text{O}_{10}$ superstructures S1 (top left), S2 (top right), S3 (bottom left), and S4 (bottom right). Each electronic structure corresponds to a different structural model presented in Figure 4.4. All Ca/ <i>RE</i> sites are assumed to be occupied by <i>RE</i> atoms only. The Sb1 <i>p</i> states and the Sb2 <i>p</i> states correspond to the ordered and disordered antimony atoms, respectively, in the parent $\text{Ca}_2\text{RE}_8\text{Sb}_3\text{O}_{10}$ structure. The Fermi levels are placed at the energies corresponding to the electron count of the $\text{Ca}_2\text{RE}_8\text{Sb}_3\text{O}_{10}$ composition	209
A3-7	Calculated electronic band structures for $\text{Ca}_2\text{Pr}_7\text{Sb}_5\text{O}_5$ (left), $\text{Ca}_2\text{Sm}_7\text{Sb}_5\text{O}_5$ (middle) and $\text{Ca}_2\text{Dy}_7\text{Bi}_5\text{O}_5$ (right).	210
A4-1	Inverse magnetic susceptibility for $\text{Ce}_{1.5}\text{Ho}_{1.5}\text{SbO}_3$ . A change in slope is observed at lower temperatures, corresponding to the ground state splitting of $\text{Ce}^{3+}$	211
A4-2	Magnetization (left) and inverse susceptibility (right) data for the $\text{Ca}_2\text{RE}_8\text{Sb}_3\text{O}_{10}$ and $\text{Ca}_2\text{RE}^{\text{I}}_4\text{RE}^{\text{II}}_4\text{Sb}_3\text{O}_{10}$ samples	212
A4-3	Magnetization data for the $\text{Ca}_2\text{RE}_7\text{Sb}_5\text{O}_5$ samples: a) $\text{Ca}_2\text{Pr}_7\text{Sb}_5\text{O}_5$ , b) $\text{Ca}_2\text{Sm}_7\text{Sb}_5\text{O}_5$ , c) $\text{Ca}_2\text{Gd}_7\text{Sb}_5\text{O}_5$ , and d) $\text{Ca}_2\text{Dy}_7\text{Sb}_5\text{O}_5$ .	212
A4-4	Magnetization data for the $\text{Ca}_2\text{RE}_7\text{Bi}_5\text{O}_5$ samples: e) $\text{Ca}_2\text{Gd}_7\text{Bi}_5\text{O}_5$ and f) $\text{Ca}_2\text{Dy}_7\text{Bi}_5\text{O}_5$ .	213

## List of Tables

Table	Description	Page
3.1	$(RE^I RE^{II})_3SbO_3$ samples prepared by high-temperature synthesis at 1550°C	70
3.2	Crystallographic and refinement data for the $(RE^I RE^{II})_3SbO_3$ crystals	72
3.3	Atomic parameters for the $(RE^I RE^{II})_3SbO_3$ crystals	73
3.4	Compositions of the tetragonal $(RE^I RE^{II})_3SbO_3$ phases based on the EPMA and the X-ray single crystal analyses. The EPMA results were normalized to one Sb atom	77
3.5	Coordination polyhedra volumes of the largest and smallest sites in the tetragonal $(RE^I RE^{II})_3SbO_3$ and monoclinic $RE_3SbO_3$ phases	85
3.6	Room temperature electrical resistivities and activation energies of the $La_{1.5}Dy_{1.5}SbO_3$ , $La_{1.5}Ho_{1.5}SbO_3$ and $Ce_{1.5}Ho_{1.5}SbO_3$ samples	87
4.1	Ca-RE-Sb-O samples prepared by high-temperature synthesis in an induction furnace	97
4.2	Crystallographic and refinement data for the $CaRE_3SbO_4$ crystals	100
4.3	Crystallographic and refinement data for the $Ca_2RE_8Sb_3O_{10}$ crystals	102
4.4	Refinement results for the $Ca_2RE_8Sb_3O_{10}$ crystals by placing Sb2 at the $4i$ and $8j$ sites	104
4.5	Comparison of experimentally determined compositions of $CaRE_3SbO_4$ , $Ca_2RE_8Sb_3O_{10}$ , and $Ca_2RE^I_4RE^{II}_4Sb_3O_{10}$ samples derived from EPMA and X-ray single crystal diffraction experiments	109
4.6	Shortest and longest possible Sb2-Sb2 distances for the $Ca_2RE_8Sb_3O_{10}$ phases	117
4.7	Room temperature electrical and Hall resistivity data for selected $CaRE_3SbO_4$ , $Ca_2RE_8Sb_3O_{10}$ , and $Ca_2RE^I_4RE^{II}_4Sb_3O_{10}$ samples	120

5.1	Crystallographic and refinement data for the $Gd_3BiO_3$ and $Gd_8Bi_3O_8$ crystals	136
5.2	Atomic parameters for the $Gd_3BiO_3$ and $Gd_8Bi_3O_8$ crystals	137
5.3	Refinement results for the $Gd_8Bi_3O_8$ crystal by placing Bi2 at the $2a$ and $4g$ sites	143
5.4	Coordination polyhedra volumes of the Sb and Bi sites in selected Gd-Sb-O and Gd-Bi-O phases	147
6.1	$Ca_2RE_7Pn_5O_5$ samples prepared by high-temperature synthesis in an induction furnace ( $Pn = Sb, Bi$ ).	159
6.2	Crystallographic and refinement data for the $Ca_2RE_7Pn_5O_5$ crystals.	161
6.3	Refinement results for the $Ca_2RE_7Pn_5O_5$ crystals based on the occupation of the $2a$ site by calcium.	163
6.4	Comparison of experimentally determined compositions of $Ca_2RE_7Sb_5O_5$ and $Ca_2RE_7Bi_5O_5$ samples derived from EPMA and X-ray single crystal diffraction experiments.	170
6.5	Room temperature electrical and activation energy data for selected $Ca_2RE_7Pn_5O_5$ samples.	172
7.1	Room temperature electrical resistivity values and electronic band gaps of selected $RE-Pn-O$ phases.	181
A2-1	Crystallographic and refinement data for the $Dy_3SbO_3$ crystal	197
A2-2	Atomic parameters for the $Dy_3SbO_3$ crystal	198
A2-3	Atomic parameters for the $CaRE_3SbO_4$ crystals	199
A2-4	Atomic parameters for the $Ca_2RE_8Sb_3O_{10}$ crystals	200
A2-5	Atomic parameters for the $Ca_2RE_7Pn_5O_5$ crystals.	203

## **Chapter 1. Introduction**

Thermoelectric materials display two unique properties that are attractive for commercial and industrial purposes: they are able to produce a current under application of a temperature gradient and vice versa. These two properties make thermoelectrics viable as operating components in power generators and heating/cooling devices.<sup>1,2</sup>

### **1.1 Discovery of Thermoelectricity**

Thermoelectricity is the combination of three phenomena: the Seebeck, Peltier, and Thomson effects, named after the scientists that discovered them. In 1822, Thomas Johann Seebeck discovered that upon application of heat at a junction of two dissimilar metals, a magnetic field would be produced, as evidenced by the deflection of a magnetic compass needle.<sup>3</sup> Upon further experimentation, he found that the degree of deflection of the compass needle was proportional to the temperature gradient applied. Not realizing the electrical nature of this phenomenon, Seebeck classified this effect as thermomagnetism and it was not until 1834 that Danish scientist Hans Christian Ørsted correctly attributed this property to the flow of electric current.<sup>4</sup>

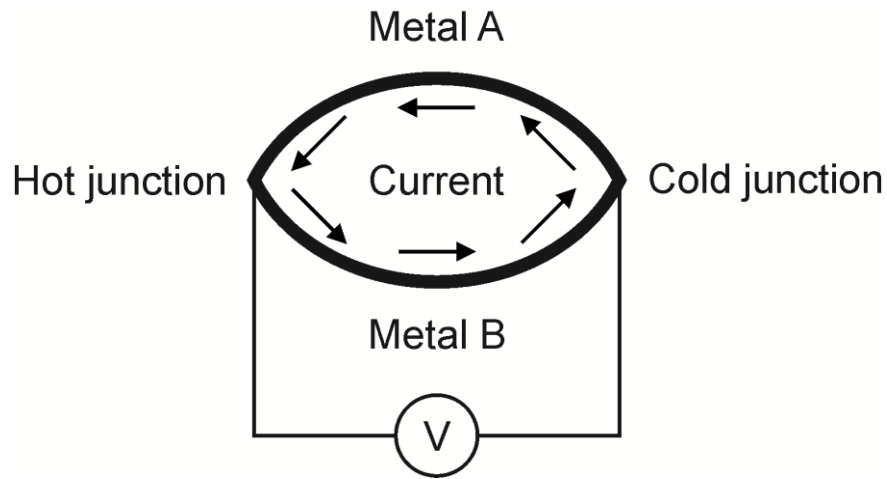


**Figure 1.1. The Seebeck effect produced from a junction of two dissimilar metals.**

The Seebeck coefficient  $\alpha$  (or  $S$ ), commonly referenced as thermopower, is defined as the change in voltage ( $\Delta V$ ) against the temperature gradient ( $\Delta T$ ) for a given distance.<sup>5</sup>

$$\alpha = -\left(\frac{\Delta V}{\Delta T}\right) \quad (1-1)$$

The heat provided at one junction causes an increase in the energy of the charge carriers, allowing them to diffuse from the hot side to the cold side. Equilibrium is reached when the thermal flow of charge carriers to the cold side is offset by the electrostatic flow of those charge carriers to the hot side.<sup>6</sup> However, since the two materials linked at the junction are not the same and have different carrier mobilities, a chemical potential (voltage) difference will be created. This naturally creates a change in voltage throughout

the entire apparatus, and the continuous flow of current. This property is most notably utilized in bimetallic thermocouples, which can accurately determine the temperature of a foreign body by measuring the voltage produced upon contact.

The Seebeck was extensively modeled after its discovery, most notably by the Fermi-Dirac distribution theory, which calculated that only electrons within a certain energy range  $\frac{k_B T}{E_F}$  of the electronic band gap contribute to the physical properties of the material<sup>7, 8</sup>, where  $k_B$  is the Boltzmann constant,  $T$  is the temperature, and  $E_F$  is the Fermi energy, defined as the energy at which the probability of finding an electron in a state is 50%. This prefactor not only accounted for previous inconsistencies in the magnitude of the Seebeck coefficient; it also explained why different materials can have different Seebeck coefficients. Furthermore, the Bloch theory of electron wavefunctions<sup>9</sup> was able to explain the origin of positive Seebeck coefficients in certain materials, which classical models failed to describe.<sup>10, 11</sup> If one assumes a free electron model in an electronic structure, then the mass of the charge carriers is proportional to the second derivative of energy with respect to the k-vector.<sup>12</sup>

$$m = \hbar^2 \left( \frac{d^2 E}{dk^2} \right)^{-1} \quad (1-2)$$

This allows for a negative mass of charge carriers, which introduces the concept of electron “holes”, which can be viewed as the absence of an electron, or more precisely, an electron that propagates in the opposite direction. Thus, these electron holes are

responsible for positive Seebeck coefficients observed in experiments. This also leads to the concept of n-type and p-type materials, those with electrical conduction dominated by electrons and holes, respectively. This is quite important for the study and design for thermoelectrics, and will be described further in the dissertation.

The second major property of thermoelectric materials was discovered in 1834 by French scientist Jean Charles Athanase Peltier. It was determined in his experiments that the change in voltage between junctions of two dissimilar metals would result in a temperature gradient being formed between the junctions; the reverse and complimentary process of the Seebeck effect.<sup>13</sup> Peltier's work was further expanded on by Russian scientist Heinrich Friedrich Emil Lenz in 1839, who related the heat transfer between junctions to the specific direction of the current in the circuit.<sup>14</sup> The Peltier effect can be expressed mathematically in terms of the Peltier coefficient  $\Pi$  which represents how much heat  $Q$  is transferred between junctions under a certain implied current  $I$ .<sup>15</sup> Furthermore, the Peltier coefficient is directly related to the Seebeck coefficient and to the temperature.

$$\Pi = \frac{Q}{I} \quad (1-3)$$

$$\Pi = \alpha T \quad (1-4)$$

The third phenomenon associated with thermoelectricity was discovered by British physicist William Thomson (who came to be known later as Lord Kelvin) in 1851,

who observed that a change in heat would occur across a single type of conductor with a temperature gradient when a current was passed through it.<sup>16</sup> The Thomson effect relates the amount of heat  $Q$  that is produced for a given electric current density  $J$  across a non-isothermal segment of length  $l$ .

$$\frac{\partial Q}{\partial T} = -KJ\nabla T = -KJ \frac{\partial T}{\partial l} \quad (1-5)$$

Where  $K$  is the Thomson coefficient, which is itself related to the Seebeck and Peltier effects by the following relationships:

$$K = T \frac{d\alpha}{dT} = \frac{d\Pi}{dT} - \alpha \quad (1-6)$$

Despite the discovery of the Seebeck, Peltier, and Thomson effects, no significant advancement in thermoelectrics was made for decades until Edmund Altenkirch first defined the general expression of thermoelectric efficiency after studying power generators<sup>17</sup> and coolers<sup>18</sup>. This concept was later refined by Abram Fedorovich Ioffe in 1957, who concluded that a good thermoelectric material should have a large Seebeck coefficient  $\alpha$  and electrical conductivity  $\sigma$ , and a low thermal conductivity  $\kappa$ . These parameters were combined into a “Figure of Merit” equation, which calculates the efficiency  $ZT$  of a thermoelectric material at a given temperature  $T$ .<sup>19</sup>

$$ZT = \frac{\alpha^2 \sigma}{\kappa} T \quad (1-7)$$

It was at this time that the choice in thermoelectric materials shifted from metals to semiconductors and semimetals for their superior power factors ( $\alpha^2 \sigma$ ).<sup>20</sup> These materials are now targeted almost exclusively for thermoelectrics research today.

## 1.2 Applications of Thermoelectric Materials

The first thermoelectric devices were produced in the 1950s and 1960s, and mainly incorporated  $\text{Bi}_2\text{Te}_3$ ,  $\text{BiSb}$ , and  $\text{PbTe}$  as the operating component. The interest in these materials grew rapidly during this time as thermoelectrics were expected to replace other forms of power generation and cooling in commercial and military applications.<sup>21-23</sup> However, despite extensive research, these devices yielded figure of merit  $ZT$  of about 1, which corresponds to a ~11% total efficiency ( $T_H = 600 \text{ K}$ ,  $T_C = 300 \text{ K}$ ). Although several advancements have been made since this time, thermoelectrics are still limited by low efficiency compared to other energy sources. As such, thermoelectrics are generally restricted to niche applications where long operation hours and compactness outweigh efficiency. However, thermoelectric devices offer several advantages over other competing technologies, including very long operation hours, quietness, precision, versatility, and scalability.

A basic closed circuit thermoelectric device is constructed from both n-type and p-type materials which are connected electrically in series and thermally in parallel (Figure 1.2). When a current is applied to the device, one side lowers in temperature while the other rejects heat. Similarly, when one side is heated or cooled, an electric current is produced in the material. Both of these processes occur by the movement of electrons and holes in the n-type and p-type materials, respectively.

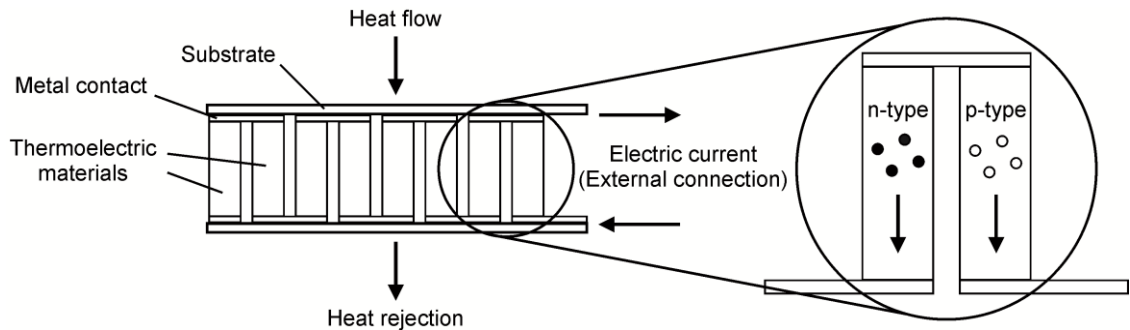


**Figure 1.2. A basic thermoelectric device constructed from p- and n-type components.**

The choice of materials is also important, as the two materials in a device must reach an optimal  $ZT$  at the same operating temperature. Furthermore, the electric current required to achieve peak efficiency may vary with temperature or between materials. This leads to the concept of compatibility factors for power generation<sup>24, 25</sup>, and is essential to the proper design of a thermoelectric device. For a good thermoelectric device with a temperature gradient  $\Delta T$  and average component efficiency  $zT$ , the compatibility factors  $s$  should be within a factor of two or less.

$$s = \frac{(\sqrt{1+zT}-1)}{\alpha T} \quad (1-8)$$

The global demand for additional forms of energy production, as well as the concern for the environment has fueled the recent reemergence of thermoelectrics research. This has led to the discovery of many new materials and a significant increase in thermoelectric device efficiency over the past two decades. As such, thermoelectric devices have found their place in several commercially available products. Thermoelectric coolers and refrigerators offer the advantage of portability and low cost over traditional vapour-based refrigerators. Small-scale electronic devices such as CCD cameras and laser diodes also utilize thermoelectric devices for refrigeration when the cooling power is not large, since device efficiency remains relatively unchanged in spite of low current or size.<sup>26</sup> Other specialized products containing thermoelectric materials include wristwatches<sup>27</sup>, wood stoves<sup>28</sup>, lamps<sup>28</sup>, and cooking pots.<sup>29</sup>

One very useful aspect of thermoelectric devices that has spurred considerable research efforts is their ability to operate with very long operation hours due to a lack of moving parts. This is most beneficial for remote locations where maintenance is not an option, such as underground, deep sea, and outer space.<sup>30</sup> Thermoelectric generators on spacecrafts and exploration rovers may operate for extended periods of time owing to their radioisotope thermoelectric generators (RTGs). These devices contain the highly radioactive, non-fissile <sup>238</sup>Pu which acts as a heat source. The heat emitted by radioactive

decay is then converted into a steady supply of electricity for the operation requirements of the machine, with outer space acting as a heat sink. Since the half-life of  $^{238}\text{Pu}$  is 87.7 years, this corresponds to less than a 1% reduction in power output each year from radiative losses, allowing the device to operate for a very long period of time. The Mars rover Curiosity, contains an RTG to perform the automotive and electronic requirements of its intended mission.<sup>31</sup> The Cassini and Voyager 1 and 2 spacecrafts also contain RTGs which have allowed operational lifetimes of several decades; Voyager 1 has been in operation since 1971 and is currently the farthest spacecraft from Earth at approximately  $2 \times 10^{10}$  km as of 2013.<sup>32-34</sup>

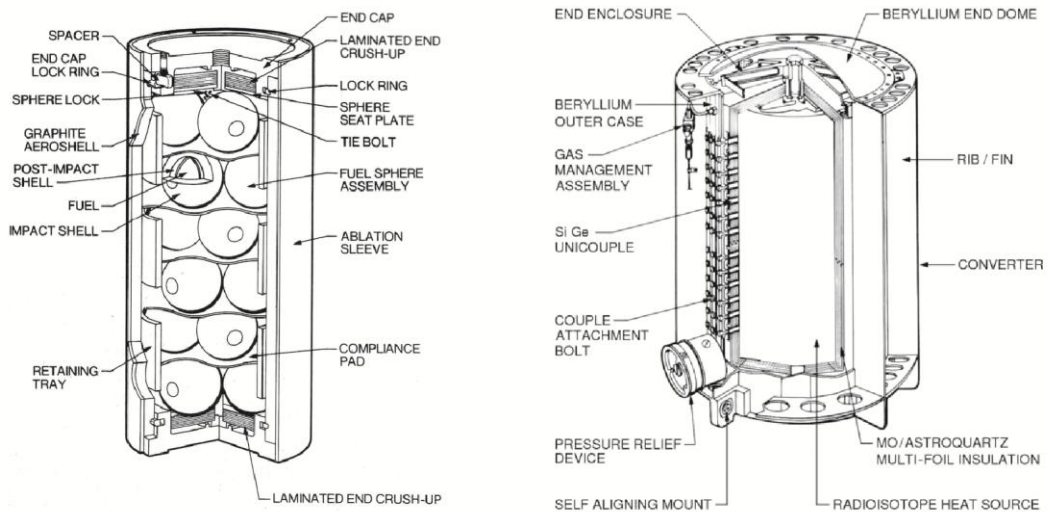


**Figure 1.3. Schematic diagram of a radioisotope thermoelectric generator (RTG).<sup>35</sup>**

Perhaps the most attractive application of a thermoelectric device is the capacity to recover waste heat from combustion and other power generation sources into reusable energy. Nearly all forms of energy production are accompanied by the release of heat, which represents energy that is lost to the surroundings and unable to be harvested. However, since thermoelectrics are able to convert heat into electricity, and thus a usable form of energy, they will likely become increasingly significant as the demand for environmentally friendly sources of energy intensifies. This has led to the incorporation of thermoelectric devices in automobiles, the latter of which loses approximately 60% of the energy generated from fuel combustion as waste heat.<sup>30</sup> The recovery of this energy can be used for air conditioning and electronic operations, which serves to not only reduce environmentally harmful emissions, but improve fuel efficiency.<sup>36</sup>

## **1.3 Thermoelectric Efficiency**

### **1.3.1 Thermoelectric Generator Efficiency**

As previously demonstrated in equation 1-7, a good thermoelectric material should possess a large Seebeck coefficient  $\alpha$ , high electrical conductivity  $\sigma$ , and a low thermal conductivity  $\kappa$ . While the figure of merit  $ZT$  is specific to each material, the efficiency of a thermoelectric *generator* is also related to the Carnot efficiency, and is expressed in terms of the amount of energy provided with respect to the amount of heat supplied, denoted as  $\eta$ .

$$\eta = \frac{T_H - T_C}{T_H} \frac{\sqrt{1 + ZT} - 1}{\sqrt{1 + ZT} + \frac{T_C}{T_H}} \quad (1-9)$$

Thus, for a given temperature difference, the efficiency of a thermoelectric generator is limited by the material efficiency and the Carnot efficiency term. For a thermoelectric material to be as effective as other forms of energy production, the material efficiency  $ZT$  would need to be infinite, in order to make the device efficiency equal to the  $\frac{T_H - T_C}{T_H}$  prefactor alone. This would require either a thermal conductivity of zero, or a power factor of infinity. This is obviously not possible in any material, thus, thermoelectrics suffer from the drawback of relatively low efficiencies. In order for thermoelectric materials to be competitive with other forms of energy production, such as engines, a  $ZT$  of at least 4 would be required.<sup>37</sup>

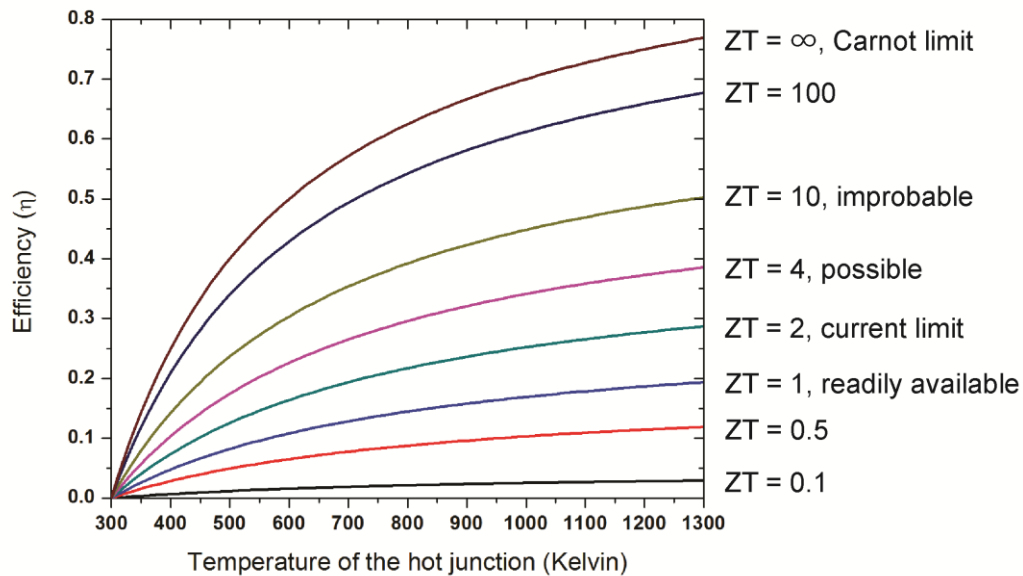


**Figure 1.4. Thermoelectric device efficiency as a function of the temperature gradient and the figure of merit ( $T_C = 300$  K).**

In order to achieve the goal of a designing a material with the highest ZT possible, the Seebeck coefficient and electrical conductivity must be maximized, while the thermal conductivity is kept as low as possible. Such a material is quite challenging to produce, as will be explained further, but there are several strategies available which can make this possible.

### 1.3.2 Optimization of the Power Factor

To achieve high efficiency, the Seebeck coefficient and the electrical conductivity must be as high as possible. A large Seebeck coefficient is necessary to produce and maintain a potential difference between junctions, while a good electrical conductivity is required to excite and transport charge carriers with minimal Joule heating; the process by which heat is produced in a conductor when a current is passed through it, with the

amount of heat released directly proportional to the electrical resistivity. Joule heating is independent of the direction of the current, and thus would eliminate the temperature gradient present.<sup>38</sup>

The electrical conductivity of a solid is directly related to its electronic structure: materials with a large concentration of charge carriers  $n$  at the Fermi level are more conductive. Furthermore, electrical conductivity is also proportional to the mobility of the charge carriers  $\mu$ , which in turn depends on the carrier relaxation time and electronic band curvature.

$$\sigma = ne\mu \quad (1-10)$$

Metals are typically the most conductive solids, due to their large carrier concentrations and carrier mobilities. Since metals are defined by having no band gap at the Fermi level, they are able to conduct electricity effectively even at low temperatures, and only experience a moderate reduction in electrical resistivity with increasing temperature due to atomic vibrations which perturb charge carrier propagation.<sup>39</sup> Conversely, semiconductors and insulators contain finite band gaps, which severely restrict electrical conduction at low temperatures. At elevated temperatures, an increasing number of charge carriers are able to traverse the band gap to the excited states in the conduction band, displaying an exponential increase in conductivity, referred to as an Arrhenius-type conduction.<sup>39</sup>

$$\sigma \propto \exp - \frac{\Delta E}{2k_B T} \quad (1-11)$$

Semiconductors may be classified as either intrinsic or extrinsic, depending on the doping level and electrical conductivity that is observed. Semiconductors of high purity will typically follow the aforementioned behavior, and are known as intrinsic semiconductors. Alternatively, extrinsic semiconductors are heavily doped with impurity atoms, and may instead display an electrical character more closely associated with metals, with a relatively large electrical conductivity even at low temperatures, along with a steady decline with increasing temperature. This is important to thermoelectric material design, as will be noted further.

The Seebeck coefficient of a material depends on the change in potential with respect to the thermal excitation of charge carriers to higher energy states. For a given solid with conduction states close to the Fermi level, such as a metal or heavily doped semiconductor, the resulting potential change is small, resulting in a low Seebeck coefficient with a linear dependence on temperature.<sup>40</sup> For non-degenerate semiconductors and insulators, the increase in Seebeck coefficient for a given temperature change is much larger, as the conduction band states are much higher in energy than the valence band states. These systems typically display Seebeck coefficients having a  $T^{-1}$  relationship with increasing temperature, which is primarily due to the increase in the number of charge carriers and the decrease in voltage change with temperature.<sup>40</sup> The

Seebeck coefficient can be represented mathematically<sup>41</sup> with respect to the charge carrier concentration  $n$ , the temperature  $T$ , and the effective mass of charge carriers  $m^*$ .

$$\alpha = \left( \frac{8\pi^2 k_B^2}{3eh^2} \right) m^* T \left( \frac{\pi}{3n} \right)^{\frac{2}{3}} \quad (1-12)$$

Thus, the Seebeck coefficient is inversely proportional (to the  $^{2/3}$  power) to the charge carrier concentration, and by extension, electrical conductivity. Furthermore, the effective mass of the charge carriers  $m^*$  is also inversely proportional to the carrier mobility. Although no obvious mathematical relationship exists, it is known that charge carriers with large effective masses are slower, and thus have low mobility. These natural tradeoffs of physical properties represent one of the greatest challenges in designing a good thermoelectric material.

As simultaneous optimization of Seebeck coefficient and electrical conductivity is generally not possible, a compromise between both parameters must be reached. In order to achieve the largest power factor possible, a material with a charge carrier concentration of approximately  $10^{19}$  to  $10^{21}$   $\text{cm}^{-3}$  is favoured<sup>20</sup>, which corresponds to a heavily doped semiconductor or semimetal. Good thermoelectric materials will generally have Seebeck coefficients between 100 and 300  $\mu\text{V K}^{-1}$  and electrical conductivities between 200 and 2000  $\text{S cm}^{-1}$ . Fine adjustment of these parameters in a solid is possible by doping and atomic substitution, which may add or subtract charge carriers in the system and achieve the desired physical properties. This is one of the most common methods of designing an

efficient thermoelectric material, and holds other benefits as well, which will be explained further.

### 1.3.3 Reduction in Thermal Conductivity

In order for a thermoelectric material to function efficiently, a temperature gradient between junctions must be maintained so that charge carriers can propagate from the hot side to the cold side and create a potential difference. Thus, the thermal conductivity of a thermoelectric material must be kept as low as possible, to minimize heat transfer between junctions.

The total thermal conductivity of a solid  $\kappa$  is the sum of its two major components: lattice thermal conductivity  $\kappa_l$  and electronic thermal conductivity  $\kappa_{el}$ . As the names imply, these two quantities represent the capacity of the solid to transfer heat by lattice vibrations (phonons) and charge carriers, respectively. One of the major drawbacks to designing a thermoelectric material is the linear relation of electronic thermal conductivity to electrical conductivity, represented mathematically by the Wiedemann-Franz law<sup>42</sup>, where  $L$  is the Lorenz number (approximately  $1.5\text{-}2.5 \times 10^{-8} \text{ V}^2 \text{ K}^{-2}$ ).

$$\kappa_{el} = L\sigma T \quad (1-13)$$

Thus, as the electrical conductivity of a solid increases, so does its ability to transfer heat by its charge carriers. The thermal conductivity of a lattice  $\kappa_l$ , however, is not dependent on any of the other physical properties, and it is this parameter that is targeted for thermal conductivity reduction in thermoelectrics research. The thermal

conductivity of a lattice can be represented mathematically<sup>43</sup> in terms of its specific heat capacity  $C_v$ , the speed of sound in the material  $v_s$ , and the phonon mean free path  $l$ .

$$\kappa_l = \frac{1}{3} C_v v_s l \quad (1-14)$$

The phonon mean free path generally decreases with increasing temperature, as atomic vibrations scatter phonons more frequently.<sup>43</sup> The speed of sound in a lattice is temperature independent, and depends on the density of the solid  $\rho$  and its Young's modulus  $Y$  (the rigidity of the lattice).

$$v_s = \sqrt{\frac{Y}{\rho}} \quad (1-15)$$

The specific heat capacity of a solid is more complicated, and is expressed in terms of temperature, the molar gas constant  $R$ , and the Debye temperature  $\theta_D$  (a characteristic temperature of a solid which corresponds to the maximum frequency of atomic vibrations).

$$C_v = 9R \left(\frac{T}{\theta_D}\right)^3 \int_0^{\frac{\theta_D}{T}} \frac{x^4 e^x}{(e^x - 1)^2} dx \quad (1-16)$$

At high temperatures ( $T \gg \theta_D$ ), the integral portion of the above equation can be simplified to the following:

$$\int_0^{\frac{\theta_D}{T}} \frac{x^4 e^x}{(e^x - 1)^2} dx \approx \frac{1}{3} \left( \frac{\theta_D}{T} \right)^3 \quad (1-17)$$

Then by substituting this quantity in the original equation:

$$C_v = 9R \left( \frac{T}{\theta_D} \right)^3 \frac{1}{3} \left( \frac{\theta_D}{T} \right)^3 = 3R \quad (1-18)$$

This property is also referred to as the Dulong-Petit law<sup>44</sup>, which states that the heat capacity of a solid reaches a constant value at sufficiently high temperature. When this limit is reached, lattice thermal conductivity will no longer increase with temperature past a certain point, which is quite beneficial for thermoelectricity.

Most solids will initially experience an increase in specific heat capacity  $C_v$  and thermal conductivity  $\kappa$  with rising temperatures as additional thermal energy allows more phonons to propagate throughout the lattice. At low temperatures, these phonons will interact with each other in a process that conserves momentum. However, there exists a certain point in which thermal conductivity will decrease with temperature, in which momentum is not conserved. This behavior is known as Umklapp scattering, and is associated with anharmonicity of atomic vibrations.<sup>39</sup> Both processes can be represented by the combination of momentum wavevectors in reciprocal space. If the combination of two wavevectors does not exceed the Brillouin zone, then momentum is conserved and the atoms will vibrate normally. However, if the wavevector sum extends outside the

Brillouin zone, then momentum is not conserved, since by definition, any point outside the Brillouin zone is equal to some point contained inside it.

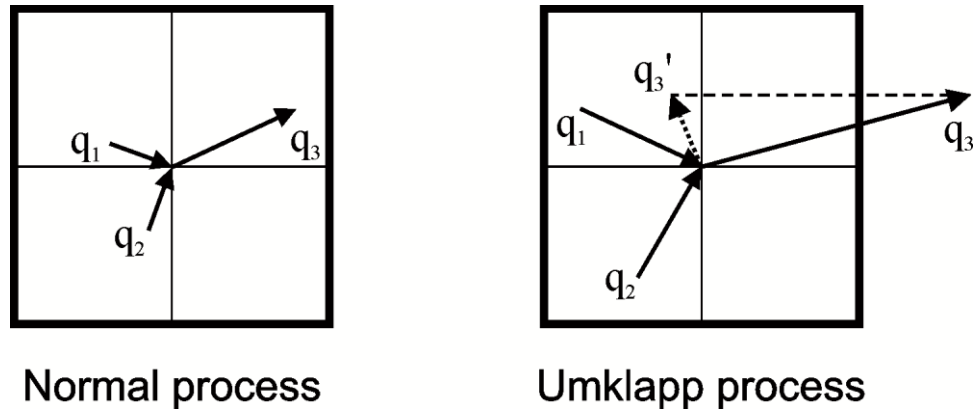


**Figure 1.5. The combination of momentum wavevectors in the Brillouin zone resulting in harmonic (normal) and anharmonic (Umklapp) vibrations.**

Umklapp scattering becomes the dominant source of phonon scattering at high temperatures, and results in a  $T^{-1}$  behavior in the lattice thermal conductivity of a solid. This process is vital for thermoelectricity, as the total thermal conductivity will generally decrease with increasing temperature, leading to better efficiency.

Several generalized strategies exist for minimizing the lattice thermal conductivity, which are generally aimed at reducing the mean free path  $l$  of phonon propagation. The most common strategy involves designing structures which incorporate heavy elements which reduce the speed of sound in the lattice  $v_s$  due to their high densities  $\rho$  (Equation 1-14 and 1-15). Complicated structures with large unit cells are also favourable, since the fraction of lattice vibrations that may effectively transport phonons

is proportional to  $N^{-2/3}$ , where  $N$  is the number of atoms in the unit cell.<sup>20</sup> Atomic disorder, either from site deficiencies or mixing, is also an effective means to reduce lattice thermal conductivity. Phonon mean free path is inversely proportional to large differences in mass between neighboring atoms which are transporting a phonon.<sup>20</sup> This relationship can be represented mathematically by the following equation, where  $V$  is the volume per atom,  $v_s$  is the speed of sound in the solid,  $f_i$  is the fraction of atoms with mass  $m_i$ ,  $m_{av}$  is the average mass of all atoms, and  $m_i$  is the mass of an atom.

$$\frac{1}{l} \propto \frac{V}{4\pi v_s^3} \sum_i f_i \left( \frac{m_{av} - m_i}{m_{av}} \right)^2 \quad (1-19)$$

Excluding contributions from optical phonons, most solids will achieve a minimum in lattice thermal conductivity at higher temperatures due to Umklapp scattering. If we assume the high temperature limit on specific heat capacity  $C_v$  ( $3R$ ) has been reached, then we can simplify equation 1-14 to determine the lowest possible lattice thermal conductivity a solid can have.

$$\kappa_l = \frac{1}{3} (3R) \sqrt{\frac{Y}{\rho}} l = R \sqrt{\frac{Y}{\rho}} l \quad (1-20)$$

For solids with heavy elements, soft chemical bonds, and a very short path length of phonon transport (approaching the size of the unit cell), a minimum in lattice thermal conductivity can be reached. The quantity is sometimes referred to as the “glass limit” of

a solid<sup>45</sup>, and has an approximate value of  $0.1\text{-}0.2 \text{ W m}^{-1} \text{ K}^{-1}$ . One of the primary goals of thermoelectrics research is to design a material that displays crystal-like charge carrier transport properties, but scatters phonons like a glass. This led to the concept of a “phonon glass, electron crystal” (PGEC) material, as postulated by Slack<sup>20</sup>, and serves as one of the principal guidelines in designing new thermoelectric materials today.

## **1.4 Benchmark Thermoelectric Materials**

In order to better understand the strategy behind designing a good thermoelectric or improving a current one, it is useful to examine the progress in thermoelectric materials to date. A summary of relevant materials and design strategies is provided in the following section.

### **1.4.1 Advancements in Thermoelectric Efficiency**

Despite the research efforts made in the 1950s, thermoelectric devices were originally restricted to small scale niche applications. After several decades of stagnancy, theoretical studies performed in the 1990s predicted that the figure of merit of a material could be greatly improved by nanostructuring<sup>46-48</sup>. This approach involves the use of smaller grains sizes in the material, which generally serves to increase the Seebeck coefficient, while reducing electrical conductivity and thermal conductivity. The main advantage of this approach, however, arises from increased grain boundary or second phase scattering, which can result in better thermoelectric efficiency primarily due to the

large reduction in lattice thermal conductivity.<sup>41, 49</sup> Thermoelectric devices incorporating these materials achieved efficiencies  $ZT$  of around 1.5, corresponding to a Carnot efficiency of 10-15%.

Current research is now focusing on new strategies yielding thermoelectrics with efficiencies  $ZT$  of about 1.8 or greater. One of the primary design strategies used to attain these values utilizes an all-length scale phonon scattering structure hierarchy. Simply put, this approach is focused on the design of a material that is able to effectively scatter phonons of short, medium, and long wavelengths. Point defects and second phase nanodomain interfaces are effective at scattering short and medium wavelength phonons, respectively, while long wavelength phonons can be scattered by grain boundaries if the sample is prepared by pulverization and sintering<sup>45</sup>. Electronic band structure engineering via matrix/second phase or intramatrix band convergence is also used as a means to preserve carrier mobility and the power factor when a compositional gradient is present<sup>50-52</sup>. This approach takes advantage of a small difference in valence/conduction bands between the matrix and second phase or between different bands of the same matrix at a given temperature. This provides two advantages: the charge carriers may easily transport between interfaces without scattering, and transport properties may occur from both bands simultaneously. Finally, some efforts have been focused into methods of decoupling the electrical conductivity and Seebeck coefficient in a single material. Charge carrier filtration is one such possibility, which involves the stacking of alternating layers of thermoelectric and barrier materials, such that only high energy carriers

contribute to the physical properties. This may result in a significant increase in Seebeck coefficient with a relatively minor decrease in electrical resistivity.<sup>53-55</sup> Similarly, it has been shown using the Mott formula<sup>56, 57</sup> that a partial decoupling of Seebeck coefficient from electrical conductivity is possible by virtue of the band shape at the Fermi level.

$$\alpha = \pm \frac{\pi^2 k_B^2 T}{3e} \frac{1}{DOS} \left[ \frac{\partial DOS}{\partial E} \right]_{E=E_F} \quad (1-21)$$

While electrical conductivity is proportional to the density of states, it does not have a dependence on the partial derivative  $\left[ \frac{\partial DOS}{\partial E} \right]$ , for which the Seebeck coefficient does. As such, an ideally designed thermoelectric material could potentially optimize both electrical conductivity and Seebeck coefficient at once.

Clearly, there has been a significant advancement in thermoelectric device efficiency in the past fifteen years, resulting in nearly a doubling of ZT. Further improvements will likely be based on the strategies mentioned above, while achieving even lower values of thermal conductivity. This may be quite possible, as it has even been suggested that further reduction of lattice thermal conductivity beyond the classical limit is perhaps possible, as interfacial phonon scattering in nanostructures is anisotropic compared to scattering in bulk materials, which is isotropic.<sup>49</sup> Nanostructuring and electronic band engineering will certainly continue to play a role in improving thermoelectric efficiency even further, as the classical interdependence of physical properties becomes increasingly broken.

### 1.4.2 $\text{Bi}_2\text{Te}_3$

Thermoelectric materials containing  $\text{Bi}_2\text{Te}_3$  are arguably the most extensively studied systems in literature. These materials have currently shown the best room temperature thermoelectric efficiencies with  $ZT$  values of  $\sim 1$ , although this value can be optimized further by dopants and second phases. This structure adopts the rhombohedral  $R\bar{3}m$  symmetry with a 2 : 3 ratio of bismuth to tellurium stacked in alternating layers along the  $c$ -direction. The structure is defined by  $\text{BiTe}_6$  octahedra which form a continuous network along the  $a$ - and  $b$ -directions and are held together by van der Waals forces along the  $c$ -direction.

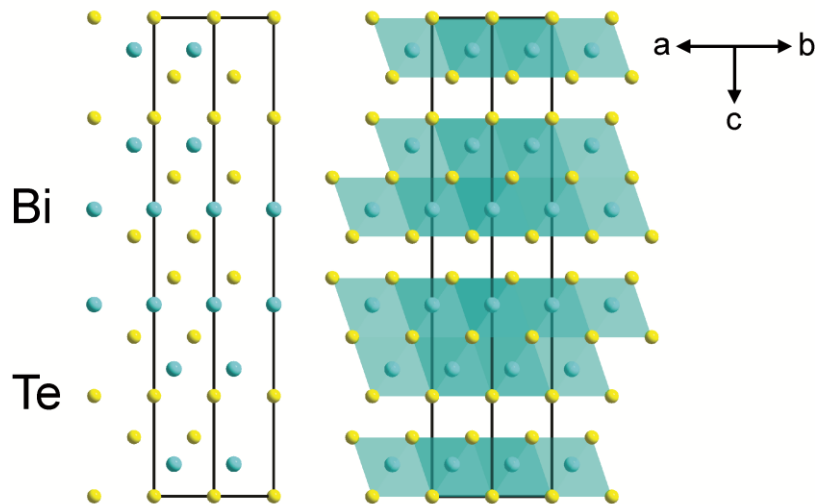


**Figure 1.6. Structure of  $\text{Bi}_2\text{Te}_3$ , viewed in the (111) direction.  $\text{BiTe}_6$  polyhedra are shown in blue.**

This phase attains its high efficiency due to its very heavy atoms, as well as its high carrier mobility and low lattice rigidity due to the small electronegativity difference

between bismuth and tellurium. Additionally, the  $\text{Bi}_2\text{Te}_3$  matrix can easily accommodate dopant atoms, allowing the tuning of its electrical properties and the reduction of lattice thermal conductivity by point defects. This versatility has led to a large number of studies investigating the effects of heteroatom substitution. Bulk nanostructured  $\text{Bi}_2\text{Te}_3$ -based materials have also been recently prepared, and have been demonstrated for use at the macroscopic scale<sup>58-60</sup>. The main drawback of  $\text{Bi}_2\text{Te}_3$ -based materials is their relatively low operating temperatures, since bismuth telluride itself reaches its maximum efficiency around 400 K. Thus, there is a need for thermoelectrics with higher operating temperatures for a greater range of applications.

#### **1.4.3 Solid solutions of PbTe**

PbTe-based materials have long been studied, but have recently emerged as some of the most efficient thermoelectrics to date. This is due to several factors, most importantly nanostructuring via precipitation of a secondary phase in the PbTe matrix. As stated previously, the secondary phases in a bulk material can dramatically improve thermoelectric efficiency by the tuning of charge carrier transport behavior and reduction of lattice thermal conductivity. The addition of a second phase was notably studied in the  $\text{AgPb}_m\text{SbTe}_{2+m}$  (LAST)<sup>61</sup>,  $\text{Ag}(\text{Pb}_{1-x}\text{Sn}_x)_m\text{SbTe}_{2+m}$  (TAGS)<sup>62</sup>, and  $\text{NaPb}_m\text{SbTe}_{2+m}$  (SALT)<sup>63</sup> systems. Studies showed that these materials contained second phase nanodomains embedded in the bulk material with only minor lattice mismatches with the host matrices. These secondary nanophases are able to scatter phonons very effectively while preserving the charge carrier transport properties of the main phase. While the

results can vary significantly depending on the amount of the additional phase present, it was demonstrated in LAST-18 and SALT-20 that the room temperature thermal conductivity of PbTe could be reduced three-fold, achieving ZT values of  $\sim 1.7$  at 675-700 K.<sup>61, 64, 65</sup> Quite recently, PbTe solid solutions containing SrTe secondary phases<sup>45</sup> have been shown to yield ZT values above 2, indicating that there is still more room for thermoelectric efficiency improvement.

#### **1.4.4 Half-Heusler phases**

One of the relatively new classes of thermoelectrics being studied is the Half-Heusler phases. These phases adopt a cubic symmetry and have the general stoichiometry  $M^{\prime}M^{\prime\prime}T$ , where  $M^{\prime}$  and  $M^{\prime\prime}$  are metals and T is a main group element, with the general condition that the three atoms maintain an 18 valence electron count. These structures are derived from the metallic Heusler phases except with vacancies of one of the atoms distributed throughout the lattice. Electronic structure calculations of these phases reveal very sharp bands near the Fermi level, resulting in a relatively large Seebeck coefficient and semiconducting to semimetallic behavior in electrical conductivity.<sup>66, 67</sup> The advantages of these phases include a remarkable flexibility with regards to doping, and excellent thermal stability at high temperatures.

A study on the thermoelectric properties of a  $Zr_{0.5}Hf_{0.5}Ni_{0.8}Pd_{0.2}Sn_{0.99}Sb_{0.01}$  alloy reported an efficiency  $ZT \sim 0.7$  at 800 K, which was primarily attributed to phonon scattering by large mass fluctuations in the lattice<sup>68</sup>. Despite this success, Half Heusler phases are limited by their relatively high thermal conductivities, typically around 8-10 W

$\text{m}^{-1} \text{K}^{-1}$ , although a recent study on a  $\text{Hf}_{0.75}\text{Zr}_{0.25}\text{Ni}_{0.9}\text{Pd}_{0.1}\text{Sn}_{0.975}\text{Sb}_{0.025}$  alloy<sup>69</sup> has shown that this value can be decreased to about  $6 \text{ W m}^{-1} \text{K}^{-1}$ . Further decreases in thermal conductivity may allow these materials to be competitive with other thermoelectrics at high temperatures due to their ease of preparation and good thermal stability.

### 1.4.5 Zintl Compounds

Zintl compounds have recently been attracting interest for thermoelectric uses, due to the fact that they may assume a wide variety of complex crystal structures with both ionic and covalent bonding, as well as multiple structural units within the same phase. The structural complexity of these phases reduces phonon propagation efficiency while the covalent bonding of the anions allows for high carrier mobility and good electrical properties.

The  $\text{Yb}_{14}\text{MnSb}_{11}$  phase may be classified as a Zintl compound, and has been shown to display excellent thermoelectric performance<sup>70</sup>. This phase adopts the tetragonal  $I4_1/acd$  space group and has a highly complicated structure with a very large unit cell containing  $\text{MnSb}_4^{10-}$  tetrahedra,  $\text{Sb}_3^{7-}$  clusters and isolated  $\text{Yb}^{2+}$  and  $\text{Sb}^{3-}$  ions. Physical property measurements have revealed this phase possesses a very low thermal conductivity, which may be attributed to its structural complexity. A maximum efficiency is obtained at  $900^\circ\text{C}$  with a ZT value of  $\sim 1$ , which is even greater than that obtained for the SiGe-based materials used for high temperature thermoelectric applications in spacecrafts<sup>71, 72</sup>.

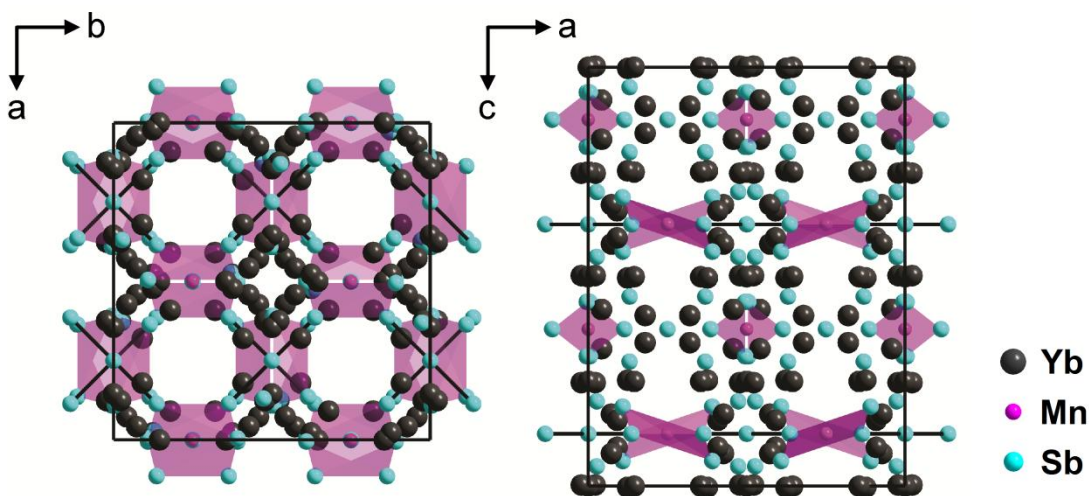


**Figure 1.7. Structure of  $\text{Yb}_{14}\text{MnSb}_{11}$ , viewed along the  $c$ - and  $b$ -directions (left and right, respectively). Hypervalent  $\text{Sb}_3^{7-}$  bonds (blue atoms linked together),  $\text{MnSb}_4^{10-}$  tetrahedra (purple) and  $\text{Yb}^{2+}$  atoms (black) are shown.**

Another noteworthy Zintl compounds,  $\beta\text{-Zn}_4\text{Sb}_3$ , possesses excellent medium temperature thermoelectric efficiency, due in large part to its remarkably low thermal conductivity.<sup>73-75</sup> The phase crystallizes with  $R\bar{3}c$  symmetry and contains  $\text{Sb}_2^{4-}$  dimers, but what makes this structure interesting is that it has three interstitial sites which are partially occupied (< 10%) by Zn atoms. This phase succeeds as a thermoelectric material by phonon scattering at the Zn interstitial sites, while allowing the remaining Zn-Sb framework to operate as an electrical conductor. The thermal conductivity of the structure was found to be one of the lowest obtained for benchmark thermoelectrics, with a value of  $\sim 0.7 \text{ W m}^{-1} \text{ K}^{-1}$  at 650 K.<sup>75</sup> As a result of its electron crystal/phonon-glass properties, this material shows one of the largest figures of merit in the medium temperature range (500-650 K), which makes it attractive for the recovery of waste energy from combustion.

### 1.4.6 Clathrates

One of the best known methods of reducing lattice thermal conductivity is accomplished in structures containing “rattling” atoms. Clathrate structures are notoriously efficient at this purpose, as their cage-like frameworks define large voids that can be filled by guest atoms. Two classes of clathrates are most commonly studied, type I and type II, with the generalized formulas of  $A_2B_6E_{46}$  and  $A_8B_{16}E_{136}$ , respectively, where A and B are different guest atom sites and E is a framework atom.<sup>76</sup>

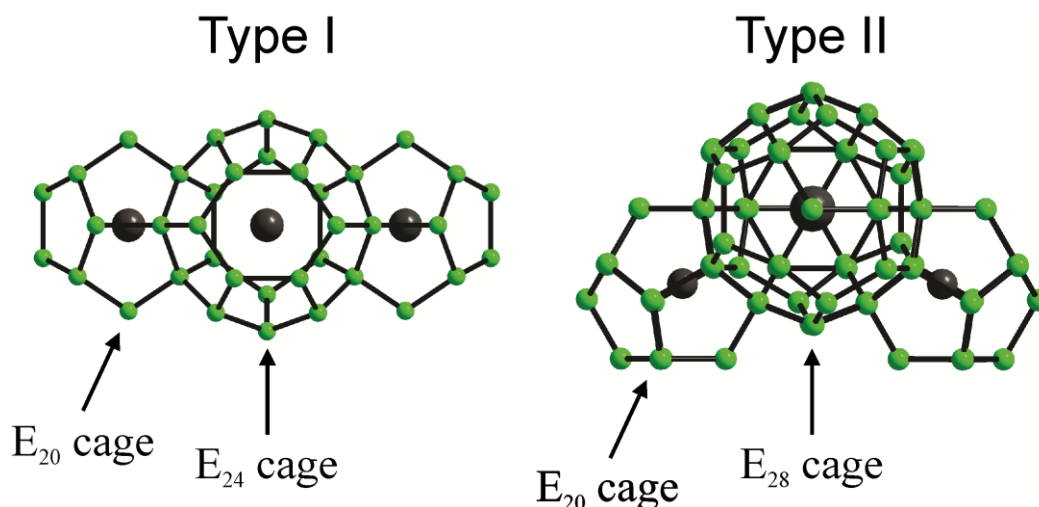


**Figure 1.8. Clathrate cage structures displaying the different guest atom arrangements for the type I (left) and type II (right) clathrates.**

The large thermal vibrations of the guest atoms significantly perturb phonon propagation and reduce lattice thermal conductivity effectively. The main advantage of these phases is that the guest atoms only serve to scatter phonons, and thus do not significantly alter the

electronic band structure of the host lattice. This property allows for a separate tuning of power factor and thermal conductivity.

Many significant advancements in clathrate thermoelectricity have been made in recent years, renewing interest in these materials. A report on a single crystal of  $\text{Ba}_8\text{Ga}_{16}\text{Ge}_{30}$  grown by the Czochralski method determined a figure of merit of  $\sim 1$  at 1000 K.<sup>77</sup> Another study on isostructural  $\text{Sr}_8\text{Ga}_{16}\text{Ge}_{30}$  reported a substantial decrease in thermal conductivity compared to  $\text{Ba}_8\text{Ga}_{16}\text{Ge}_{30}$ , which was attributed to the increased vibrations of the Sr guest atoms due to their smaller size. Another recent study on the  $\text{Ba}_8\text{Au}_{16}\text{P}_{30}$  clathrate revealed one of the lowest values of lattice thermal conductivity ever reported for a thermoelectric: a value of  $0.18 \text{ W m}^{-1} \text{ K}^{-1}$  at room temperature.<sup>78</sup> Apart from the guest atom rattling, the ultralow lattice thermal conductivity of this phase was attributed to the heavy Au framework atoms, large mass differences, and twinning interfaces which scatter phonons but do not significantly affect charge carriers. Although the efficiency of this phase suffers due to its relatively low Seebeck coefficient, it nevertheless serves as a standard for the minimum lattice thermal conductivity in a thermoelectric material.

#### **1.4.7 Natural Superlattices**

As stated previously, the golden standard for a thermoelectric material is for it to display charge carrier transport properties typical of a crystal, yet scatter phonons like a glass. One possible method to attain such a material is to target and design “hybrid” structures containing a natural superlattice. The philosophy behind this approach is that a

structure containing two or more substructure components will be able to preserve the physical properties of each. If this is true, then a natural superlattice structure may contain separate components that are responsible for electrical conduction and phonon scattering, with each component operating at least partially independent of the other. The advantage of such a material would be the ability to tune each physical property by selectively altering one of the components to the desired effect.

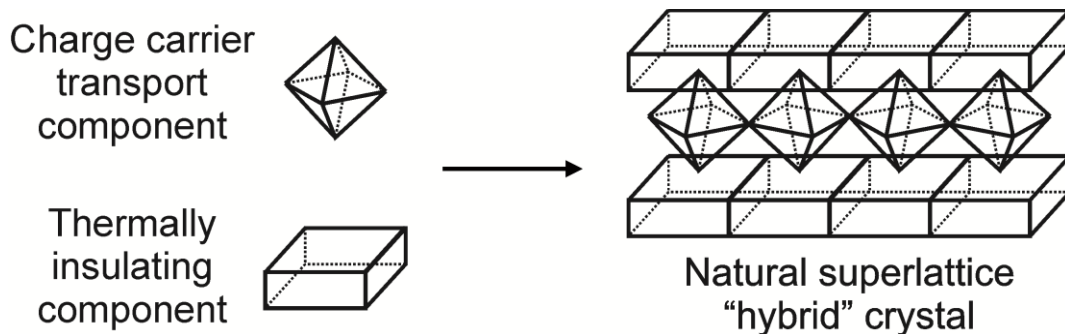


**Figure 1.9. Schematic diagram of a natural superlattice structure combining two distinct building blocks into one phase.**

The  $\text{Ca}_{1-x}\text{Yb}_x\text{Zn}_2\text{Sb}_2$  Zintl phase system contains a natural superlattice type structure, and has been shown to display very good thermoelectric properties.<sup>79</sup> This structure adopts the  $\text{CaAl}_2\text{Si}_2$ -type  $P\bar{3}m$  symmetry and is defined by alternating  $\text{Zn}_2\text{Sb}_2^{2-}$  and  $\text{Ca}^{2+}/\text{Yb}^{2+}$  layers. The mixed  $\text{Ca}^{2+}/\text{Yb}^{2+}$  layers fully donate their electrons to the  $\text{Zn}_2\text{Sb}_2^{2-}$  framework, and do not significantly contribute to the electrical conduction of the sample. As such, the  $\text{Ca}^{2+}/\text{Yb}^{2+}$  layers only serve to disrupt the phonon mean free path by virtue of the large mass contrast between calcium and ytterbium, while the  $\text{Zn}_2\text{Sb}_2^{2-}$  layers

are responsible for the electrical conduction in the sample. Due to the similar atomic radii of  $\text{Ca}^{2+}$  and  $\text{Yb}^{2+}$ , the charge carrier concentration and lattice thermal conductivity of this structure can be modified by altering the  $\text{Ca}^{2+}/\text{Yb}^{2+}$  ratio while preserving the phase symmetry. A sample of  $\text{Ca}_{0.25}\text{Yb}_{0.75}\text{Zn}_2\text{Sb}_2$  was measured to have a figure of merit  $ZT \sim 0.6$  at 773 K and was determined to equal or outperform the pristine  $\text{CaZn}_2\text{Sb}_2$  and  $\text{YbZn}_2\text{Sb}_2$  phases in the entire measured temperature range.<sup>79</sup>

Perhaps one of the most interesting cases of natural superlattices being exploited for thermoelectricity is observed in metal oxides. While these phases have been historically ignored due to their poor carrier mobilities and high electrical resistivities, it has been shown recently in certain metal cobaltates that this need not be the case. In particular, the  $\text{Na}_x\text{Co}_2\text{O}_4$  series ( $0.5 \leq x \leq 1$ ) shows surprisingly good thermoelectric properties, owing to the separation of physical properties into different components of the lattice.<sup>80</sup> This phase contains alternating layers of  $\text{Na}^+$  atoms/vacancies and  $\text{CoO}_2$  octahedra, analogous to the  $\text{Ca}_{1-x}\text{Yb}_x\text{Zn}_2\text{Sb}_2$  system.

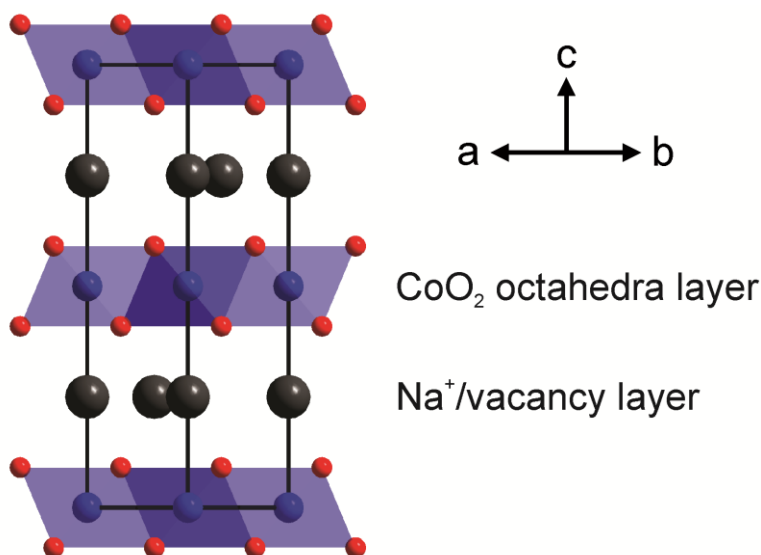


**Figure 1.10. Structure of  $\text{Na}_x\text{Co}_2\text{O}_4$ , viewed along the (111) direction.  $\text{CoO}_6$  octahedra are shown in blue.**

Separation of physical properties into different layers is also achieved in this phase, with certain samples achieving  $ZT \sim 0.8 - 1$  at high temperatures ( $\geq 800$  K).<sup>81, 82</sup> Several other metal oxide systems have been demonstrated to have good thermoelectric properties, such as  $\text{Ca}_3\text{Co}_4\text{O}_9$ <sup>83, 84</sup>,  $(\text{Bi}, \text{Pb})_2\text{Sr}_2\text{Co}_2\text{O}_8$ <sup>85, 86</sup>,  $\text{SrTiO}_3$ <sup>87-90</sup>, and  $\text{TlSr}_2\text{Co}_2\text{O}_y$ .<sup>91</sup>

The idea of physical property separation into different components of a superlattice was applied to the pursuit and study of new thermoelectric materials that are covered in this dissertation. While the phases discovered in our work did not completely match the idealized superlattice type structure, they do represent examples of chemical fusion of two distinct components that may be responsible for different physical properties.<sup>92</sup> The specific synthetic approaches and design strategies used will be discussed further in each respective section.

## **1.5 Materials in focus: Rare-earth pnictide oxides (*RE-Pn-O*) (*Pn* = Sb, Bi)**

Our strategies for designing new materials and optimizing preexisting materials encompass many of the well-established techniques for the improvement of efficiency used in other successful systems. This dissertation is focused on the preparation and characterization, and modification of phases constructed from rare-earth oxides and rare-earth pnictides for thermoelectric purposes.

Rare-earth (*RE*) pnictide suboxides may yield interesting thermoelectric properties; these materials combine the highly stable *RE-Pn* and *RE<sub>2</sub>O<sub>3</sub>* binaries into a single structure, which may conserve the desirable properties of each. Rare-earth antimonides are semiconducting/semimetallic and display good electrical conductivity, but relatively low thermopower. They are also expected to possess high thermal conductivities owing to their simplistic structures<sup>93</sup>. However, if a thermally insulating sublattice could be integrated into this structure, then the added complexity may significantly reduce phonon propagation while preserving the electrical properties of the *RE-Pn* framework. Rare-earth oxides (*RE<sub>2</sub>O<sub>3</sub>*) were chosen since they are excellent thermal insulators and may seamlessly integrate with a *RE-Pn* lattice on the basis of both frameworks containing rare-earth atoms. The strong *RE-Pn* and *RE-O* bonds also offer the advantage of producing a structure with good thermal stability and a high melting point, allowing performance at elevated temperatures.<sup>94</sup> Furthermore, these systems offer the flexibility of modifying atomic disorder and orbital overlap simply by substituting one

rare-earth atom for another. Since most rare earth atoms exist in the trivalent state, atomic substitution does not alter the number of charge carriers in the system, and only serves to alter bond distances and coordination polyhedra of specific atoms. Finally, rare-earth and antimony/bismuth atoms are some of the heaviest elements in the periodic table, which would serve to lower the thermal conductivity of any lattice containing them.

The research topics covered in this dissertation were focused solely on phases that at least partially preserve the *RE-Pn* framework upon chemical fusion with oxygen. It should be mentioned that several known *RE-Pn-O* phases were already known to exist prior to the commencement of our work. Previous studies on these systems led to the discovery of several rare-earth pnictates, such as  $RESb_3O_9$ <sup>95</sup>,  $RE_3Sb_5O_{12}$ <sup>95</sup>,  $RE_3SbO_7$ <sup>96</sup> and  $RESbO_4$ <sup>97</sup> for antimony and  $RE_{10}Bi_8O_{27}$ <sup>98</sup> for bismuth. These phases contain wide band gaps and are highly insulating, primarily due to the presence of  $Pn^{3+}$  and  $Pn^{5+}$ , which instead coordinate to oxygen only and do not maintain the electrical properties of the *RE-Pn* framework.

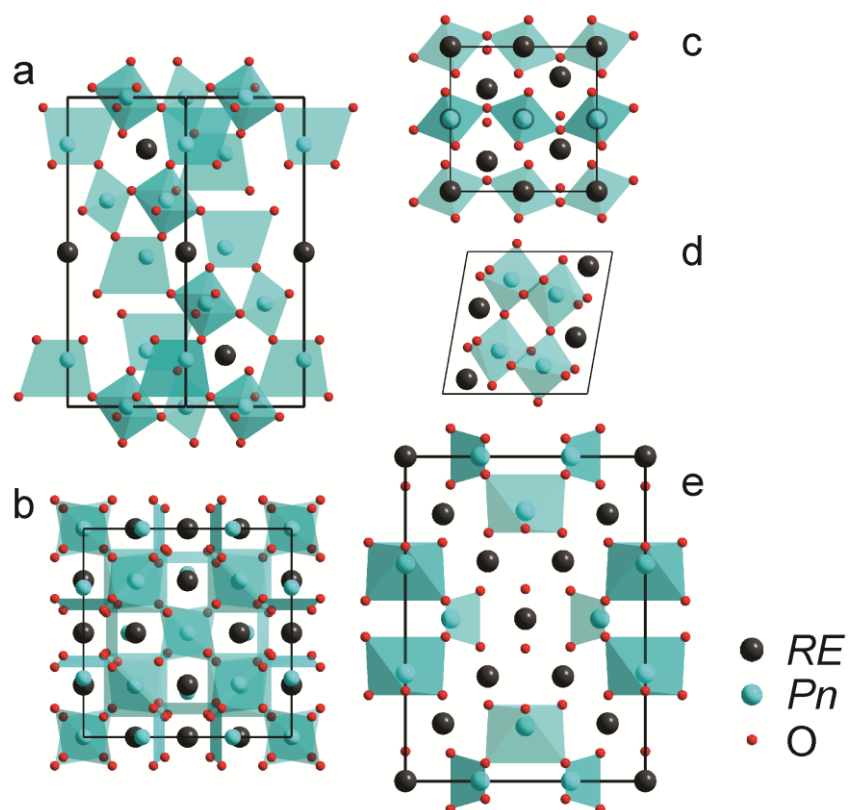


**Figure 1.11. Rare-earth antimonate and bismuthate crystal structures. (a)  $RE_3Sb_5O_{12}$ , (b)  $RE_3Sb_5O_{12}$ , (c)  $RE_3SbO_7$ , (d)  $RESbO_4$ , (e)  $RE_{10}Bi_8O_{27}$ .**

While this synthetic approach could not predict the structures of the new phases our group discovered, each phase was found to preserve the original oxidation states of all species present. As such, the following sections focus on  $RE-Pn-O$  phases in which the pnictide present exists solely in the  $Pn^{3-}$  state. The reaction conditions for each system were tested extensively and yielded consistent results in all cases discussed herein.

### 1.5.1 Tetragonal $(RE^I RE^{II})_3SbO_3$ Phases

The reaction of two distinct types of rare-earth antimonide and oxide binaries at high temperature ( $\geq 1550^\circ\text{C}$ ) was discovered to yield the novel  $(RE^I RE^{II})_3SbO_3$  phases ( $RE^I = \text{La, Ce}$ ;  $RE^{II} = \text{Dy, Ho}$ ). Unlike the other  $RE$ -Sb-O phases, this structure is only obtainable when two distinct rare-earth atoms are used, and when the difference in atomic radii of those atoms is sufficiently large. This condition exists due to the two rare-earth sites in the crystal structure, which are significantly different in the size of their coordination polyhedra. As such, large and small rare-earth atoms are required to fill the two sites separately, although some mixing is still present. This structure shares some similarities to the  $RE_3SbO_3$  and  $RE_8Sb_3O_8$  phases<sup>99</sup>, namely  $RE_4O$  tetrahedral building blocks and empty channels along one crystallographic axis that are occupied by Sb atoms. The  $(RE^I RE^{II})_3SbO_3$  phase is distinct from  $RE_3SbO_3$  and  $RE_8Sb_3O_8$  due to the fact that it only contains one type of building block which is unique to it: a three tetrahedral  $RE_4O$  ( $RE_8O_3$ ) unit.

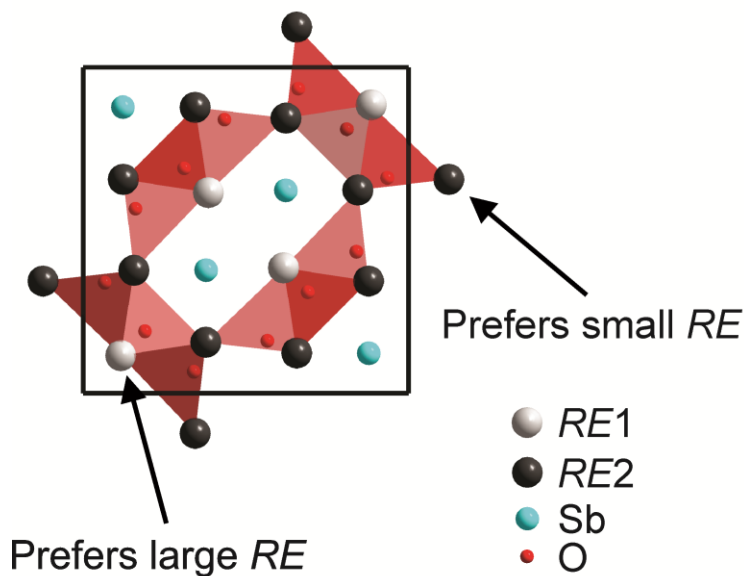


**Figure 1.12.** The  $(RE^I RE^{II})_3 SbO_3$  phase shown with the *RE*<sup>I</sup> and *RE*<sup>II</sup> sites (light gray and dark gray, respectively).

Due to the presence of  $Sb^{3-}$  anions in the structure, it was hoped that the electrical conduction properties of the *RE*Sb binaries would be preserved while the complexity introduced by a *RE*-O framework would yield low thermal conductivity. While this phase does indeed behave as a semiconductor, its electrical resistivity is too high for use in thermoelectric applications. Electronic structure calculations confirmed the presence of a band gap, which would result in the observed semiconducting behavior. The preparation, crystal structures, physical properties, and electronic structures of these phases are discussed in Chapter 3.

### 1.5.2 $CaRE_3SbO_4$ and $Ca_2RE_8Sb_3O_{10}$ phases

The discovery of the tetragonal  $(RE^I RE^{II})_3 SbO_3$  phase<sup>100</sup> motivated us to search for new phases by incorporation of additional elements in the periodic table. It was from

these experiments that the  $\text{CaRE}_3\text{SbO}_4$  and  $\text{Ca}_2\text{RE}_8\text{Sb}_3\text{O}_{10}$  phases were discovered ( $\text{RE} = \text{Ce} - \text{Dy}$ ). Like other  $\text{RE-Sb-O}$  phases before them, both of these phases adopt new crystal structures which are defined by  $\text{RE}_4\text{O}$  tetrahedra building blocks and empty channels occupied by Sb atoms. Calcium is necessary to form each phase since they both contain  $\text{Ca}^{2+}/\text{RE}^{3+}$  site mixing. The  $\text{CaRE}_3\text{SbO}_4$  and  $\text{Ca}_2\text{RE}_8\text{Sb}_3\text{O}_{10}$  phases are analogous to the  $\text{RE}_3\text{SbO}_3$  and  $\text{RE}_8\text{Sb}_3\text{O}_8$  phases<sup>99</sup> in several respects. For instance the  $\text{CaRE}_3\text{SbO}_4$  phase will convert into the  $\text{Ca}_2\text{RE}_8\text{Sb}_3\text{O}_{10}$  phase with sufficient heat treatment in a manner similar to the conversion of  $\text{RE}_3\text{SbO}_3$  into  $\text{RE}_8\text{Sb}_3\text{O}_8$ . Additionally, the  $\text{Ca}_2\text{RE}_8\text{Sb}_3\text{O}_{10}$  does not have a charge balanced stoichiometry, much like  $\text{RE}_8\text{Sb}_3\text{O}_8$ . The  $\text{Ca}_2\text{RE}_8\text{Sb}_3\text{O}_{10}$  and  $\text{RE}_8\text{Sb}_3\text{O}_8$  phases also contain disordered Sb atoms along the  $b$ -directions of their unit cells.

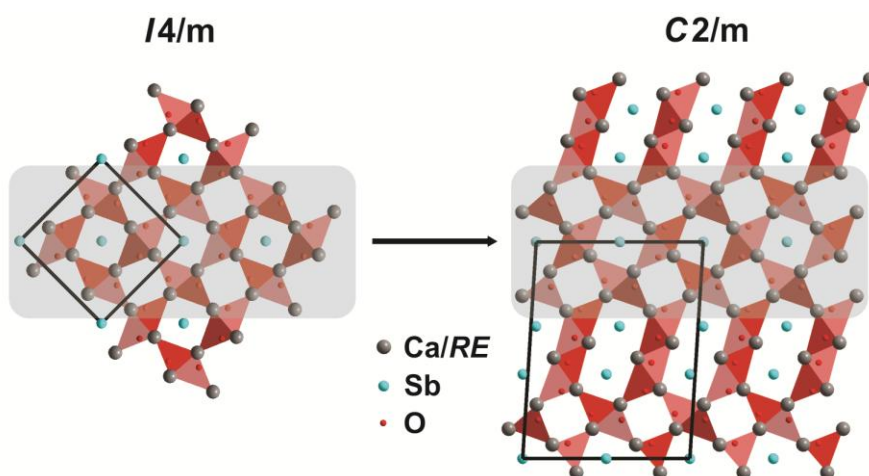


**Figure 1.13. Conversion of  $\text{CaRE}_3\text{SbO}_4$  into  $\text{Ca}_2\text{RE}_8\text{Sb}_3\text{O}_{10}$ . A portion of the  $\text{CaRE}_3\text{SbO}_4$  framework is preserved in  $\text{Ca}_2\text{RE}_8\text{Sb}_3\text{O}_{10}$  (gray background).**

These two phases were investigated in order to establish the relationship between crystal structure and physical properties. Both  $\text{CaRE}_3\text{SbO}_4$  and  $\text{Ca}_2\text{RE}_8\text{Sb}_3\text{O}_{10}$  were determined to have semiconducting properties with electrical resistivities too high for thermoelectric applications. Interestingly, the  $\text{Ca}_2\text{RE}_8\text{Sb}_3\text{O}_{10}$  phase does not display metallic-type conductivity as indicative of its non-charge balanced stoichiometry and calculate electronic structure. Instead, this phase behaves as a semiconductor, but possesses a wide difference in electrical resistivity depending on the rare-earth that is used, with smaller rare-earth atom samples yielding lower electrical resistivity. The details of this phenomenon, as well as the information regarding synthesis, crystal structures, and electronic structures of these phases are discussed in Chapter 4.

### 1.5.3 $\text{RE}_3\text{BiO}_3$ and $\text{RE}_8\text{Bi}_3\text{O}_8$

Although the  $\text{RE-Sb-O}$  phases contain many interesting structural features, most are limited by their relatively high electrical resistivities, rendering them unusable for thermoelectric applications. Thus, we embarked on a set of experiments to determine which of the  $\text{RE-Sb-O}$  phases known can be prepared as the corresponding  $\text{RE-Bi-O}$  phases, or if any new phases could be prepared altogether. The advantages of using bismuth over antimony were not inherently obvious from the start, but we considered that the larger size of bismuth would restrict its thermal vibration. This would possibly yield better electrical conductivity in the disordered structures, where the disorder of the pnictide atom is the source of the semiconducting behavior. Such a behavior was observed in the  $\text{Ho}_2\text{Sb}_{1-x}\text{Bi}_x\text{O}_2$  set of phases<sup>101</sup>, where the electrical properties of the

sample change from semiconducting to metallic, depending on the concentration of Sb/Bi.

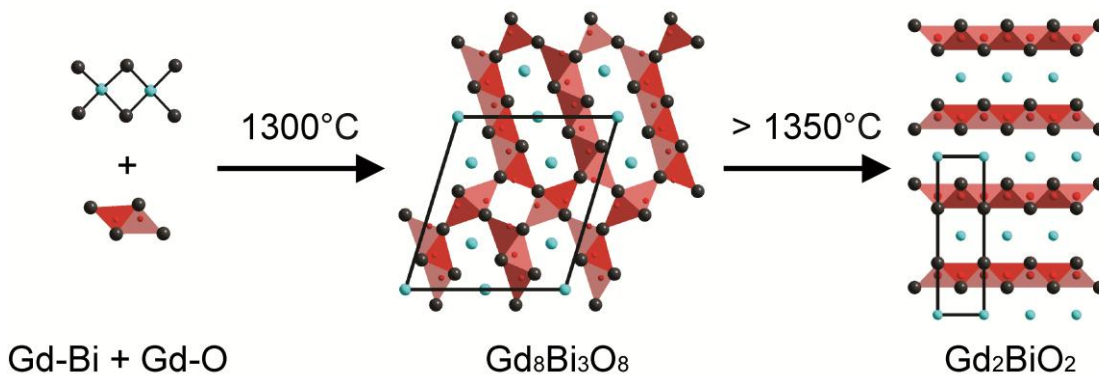


**Figure 1.14. Reaction pathway of GdBi and Gd<sub>2</sub>O<sub>3</sub> to Gd<sub>8</sub>Bi<sub>3</sub>O<sub>8</sub> and ultimately Gd<sub>2</sub>BiO<sub>2</sub>.**

After much experimentation, it was determined that not only could no new phases be formed with bismuth, but out of all the new structures that our group discovered, only the Gd<sub>3</sub>BiO<sub>3</sub> and Gd<sub>8</sub>Bi<sub>3</sub>O<sub>8</sub> phases were found to exist. The Gd<sub>3</sub>BiO<sub>3</sub> and Gd<sub>8</sub>Bi<sub>3</sub>O<sub>8</sub> phases crystallize with the same respective structures as RE<sub>3</sub>SbO<sub>3</sub> and RE<sub>8</sub>Sb<sub>3</sub>O<sub>8</sub>.<sup>99</sup> The Gd<sub>8</sub>Bi<sub>3</sub>O<sub>8</sub> phase was also observed to contain disordered bismuth atoms along the b-direction. In spite of our best efforts, only samples with RE = Gd could be prepared, which is likely due to the overwhelming thermodynamic stability of the corresponding RE<sub>2</sub>BiO<sub>2</sub> phase. As such, a pure sample of Gd<sub>3</sub>BiO<sub>3</sub> could not be made, and obtaining Gd<sub>8</sub>Bi<sub>3</sub>O<sub>8</sub> is quite difficult, and requires very precise control on the time and temperature of the reaction. The full details of our synthetic approach, as well as the experimentally determined physical properties and electronic structure, are presented in Chapter 5.

#### 1.5.4 $\text{Ca}_2\text{RE}_7\text{Pn}_5\text{O}_5$ Phases

Of all the known  $\text{RE-Pn-O}$  phases, only  $\text{RE}_2\text{PnO}_2$ <sup>102</sup> and  $\text{RE}_9\text{Pn}_5\text{O}_5$ <sup>103</sup> adopt a natural superlattice type structure, as defined by their alternating  $\text{RE-Pn}$  and  $\text{RE-O}$  building blocks. The  $\text{RE}_2\text{PnO}_2$  series has been extensively studied to this point, but only the structure and basic properties of the  $\text{RE}_9\text{Pn}_5\text{O}_5$  phase are known, and only for  $\text{Pn} = \text{Sb}$ . Previous studies determined that  $\text{RE}_9\text{Sb}_5\text{O}_5$  crystallizes in the  $P4/n$  space group<sup>104</sup> as an oxygen-stuffed, rare-earth deficient variant of the  $\text{Sc}_2\text{Sb}$ -type structure. Interestingly, this structure displays a complex twinning law, with each crystal containing at least two domains. This is beneficial for thermoelectricity, since phonon scattering may occur at these interfaces, but charge carriers are relatively unaffected.<sup>105</sup> Unfortunately, the pristine  $\text{RE}_9\text{Sb}_5\text{O}_5$  phase is clearly unsuitable for thermoelectric applications, since it displays metallic-type conduction due to its non-charge balanced stoichiometry. Additionally, it is quite air sensitive, rendering measurements and long-term usage difficult to accomplish. A study on carbon incorporation in this phase was performed in an attempt to stabilize it via charge balance, but a pure sample could not be obtained for measurement.<sup>106</sup>

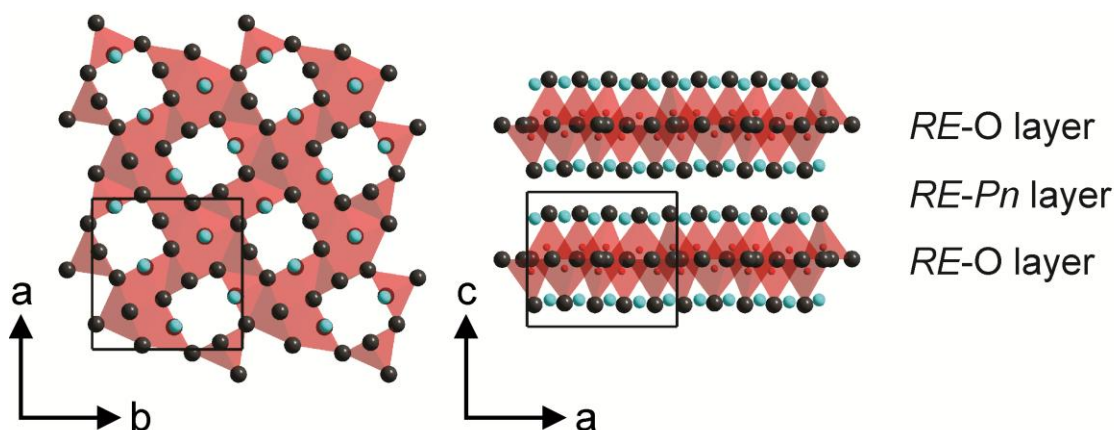


**Figure 1.15. Structure of  $\text{Ca}_2\text{RE}_7\text{Sb}_5\text{O}_5$ , viewed along the  $c$ - and  $b$ -directions, respectively.**

Based on our success with the  $\text{CaRE}_3\text{SbO}_4$  and  $\text{Ca}_2\text{RE}_8\text{Sb}_3\text{O}_{10}$  series<sup>107</sup>, we explored the substitution of rare-earth with calcium in  $\text{RE}_9\text{Sb}_5\text{O}_5$ . Our experiments determined that a more stable, charge balanced form of this phase could be produced, with a stoichiometry of  $\text{Ca}_2\text{RE}_7\text{Sb}_5\text{O}_5$ . Due to the site mixing of calcium and rare-earth, this substitution has only a minor impact on the lattice. However, it is expected that the physical properties can be shifted to a level more suitable for thermoelectric applications due to the reduction of conduction electrons. The individual  $\text{RE-Pn}$  and  $\text{RE-O}$  layers are also expected to retain their properties such that the  $\text{RE-Pn}$  layers are responsible for electrical conduction while the  $\text{RE-O}$  layers effectively scatter phonons. Our studies on the  $\text{Ca}_2\text{RE}_7\text{Pn}_5\text{O}_5$  series, including syntheses, crystal structures, electronic structures, and physical properties are summarized in Chapter 6.

## Chapter 2. Methodology and Experimentation

### 2.1 Synthetic Approach

The samples studied in the works covered in this dissertation were obtained primarily by solid state reaction techniques. Since many of the reagents used for synthesis have relatively high melting points and are chemically inert at room temperature, high temperature synthesis is required. However, it is imperative to carry out these reactions in such a way that does not result in oxidation, contamination, or damage to laboratory equipment. As such, all sample preparation discussed in this report was accomplished through the use of an argon-filled glove box. This section will give a general outline as to the preparation of the desired materials; a more detailed summary of each specific synthetic route can be found in the respective chapters.

As a general rule, it is neither safe nor wise to form *RE-Pn-O* phases directly from the elements. This is primarily due to the fact that elemental antimony/bismuth have high vapour pressures at elevated temperatures ( $T > 650^{\circ}\text{C}$ ), resulting in side reactions and damage to equipment. In order to circumvent this problem, we must first prepare a precursor in the form of a binary phase. Several *RE-Sb/Bi* binary phases exist, but we have determined the best choice to be the *RESb/REBi* binaries. These phases have the NaCl-type structure and can be made in very good purity, but most importantly, they have very high thermal stability, which suits our purpose.



**Figure 2.1. A sample of PrSb before (top) and after (bottom) reaction at high temperature.**

These *RESb* binaries can be prepared simply by measuring out the stoichiometric amounts of each element required and combining them together by means of a hydraulic press. The pellets obtained from this method are then sealed in silica ampoules of about 10 to 15 cm in length under  $10^{-4}$  torr. The sample is heated in a box furnace, first at  $600^{\circ}\text{C}$  for 24 hours to induce the chemical reaction, and then at  $850^{\circ}\text{C}$  for 48 hours to ensure a complete reaction and a pure product, as confirmed by X-ray diffraction data. The *REBi* binaries can be made a similar way, using reactions temperatures of  $235^{\circ}\text{C}$ , then  $350^{\circ}\text{C}$ , and finally  $850^{\circ}\text{C}$ . However, these samples are not pressed into pellets, and are instead added as powders to a carbon coated silica tube, which is then sealed. The reasoning behind these changes is the fact that bismuth has a lower melting temperature and is prone to react explosively with early rare earths ( $RE = \text{La} - \text{Eu}$ ) if the sample is in pellet form. The *REBi* binaries obtained from these experiments are difficult to verify for purity

due to the amorphous features in their X-ray diffraction data, but can be at least viewed as a method to obtain a thermally stable reactant containing bismuth.

Once the *RESb/REBi* precursors have been obtained, they must be reacted with calcium or rare-earth oxides at very high temperatures ( $T \geq 1300^{\circ}\text{C}$ ) in order to yield *RE-Pn-O* phases. This is difficult to achieve with the aforementioned methods, as evacuated silica tubes will collapse under vacuum due to softening and compromise sample integrity. A far more reliable technique for high temperature synthesis is the use of an induction furnace. First, samples are sealed in 0.1 – 0.8 g amounts in a tantalum ampoule using an arc melter. This is done as tantalum is both chemically inert to most reactions we consider, and also has a very high melting point, making it an excellent choice for containing our reactions. These ampoules are then placed in a molybdenum susceptor and suspended on a custom made boronitride sample holder, which itself is suspended on a silica sample holder to allow ease of removal. The boronitride acts as a thermally insulating barrier to prevent the heat of the susceptor from melting the entire sample stage. The entire apparatus is evacuated to  $10^{-5}$  torr through the use of a diffusion pump to avoid oxidation. Heating is accomplished using a radio frequency current applied in a water-chilled copper coil around the outside of the sample. The entire furnace is cooled by a water jacket to prevent the silica from melting, and the monitoring of sample temperature is accomplished through the use of an optical pyrometer. By this method, we may obtain temperatures of up to  $1650^{\circ}\text{C}$  in a safe, controlled environment which can operate undisturbed for several days.

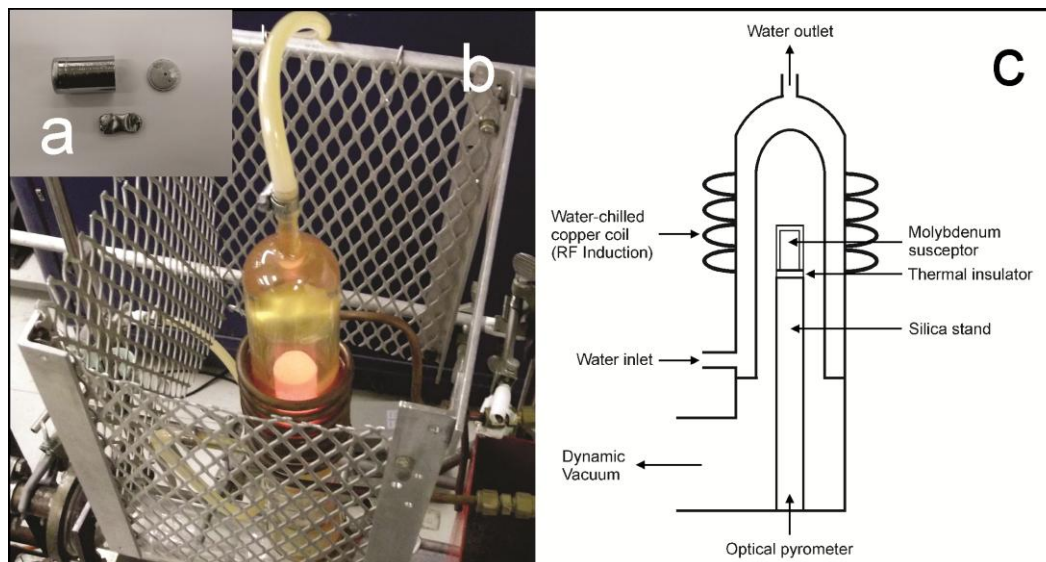


**Figure 2.2. Radio Frequency Induction Furnace used for high temperature synthesis. The molybdenum susceptor containing samples sealed in tantalum ampoules (a) is heated in the apparatus shown in (b). A schematic diagram of the equipment is shown in (c).**

## 2.2 X-ray Diffraction Analysis

### 2.2.1 Basic Theory

One of the most important methods of structure determination of solids is the application of X-ray diffraction. This method involves a systematic scattering of incident wavelengths of X-rays, which are in turn collected by a detector. This data can then be used to determine the three dimensional arrangement of atoms in a solid, which can give insight into the composition and physical properties of a sample.

X-rays are able to probe the atomic structure of solids due to the fact that they are diffracted by electrons, and have wavelengths that correspond to typical atomic separations ( $\sim 1 - 3 \text{ \AA}$ ). In order for X-ray diffraction to succeed, it is imperative for the sample under study to be in crystalline form, with the atoms arranged in an ordered, periodic lattice in three dimensional space for diffraction to occur, as opposed to a disordered glass. As X-rays collide with the sample, they will be scattered by electrons and will overlap, often causing destructive interference and the absence of a signal. Under certain conditions, the overlapping wavelengths will interfere constructively, and can be detected and measured experimentally. This phenomenon is described by Bragg's law (Equation 2-1):

$$n\lambda = 2d_{hkl}\sin\theta \quad (2-1)$$

Where  $n$  is an integer,  $\lambda$  is the wavelength of the incident beam,  $d_{hkl}$  is the spacing between lattice planes, and  $\theta$  is the angle of diffraction between the incident beam and the lattice planes.

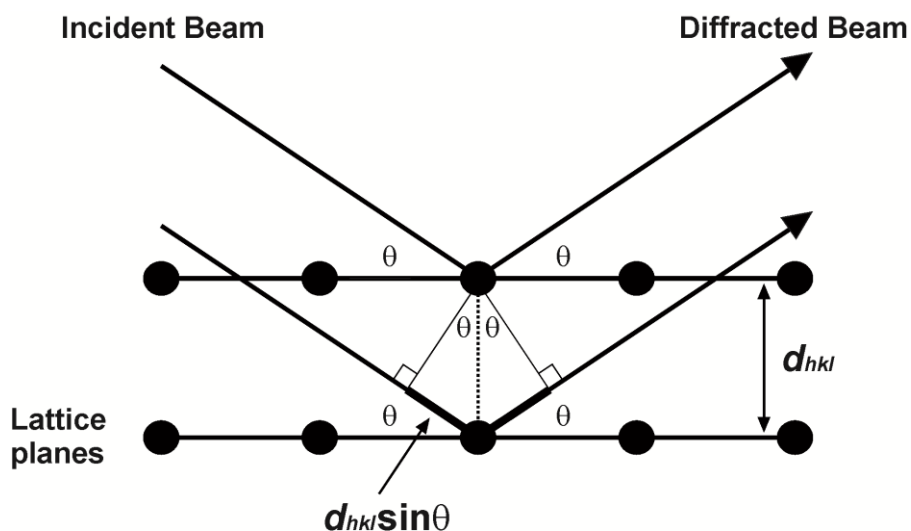


**Figure 2.3. Diffraction of X-rays in a periodic lattice. When the path difference (bolded lines) between adjacent beams,  $2d_{hkl}\sin\theta$ , is equal to a multiple of the incident wavelength  $\lambda$ , constructive interference occurs and a signal is detected.**

All crystalline solids can be viewed as repeating arrangements of atoms in three dimensional space. As such, there exists a basic building block, known as the unit cell, which serves as the repeating unit in the crystal. The unit cell is composed of three basic vectors  $a$ ,  $b$ , and  $c$ , as well as three angles,  $\alpha$ ,  $\beta$ , and  $\gamma$ . When X-ray diffraction is considered, it is convenient to describe the  $d_{hkl}$  spacings between diffraction planes as with respect to the unit cell. These spacings, also known as Miller indices, are labeled with respect to the number of times the unit cell is divided by the diffraction plane in each direction. The resulting data is modeled in reciprocal space as points described by reciprocal lattice vectors  $a^*$ ,  $b^*$ , and  $c^*$ . Each vector is related to its real space analogue as the cross product of the other two real space vectors divided by the volume of the unit cell  $V$ .

$$a^* = \frac{b \times c}{V}, b^* = \frac{a \times c}{V}, c^* = \frac{b \times a}{V} \quad (2-2)$$

The arrangements of these reflections can be related to real space conditions through the concept of Ewald's sphere<sup>108</sup> (Figure 2.2). In principle, Ewald's sphere consists of a boundary of points in reciprocal space defined by a sphere of radius  $1/\lambda$ . The sphere is placed about the origin of diffraction A, with a wavevector R extending from A to the origin of reciprocal space O. If it is assumed that elastic scattering occurs, which is the case for X-ray diffraction, then there exists a wavevector k which extends from point A to point P at the surface of the sphere. A separate vector S can then be constructed from connecting the two points O and P on the surface of the sphere, normal to the diffraction plane. Upon inspection, it is calculated that vector S has a length of  $2R\sin\theta$ , but since the radius of the sphere is  $1/\lambda$ , it can be rewritten as  $2\sin\theta/\lambda$ , which is equal to the inverse of the  $d_{hkl}$  spacing. The result is that only reciprocal lattice points which exist on the surface of Ewald's sphere can satisfy Bragg's law, and thus, diffraction will only occur for those points at a given  $\theta$  angle.

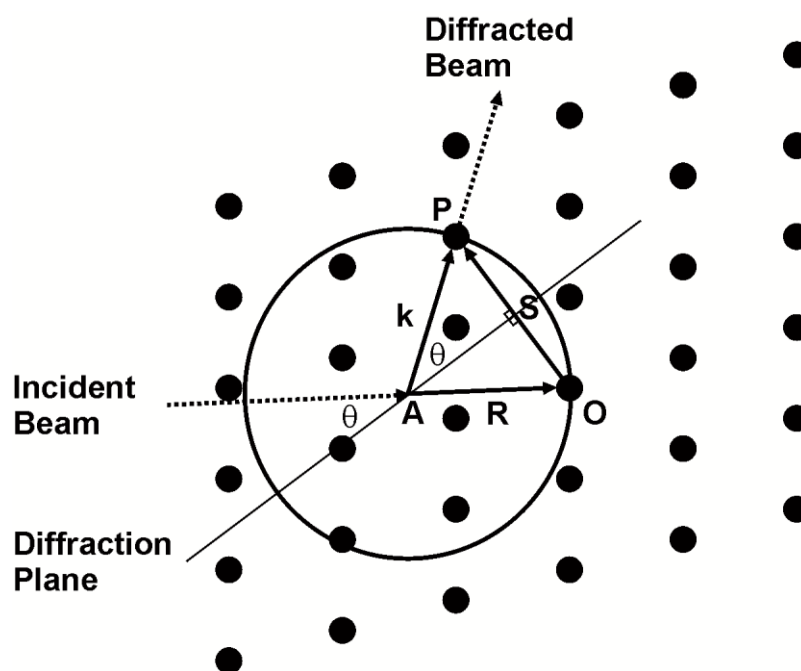


**Figure 2.4. Schematic diagram of Ewald's sphere, displaying the relationship between the incident wavelength, reciprocal space, and real space.**

The efficiency of an atom to scatter X-rays is known as the atomic scattering factor  $f$ , which is proportional to the size of the atom, the angle of diffraction, and the incident wavelength. It is known that larger atoms will scatter X-rays more strongly due to the fact that they contain more electrons, but the intensity of the scattered beam also decreases as the diffraction angle increases. This is due to the fact that diffracted beams at any angle besides zero will become increasingly out of phase with one another as  $\theta$  increases (Figure 2.4). When the angle of diffraction is zero, adjacent beams scattered by electrons A and B will have a path difference of zero and will not interfere destructively. However, when the angle of diffraction is not zero, a path difference is introduced which is equal to  $CB - AD$ , and becomes greater as  $\theta$  increases. Furthermore, as  $\lambda$  decreases, the

relative path difference between adjacent beams becomes larger, leading to greater destructive interference.

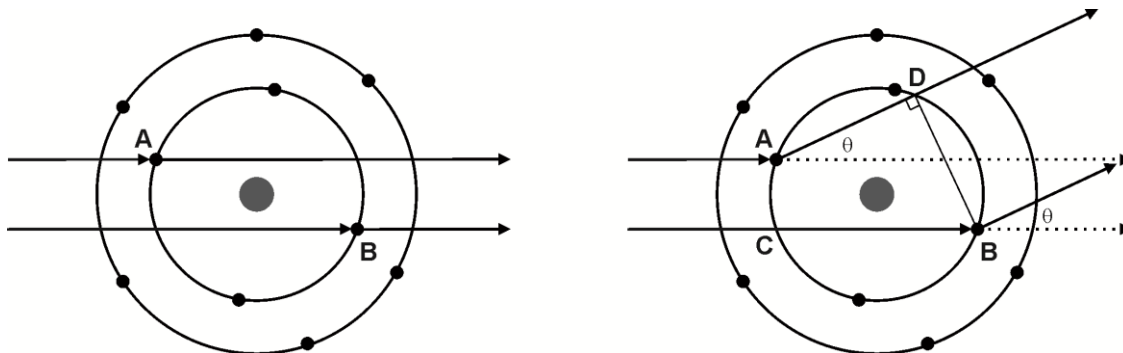


**Figure 2.5. Scattering of X-rays by an atom with a diffraction angle of  $\theta$  equal to  $0^\circ$  (left) and  $\theta$  greater than  $0^\circ$  (right).**

With the concept of atomic scattering and lattice periodicity established, the structure factor of a reflection can now be introduced. Simply put, the structure factor contains all the information of a diffraction plane, including its intensity and phase angle, which can be used to determine the positions of atoms in a crystal structure. Since a crystal is periodic, the structure factor can be expressed for a given reflection as a Fourier series including the atomic scattering factors and the individual atomic positions relative to the unit cell<sup>109</sup> (Equation 2-3).

$$F_{hkl} = \sum_1^N f_n e^{2\pi i(hx_n + ky_n + lz_n)} \quad (2-3)$$

The exponential part of the equation can be rewritten as a an Euler expansion of sin and cosine terms, and plotted in real and imaginary space with a phase angle  $\varphi = 2\pi(hx_n + ky_n + lz_n)$ .

$$e^{2\pi i(hx_n + ky_n + lz_n)} = \cos 2\pi(hx_n + ky_n + lz_n) + i \sin 2\pi(hx_n + ky_n + lz_n) \quad (2-4)$$

The intensity of a given reflection can be determined experimentally, and is proportional to  $|F_{hkl}|^2$ , thus, we are able to gain information about the electron density based on the atomic scattering factor  $f_n$ . However, the value of  $|F_{hkl}|^2$  or  $|F_{hkl}|$  contains no information regarding the phase angle; this data is lost to diffraction experiments.<sup>109</sup> Due to this constraint, it is impossible to directly determine atomic coordinates based solely on diffraction data.

Two standard methods are commonly used to reach a solution: the direct method and Patterson function method. In the case of the direct method solution, an initial phase angle is assigned to a reflection and is expanded on by three additional reflections which are not related by symmetry. Due to the nature of atoms arranged in a lattice, there exist statistical relationships between structure factors of these reflections. This process can be repeated until the correct phase angles are determined and an acceptable solution is obtained.<sup>110</sup> The Patterson method utilizes a Fourier transform of the observed intensities, and generates a map with information regarding vectors between atoms. The atom positions in real space can then be assigned based on the observed intensity (electron density) in the map.<sup>110</sup>

In order to determine the atomic positions of a structure from intensity data alone, one must resort to a trial and error system. First, a model of the target structure must be created. In the cases where there is no knowledge of similar structures, a space group is chosen based on the systematic absences determined from the experimental data. The absence of observed intensity in the diffraction data at set intervals corresponds to a symmetry element in a crystal with translational symmetry; this can be proven mathematically, but is not shown here. Afterwards, the calculated intensity profile is compared to the experimental data obtained and an agreement factor is produced.<sup>111</sup>

$$R^2 = \frac{\sum ||F_{obs}^2| - |F_{calc}^2||}{\sum |F_{obs}^2|} \quad (2-5)$$

To obtain a solution, it is imperative to inspect bonding distances, angles, and arrangements as a tool to determine if the correct structure has been assigned. With this knowledge, the resulting model can then be further tuned in terms of atomic identities, positions, occupancies, thermal vibration, and disorder until a satisfactory agreement is reached.

### **2.2.2 X-ray Single Crystal Diffraction**

Several new structures were prepared and discovered in the work covered in this dissertation. As such, X-ray single crystal diffraction was necessary to determine the crystal structures of these phases. Samples were prepared at temperatures suitable for

formation and crystallization, were crushed into powder, and mounted using epoxy resin under a microscope.

Most of the X-ray single data presented in this report was collected on a STOE IPDSII diffractometer with Mo  $K_{\alpha}$  radiation and an image plate detector. This device comes equipped with a goniometer for rotation about the origin of diffraction and the crystal itself ( $\omega$  and  $\varphi$ , respectively). A numerical absorption correction was based on the crystal shape originally determined by optical face indexing but later optimized against equivalent reflections using the STOE X-Shape software<sup>112</sup>. The data for the  $Gd_8Bi_3O_8$  crystal was collected on a Bruker SMART Apex II diffractometer with Mo  $K_{\alpha}$  radiation and a CCD detector. The SAINT program<sup>113</sup> was employed to apply corrections to Lorentz and polarization effects. A multi-scan absorption correction was based on the crystal shape obtained from optical face indexing. All crystals were collected with data in the whole reciprocal sphere, to ensure sufficient data completeness and to avoid the bias of centrosymmetry.

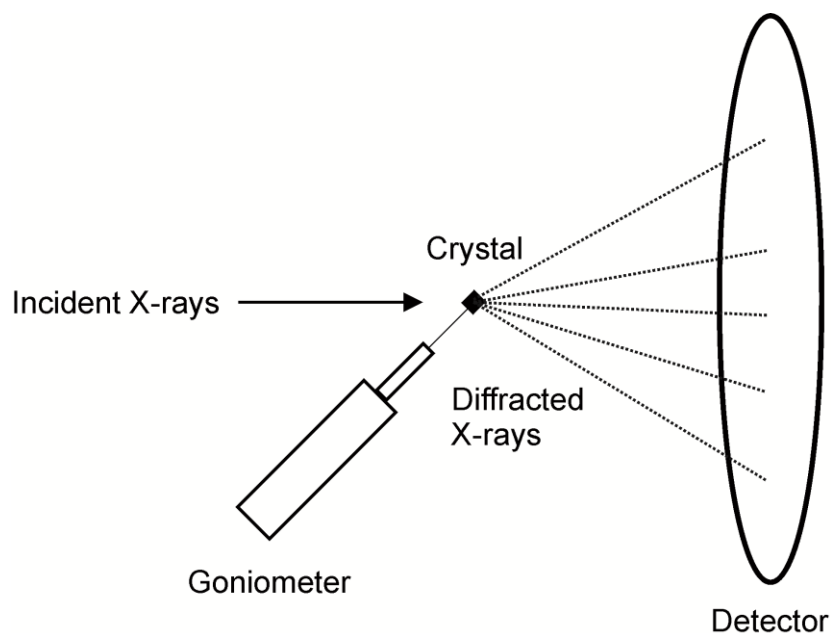


**Figure 2.6. Generalized X-ray single crystal diffraction instrument diagram.**

### 2.2.3 X-ray Powder Diffraction

Although X-ray single crystal data is invaluable to the determination of a crystal structure, it is not ideal to resolve the identity of an entire sample from which it is collected, as it may only represent a minor phase that is present. As such, in order to ensure that the physical properties measured for a sample are intrinsic to the phase under study, it is absolutely necessary to analyze bulk samples to determine purity. One of the best methods to accomplish this is by X-ray powder diffraction experiments.

By this method, a sample is exposed to incident X-rays in a manner similar to X-ray single crystal diffraction, but since the sample contains crystallites of random orientations, concentric cones of diffraction are produced. Depending on the instrument, a one- or two-dimensional detector may be used to record the data. Since each crystallite

obeys Bragg's law of diffraction and produces its characteristic diffraction pattern if one only considers one-dimension scattering, the identity of each known phase in a sample can be determined by refinement or by comparison to a database.

All rare-earth pnictide oxides discussed in this report were analyzed by a PANalytical X'Pert Pro diffractometer equipped with a one-dimensional X'Celerator detector. An incident X-ray wavelength of Cu  $K_{\alpha 1}$  was chosen for diffraction. A wafer-shaped sample holder manufactured from a single crystal of silicon was chosen for measurements. The sample holder was cut in a direction that excluded any diffraction in the measurable  $2\theta$  range of our experiments. A germanium single crystal monochromator was used to eliminate unwanted Cu  $K_{\alpha 2}$  radiation, while a one degree slit was used to reduce the background signal. Approximately 20 to 50 mg of sample was analyzed for each trial. Most samples were collected in the  $2\theta$  diffraction range from  $20^\circ$  to  $70^\circ$ . The resulting data was analyzed and refined by the Rietveld refinement method (Rietica program<sup>114</sup>) with the respective crystal structures obtained from literature and our own research.

### **2.3 Energy-dispersive X-ray Spectroscopy and Electron Micro-probe Analysis**

While X-ray diffraction is an invaluable tool in determining crystal structure and phase purity, it is not without its limitations. In the cases where elements of similar electron

counts (and thus scattering factors) are considered, it may become difficult to correctly assign the identity of each atom in a crystal structure. This may lead to large standard deviations in the calculated stoichiometry and an erroneous model. Furthermore, contamination from outside sources in the sample preparation step may go undetected by X-ray powder diffraction if the impurity is amorphous or in small amounts. Such a problem can be devastating for physical property measurements if the data obtained is not intrinsic to the sample, but the result of the impurity. In these cases, it becomes necessary to analyze a sample both qualitatively and quantitatively for the presence of specific elements.

One of the best ways to probe the identity of the atoms in a sample is to perform Energy dispersive X-ray spectroscopy (EDS). A sample under study is exposed to an electron beam which ejects a core electron from an atom, creating a hole. An electron from a higher energy level in this atom emits an X-ray photon and relaxes to a state that replaces the lost core electron. The photon produced is characteristic to both the atom and the specific energy level difference of relaxation.<sup>115</sup> Thus, elemental composition of a sample can be determined by in this manner.

The EDS experiments described in this dissertation were conducted on a JEOL 7000F scanning electron microscope. Copper and Nickel metal were used as standards for calibration. A scanning electron microscope was also used to selectively choose regions of a sample for EDS analysis, as well as to obtain high resolution surface images at the micrometer scale. Unfortunately, analysis of single crystals and unprocessed bulk samples

by this method is purely qualitative, as the calculated stoichiometries may deviate based on sample coarseness.

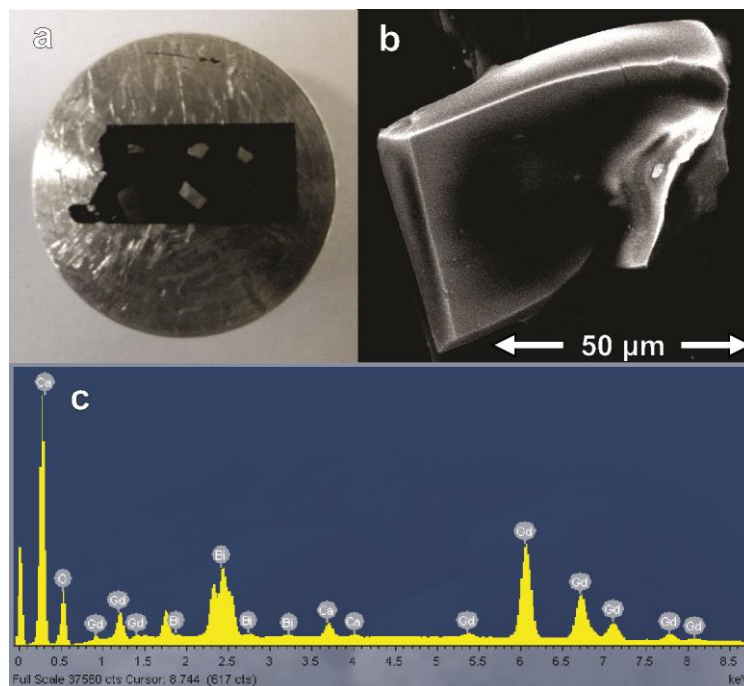


**Figure 2.7.** A sample holder (a) containing bulk samples and single crystals for energy dispersive X-ray spectroscopy (EDS) measurements. A scanning electron microscope (SEM) image of a crystal is shown in (b), while an example EDS spectrum is shown in (c).

To obtain a better understanding of sample composition, quantitative analyses were performed by electron microprobe microanalysis (EPMA). The samples described in this dissertation were analyzed using wavelength-dispersive (WDS) X-ray spectroscopy (model JXA-8500F, JEOL). Samples under study were mounted in discs of epoxy resin one inch in diameter and approximately 10 mm in thickness. Polishing was accomplished

using a Struers Rotopol-31 unit with a Struers RotoForce-4 revolving sample holder. The final step of polishing used a solution of diamond dust in each case. A series of standards were used for calibration, and are outlined for each specific chapter.

## 2.4 Physical Property Measurements

In order to determine the thermoelectric efficiency of a sample, the electrical resistivity, Seebeck coefficient, and thermal conductivity must be determined. To do so, sufficiently pure samples were first cold pressed into pellets and annealed at low temperatures. The annealed samples were then cut into 0.2 mm x 0.2 mm x 0.8 mm bars using a revolving alumina blade. Kerosene was used as a lubricant to avoid sample oxidation. Certain air sensitive samples were then coated with a thin layer of Epo-Tek epoxy and evacuated to remove air bubbles. After cutting, all samples were stored in argon until use. A small amount of Drierite was added to packages containing moisture sensitive samples to avoid decomposition.

All samples were measured on a Quantum Design Physical Property Measurement System (PPMS). The mixed tetragonal  $(RE^I RE^{II})_3SbO_3$ ,  $Gd_8Bi_3O_8$ ,  $Ca_2RE_7Sb_5O_5$ , and  $RE_9Pn_5O_5$  samples were measured in Tsukuba, Ibaraki, Japan, while the  $CaRE_3SbO_4$  and  $Ca_2RE_8Sb_3O_{10}$  samples were measured in Oak Ridge, Tennessee, United States. Platinum leads were attached on the rectangular bars using Epo-Tek H20E silver epoxy. The

contacts for all samples were cured under a stream of ultra-high purity Ar inside a tube furnace.

In some cases, it is also useful to measure samples for the Hall effect, as information regarding the electrical properties of a material can be obtained in this way. The nature of this phenomenon originates from the movement of charge carriers in a material when a magnetic field is applied in a perpendicular direction. A Lorentz force is exerted on the charge carriers which cause them to propagate in a curved direction. This causes an uneven distribution throughout the material, creating a voltage that is perpendicular to both the direction of the current and the magnetic field.<sup>116</sup> Depending on the nature of the material, the resultant voltage may be either positive or negative, and its magnitude corresponds to the charge carrier mobility and magnetic field strength. This information can be useful for tuning and optimizing thermoelectric materials, since electrical conductivity is directly proportional to both charge carrier concentration  $n$  and carrier (Hall) mobility  $\mu$  (Equation 1-10).

A selected set of samples were also analyzed using an Accent Hall system HL5580 to measure their room temperature electrical resistivities, carrier mobilities, and carrier concentrations, as well as to determine if they are n- or p-type conductors. These samples were pressed as flat pellets of approximately one centimeter in diameter and two millimeters in thickness. A four point probe with Pt/Ir contacts was used for measurement, and an applied current of 0.1 mA was directed to each sample. A magnetic field of 0.323 Tesla was applied perpendicular to the direction of the current flow.

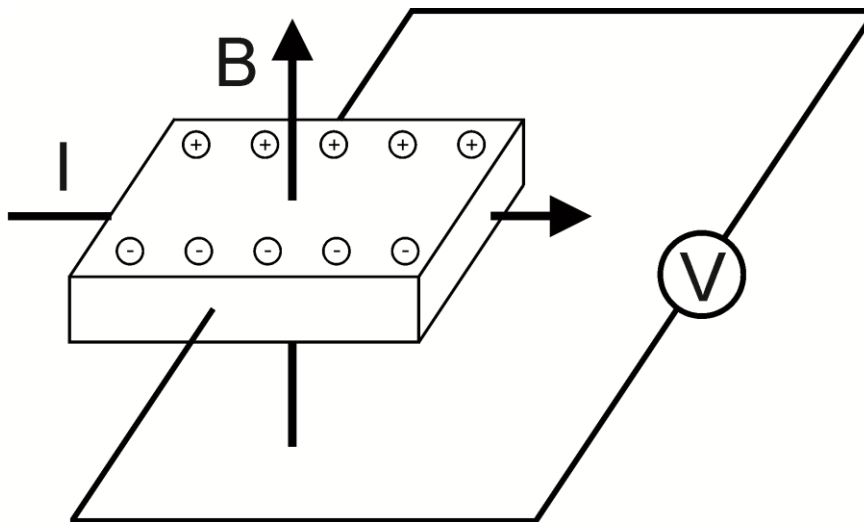


**Figure 2.8. Illustration of the Hall effect. A current  $I$  is passed through a material with a magnetic field  $B$  applied at a 90 degree angle. The result is a voltage  $V$  perpendicular to both the current and the magnetic field.**

## 2.5 Electronic Structure Calculations

In order to fully characterize a material and understand the nature of its physical properties, its electronic structure must be determined. This data may be calculated based on its crystal structure, and gives valuable information regarding the population and distribution of bonding and antibonding electronic states. If the electronic structure of a material is known, the structure can be tuned by elemental substitution to modify its electron count and disorder to yield better thermoelectric properties. Thus, the electronic structure of each new phase was calculated to resolve the nature of its physical properties and as a potential tool for the improvement of thermoelectric efficiency.

The electronic band structures of the rare earth pnictide oxides included in this dissertation were calculated using the tight-binding, linear-muffin tin orbital method<sup>117</sup> with the atomic sphere approximation (TB-LMTO-ASA) as implemented in the Stuttgart program<sup>118</sup>. The experimental lattice and atomic parameters obtained from the X-Ray single crystal refinements of each phase were used for calculations. In the cases where atomic mixing could not be treated during calculations, the atom with the highest occupancy on each site in the crystal data was assigned to 100% occupancy. All 4*f* electrons were considered as core electrons. Exchange and correlation were treated by the local density approximation (LDA)<sup>119</sup>. A scalar relativistic approximation<sup>120</sup> was employed to account for all relativistic effects except spin-orbit coupling. Overlapping Wigner-Seitz cells were constructed with radii determined by requiring the overlapping potential to be the best approximation to the full potential, according to the atomic sphere approximation (ASA). Automatic sphere generation<sup>121</sup> was performed to construct empty spheres to be included in the unit cell in order to satisfy the overlap criteria of the TB-LMTO-ASA model.

In the certain cases, the electronic structures calculated by the method mentioned above yielded results which seemingly contradicted the data obtained from experiments. Most notably, the calculated electronic band gaps may differ somewhat from the values obtained from electrical resistivity data due to the approximations made. Additionally, in the cases of  $\text{Ca}_2\text{RE}_8\text{Sb}_3\text{O}_8$  and  $\text{Gd}_8\text{Bi}_3\text{O}_8$ , the calculated structure suggests a metallic type distribution of states, despite the electrical resistivity data indicating they are

semiconductors. This will be further discussed in Chapters 4 and 5. Finally, in the case of  $\text{Ca}_2\text{RE}_8\text{Sb}_3\text{O}_{10}$ , four superstructures represented by different arrangements of Sb atoms were constructed in an effort to better describe the discrepancy between the original calculated electronic structure and the electrical resistivity data. The details and results of these calculations will be presented in Chapter 4.

### **Chapter 3. Synthesis, Crystal Structure, and Electronic Properties of the Tetragonal $(RE^I RE^{II})_3SbO_3$ Phases ( $RE^I = La, Ce$ ; $RE^{II} = Dy, Ho$ )**

This chapter contains the material covered in the manuscript “Synthesis, Crystal Structure, and Electronic Properties of the Tetragonal  $(RE^I RE^{II})_3SbO_3$  Phases ( $RE^I = La, Ce$ ;  $RE^{II} = Dy, Ho$ )”, which was published in *Inorganic Chemistry* (*Inorg. Chem.* **2013**, 52 (2), 1025-1031). The experimental procedures, structure determinations, and data interpretations were performed by the candidate. Dr. Peng Wang assisted with the electronic structure calculations, Dr. Jinlei Yao carried out magnetic susceptibility measurements, and Dr. Taras Kolodiazhnyi performed physical property measurements on bulk samples.

Reproduced with permission from Scott Forbes, Peng Wang, Jinlei Yao, Taras Kolodiazhnyi, and Yuriy Mozharivskyj, *Inorg. Chem.* **2013**, 52 (2), 1025-1031. Copyright 2013 American Chemical Society.

In our efforts to tune the charge transport properties of the recently discovered  $RE_3SbO_3$  phases ( $RE$  is a rare earth), we have prepared mixed  $(RE^I RE^{II})_3SbO_3$  phases ( $RE^I = La, Ce$ ;  $RE^{II} = Dy, Ho$ ) via high temperature reactions at 1550°C or greater. In contrast to monoclinic  $RE_3SbO_3$ , the new phases adopt the  $P4_2/mnm$  symmetry but have a structural framework similar to that of  $RE_3SbO_3$ . The formation of the tetragonal  $(RE^I RE^{II})_3SbO_3$  phases is driven by the ordering of the large and small  $RE$  atoms on different atomic sites. The  $La_{1.5}Dy_{1.5}SbO_3$ ,  $La_{1.5}Ho_{1.5}SbO_3$  and  $Ce_{1.5}Ho_{1.5}SbO_3$  samples were subjected to elemental microprobe analysis to verify their compositions and to electrical resistivity measurements to evaluate their thermoelectric potential. The electrical resistivity data indicate the presence of a band gap, which is supported by electronic structure calculations.

### 3.1 Introduction

The ever-increasing global demand for natural resources continues to fuel the research on and development of new and efficient ways for energy use. One potential approach is the use of thermoelectric materials for energy recovery from the waste heat, released by internal combustion engines, e.g. in cars and trucks.<sup>122, 123</sup> For such applications, thermoelectrics yield many advantages over other forms of energy recovery and production such as compactness, reliability, a lack of moving parts, and a long operational life. These properties have already allowed thermoelectrics to be used in some unique applications, such as power generation on spacecrafts<sup>30</sup> or wristwatches.<sup>124</sup>

The current drawback of thermoelectric materials is their low efficiency, which reaches 5-15% of the Carnot efficiency in the best materials known.<sup>13</sup> As such, thermoelectrics have only seen use in small, niche applications in which compactness and reliability outweigh efficiency. A good thermoelectric material must have a high Seebeck coefficient and electrical conductivity and a low thermal conductivity. Unfortunately, the Seebeck coefficient and electrical conductivity of a material compromise each other, and usually cannot both be optimized simultaneously. Likewise, designing a material with good electrical properties and a low thermal conductivity presents a great challenge due to the thermal conductivity provided by charge carriers. Different strategies have been employed to optimize thermoelectric properties. One such method is to prepare phases with electrical properties of a crystalline solid, but with thermal conductivities of a glass.<sup>20</sup> Such a material, known as a phonon-glass electron-crystal (PGEC), has been realized in few systems, e.g. in  $\text{Zn}_4\text{Sb}_3$ <sup>73-75</sup> and PbTe-based phases.<sup>125, 126</sup>

In pursuit of novel PGEC phases, our group has focused on the synthesis of complex rare-earth (*RE*) antimonide suboxides, such as  $\text{RE}_3\text{SbO}_3$ ,  $\text{RE}_8\text{Sb}_{3-\delta}\text{O}_8$  and  $\text{RE}_2\text{SbO}_2$ .<sup>99, 127</sup> In the case of  $\text{RE}_3\text{SbO}_3$ , we have combined the electrically conductive, semimetallic  $\text{RESb}$  and thermally insulating  $\text{RE}_2\text{O}_3$  binaries into a single structure, with the goal of conserving the desirable properties of each. The new  $\text{RE}_3\text{SbO}_3$  phases feature high thermal stability and low thermal conductivity but possess high electrical resistivities, which make them unsuitable for thermoelectric applications. Although the desired properties could not be obtained, we have succeeded in the direct combination of

$RESb$  and  $RE_2O_3$  and the opening of a band gap within the  $RE$ -Sb framework. As such, there is a potential for the  $RE_3SbO_3$  phases if their electrical resistivities can be reduced to a more suitable level, either by elemental substitution or further structural modifications.

Originally, we have explored substitution of Ce for the trivalent  $RE$  in  $RE_3SbO_3$ . However, it was established that Ce is also trivalent in the prepared  $(CeRE^{II})_3SbO_3$  phases. These new, mixed phases were discovered to have tetragonal symmetry while the parent  $RE_3SbO_3$  structures were monoclinic. The subsequent experiments revealed that this structural change is possible only through the use of two  $RE$  atoms with a sufficiently large difference in atomic radii, which results in the preferential ordering of large and small rare-earths on different atomic sites. In this paper, we discuss the synthetic conditions, characterization, and electronic structures of the new, tetragonal  $(RE^I RE^{II})_3SbO_3$  phases ( $RE^I = La, Ce$ ;  $RE^{II} = Dy, Ho$ ).

## 3.2 Experimental

### 3.2.1 Synthesis.

Samples were made using high-purity  $RE$  metals (99.99 wt.%, SmartElements) ( $RE = La, Ce, Dy, Ho$ ), antimony metal (99.999 wt.%, CERAC Inc.) and  $RE_2O_3$  and  $CeO_2$  powder (99.999 wt.%, Rhône-Poulenc). In order to avoid the volatility of elemental antimony and its reactivity with tantalum at elevated temperatures, the corresponding  $RESb$  binaries were first prepared. The  $RESb$  binaries were prepared by mixing  $RE$  filings

with ground antimony powder in equimolar amounts within a glove box filled with argon. These mixtures were then pressed into pellets of 1 to 2 grams and sealed below  $10^{-5}$  torr in silica tubes. Samples were annealed in box furnaces at a temperature of  $600^{\circ}\text{C}$  for 12 hours and then at  $850^{\circ}\text{C}$  for 48 hours to complete the reaction. Upon quenching in air, black pellets of *RESb* were obtained. X-Ray powder diffraction was performed on all samples to confirm their purity.

Samples of  $RE^{\text{I}}_{1.5}RE^{\text{II}}_{1.5}\text{SbO}_3$  were prepared by mixing the *RESb* binaries and  $RE_2\text{O}_3$  for each of the respective *RE* present in a 1:1:1:1 molar ratio. The uneven  $RE^{\text{I}}:RE^{\text{II}}$  ratio  $(RE^{\text{I}}RE^{\text{II}})_3\text{SbO}_3$  samples were prepared by mixing the respective *RESb* and  $RE_2\text{O}_3$  binaries to produce the desired stoichiometry. The  $(\text{Ce}RE^{\text{II}})_3\text{SbO}_3$  samples were prepared by mixing filed *RE* metal, the *RESb* binaries, and  $\text{CeO}_2$  in the desired molar ratio. The respective mixtures were pressed into pellets of 1 gram and placed inside tantalum ampoules which were then sealed by arc-melting under argon atmosphere. High-temperature reaction conditions were accomplished through the use of an induction furnace. The tantalum ampoules containing samples were placed inside a molybdenum susceptor which was heated in the radio frequency furnace under dynamic vacuum below  $10^{-5}$  torr. An optical pyrometer was used to monitor the temperature of reaction. All samples were heated at  $1550^{\circ}\text{C}$  for 10 hours to ensure a complete reaction. Samples were allowed to cool down to room temperature inside the furnace under vacuum over a period of 1 hour. The obtained products were black, molten, crystalline, and stable in air. According to X-ray powder diffraction analysis, samples exposed to air for several weeks

showed no signs of decomposition. A list of all samples prepared is presented in Table 3.1.

**Table 3.1.  $(RE^I RE^{II})_3SbO_3$  samples prepared by high-temperature synthesis at 1550°C.**

System	$RE^I_{2.5}RE^{II}_{0.5}SbO_3$	$RE^I_2RE^{II}SbO_3$	$RE^I_{1.5}RE^{II}_{1.5}SbO_3$	$RE^I RE^{II}_2SbO_3$	$RE^I_{0.5}RE^{II}_{2.5}SbO_3$
Ce-Gd-Sb-O	-	-	Monoclinic $RE_3SbO_3$	-	-
Ce-Ho-Sb-O	-	-	Tetragonal $RE_3SbO_3$	Monoclinic $RE_3SbO_3$ and $RE_2SbO_2$	$RE_2SbO_2$
Ce-Er-Sb-O	-	-	Tetragonal $RE_3SbO_3$ and $RE_2SbO_2$	-	-
La-Dy-Sb-O	Monoclinic $RE_3SbO_3$	Monoclinic $RE_3SbO_3$	Tetragonal $RE_3SbO_3$	Tetragonal $RE_3SbO_3$	$RE_2SbO_2$
La-Ho-Sb-O	Monoclinic $RE_3SbO_3$	Monoclinic $RE_3SbO_3$	Tetragonal $RE_3SbO_3$	$RE_2SbO_2$	$RE_2SbO_2$

### 3.2.2 X-ray Single Crystal Diffraction

Single crystals picked up from the samples were analyzed on a STOE IPDSII diffractometer using Mo  $K_\alpha$  radiation in the whole reciprocal sphere. A numerical absorption correction was based on the crystal shape originally determined by optical face indexing, but was later optimized against equivalent reflections using the STOE X-Shape software.<sup>112</sup> Crystal structures were determined and solved using the SHELX software.<sup>128</sup> All structures studied adopt the  $P4_2/mnm$  space group. The lattice parameters of structures were observed to expand with larger  $RE$  atoms. During refinement, the  $RE$  atoms were permitted to mix on the  $RE1$  and  $RE2$  sites, yielding mixed occupancy on both sites for all

structures. While the occupancies of Dy and Ho on the *RE1* site in  $\text{La}_{1.47(7)}\text{Dy}_{1.53(7)}\text{SbO}_3$  and  $\text{Ce}_{1.34(9)}\text{Ho}_{1.66(9)}\text{SbO}_3$  are within three standard deviations from zero, the Hamilton test<sup>129</sup> indicated that their presence on this site can be accepted with a higher than 0.995 confidence level. A summary of the refinement results is presented in Tables 3.2 and 3.3. Further information on the crystal structures of all compounds presented, including the monoclinic  $\text{Dy}_3\text{SbO}_3$  structure collected for this work, can be obtained from the Fachinformationszentrum Karlsruhe, 76344 Eggenstein-Leopoldshafen, Germany (fax (49) 7247-808-666; email [crysdata@fiz.karlsruhe.de](mailto:crysdata@fiz.karlsruhe.de)), by quoting the CSD depository numbers 425138 for  $\text{Ce}_{1.5}\text{Ho}_{1.5}\text{SbO}_3$ , 425139 for  $\text{La}_{1.5}\text{Dy}_{1.5}\text{SbO}_3$ , 425140 for  $\text{La}_{1.5}\text{Ho}_{1.5}\text{SbO}_3$ , 425141 for  $\text{Dy}_3\text{SbO}_3$ , and 425150 for  $\text{LaDy}_2\text{SbO}_3$ .

**Table 3.2. Crystallographic and refinement data for the  $(RE^I RE^{II})_3SbO_3$  crystals.**

	La <sub>1.5</sub> Dy <sub>1.5</sub> SbO <sub>3</sub>	LaDy <sub>2</sub> SbO <sub>3</sub>	La <sub>1.5</sub> Ho <sub>1.5</sub> SbO <sub>3</sub>	Ce <sub>1.5</sub> Ho <sub>1.5</sub> SbO <sub>3</sub>
<b>Refined composition</b>	La <sub>1.47(7)</sub> Dy <sub>1.53(7)</sub> SbO <sub>3</sub>	La <sub>0.96(9)</sub> Dy <sub>2.04(9)</sub> SbO <sub>3</sub>	La <sub>1.32(4)</sub> Ho <sub>1.68(4)</sub> SbO <sub>3</sub>	Ce <sub>1.34(9)</sub> Ho <sub>1.66(9)</sub> SbO <sub>3</sub>
<b>Space group</b>	<i>P4<sub>2</sub>/mnm</i>	<i>P4<sub>2</sub>/mnm</i>	<i>P4<sub>2</sub>/mnm</i>	<i>P4<sub>2</sub>/mnm</i>
<b><i>a</i> (Å)</b>	11.947(1)	11.864(2)	11.920(2)	11.880(2)
<b><i>c</i> (Å)</b>	3.9263(8)	3.8920(8)	3.9057(8)	3.8906(8)
<b>Volume (Å<sup>3</sup>)</b>	560.4(1)	547.8(3)	555.0(2)	549.1(2)
<b><i>Z</i></b>	4	4	4	4
<b>Index ranges</b>	-19 ≤ <i>h</i> ≤ 15 -18 ≤ <i>k</i> ≤ 18 -6 ≤ <i>l</i> ≤ 6	-15 ≤ <i>h</i> ≤ 18 -18 ≤ <i>k</i> ≤ 18 -6 ≤ <i>l</i> ≤ 6	-18 ≤ <i>h</i> ≤ 15 -18 ≤ <i>k</i> ≤ 18 -6 ≤ <i>l</i> ≤ 5	-18 ≤ <i>h</i> ≤ 18 -18 ≤ <i>k</i> ≤ 14 -6 ≤ <i>l</i> ≤ 6
<b>2θ range</b>	6.82° - 68.96°	6.68° - 69.01°	6.84° - 68.70°	6.86° - 68.96°
<b>Total reflections</b>	6684	4159	5522	5304
<b>Goodness-of-fit on F<sup>2</sup></b>	1.187	1.169	1.091	1.029
<b>R indices</b>	<i>R</i> <sub>1</sub> = 0.0378 <i>wR</i> <sub>2</sub> = 0.0760 <i>R</i> <sub>1</sub> (all data) = 0.0532	<i>R</i> <sub>1</sub> = 0.0557 <i>wR</i> <sub>2</sub> = 0.0759 <i>R</i> <sub>1</sub> (all data) = 0.0883	<i>R</i> <sub>1</sub> = 0.0380 <i>wR</i> <sub>2</sub> = 0.0445 <i>R</i> <sub>1</sub> (all data) = 0.0625	<i>R</i> <sub>1</sub> = 0.0519 <i>wR</i> <sub>2</sub> = 0.0617 <i>R</i> <sub>1</sub> (all data) = 0.1019
<b>Extinction coefficient</b>	0.0026(2)	0.0012(1)	0.00175(9)	0.00073(6)

**Table 3.3. Atomic parameters for the  $(RE^I RE^{II})_3SbO_3$  crystals.**

Atom	Site	Occupancy	x	y	z	$U_{eq}$
<b>La<sub>1.47(7)</sub>Dy<sub>1.53(7)</sub>SbO<sub>3</sub></b>						
<b>La/Dy1</b>	4 <i>f</i>	0.93/0.07(3)	0.11537(4)	0.11537(4)	0	0.0119(2)
<b>La/Dy2</b>	8 <i>i</i>	0.27/0.73(3)	0.12314(4)	0.65651(5)	0	0.0135(2)
<b>Sb1</b>	4 <i>f</i>	1	0.37828(5)	0.37828(5)	0	0.0124(3)
<b>O1</b>	4 <i>g</i>	1	0.3104(5)	0.6896(5)	0	0.013(2)
<b>O2</b>	8 <i>i</i>	1	0.0660(7)	0.3383(8)	0	0.028(2)
<b>La<sub>0.96(9)</sub>Dy<sub>2.04(9)</sub>SbO<sub>3</sub></b>						
<b>La/Dy1</b>	4 <i>f</i>	0.75/0.25(4)	0.11601(7)	0.11601(7)	0	0.0135(2)
<b>La/Dy2</b>	8 <i>i</i>	0.11/0.89(4)	0.12298(7)	0.65631(6)	0	0.0116(2)
<b>Sb1</b>	4 <i>f</i>	1	0.37824(8)	0.37824(8)	0	0.0123(4)
<b>O1</b>	4 <i>g</i>	1	0.3110(8)	0.6890(8)	0	0.016(3)
<b>O2</b>	8 <i>i</i>	1	0.0660(9)	0.339(1)	0	0.025(3)
<b>La<sub>1.32(4)</sub>Ho<sub>1.68(4)</sub>SbO<sub>3</sub></b>						
<b>La/Ho1</b>	4 <i>f</i>	0.92/0.08(2)	0.11539(5)	0.11539(5)	0	0.0119(2)
<b>La/Ho2</b>	8 <i>i</i>	0.20/0.80(2)	0.12319(4)	0.65604(4)	0	0.0139(1)
<b>Sb1</b>	4 <i>f</i>	1	0.37756(5)	0.37756(5)	0	0.0119(2)
<b>O1</b>	4 <i>g</i>	1	0.3100(5)	0.6900(5)	0	0.012(2)
<b>O2</b>	8 <i>i</i>	1	0.0660(6)	0.3394(8)	0	0.029(2)
<b>Ce<sub>1.34(9)</sub>Ho<sub>1.66(9)</sub>SbO<sub>3</sub></b>						
<b>La/Ce1</b>	4 <i>f</i>	0.88/0.12(4)	0.11523(9)	0.11523(9)	0	0.0130(3)
<b>La/Ce2</b>	8 <i>i</i>	0.23/0.77(4)	0.12372(8)	0.65599(6)	0	0.0130(2)
<b>Sb1</b>	4 <i>f</i>	1	0.37815(9)	0.37815(9)	0	0.0121(4)
<b>O1</b>	4 <i>g</i>	1	0.3122(8)	0.6878(8)	0	0.013(3)
<b>O2</b>	8 <i>i</i>	1	0.067(1)	0.339(1)	0	0.032(3)

### 3.2.3 X-ray Powder Diffraction

All samples studied were analyzed by X-ray powder diffraction using a PANalytical X'Pert Pro diffractometer with Cu  $K_{\alpha 1}$  radiation and an X'Celerator detector. This was done to determine reaction progression, sample purity, and lattice constants. Samples were ground in 20 to 50 mg amounts in a mortar and pestle until a fine powder was obtained. The obtained powder was distributed evenly on disks manufactured from single crystals of silicon which were coated with a thin film of Vaseline. Diffraction data were collected in the  $20^{\circ}$ - $70^{\circ}$   $2\theta$  range for all samples. The Rietvald refinement method (Rietica program<sup>114</sup>) was employed to determine sample purity and lattice constants. The structural parameters obtained from the single crystal refinements were used as starting models.

### 3.2.4 Coordination Polyhedra Analysis

Coordination polyhedra of the new tetragonal  $(RE^I RE^{II})_3SbO_3$  structures, the previously studied monoclinic  $Ho_3SbO_3$  phase<sup>99</sup>, and the monoclinic  $Dy_3SbO_3$  phase prepared for this work were analyzed with the Dido95 program.<sup>130</sup> For this purpose, we have calculated the volumes of the  $RE$  sites, which are represented by the volumes of the Wigner-Seitz polyhedra. Atomic positions determined from the X-ray single crystal solutions were used for calculations.

### 3.2.5 Microprobe Measurements

The quantitative elemental analysis of the selected samples was performed employing the electron probe microanalysis (EPMA) through a wavelength dispersive

(WDS) X-Ray spectroscopy (Model JXA-8500F, JEOL, Tokyo, Japan).  $\text{LaB}_6$ ,  $\text{CeB}_6$ ,  $\text{Al}_2\text{O}_3$ ,  $\text{Ho}_5\text{Sb}_3$  and  $\text{DySb}$  were used as standards to determine the concentrations of La, Ce, Ho, Sb, Dy and O in the title compounds. The EPMA was performed on polished surfaces samples by averaging the data taken from 5 to 10 locations of selected grains. Only the  $RE^I_{1.5}RE^{II}_{1.5}\text{SbO}_3$  samples were analyzed for measurement as these samples yielded the best purities.

### 3.2.6 Electrical Resistivity Measurements

Samples of  $\text{La}_{1.5}\text{Dy}_{1.5}\text{SbO}_3$ ,  $\text{La}_{1.5}\text{Ho}_{1.5}\text{SbO}_3$  and  $\text{Ce}_{1.5}\text{Ho}_{1.5}\text{SbO}_3$  were ground and pressed into pellets with a tungsten carbide press die in a glove box under argon atmosphere. Only the  $RE^I_{1.5}RE^{II}_{1.5}\text{SbO}_3$  set of samples were chosen for measurement as the highest purities were obtained for this stoichiometry. Samples were then sealed in evacuated silica tubes and annealed at  $1000^\circ\text{C}$  for 24 hours to ensure rigidity. X-Ray powder diffraction revealed no decomposition or generation of impurities.

The electrical resistivity was measured in the 2-400 K range on rectangular shaped samples with a four-probe technique using a press contact assembly produced by Wimbush Science & Technology and on a PPMS instrument (Quantum Design, USA). During the measurements, the samples were heated with a speed of 1 K/min to allow thermal equilibration with a cryostat.

### 3.2.7 Electronic Band Structure Calculations

The band structures of the tetragonal fully ordered  $RE^I RE^{II}_2\text{SbO}_3$  phases ( $\text{LaDy}_2\text{SbO}_3$ ,  $\text{LaHo}_2\text{SbO}_3$  and  $\text{CeHo}_2\text{SbO}_3$ ) were calculated using the tight-binding, linear-

muffin tin orbital method<sup>117</sup> with the atomic sphere approximation (TB-LMTO-ASA) as implemented in the Stuttgart program.<sup>118</sup> The experimental lattice and atomic parameters obtained from the X-Ray single crystal refinements of the  $\text{LaDy}_2\text{SbO}_3$ ,  $\text{La}_{1.5}\text{Dy}_{1.5}\text{SbO}_3$ ,  $\text{La}_{1.5}\text{Ho}_{1.5}\text{SbO}_3$ , and  $\text{Ce}_{1.5}\text{Ho}_{1.5}\text{SbO}_3$  samples were used for calculations. Since the atomic mixing cannot be treated during calculations, the *RE1* and *RE2* sites in each structure were assumed to be fully occupied by the larger and smaller *RE*, respectively. All *4f* electrons were considered as core electrons. Exchange and correlation were treated by the local density approximation (LDA).<sup>119</sup> A scalar relativistic approximation<sup>120</sup> was employed to account for all relativistic effects except spin-orbit coupling. Overlapping Wigner-Seitz cells were constructed with radii determined by requiring the overlapping potential to be the best approximation to the full potential, according to the atomic sphere approximation (ASA). Automatic sphere generation<sup>121</sup> was performed to construct empty spheres to be included in the unit cell in order to satisfy the overlap criteria of the TB-LMTO-ASA model.

### 3.3 Results and Discussion

#### 3.3.1 Composition and Formation of $(RE^I RE^{II})_3\text{SbO}_3$

The X-ray single crystal refinements of the  $\text{La}_{1.5}\text{Dy}_{1.5}\text{SbO}_3$  and  $\text{Ce}_{1.5}\text{Ho}_{1.5}\text{SbO}_3$  sample yielded compositions (Table 3.3) that are within 1 and 2 standard deviations from the loading compositions, respectively. Refinement of the  $\text{La}_{1.5}\text{Ho}_{1.5}\text{SbO}_3$  crystal yielded

the  $\text{La}_{1.32(4)}\text{Ho}_{1.68(4)}\text{SbO}_3$  composition that is statistically different from the loading one. In some cases, X-ray single crystal results may not represent the actual composition, particularly when a site mixing is present and difference between the atomic scattering factors is not large. To establish true compositions (and verify refinement results), electron probe microanalyses (EPMA) were performed on three samples. (Table 3.4) Upon inspecting Table 3.4, it is readily apparent that the equimolar loading ratios of the  $RE$  atoms are preserved across all samples within one standard deviation. An excess of oxygen is observed, but this can be attributed to the surface oxidation during polishing. Based on the EPMA results, we can conclude that  $(RE^I RE^{II})_3\text{SbO}_3$  phases maintain the same rare-earth compositions that are used in their formation.

**Table 3.4. Compositions of the tetragonal  $(RE^I RE^{II})_3\text{SbO}_3$  phases based on the EPMA and the X-ray single crystal analyses. The EPMA results were normalized to one Sb atom.**

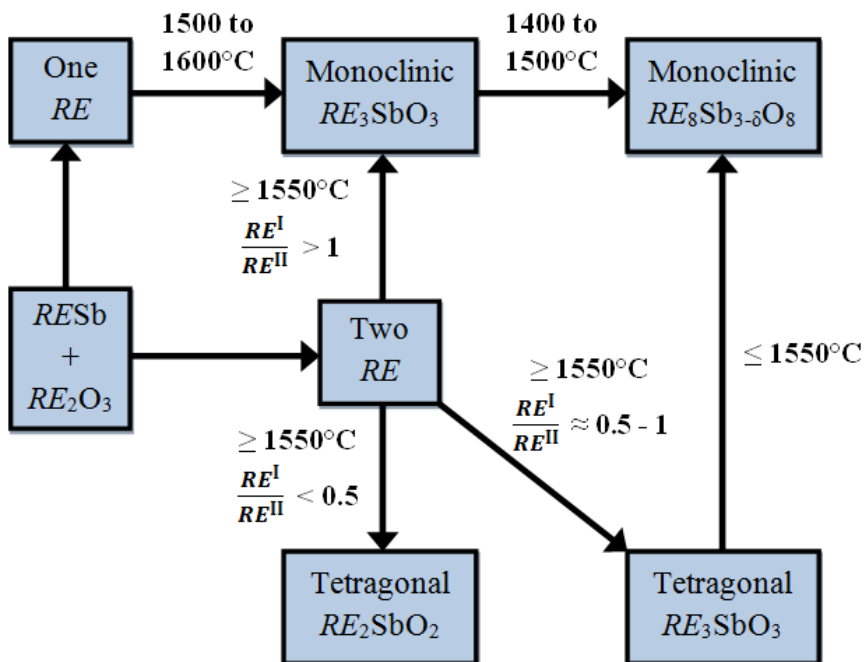
Loading Composition	EPMA	X-Ray
$\text{La}_{1.5}\text{Dy}_{1.5}\text{SbO}_3$	$\text{La}_{1.45(7)}\text{Dy}_{1.55(7)}\text{Sb}_{1.00(8)}\text{O}_{6.42(5)}$	$\text{La}_{1.47(7)}\text{Dy}_{1.53(7)}\text{SbO}_3$
$\text{La}_{1.5}\text{Ho}_{1.5}\text{SbO}_3$	$\text{La}_{1.54(6)}\text{Ho}_{1.52(6)}\text{Sb}_{1.00(8)}\text{O}_{5.98(5)}$	$\text{La}_{1.32(4)}\text{Ho}_{1.68(4)}\text{SbO}_3$
$\text{Ce}_{1.5}\text{Ho}_{1.5}\text{SbO}_3$	$\text{Ce}_{1.54(6)}\text{Ho}_{1.47(6)}\text{Sb}_{1.00(7)}\text{O}_{5.13(5)}$	$\text{Ce}_{1.34(9)}\text{Ho}_{1.66(9)}\text{SbO}_3$

Samples with loading compositions containing different ratios of  $RE^I$  to  $RE^{II}$  were also prepared using similar reaction conditions as the samples with the equimolar ratios. The synthesis of  $\text{LaDy}_2\text{SbO}_3$  ( $RE^I = \text{La}$  and  $RE^{II} = \text{Dy}$ ) was confirmed to produce the tetragonal  $RE_3\text{SbO}_3$  structure, but with a smaller unit cell when compared to

$\text{La}_{1.5}\text{Dy}_{1.5}\text{SbO}_3$ . Reactions of the  $RE^I_2RE^{II}\text{SbO}_3$  and  $RE^I_{2.5}RE^{II}_{0.5}\text{SbO}_3$  phases yielded only the monoclinic  $RE_3\text{SbO}_3$  phases; these samples were not analyzed further. In contrast, the  $RE^I RE^{II}_2\text{SbO}_3$  and  $RE^I_{0.5}RE^{II}_{2.5}\text{SbO}_3$  samples, excluding  $\text{LaDy}_2\text{SbO}_3$ , were shown to produce the  $RE_2\text{SbO}_2$  phase. The rationalization for forming each phase at different  $RE^I$  to  $RE^{II}$  ratios will be discussed later.

The tetragonal  $(RE^I RE^{II})_3\text{SbO}_3$  phases can be obtained only at reaction temperatures of  $1550^\circ\text{C}$  and greater; at temperatures less than  $1500^\circ\text{C}$ , either the corresponding  $RE_8\text{Sb}_{3-\delta}\text{O}_8$  or  $RE_2\text{SbO}_2$  phase is formed depending on the  $RE^I$  and  $RE^{II}$  used and their ratios. When only one type of  $RE$  is used, the resulting phase is always either the monoclinic  $RE_3\text{SbO}_3$  phase or the monoclinic  $RE_8\text{Sb}_{3-\delta}\text{O}_8$  phase at temperatures of at least  $1550^\circ\text{C}$ . The formation conditions for  $(RE^I RE^{II})_3\text{SbO}_3$  are summarized in Scheme 1. It is worth mentioning that prolonged heat treatments below  $1550^\circ\text{C}$  will irreversibly convert the tetragonal  $(RE^I RE^{II})_3\text{SbO}_3$  phase into the corresponding monoclinic  $RE_3\text{SbO}_3$  and  $RE_8\text{Sb}_{3-\delta}\text{O}_8$  phases, with mixing on all  $RE$  sites. The tetragonal phase can be prepared for samples containing two  $RE$  of significantly different sizes, which limits the possible combinations. Based on the crystal radii of the rare-earth atoms<sup>131</sup> used, the lowest large-to-small ratio of rare-earth radii shown to produce the phase is 1.23, accomplished with  $\text{Ce}_{1.5}\text{Ho}_{1.5}\text{SbO}_3$ . Furthermore, an attempt to prepare the tetragonal  $\text{Ce}_{1.5}\text{Gd}_{1.5}\text{SbO}_3$  analogue was unsuccessful. Considering the crystal radii ratio of Ce to Gd is 1.19, it appears the minimum ratio required may lie between these two

values. The reasons for the formation of the tetragonal structure as opposed to the monoclinic phase for the mixed  $(RE^I RE^{II})_3SbO_3$  phases are discussed below.



**Scheme 3.1. Procedures of formation of the phases studied in the RE-Sb-O system.**

### 3.3.2 Structures and Preferential Site Occupancy

The  $(RE^I RE^{II})_3SbO_3$  phases of interest adopt a novel crystal structure with the  $P4_2/mnm$  space group. The structure is defined by a REO framework composed of edge-sharing  $RE_4O$  tetrahedra. Three  $RE_4O$  tetrahedra are fused via edge-sharing to form  $RE_8O_3$  units referred to as building blocks. Within the  $ab$  plane, these blocks connect to each other via corners to build 2D slabs (Figure 3.1). In turn, the slabs stack along the  $c$

direction via edge-sharing to form the 3D *REO* framework. Additionally, square and rectangular channels along the *c* direction are created by this arrangement. The rectangular voids are occupied by two Sb atoms and the square voids are left unoccupied. The Sb–Sb separations are too large to support dimer formation, as the shortest distance between these atoms is  $\sim 4\text{\AA}$ .<sup>132</sup> An interesting aspect of the  $(RE^I RE^{II})_3\text{SbO}_3$  phases is the position and displacement parameters for the O2 atoms located in the tetrahedral voids on each side of a  $RE_8\text{O}_3$  building block. The O2 atoms are displaced from the center of *RE* tetrahedra towards the centre of a terminal triangular face. The large displacement parameters of the O2 atoms are also directed towards the centers of these terminal triangular faces. Such feature is likely due to anion-anion repulsion between O1 and O2 atoms in the same building block, which pushes the outside O2 atoms further away from their ideal position at the centre of each  $RE_4\text{O}$  unit, and as a result yields high displacement parameters.

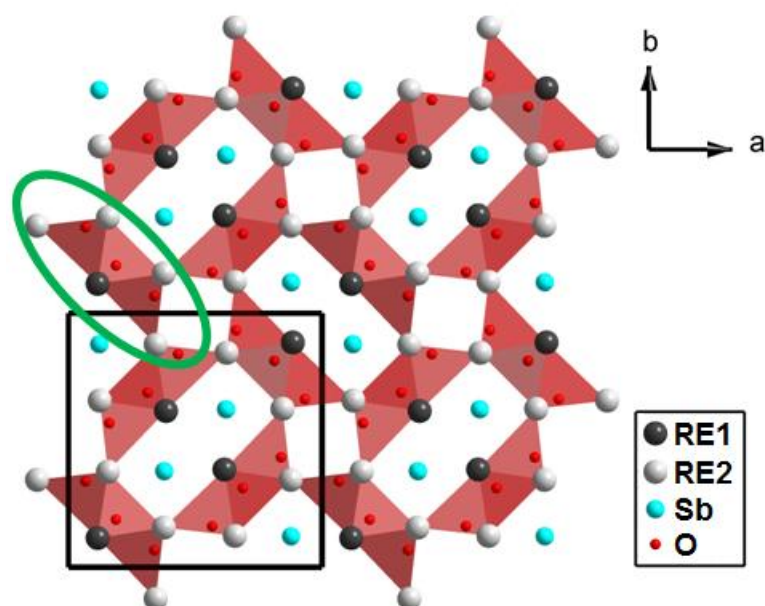


**Figure 3.1.** The tetragonal  $(RE^I RE^{II})_3SbO_3$  structure and its building block type composed of  $RE_4O$  tetrahedra.

It is useful to view these phases in a simplified form as  $RE_3SbO_3$ , which has the same composition as the previously studied monoclinic  $RE_3SbO_3$  phases.<sup>99</sup> Both structures include  $REO$  frameworks which define the overall structure and empty channels occupied by Sb atoms. Aside from their differences in symmetry, the two  $RE_3SbO_3$  phases can be easily distinguished by their building block types and arrangements (Figure 3.2). The previously studied monoclinic  $RE_3SbO_3$  phase contains two distinct building blocks A and B, which are four and two tetrahedral  $RE_4O$  units long, respectively. In contrast, the newly discovered tetragonal  $(RE^I RE^{II})_3SbO_3$  phase contains only one type of building block, which is three  $RE_4O$  tetrahedra long in all directions, accounting for its higher symmetry. Both structures also have large displacement

parameters for the oxygen atoms located at the ends of the building blocks. This unusual feature appears to be preserved amongst the rare-earth antimonide oxide series, as the  $RE_8Sb_{3-\delta}O_8$  phase (Figure 3.2) also has terminal O atoms with large displacement parameters.

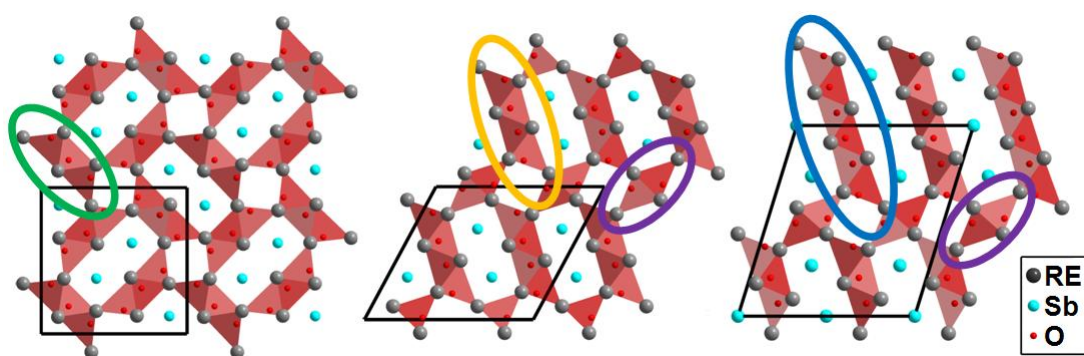


**Figure 3.2. Comparison of the tetragonal  $(RE^I RE^{II})_3SbO_3$  (left), monoclinic  $RE_3SbO_3$  (middle), and monoclinic  $RE_8Sb_{3-\delta}O_8$  (right) phases. Different building block types are highlighted with different colours.**

The  $(RE^I RE^{II})_3SbO_3$  structure contains two  $RE$  sites which both have mixed occupancy. The  $RE1$  site ( $4f$ ), located in the centre of each building block strongly, is preferentially ( $> 75\%$ ) occupied by larger  $RE$  atoms (Table 3.3). Conversely, the  $RE2$  site ( $8i$ ), located at the outside corners of the  $RE_8O_3$  building blocks ( $> 73\%$ ) prefers the smaller  $RE$  atoms. The site preference was analyzed based on the polyhedra volume (Figure 3.3) and electronegativity of the  $RE^I$  and  $RE^{II}$  atoms. In  $(RE^I RE^{II})_3SbO_3$ ,  $RE1$  atoms occupy distorted square antiprisms with one face consisting of oxygen atoms and another face consisting of Sb atoms, while  $RE2$  atoms sit in distorted octahedra made of

four oxygen atoms and two antimony atoms,. The site volumes, calculated with the Dido95 program<sup>130</sup>, are given in Table 3.5. The *RE1* site volume is almost 25% larger than the *RE2* site volume, and thus it should be preferentially occupied by larger *RE* atoms. Also, the electronegativity difference favors such *RE* distribution; the larger *RE* atoms are more electropositive and as such they can support anion-rich environments (*RE1* site) better than the smaller and more electronegative *RE* atoms.

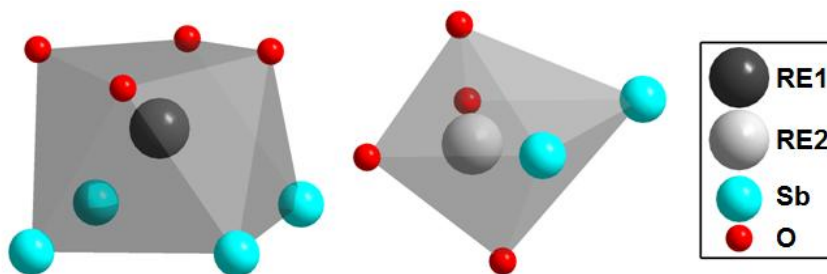


**Figure 3.3. Coordination polyhedra of the *RE1* site (left) and the *RE2* site (right) in the tetragonal  $(RE^I RE^{II})_3SbO_3$  phases.**

The presence of the *RE1* and *RE2* sites with largely different volumes within the tetragonal  $(RE^I RE^{II})_3SbO_3$  structures appears to be the reason for the existence of these mixed phases. Table 3.5 gives the site volumes for the monoclinic  $Dy_3SbO_3$  and  $Ho_3SbO_3$  phases in addition to those for the mixed phases. It is evident that in the monoclinic  $RE_3SbO_3$  phase, the *RE* sites are quite similar in volume to one another, as the maximum relative volume difference of the *RE* sites in the monoclinic  $RE_3SbO_3$  structures is only about 15%, yet this difference is about 10% higher in each of the tetragonal  $(RE^I RE^{II})_3SbO_3$  structures. Thus, it is easy for any *RE* atom to occupy the *RE* sites evenly

in the monoclinic  $RE_3SbO_3$  phase. However, in the tetragonal  $(RE^I RE^{II})_3SbO_3$  phase, the two  $RE$  sites are significantly different in size and, if only one  $RE$  atom is used, it is not possible for simultaneous occupation of both sites due to their large volume difference, and as a result, the structure cannot be formed. Through the usage of two different  $RE$  with significantly different sizes, a preference of one  $RE$  to occupy one site over another is introduced and this supports the novel tetragonal  $REO$  framework. However, a full separation of the  $RE^I$  and  $RE^{II}$  atoms on the two sites is not achieved.

The tetragonal structure can be preserved with the  $RE^I RE^{II}_2SbO_3$  stoichiometry, for at least  $LaDy_2SbO_3$ , as the larger  $RE1$  site can easily accommodate more of the small  $RE$  with some additional occupation on the  $RE2$  site. The net result is no change in the coordination polyhedra volume between the  $La_{1.5}Dy_{1.5}SbO_3$  and  $LaDy_2SbO_3$  structures (24.6(3)% vs. 24.7(3)%). It is not known why  $LaDy_2SbO_3$  formed the tetragonal  $(RE^I RE^{II})_3SbO_3$  phase while the  $LaHo_2SbO_3$  and  $CeHo_2SbO_3$  samples did not. However, based on the occupations of the  $RE$  sites in the  $LaDy_2SbO_3$  crystal solution, it is likely that the  $RE^I RE^{II}_2SbO_3$  stoichiometry is near the limit of compositions that can form the tetragonal  $(RE^I RE^{II})_3SbO_3$  phase, and perhaps a small change in site occupations for the  $LaHo_2SbO_3$  and  $CeHo_2SbO_3$  samples would result in the destruction of the desired phase.

The  $RE^I_2RE^{II}SbO_3$  and  $RE^I_{2.5}RE^{II}_{0.5}SbO_3$  phases studied were shown to not preserve the tetragonal  $(RE^I RE^{II})_3SbO_3$  structure. This is because the larger  $RE1$  site is already nearly fully occupied by the large  $RE$  (~90% in each structure) and as a result, the smaller  $RE2$  site must be occupied instead. This in turn destroys the size difference

between the two sites and leads to destabilization of the phase. Finally, the  $RE^I RE^{II}_2 SbO_3$  and  $RE^I_{0.5} RE^{II}_{2.5} SbO_3$  samples (excluding  $LaDy_2 SbO_3$ ) were shown to form the  $RE_2 SbO_2$  phase. This may occur since the high  $RE^{II}$  content cannot maintain the large size difference in the  $RE$  sites for the tetragonal structure, and as pointed out in previous literature<sup>99</sup>, the monoclinic  $RE_3 SbO_3$  phases require higher temperatures to form for the late rare earths. Since the  $Ce_{0.5} Ho_{2.5} SbO_3$  and  $La_{0.5} Ho_{2.5} SbO_3$  samples mostly consist of holmium, they can be viewed as  $Ho_3 SbO_3$ , which requires at least 1600°C to form monoclinic  $RE_3 SbO_3$ . Since neither the monoclinic nor the tetragonal  $RE_3 SbO_3$  phase can form, the  $RE_2 SbO_2$  phase becomes the preferred outcome for the  $RE^I_{0.5} RE^{II}_{2.5} SbO_3$  samples.

**Table 3.5. Coordination polyhedra volumes of the largest and smallest sites in the tetragonal  $(RE^I RE^{II})_3 SbO_3$  and monoclinic  $RE_3 SbO_3$  phases.**

Phase	Smallest $RE$ site volume*	Largest $RE$ site volume*	Relative size difference
Tetragonal phases			
$La_{1.47(7)} Dy_{1.53(7)} SbO_3$	17.02(3) Å <sup>3</sup>	21.20(4) Å <sup>3</sup>	24.6(3)%
$La_{1.32(4)} Ho_{1.68(4)} SbO_3$	16.76(3) Å <sup>3</sup>	21.15(4) Å <sup>3</sup>	26.2(3)%
$Ce_{1.34(9)} Ho_{1.66(9)} SbO_3$	16.73(3) Å <sup>3</sup>	20.67(4) Å <sup>3</sup>	23.5(3)%
$La_{0.96(9)} Dy_{2.04(9)} SbO_3$	16.62(3) Å <sup>3</sup>	20.72(4) Å <sup>3</sup>	24.7(3)%
Monoclinic phases			
$Dy_3 SbO_3$	15.98(3) Å <sup>3</sup>	18.44(4) Å <sup>3</sup>	15.4(3)%
$Ho_3 SbO_3$	15.79(3) Å <sup>3</sup>	18.28(4) Å <sup>3</sup>	15.8(3)%

\* In tetragonal  $(RE^I RE^{II})_3 SbO_3$ , the largest  $RE$  site is  $RE1$  and the smallest is  $RE2$ .

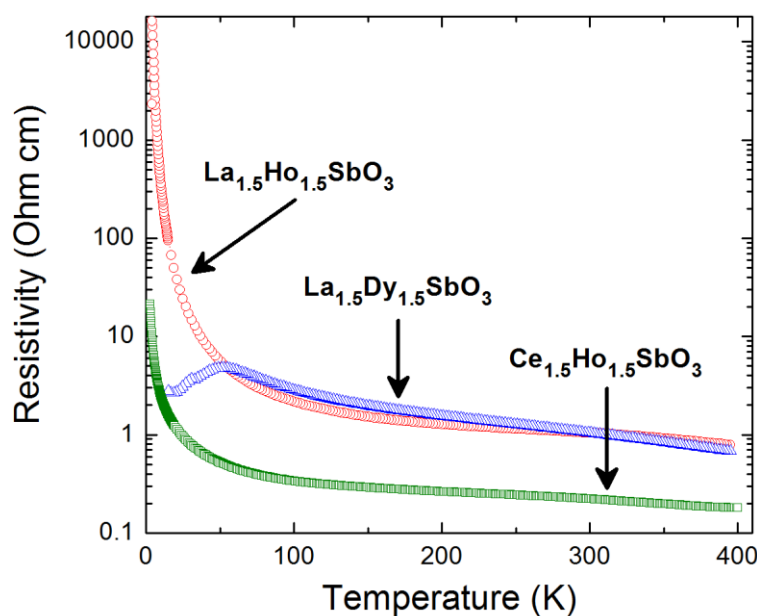
### 3.3.3 Electrical Resistivity and Electronic Structure

Assuming that La, Dy and Ho atoms are in +3 oxidation states and that Sb and O atoms act as isolated anions, the electronic formulas of  $(RE^I RE^{II})_3 SbO_3$  can be written as  $(RE^{I(3+)} RE^{II(3+)})_3 (Sb^{3-})(O^{2-})_3$ . It is readily apparent that the  $La_{1.5}Dy_{1.5}SbO_3$  and  $La_{1.5}Ho_{1.5}SbO_3$  structures are charge balanced and may be semiconducting. However, the  $Ce_{1.5}Ho_{1.5}SbO_3$  structure is somewhat ambiguous;  $CeO_2$  was used as a reactant which contains cerium atoms in the +4 oxidation state. While it is true that Ho metal is oxidized in the reaction with  $CeO_2$  to make  $Ce_{1.5}Ho_{1.5}SbO_3$ , cerium in the mixed valence state could still be present in the structure, giving the sample metallic behavior. This ambiguity was later resolved through electrical conductivity measurements.

The  $Ce_{1.5}Ho_{1.5}SbO_3$ ,  $La_{1.5}Dy_{1.5}SbO_3$ , and  $La_{1.5}Ho_{1.5}SbO_3$  samples show an Arrhenius-type exponential decrease in electrical resistivity with increasing temperature, which is indicative of semiconducting behaviour and in support of the charge-balanced formulas. This also suggests that  $Ce_{1.5}Ho_{1.5}SbO_3$  contains only  $Ce^{3+}$  and no  $Ce^{4+}$ , as this would lead to extra carrier electrons and metallic-type behaviour in the sample. The activation energies were calculated based on Arrhenius-type behaviour for a non-degenerate semiconductor with both electrons and holes as charge carriers. The room temperature electrical conductivities and activation energies are presented in Table 3.6. The electrical resistivities for all samples measured in this work are shown in Figure 3.4.

**Table 3.6. Room temperature electrical resistivities and activation energies of the  $\text{La}_{1.5}\text{Dy}_{1.5}\text{SbO}_3$ ,  $\text{La}_{1.5}\text{Ho}_{1.5}\text{SbO}_3$  and  $\text{Ce}_{1.5}\text{Ho}_{1.5}\text{SbO}_3$  samples.**

Sample	Electrical resistivity ( $\Omega$ cm)	Activation energy (eV)
$\text{La}_{1.5}\text{Dy}_{1.5}\text{SbO}_3$	1.05	0.11
$\text{La}_{1.5}\text{Ho}_{1.5}\text{SbO}_3$	1.05	0.093
$\text{Ce}_{1.5}\text{Ho}_{1.5}\text{SbO}_3$	0.223	0.044

**Figure 3.4. Electrical resistivities of the  $\text{Ce}_{1.5}\text{Ho}_{1.5}\text{SbO}_3$ ,  $\text{La}_{1.5}\text{Dy}_{1.5}\text{SbO}_3$ , and  $\text{La}_{1.5}\text{Ho}_{1.5}\text{SbO}_3$  samples.**

The La-containing samples displayed fairly similar electrical resistivities above 50 K, which is expected considering the similar chemistry between Dy and Ho. However below 50 K, the resistivity of  $\text{La}_{1.5}\text{Dy}_{1.5}\text{SbO}_3$  was found to increase. Such behavior may be due to (1) an highly-conductive impurity, which dominates the electrical transport

properties at low temperature, (2) minor deficiencies, which would change conductivity from semiconductor-like to metal-like, or (3) a semiconductor-to-metal transition, which may occur as the result of the  $\text{Sb}_2^{4-}$  dimer formation, accompanied by the release of conduction electrons. To date, we have not resolved the origin of this unexpected behaviour; we leave this work for future investigation.

Upon inspection, it is also observed that all samples measured have electrical resistivities of  $\sim 0.1\text{-}1 \text{ } \Omega \text{ cm}$  or greater at all temperatures measured, which are roughly two orders of magnitude greater than the resistivities of benchmark thermoelectric materials.<sup>37</sup> Additionally, these samples generally have electrical resistivities roughly equal to the monoclinic  $RE_3\text{SbO}_3$  and  $RE_8\text{Sb}_{3.5}\text{O}_8$  phases. Taking these facts into consideration, these new phases do not pose any foreseeable use for thermoelectric applications in their current states.

Semiconducting properties of the  $(RE^I RE^{II})_3\text{SbO}_3$  phases were verified through the electronic structure calculations on fully-ordered  $RE^I RE^{II}_2\text{SbO}_3$  structures. The calculated densities of states, DOS, of  $\text{LaDy}_2\text{SbO}_3$ ,  $\text{LaHo}_2\text{SbO}_3$  and  $\text{CeHo}_2\text{SbO}_3$  are very similar. The electronic structure of  $\text{LaDy}_2\text{SbO}_3$  is presented in Figure 3.5. An important feature of the DOS is the presence of a small band gap of about 0.3 eV, which separates the conduction band from the valence band. In agreement with the  $(RE^{(3+)I} RE^{(3+)II})_3(\text{Sb}^{3-})(\text{O}^{2-})_3$  formula, the conduction band is primarily composed of the  $RE$   $d$  states and the valence band is dominated by the  $\text{Sb}$   $p$  states, as the  $\text{O}$   $p$  states are much lower in energy.

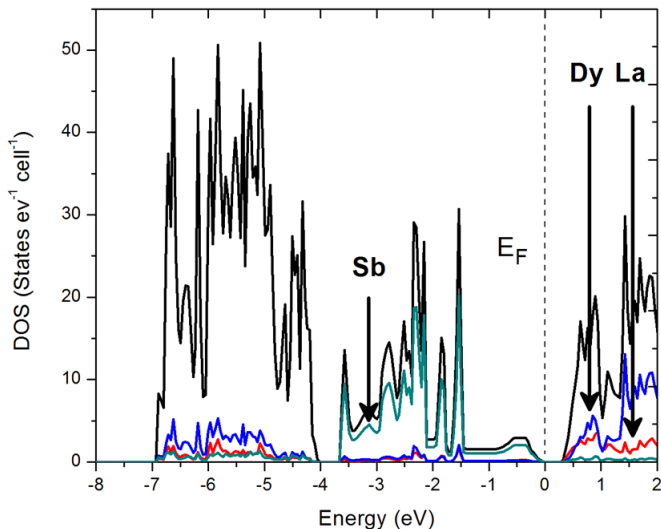


**Figure 3.5. Contribution of orbitals to bands near the Fermi levels in the electronic band structure of  $\text{LaDy}_2\text{SbO}_3$ .**

### 3.4 Conclusions

The mixed tetragonal  $(RE^I RE^{II})_3\text{SbO}_3$  compounds are small-band gap semiconductors similar to the previously studied monoclinic  $RE_3\text{SbO}_3$  and  $RE_8\text{Sb}_{3-\delta}\text{O}_8$  phases. Based on the electronic structure calculations, combining semimetallic  $RE\text{Sb}$  with corresponding  $RE_2\text{O}_3$  opens a band gap between the valence band dominated by the Sb states and the conduction band composed of the  $RE$  states. The semiconducting properties of the  $\text{Ce}_{1.5}\text{Ho}_{1.5}\text{SbO}_3$  phase support the +3 oxidation state for Ce, as a mixed valence state would yield a metallic behavior. The  $RE^I_{1.5}RE^{II}_{1.5}\text{SbO}_3$  samples display room-temperature electrical resistivities in the 0.1-1  $\Omega$  cm range, similar to the  $RE_3\text{SbO}_3$  and  $RE_8\text{Sb}_{3-\delta}\text{O}_8$  phases, which is too large for thermoelectric applications.

The tetragonal  $(RE^I RE^{II})_3SbO_3$  phases are obtained at temperatures above  $1550^\circ\text{C}$  and only when two  $RE$  atoms with highly different atomic radii are used. While the  $RE^I$  and  $RE^{II}$  atoms are distributed on both  $RE$  sites, there is a pronounced site preference; larger atoms tend to occupy the larger site ( $4f$ ) and smaller atoms occupy the smaller site ( $8i$ ). Compared to the analogous monoclinic  $RE_3SbO_3$  structures, the  $RE$  site volumes differ significantly in the tetragonal  $(RE^I RE^{II})_3SbO_3$  structures. Such difference supports incorporation of two different  $RE$  atoms into the structure and, ultimately, its stability.

## **Chapter 4. Synthesis, Crystal Structure, and Electronic Properties of the $\text{CaRE}_3\text{SbO}_4$ and $\text{Ca}_2\text{RE}_8\text{Sb}_3\text{O}_{10}$ Phases ( $\text{RE}$ is a rare-earth metal)**

This chapter contains the material covered in the manuscript “Synthesis, Crystal Structure, and Electronic Properties of the  $\text{CaRE}_3\text{SbO}_4$  and  $\text{Ca}_2\text{RE}_8\text{Sb}_3\text{O}_{10}$  Phases ( $\text{RE}$  is a rare-earth metal)”, which was published in *Chemistry of Materials* (*Chem. Mater.* **2014**, *26*, 2289-2298). The experimental procedures, structure determinations, and data interpretations were performed by the candidate. Ms. Fang Yuan carried out magnetic susceptibility measurements, Dr. Bayrammurad Saparov, Dr. Athena S. Sefat, and Dr. Taras Kolodiazhnyi performed physical property measurements on bulk samples, and Dr. Kosuke Kosuda performed electron microprobe analyses on selected samples.

Reproduced with permission from Scott Forbes, Fang Yuan, Bayrammurad Saparov, Athena S. Sefat, Taras Kolodiazhnyi, and Yuriy Mozharivskyj. *Chem. Mater.* **2014**, *26*, 2289-2298. Copyright 2014 American Chemical Society.

Through high temperature synthesis at 1300°C and above, our group has discovered and characterized the novel  $\text{CaRE}_3\text{SbO}_4$  and  $\text{Ca}_2\text{RE}_8\text{Sb}_3\text{O}_{10}$  phases ( $RE = \text{Ce} - \text{Nd}, \text{Sm} - \text{Dy}$  for  $\text{CaRE}_3\text{SbO}_4$ ,  $RE = \text{La} - \text{Nd}, \text{Sm} - \text{Dy}$  for  $\text{Ca}_2\text{RE}_8\text{Sb}_3\text{O}_{10}$ ). This result was motivated by the idea of opening a band gap and introducing structural complexity in the rare-earth antimonide framework by incorporation of rare-earth oxide and calcium oxide. The  $\text{CaRE}_3\text{SbO}_4$  phases adopt the tetragonal  $I4/m$  symmetry while the  $\text{Ca}_2\text{RE}_8\text{Sb}_3\text{O}_{10}$  ones adopt the monoclinic  $C2/m$  symmetry. These structures show many similarities to the other  $RE\text{-Sb-O}$  phases discovered recently, particularly to the  $\text{RE}_3\text{SbO}_3$  and  $\text{RE}_8\text{Sb}_3\text{O}_8$  phases, in which a prolonged heat treatment results in one structure converting to another by elongation of the rare-earth oxide slabs. Electrical resistivity measurements yielded semiconducting properties for both series, despite the unbalanced electron count for  $\text{Ca}_2\text{RE}_8\text{Sb}_3\text{O}_{10}$  and electronic structure calculations that support metallic-type conduction. This unusual behaviour is attributed to Anderson-type localization of Sb  $p$  states near the Fermi level, which arises from the highly disordered Sb layers in the structure. This Sb disorder was shown to be tunable with respect to the size of the rare-earth used, improving the electrical resistivity by approximately one order of magnitude for each rare-earth in the series.

## 4.1 Introduction

Thermoelectric materials display two interesting phenomena which makes them industrially attractive. Upon application of a current, the junctions of two thermoelectric materials experience a temperature change (Peltier effect), while heating or cooling a junction induces the flow of current (Seebeck effect).<sup>1</sup> The latter property allows power generation when other methods cannot be used, e.g. in deep space missions<sup>30</sup>, and is also seen as a way to recover waste heat and convert it into electricity, e.g. in automobiles.<sup>123,</sup>  
<sup>133</sup> Efficient thermoelectric materials should possess high Seebeck coefficient  $\alpha$  and electrical conductivity  $\sigma$ , and low thermal conductivity  $\kappa$ .<sup>2</sup> Unfortunately, it is quite challenging to realize all of these properties in a single material, as optimization of one parameter generally comes at the expense of the other<sup>41</sup>; e.g. improvement in the electrical conductivity reduces the Seebeck coefficient and increases the electronic contribution to the thermal conductivity. For this reason, heavily doped semiconductors and semimetals are often targeted as potential thermoelectric materials, as the carrier concentrations for this class of materials typically yield an optimized power factor,  $\alpha^2\sigma$ .<sup>134</sup> Materials containing heavy atoms and being structurally complex are also often favored due to their reduced lattice thermal conductivity.<sup>37</sup>

Recently, many promising classes of materials have been explored and studied with the hope of producing a highly efficient thermoelectric material, including Zintl phases ( $\text{Yb}_{14}\text{MnSb}_{11}$  and  $\text{Zn}_4\text{Sb}_3$ )<sup>70, 73-75</sup>, metal-telluride solid solutions<sup>61, 63</sup>, clathrates<sup>135,</sup>

<sup>136</sup>, and skutterudites<sup>137, 138</sup>, among others. Since the best thermoelectric materials display charge transport properties of an electron crystal and have thermal conductivities similar to glasses, they are often referred to as a phonon-glass electron-crystal (PGEC).<sup>20</sup> A chemically appealing technique of making PGEC phases is to design hybrid structures, in which electrically conductive and thermally insulating layers are interwoven into a single lattice. Such an approach is realized in the  $\text{NaCo}_2\text{O}_4$  system and explains its unusually high thermopower.<sup>80</sup>

Utilizing this superstructure approach, our group has focused on synthesis of rare-earth (*RE*) antimonide and bismuthide suboxides.<sup>92</sup> By using high temperatures, we were able to fuse metallic or semimetallic *RESb* and *REBi* with the corresponding  $\text{RE}_2\text{O}_3$  and prepare novel semiconducting phases.<sup>99-101, 106, 127</sup> Some of the obtained materials are particularly interesting due to their potential for band structure engineering and tunable electrical properties, as was demonstrated in the  $\text{RE}_2\text{SbO}_2$  set of phases. By substitution of one rare-earth for another while maintaining the same structure and charge carrier concentration, the dominant electrical transport properties could be modified, resulting in a decoupling of Seebeck coefficient from electrical conductivity and a simultaneous increase in both values<sup>127</sup>. A similar case was studied in which antimony was gradually substituted with bismuth, resulting in a modification of the site disorder and controlled manipulation of physical properties in  $\text{RE}_2(\text{Sb/Bi})\text{O}_2$ .<sup>101</sup> In our efforts to design new PGEC rare-earth suboxides with structural features similar to the  $\text{RE}_2(\text{Sb/Bi})\text{O}_2$  and other *RE-Sb-O* phases, we have discovered and characterized the two new  $\text{CaRE}_3\text{SbO}_4$  and

$\text{Ca}_2\text{RE}_8\text{Sb}_3\text{O}_{10}$  series. The preparation, characterization, physical properties, and calculated electronic structures of the relevant structures are presented in this work.

## 4.2 Experimental

### 4.2.1 Synthesis.

Samples were made using high-purity *RE* metals (*RE* = La – Nd, Sm – Ho, 99.9 wt.% or better, SmartElements), calcium metal (99.98 wt.% Alfa Aesar), antimony metal (99.999 wt.%, CERAC Inc.),  $\text{RE}_2\text{O}_3$ , and  $\text{CeO}_2$  powders (99.99 wt.%, Rhône-Poulenc for *RE* = La, Ce, Nd, Sm – Ho; Alfa Aesar for *RE* = Pr), and calcium oxide (99.99 wt. %, CERAC). The *RESb* binary phases were also prepared as precursors in order to eliminate the use of elemental antimony, when applicable. These samples were prepared in an argon-filled glove box by pressing pellets of filed rare-earth and ground antimony in stoichiometric amounts and were sealed below  $10^{-4}$  torr in evacuated quartz ampoules of 10 to 15 cm in length. The respective samples were then heated in a box furnace at 600°C for 12 hours, then at 850°C for 48 hours. Black, solid chunks of rare-earth antimonides were obtained in this manner, and the purity of each sample was confirmed by X-ray powder diffraction experiments.

Samples of  $\text{CaRE}_3\text{SbO}_4$  (*RE* = Pr – Dy) were prepared by mixing stoichiometric amounts of calcium oxide, rare-earth sesquioxide ( $\text{RE}_2\text{O}_3$ ), and *RESb* precursors in an argon-filled glove box. The  $\text{Ca}_2\text{RE}_8\text{Sb}_3\text{O}_{10}$  and mixed rare-earth  $\text{Ca}_2\text{RE}^{\text{I}}_4\text{RE}^{\text{II}}_4\text{Sb}_3\text{O}_{10}$  (*RE*

= Pr – Dy) samples were prepared in a similar manner, using calcium oxide, rare-earth sesquioxides, and rare-earth antimonides, but also required additional calcium metal and antimony powder in order to achieve the correct composition. In the cases where the rare-earth used was cerium, the  $\text{CeO}_2$  dioxide was combined with extra filed cerium metal, resulting in the desired formula. In order to acquire more data and measure additional  $\text{Ca}_2\text{RE}_8\text{Sb}_3\text{O}_{10}$  samples to determine the effect of *RE* on physical properties, two mixed  $\text{Ca}_2\text{Nd}_4\text{Sm}_4\text{Sb}_3\text{O}_{10}$  and  $\text{Ca}_2\text{Sm}_4\text{Gd}_4\text{Sb}_3\text{O}_{10}$  ( $\text{Ca}_2\text{RE}^{\text{I}}_4\text{RE}^{\text{II}}_4\text{Sb}_3\text{O}_{10}$ ) samples were also prepared as a substitute for the promethium and europium analogues ( $\text{Ca}_2\text{Eu}_8\text{Sb}_3\text{O}_{10}$  will not form by our synthetic approach). The Nd/Sm and Sm/Gd mixtures yield average atomic radii and (ideally) physical properties close to the rare-earths which they are being used as replacements for. The powders were consolidated with the use of a hydraulic press to form small pellets, which were then sealed in tantalum ampoules via arc melting.

High-temperature reaction conditions were accomplished through the use of an induction furnace. The tantalum ampoules containing samples were placed in a molybdenum susceptor, which was heated under dynamic vacuum below  $10^{-4}$  torr by radio frequency induction from a water-chilled copper coil. The  $\text{CaRE}_3\text{SbO}_4$  samples were annealed at  $1300^\circ\text{C}$  for five hours in order to form crystals suitable for X-ray diffraction experiments. However, in order to obtain pure phases, a heat treatment of  $1600^\circ\text{C}$  for two hours was necessary. This was accomplished for *RE* = Ce – Nd, Sm (samples with later *RE* could not be made pure). The  $\text{Ca}_2\text{RE}_8\text{Sb}_3\text{O}_{10}$  and  $\text{Ca}_2\text{RE}^{\text{I}}_4\text{RE}^{\text{II}}_4\text{Sb}_3\text{O}_{10}$  set of samples were heated at  $1300^\circ\text{C}$  for 48 hours, yielding both

good quality crystals and pure phases for  $RE = \text{Nd}$  and  $\text{Sm}$ . Upon completion of heat treatments, samples were allowed to cool for one hour before removal. The obtained products were black for all samples. Both the  $\text{CaRE}_3\text{SbO}_4$  and  $\text{Ca}_2\text{RE}_8\text{Sb}_3\text{O}_{10}$  phases were observed to have melting points close to  $1400^\circ\text{C}$ , and as a result, heat treatments at  $1300^\circ\text{C}$  yielded solid products, while heating at  $1600^\circ\text{C}$  resulted in molten products. All samples were observed to be moisture sensitive, and significant decomposition of the samples exposed to the air for 48 hours was confirmed by powder X-ray diffraction, particularly for samples containing early  $RE$ . As a result, the samples were kept in a vacuum-sealed desiccator filled with drierite. This manner of preservation was proven to maintain sample integrity for at least several months. A list of all samples prepared is presented in Table 4.1.

**Table 4.1. Ca-RE-Sb-O samples prepared by high-temperature synthesis in an induction furnace.**

System	Loading composition	Heat treatment	Pure phases by $RE$ used
$\text{CaRE}_3\text{SbO}_4$	$\text{CaO} + \text{RESb} + \text{RE}_2\text{O}_3^{\text{a}}$	$1300^\circ\text{C}$ for 5 h. for crystals $1600^\circ\text{C}$ for 2 h. for pure phases	Ce - Sm
$\text{Ca}_2\text{RE}_8\text{Sb}_3\text{O}_{10}$	$\text{Ca} + \text{Sb} + \text{CaO} + 2\text{RESb} + 3\text{RE}_2\text{O}_3^{\text{a}}$	$1300^\circ\text{C}$ for 48 h.	Nd, Sm
$\text{Ca}_2\text{RE}^{\text{I}}_4\text{RE}^{\text{II}}_4\text{Sb}_3\text{O}_{10}$	$\text{Ca} + \text{Sb} + \text{CaO} + \text{RE}^{\text{I}}\text{Sb} + \text{RE}^{\text{II}}\text{Sb} + 1.5\text{RE}^{\text{I}}_2\text{O}_3 + 1.5\text{RE}^{\text{II}}_2\text{O}_3$	$1300^\circ\text{C}$ for 48 h.	Nd/Sm and Sm/Gd

<sup>a</sup> For the Ce samples, a  $\text{CeO}_2 + \text{Ce}$  mixture was used.

#### 4.2.2 X-ray Single Crystal Diffraction

Single crystals picked up from the samples were analyzed on a STOE IPDSII diffractometer using Mo  $K_{\alpha}$  radiation in the whole reciprocal sphere. A numerical absorption correction was based on the crystal shape originally determined by optical face indexing but later optimized against equivalent reflections using the STOE X-Shape software.<sup>112</sup> Crystal structures were determined and solved using the SHELX software.<sup>128</sup> A summary of the refinement results is presented in Tables 4.2 – 4.4. The  $\text{CaRE}_3\text{SbO}_4$  phases adopt the tetragonal  $I4/m$  space group, with calcium and rare earth being mixed on the same  $8h$  site. Likewise, the  $\text{Ca}_2\text{RE}_8\text{Sb}_3\text{O}_{10}$  phases adopt the monoclinic  $C2/m$  space group, with calcium and rare earth being mixed on all five cationic sites. The derived  $\text{Ca}/\text{RE}$  occupancies yielded compositions similar to the loaded amounts. The initial structure model in  $\text{Ca}_2\text{RE}_8\text{Sb}_3\text{O}_{10}$  restrained the mixed Ca and RE atoms to have the same atomic coordinates, however, large residual electron densities remained in close proximity to each  $\text{Ca}/\text{RE}$  site after refinement. Thus, the Ca and RE atoms were allowed to refine with different atomic coordinates, which dramatically reduced the residual electron densities and greatly improved the  $R$  factors. The resulting structural change yielded a separation of  $\sim 0.1 - 0.3 \text{ \AA}$  between the Ca and RE atoms, previously occupying the same site. Furthermore, the Sb2 atoms in all  $\text{Ca}_2\text{RE}_8\text{Sb}_3\text{O}_{10}$  phases were noticed to have a large anisotropic vibration elongated along the  $b$  direction. As a result, the  $y$  coordinate of Sb2 was refined by moving Sb2 off of the mirror plane and placing it onto the  $8j$  site. In order to compensate for the change in the Wyckoff position and maintain

stoichiometry, the site occupancy of the Sb2 atom in each phase was allowed to refine, achieving values of approximately 50%. As summarized in Table 4.4, such an approach reduced the final  $U_{22}$  parameters for Sb2 and improved the  $R$  factors. The reciprocal space for each X-ray single crystal was carefully inspected and no additional diffraction peaks indicative of a superstructure could be detected. Further information on the crystal structures can be found in the Supporting information and may be obtained from the Fachinformationszentrum Karlsruhe, 76344 Eggenstein-Leopoldshafen, Germany (fax (49) 7247-808-666; email [crysdata@fiz.karlsruhe.de](mailto:crysdata@fiz.karlsruhe.de)), by quoting the CSD depository numbers 426810 – 426814 for  $\text{CaRE}_3\text{SbO}_4$  and 426815 – 426818, and 427079 for  $\text{Ca}_2\text{RE}_8\text{Sb}_3\text{O}_{10}$ .

**Table 4.2. Crystallographic and refinement data for the  $\text{CaRE}_3\text{SbO}_4$  crystals.**

	$\text{CaCe}_3\text{SbO}_4$	$\text{CaPr}_3\text{SbO}_4$	$\text{CaNd}_3\text{SbO}_4$	$\text{CaSm}_3\text{SbO}_4$	$\text{CaGd}_3\text{SbO}_4$
<b>Refined composition</b>	$\text{Ca}_{0.95(4)}\text{Ce}_{2.95(4)}\text{SbO}_4$	$\text{Ca}_{1.01(2)}\text{Pr}_{2.99(2)}\text{SbO}_4$	$\text{Ca}_{1.01(4)}\text{Nd}_{2.99(4)}\text{SbO}_4$	$\text{Ca}_{1.15(2)}\text{Sm}_{2.85(2)}\text{SbO}_4$	$\text{Ca}_{1.17(2)}\text{Gd}_{2.83(2)}\text{SbO}_4$
<b>Space group</b>	<i>I4/m</i>	<i>I4/m</i>	<i>I4/m</i>	<i>I4/m</i>	<i>I4/m</i>
<b>Radiation</b>	Mo $K_\alpha$ (0.71073 nm)				
<b>Scan mode</b>	Omega				
<b>Temperature</b>	293 K				
<b>Crystal dimensions (mm)</b>	0.0698 x 0.0582 x 0.0388	0.0797 x 0.0565 x 0.0496	0.0690 x 0.0658 x 0.0351	0.0658 x 0.0642 x 0.0444	0.0594 x 0.0542 x 0.0475
<b><i>a</i> (Å)</b>	9.608(1)	9.563(1)	9.554(1)	9.441(1)	9.421(1)
<b><i>c</i> (Å)</b>	4.0148(7)	3.9754(8)	3.9507(8)	3.8960(8)	3.8388(8)
<b>Volume (Å<sup>3</sup>)</b>	370.7(1)	363.6(1)	360.6(1)	347.3(1)	340.7(1)
<b><i>a/c</i> ratio</b>	2.3931(5)	2.4055(5)	2.4183(6)	2.4233(6)	2.4542(6)
<b><math>\rho_{\text{calc}}</math> (g/cm<sup>3</sup>)</b>	5.79	5.94	6.10	6.48	6.80
<b><i>Z</i></b>	2	2	2	2	2
<b>Index ranges</b>	$-15 \leq h \leq 15$ $-15 \leq k \leq 12$ $-6 \leq l \leq 6$	$-15 \leq h \leq 15$ $-15 \leq k \leq 14$ $-5 \leq l \leq 6$	$-14 \leq h \leq 15$ $-15 \leq k \leq 13$ $-5 \leq l \leq 6$	$-14 \leq h \leq 14$ $-15 \leq k \leq 12$ $-5 \leq l \leq 6$	$-14 \leq h \leq 14$ $-14 \leq k \leq 14$ $-3 \leq l \leq 6$
<b><math>2\theta</math> max</b>	69.19°	69.51°	69.48°	69.81°	69.29°
<b>Measured reflections</b>	3109	2236	2113	2039	1830
<b>Unique reflections</b>	435	431	416	411	722

<b>Reflections used</b>	356	376	357	370	625
<b>Max/min transmission</b>	0.2907/0.4252	0.3066/0.4131	0.2835/0.4414	0.1867/0.3919	0.2378/0.3060
<b>Number of parameters</b>	17	17	17	17	17
<b>Max/min electron density</b>	2.42/-2.75	1.56/-1.34	2.87/-2.96	2.49/-1.76	2.11/-1.94
<b>Goodness-of-fit on <math> F^2 </math></b>	1.157	1.102	1.222	1.115	1.156
<b>R indices</b>	$R_1 (>4\sigma) = 0.0478$	$R_1 (>4\sigma) = 0.0231$	$R_1 (>4\sigma) = 0.0524$	$R_1 (>4\sigma) = 0.0249$	$R_1 (>4\sigma) = 0.0226$
	$wR_2 = 0.0713$	$wR_2 = 0.0298$	$wR_2 = 0.0588$	$wR_2 = 0.0378$	$wR_2 = 0.0298$
	$R_1 (\text{all data}) = 0.0660$	$R_1 (\text{all data}) = 0.0321$	$R_1 (\text{all data}) = 0.0658$	$R_1 (\text{all data}) = 0.0332$	$R_1 (\text{all data}) = 0.0297$

**Table 4.3. Crystallographic and refinement data for the  $\text{Ca}_2\text{RE}_8\text{Sb}_3\text{O}_{10}$  crystals.**

	$\text{Ca}_2\text{Pr}_8\text{Sb}_3\text{O}_{10}$	$\text{Ca}_2\text{Nd}_8\text{Sb}_3\text{O}_{10}$	$\text{Ca}_2\text{Sm}_8\text{Sb}_3\text{O}_{10}$	$\text{Ca}_2\text{Gd}_8\text{Sb}_3\text{O}_{10}$	$\text{Ca}_2\text{Tb}_8\text{Sb}_3\text{O}_{10}$
<b>Refined composition</b>	$\text{Ca}_{2.03(4)}\text{Pr}_{7.97(4)}\text{Sb}_{2.96(3)}\text{O}_{10}$	$\text{Ca}_{2.23(3)}\text{Nd}_{7.77(3)}\text{Sb}_{2.97(2)}\text{O}_{10}$	$\text{Ca}_{2.11(4)}\text{Sm}_{7.89(4)}\text{Sb}_{2.99(3)}\text{O}_{10}$	$\text{Ca}_{2.08(4)}\text{Gd}_{7.92(4)}\text{Sb}_{2.97(3)}\text{O}_{10}$	$\text{Ca}_{1.91(5)}\text{Tb}_{8.09(5)}\text{Sb}_{3.01(2)}\text{O}_{10}$
<b>Space group</b>	<i>C2/m</i>	<i>C2/m</i>	<i>C2/m</i>	<i>C2/m</i>	<i>C2/m</i>
<b>Radiation</b>	Mo $K_\alpha$ (0.71073 nm)				
<b>Scan mode</b>	Omega				
<b>Temperature</b>	293 K				
<b>Crystal dimensions (mm)</b>	0.0709 x 0.0590 x 0.0546	0.0970 x 0.0888 x 0.0836	0.0813 x 0.0656 x 0.0267	0.0632 x 0.0586 x 0.0475	0.0453 x 0.0441 x 0.0386
<b><i>a</i> (Å)</b>	13.651(3)	13.605(3)	13.462(3)	13.386(3)	13.307(3)
<b><i>b</i> (Å)</b>	3.9229(8)	3.8884(8)	3.8429(8)	3.7985(8)	3.7791(8)
<b><i>c</i> (Å)</b>	17.628(4)	17.594(4)	17.458(4)	17.369(4)	17.271(3)
<b><math>\beta</math></b>	93.54(3)	93.47(3) <sup>o</sup>	93.62(3) <sup>o</sup>	93.59(3) <sup>o</sup>	93.67(3) <sup>o</sup>
<b>Volume (Å<sup>3</sup>)</b>	942.2(3)	929.1(3)	901.4(3)	881.4(3)	866.8(3)
<b><math>\rho_{\text{calc}}</math> (g/cm<sup>3</sup>)</b>	6.08	6.19	6.61	6.97	7.24
<b>Z</b>	2	2	2	2	2
<b>Index ranges</b>	$-21 \leq h \leq 19$ $-6 \leq k \leq 6$ $-28 \leq l \leq 27$	$-21 \leq h \leq 21$ $-6 \leq k \leq 6$ $-28 \leq l \leq 25$	$-21 \leq h \leq 21$ $-6 \leq k \leq 6$ $-27 \leq l \leq 27$	$-21 \leq h \leq 21$ $-6 \leq k \leq 6$ $-27 \leq l \leq 27$	$-20 \leq h \leq 20$ $-6 \leq k \leq 6$ $-27 \leq l \leq 27$
<b>2<math>\theta</math> max</b>	69.67 <sup>o</sup>	69.45 <sup>o</sup>	69.88 <sup>o</sup>	69.50 <sup>o</sup>	69.30 <sup>o</sup>
<b>Measured reflections</b>	5330 <sup>a</sup>	18831	18957	14080	15270

<b>Unique reflections</b>	2146	2217	2154	2091	2059
<b>Reflections used</b>	1265	1808	1539	1480	1478
<b>Max/min transmission</b>	0.3046/0.3845	0.1180/0.2547	0.1696/0.3587	0.2161/0.3465	0.1926/0.3891
<b>Number of parameters</b>	91	91	91	91	91
<b>Peak/hole [e/Å<sup>3</sup>]</b>	2.29/-2.05	2.60/-2.34	2.82/-3.08	2.76/-3.11	2.77/-2.54
<b>Goodness-of-fit on  F<sup>2</sup> </b>	0.802	1.064	0.954	1.007	0.936
<b>R indices</b>	$R_1 (>4\sigma) = 0.0356$ $wR_2 = 0.0395$ $R_1 (\text{all data}) = 0.0881$	$R_1 (>4\sigma) = 0.0367$ $wR_2 = 0.0590$ $R_1 (\text{all data}) = 0.0540$	$R_1 (>4\sigma) = 0.0380$ $wR_2 = 0.0475$ $R_1 (\text{all data}) = 0.0740$	$R_1 (>4\sigma) = 0.0404$ $wR_2 = 0.0590$ $R_1 (\text{all data}) = 0.0772$	$R_1 (>4\sigma) = 0.0344$ $wR_2 = 0.0420$ $R_1 (\text{all data}) = 0.0680$

<sup>a</sup> The Ca<sub>2</sub>Pr<sub>8</sub>Sb<sub>3</sub>O<sub>10</sub> crystal was collected for a shorter period of time in order to avoid decomposition in air.

**Table 4.4. Refinement results for the  $\text{Ca}_2\text{RE}_8\text{Sb}_3\text{O}_{10}$  crystals by placing Sb2 at the 4*i* and 8*j* sites.**

Phase	Site	Site occupancy	y coordinate	$U_{22}$ parameter	$U_{\text{eq}}$ parameter	$R_1$ value
$\text{Ca}_2\text{Pr}_8\text{Sb}_3\text{O}_{10}$	4 <i>i</i>	1	0	0.0624(8)	0.0303(3)	0.0412
	8 <i>j</i>	0.491(4)	0.036(2)	0.044(3)	0.024(1)	0.0356
$\text{Ca}_2\text{Nd}_8\text{Sb}_3\text{O}_{10}$	4 <i>i</i>	1	0	0.0648(7)	0.0305(3)	0.0447
	8 <i>j</i>	0.491(3)	0.041(1)	0.037(2)	0.0217(7)	0.0367
$\text{Ca}_2\text{Sm}_8\text{Sb}_3\text{O}_{10}$	4 <i>i</i>	1	0	0.0609(6)	0.0288(3)	0.0408
	8 <i>j</i>	0.497(4)	0.0446(9)	0.027(2)	0.0174(6)	0.0380
$\text{Ca}_2\text{Gd}_8\text{Sb}_3\text{O}_{10}$	4 <i>i</i>	1	0	0.0526(7)	0.0258(3)	0.0427
	8 <i>j</i>	0.492(4)	0.045(1)	0.019(2)	0.0143(7)	0.0404
$\text{Ca}_2\text{Tb}_8\text{Sb}_3\text{O}_{10}$	4 <i>i</i>	1	0	0.0502(6)	0.0237(2)	0.0358
	8 <i>j</i>	0.504(3)	0.0458(7)	0.015(1)	0.0120(5)	0.0344

### 4.2.3 X-ray Powder Diffraction

Each sample under study was analyzed by X-ray powder diffraction on a PANalytical X'Pert Pro instrument using Cu  $K_{\alpha 1}$  incident radiation and an X'Celerator detector. Approximately 50 mg of sample was ground up using a mortar and pestle and deposited on a zero-background Si holder. The data was collected in the  $2\theta$  range between  $20^\circ$  and  $70^\circ$  and analyzed using the Rietveld refinement method (Rietica program<sup>114</sup>) to determine sample purity and lattice constants. The structural parameters obtained from the single crystal solutions were used for the refinements, and site occupancies for calcium, rare-earth and antimony were fixed.

#### **4.2.4 Electron Microprobe Analysis (EPMA)**

The samples of interest were mounted in discs of epoxy resin one inch in diameter and approximately 10 mm in thickness. Polishing was accomplished using a Struers Rotopol-31 unit with a Struers RotoForce-4 revolving sample holder. The final step of polishing used a solution of diamond dust of approximately 10 $\mu$ m in size. Quantitative elemental analysis of the samples was performed by electron probe microanalysis (EPMA) using wavelength-dispersive (WDS) X-ray spectroscopy (model JXA-8500F, JEOL). CaSiO<sub>3</sub>, NdB<sub>6</sub>, SmB<sub>6</sub>, antimony metal, Gd<sub>3</sub>Ga<sub>5</sub>O<sub>12</sub>, CeB<sub>6</sub>, and PrB<sub>6</sub>, were used as standards to determine the concentration of oxygen, Ca, Nd, Sm, Sb, Gd, Ce, and Pr in the samples.

#### **4.2.5 Hall Resistivity Measurements**

A selected set of pure CaRE<sub>3</sub>SbO<sub>4</sub>, Ca<sub>2</sub>RE<sub>8</sub>Sb<sub>3</sub>O<sub>10</sub>, and Ca<sub>2</sub>RE<sup>I</sup><sub>4</sub>RE<sup>II</sup><sub>4</sub>Sb<sub>3</sub>O<sub>10</sub> samples were analyzed using an Accent Hall system HL5580 to measure their room temperature electrical resistivities, carrier mobilities, and carrier concentrations, as well as to determine if they are n- or p-type conductors. These samples were pressed as flat pellets of approximately one centimeter in diameter and two millimeters in thickness. A four point probe with Pt/Ir contacts was used for measurement, and an applied current of 0.1 mA was directed to each sample. A magnetic field of 0.323 Tesla was applied perpendicular to the direction of the current flow.

#### 4.2.6 Electrical Resistivity Measurements

Pure samples of  $\text{CaRE}_3\text{SbO}_4$  ( $RE = \text{Ce} - \text{Nd}, \text{Sm}$ ),  $\text{Ca}_2\text{RE}_8\text{Sb}_3\text{O}_{10}$  ( $RE = \text{Nd}, \text{Sm}$ ), and  $\text{Ca}_2\text{RE}^{\text{I}}_4\text{RE}^{\text{II}}_4\text{Sb}_3\text{O}_{10}$  ( $RE = \text{Nd}/\text{Sm}, \text{Sm}/\text{Gd}$ ) were prepared, pressed, sealed in evacuated quartz ampoules, and annealed at  $700^\circ\text{C}$  for 48 hours to ensure rigidity. Powder X-ray diffraction analysis confirmed no decomposition or generation of impurities by this method. Once annealed, samples were cut into bars of approximately  $8 \times 2 \times 2$  mm in dimensions using a kerosene lubricant to avoid sample oxidation, and were subsequently stored in an argon atmosphere. Four-probe electrical resistivity measurements were carried out on a Quantum Design Physical Property Measurement System (PPMS). Platinum leads were attached on the rectangular bars using Epo-Tek H20E silver epoxy. The contacts for all samples were cured under a stream of ultra-high purity Ar inside a tube furnace.

#### 4.2.7. Electronic Band Structure Calculations

The electronic structures of all samples for which a crystal could be obtained and solved were calculated using the tight-binding, linear-muffin tin orbital method<sup>117</sup> with the atomic sphere approximation (TB-LMTO-ASA) as implemented in the Stuttgart program.<sup>118</sup> All  $4f$  electrons were considered as core electrons. Exchange and correlation were treated by the local density approximation (LDA).<sup>119</sup> A scalar relativistic approximation<sup>120</sup> was employed to account for all relativistic effects except spin-orbit coupling. Overlapping Wigner-Seitz cells were constructed with radii determined by requiring the overlapping potential to be the best approximation to the full potential,

according to the atomic sphere approximation (ASA). Automatic sphere generation<sup>121</sup> was performed to construct empty spheres to be included in the unit cell in order to satisfy the overlap criteria of the TB-LMTO-ASA model. The X-ray single crystal data, including lattice parameters and atomic coordinates, were used as the model for calculations. The Ca/*RE* sites in the  $\text{CaRE}_3\text{SbO}_4$  and  $\text{Ca}_2\text{RE}_8\text{Sb}_3\text{O}_{10}$  phases were set to be fully occupied by rare-earth atoms, resulting in idealized  $\text{RE}_4\text{SbO}_4$  and  $\text{RE}_{10}\text{Sb}_3\text{O}_{10}$  structures with no changes in atomic parameters (such approach neglects a size difference between  $\text{Ca}^{2+}$  and  $\text{RE}^{3+}$ ).<sup>131</sup> Only the *RE* sites in the  $\text{Ca}_2\text{RE}_8\text{Sb}_3\text{O}_{10}$  structure were used. The Sb2 site in the  $\text{Ca}_2\text{RE}_8\text{Sb}_3\text{O}_{10}$  phases was set to be on the *4i* site with 100% occupancy as a starting model, but four additional models were also constructed by doubling the *b* direction, creating supercells with Sb2 displaced off the mirror plane with varying symmetries and Sb2 coordination (See Appendix Figure A3-6 for the calculated electronic structures of these models).

## 4.3 Results and Discussion

### 4.3.1 Composition of $\text{CaRE}_3\text{SbO}_4$ and $\text{Ca}_2\text{RE}_8\text{Sb}_3\text{O}_{10}$

In most cases, the X-ray single crystal refinements for each phase yielded elemental compositions nearly identical to the initial stoichiometries. Notable exceptions occurred in the phases containing later *RE*, as well as the  $\text{Ca}_2\text{Nd}_8\text{Sb}_3\text{O}_{10}$  phase, which yielded Ca/*RE* amounts up to eight standard deviations away from the loaded

compositions. The Sb2 site refinement for the  $\text{Ca}_2\text{RE}_8\text{Sb}_3\text{O}_{10}$  crystals also yielded a small deficiency in antimony for the early *RE* (Pr, Nd, Sm), and a slight excess for  $\text{Ca}_2\text{Tb}_8\text{Sb}_3\text{O}_{10}$ . Furthermore, with the exception of the  $\text{CaCe}_3\text{SbO}_4$  and  $\text{Ca}_2\text{Tb}_8\text{Sb}_3\text{O}_{10}$  crystals, the refined calcium amount was always in excess with respect to the loading composition. To avoid any possible compositional bias resulting from refining mixed or deficient sites, a set of pure, bulk samples of  $\text{CaRE}_3\text{SbO}_4$  and  $\text{Ca}_2\text{RE}_8\text{Sb}_3\text{O}_{10}$  were analyzed by electron microprobe analysis to determine elemental compositions with high precision. The resulting data are shown in Table 4.5, along with the X-ray single crystal data for comparison.

**Table 4.5. Comparison of experimentally determined compositions of  $\text{CaRE}_3\text{SbO}_4$ ,  $\text{Ca}_2\text{RE}_8\text{Sb}_3\text{O}_{10}$ , and  $\text{Ca}_2\text{RE}^{\text{I}}_4\text{RE}^{\text{II}}_4\text{Sb}_3\text{O}_{10}$  samples derived from EPMA and X-ray single crystal diffraction experiments.**

Phase	Loading composition	EPMA results	X-ray single crystal data
$\text{CaRE}_3\text{SbO}_4^{\text{a}}$	$\text{CaCe}_3\text{SbO}_4$	$\text{Ca}_{0.9(1)}\text{Ce}_{3.11(8)}\text{Sb}_{1.0(1)}\text{O}_{7.28(6)}$	$\text{Ca}_{0.95(4)}\text{Ce}_{2.95(4)}\text{SbO}_4$
	$\text{CaPr}_3\text{SbO}_4$	$\text{Ca}_{0.9(1)}\text{Pr}_{3.16(7)}\text{Sb}_{1.0(1)}\text{O}_{7.12(6)}$	$\text{Ca}_{1.01(2)}\text{Pr}_{2.99(2)}\text{SbO}_4$
	$\text{CaNd}_3\text{SbO}_4$	$\text{Ca}_{0.9(1)}\text{Nd}_{3.06(7)}\text{Sb}_{1.0(1)}\text{O}_{6.37(6)}$	$\text{Ca}_{1.01(4)}\text{Nd}_{2.99(4)}\text{SbO}_4$
	$\text{CaSm}_3\text{SbO}_4$	$\text{Ca}_{1.00(8)}\text{Sm}_{2.94(5)}\text{Sb}_{1.00(8)}\text{O}_{4.24(6)}$	$\text{Ca}_{1.15(2)}\text{Sm}_{2.85(2)}\text{SbO}_4$
$\text{Ca}_2\text{RE}_8\text{Sb}_3\text{O}_{10}^{\text{b,c}}$	$\text{Ca}_2\text{Nd}_8\text{Sb}_3\text{O}_{10}$	$\text{Ca}_{1.9(3)}\text{Nd}_{7.9(1)}\text{Sb}_{3.0(2)}\text{O}_{11.3(2)}$	$\text{Ca}_{2.23(3)}\text{Nd}_{7.77(3)}\text{Sb}_{2.97(2)}\text{O}_{10}$
	$\text{Ca}_2\text{Nd}_4\text{Sm}_4\text{Sb}_3\text{O}_{10}$	$\text{Ca}_{2.3(3)}\text{Nd}_{4.4(2)}\text{Sm}_{3.7(2)}\text{Sb}_{3.0(2)}\text{O}_{14.0(2)}$	-
	$\text{Ca}_2\text{Sm}_8\text{Sb}_3\text{O}_{10}$	$\text{Ca}_{1.9(3)}\text{Sm}_{8.3(1)}\text{Sb}_{3.0(2)}\text{O}_{11.4(2)}$	$\text{Ca}_{2.11(4)}\text{Sm}_{7.89(4)}\text{Sb}_{2.99(3)}\text{O}_{10}$
	$\text{Ca}_2\text{Sm}_4\text{Gd}_4\text{Sb}_3\text{O}_{10}$	$\text{Ca}_{1.7(3)}\text{Nd}_{4.0(2)}\text{Sm}_{3.9(2)}\text{Sb}_{3.0(2)}\text{O}_{10.7(2)}$	-

<sup>a</sup> The  $\text{CaRE}_3\text{SbO}_4$  samples were normalized to compositions containing one antimony atom.

<sup>b</sup> The  $\text{Ca}_2\text{RE}_8\text{Sb}_3\text{O}_{10}$  and  $\text{Ca}_2\text{RE}^{\text{I}}_4\text{RE}^{\text{II}}_4\text{Sb}_3\text{O}_{10}$  samples were normalized to compositions containing three antimony atoms.

<sup>c</sup> The  $\text{Ca}_2\text{Nd}_4\text{Sm}_4\text{Sb}_3\text{O}_{10}$  and  $\text{Ca}_2\text{Sm}_4\text{Gd}_4\text{Sb}_3\text{O}_{10}$  samples have the same structure type as  $\text{Ca}_2\text{RE}_8\text{Sb}_3\text{O}_{10}$ . No X-ray single crystal data is available for these compositions.

The EPMA data yielded relative atomic amounts which are no greater than three standard deviations from the expected values. No tantalum signal was observed in any of the data, suggesting no contamination from the ampoules during reaction. The oxygen concentrations are notably higher, which is due to the surface oxidation as a result of polishing. The calcium and antimony percentages were also observed to have unusually high standard deviations, which can be explained by the fact that the  $\text{K}_\alpha/\text{K}_\beta$  peaks of

calcium and the  $L_\alpha/L_\beta$  peaks of antimony overlap. Based on both the EPMA and X-ray single crystal data sets, we conclude that all samples under study maintain the same compositions used for their respective synthesis.

#### 4.3.2 Formation and Stability of $\text{CaRE}_3\text{SbO}_4$

The  $\text{CaRE}_3\text{SbO}_4$  structures can be synthesized at temperatures between  $1100^\circ\text{C}$  and  $1600^\circ\text{C}$  for all rare-earths between cerium and dysprosium, but not europium (only the  $(\text{Ca}/\text{Eu})_4\text{Sb}_2\text{O}$  phase<sup>139</sup> will form). The  $\text{CaLa}_3\text{SbO}_4$  phase could not be obtained, instead the  $\text{La}_8\text{Sb}_3\text{O}_8$  phase formed. The purity of the  $\text{CaRE}_3\text{SbO}_4$  samples with  $RE = \text{Gd} - \text{Dy}$  decreases as the size of  $RE$  decreases, with no crystals suitable for X-ray diffraction available for  $RE = \text{Tb}$  and  $\text{Dy}$ . Beyond  $\text{Dy}$ ,  $\text{CaRE}_3\text{SbO}_4$  phases could not be obtained. All attempts to prepare the pure  $\text{Ca}_4\text{SbO}_4$  and  $\text{RE}_4\text{SbO}_4$  phases were also unsuccessful, indicating that the charge balance must be maintained in order for the phase to form.

It should be noted that the  $\text{CaRE}_3\text{SbO}_4$  phases can be prepared at  $1100^\circ\text{C}$ , among the lowest temperatures yet used for rare-earth pnictide oxides, although low temperature synthesis always yields large amounts of impurities, most notably rare-earth oxides. In order to generate pure samples, synthesis at  $1600^\circ\text{C}$  for two hours was required, which yielded molten, black products confirmed to be phase pure by X-ray powder diffraction for the early rare-earths only. At  $1600^\circ\text{C}$ , the later rare-earths tend to yield rare-earth oxide and other impurities, which may be due to inefficient mixing between calcium and rare-earth, as the disparity in atomic radius increases from early to later  $RE$ , while reaching a minimum between cerium and praseodymium<sup>131</sup>.

With increasing annealing time and lower temperatures, the  $\text{CaRE}_3\text{SbO}_4$  phase will gradually convert into the  $\text{Ca}_2\text{RE}_8\text{Sb}_3\text{O}_{10}$  phase. A set of X-ray powder diffraction data detailing this transformation for  $\text{CaGd}_3\text{SbO}_4$  into  $\text{Ca}_2\text{Gd}_8\text{Sb}_3\text{O}_{10}$  at  $1300^\circ\text{C}$  is presented in Figure 4.1. Based on these results, the  $\text{CaRE}_3\text{SbO}_4$  structure appears to be kinetically stable at lower temperatures, forming initially, while the  $\text{Ca}_2\text{RE}_8\text{Sb}_3\text{O}_{10}$  phase can be viewed as the thermodynamic product. The conversion of  $\text{CaRE}_3\text{SbO}_4$  into  $\text{Ca}_2\text{RE}_8\text{Sb}_3\text{O}_{10}$  after prolonged heat treatment mirrors the transformation of the  $\text{RE}_3\text{SbO}_3$  phases into the  $\text{RE}_8\text{Sb}_3\text{O}_8$  phases, studied previously by our group.<sup>99</sup> However, while the  $\text{RE}_3\text{SbO}_3 \rightarrow \text{RE}_8\text{Sb}_3\text{O}_8$  transformation was exploited to yield the  $\text{RE}_8\text{Sb}_3\text{O}_8$  phases in high purity, the same method cannot be used to obtain  $\text{Ca}_2\text{RE}_8\text{Sb}_3\text{O}_{10}$ , as the  $\text{CaRE}_3\text{SbO}_4 \rightarrow \text{Ca}_2\text{RE}_8\text{Sb}_3\text{O}_{10}$  conversion is too slow and inefficient, yielding large amounts of CaO and  $\text{RE}_2\text{O}_3$  impurities. This may be due to the fact that there is additional complexity during the  $\text{CaRE}_3\text{SbO}_4 \rightarrow \text{Ca}_2\text{RE}_8\text{Sb}_3\text{O}_{10}$  transformation, including a downgrade from tetragonal to monoclinic symmetry, and different Ca/RE ratios between the two structures (the Ca:RE ratio is 1:3 in  $\text{CaRE}_3\text{SbO}_4$  and 1:4 in  $\text{Ca}_2\text{RE}_8\text{Sb}_3\text{O}_{10}$ ).

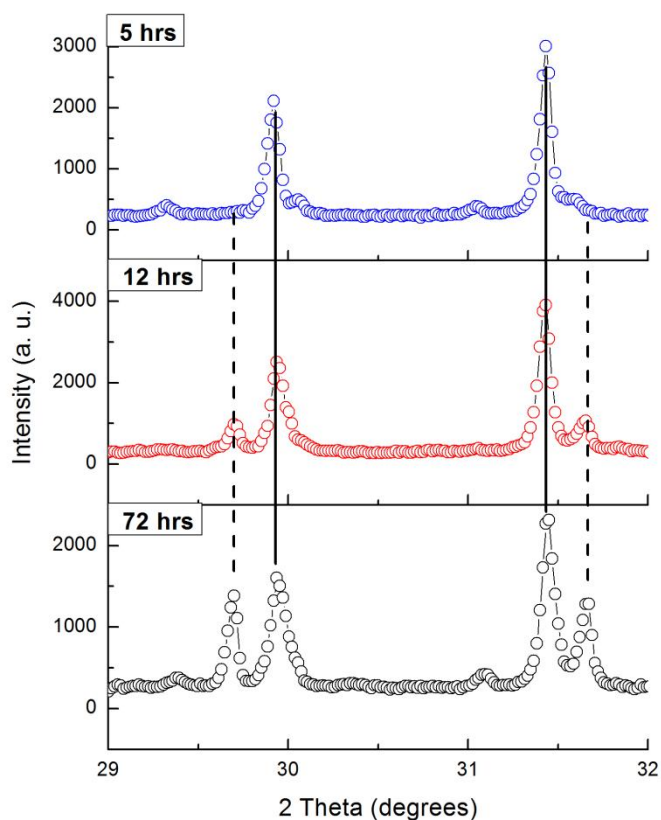


**Figure 4.1.** X-ray powder diffraction patterns showing the conversion of  $\text{CaGd}_3\text{SbO}_4$  into  $\text{Ca}_2\text{Gd}_8\text{Sb}_3\text{O}_{10}$  after heat treatments at  $1300^\circ\text{C}$ . The dashed lines correspond to the positions of the  $\text{Ca}_2\text{Gd}_8\text{Sb}_3\text{O}_{10}$  diffraction peaks only, while the solid lines correspond to a set of overlapping peaks of both  $\text{CaGd}_3\text{SbO}_4$  and  $\text{Ca}_2\text{Gd}_8\text{Sb}_3\text{O}_{10}$ .

#### 4.3.3 Formation and Stability of $\text{Ca}_2\text{RE}_8\text{Sb}_3\text{O}_{10}$

The  $\text{Ca}_2\text{RE}_8\text{Sb}_3\text{O}_{10}$  and  $\text{Ca}_2\text{RE}_4^{\text{I}}\text{RE}_4^{\text{II}}\text{Sb}_3\text{O}_{10}$  samples with crystals suitable for X-ray diffraction could be prepared at  $1300^\circ\text{C}$  for 48 hours. Temperatures below  $1300^\circ\text{C}$  did not yield any products, while temperatures above the melting point (ca.  $1400^\circ\text{C}$ ) yield almost exclusively  $\text{RE}_8\text{Sb}_3\text{O}_8$ . Similar to the  $\text{CaRE}_3\text{SbO}_4$  series, the corresponding

$\text{Ca}_{10}\text{Sb}_3\text{O}_{10}$  and  $\text{RE}_{10}\text{Sb}_3\text{O}_{10}$  phases do not exist, indicating that calcium incorporation is vital to the phase stability. Unlike the  $\text{CaRE}_3\text{SbO}_4$  structure, however, the  $\text{Ca}_2\text{RE}_8\text{Sb}_3\text{O}_{10}$  structure is inherently non-charge balanced (more on that below), and thus  $\text{Ca}_2\text{RE}_8\text{Sb}_3\text{O}_{10}$  could not be obtained by combining the corresponding  $\text{RESb}$ ,  $\text{CaO}$ , and  $\text{RE}_2\text{O}_3$  binaries only. The loading composition that was ultimately used required elemental calcium and antimony. We were very cautious about such an approach, since antimony has a low boiling point and is known to react with tantalum (there are three tantalum-antimony binary phases<sup>140</sup> and  $\text{Ta}_3\text{Sb}$  is occasionally observed in the samples when an excess of elemental antimony is used). However, X-ray powder diffraction did not reveal any tantalum-containing impurities, indicating that antimony reacted with calcium before any evaporation or reaction with tantalum took place. Similar to the  $\text{CaRE}_3\text{SbO}_4$  phases, the  $\text{Ca}_2\text{RE}_8\text{Sb}_3\text{O}_{10}$  phases could not be made pure for rare-earths heavier than samarium, most likely because of inefficient mixing between calcium and rare-earth, although the phase will still form for  $\text{RE}$  as small as dysprosium. With regards to the larger rare-earths, samples with  $\text{RE} = \text{La} - \text{Pr}$  contained the  $\text{Ca}_2\text{RE}_8\text{Sb}_3\text{O}_{10}$  phase, but were observed to favor the formation of  $\text{RE}_8\text{Sb}_3\text{O}_8$  at all temperatures.

#### 4.3.4 Structural Features of $\text{CaRE}_3\text{SbO}_4$

The  $\text{CaRE}_3\text{SbO}_4$  structure adopts the  $I4/m$  space group and contains one crystallographically distinct site for the  $\text{Ca}/\text{RE}$ ,  $\text{Sb}$ , and  $\text{O}$  atoms in the structure. The calcium and rare-earth atoms mix on the  $8h$  site in approximately a 1:3 ratio, providing a charge-balanced formula. The structural framework is defined by  $\text{RE}_4\text{O}$  tetrahedra, which

by sharing edges in the *ab* plane make a basic  $RE_6O_2$  building block (to simplify the structural analysis, only *RE* atoms are assumed on the *Ca/RE* sites). In turn, the  $RE_6O_2$  blocks share corners to form 2D slabs (Figure 4.2) that stack along the *c* direction, forming the overall 3D framework with square channels. The channels are half-filled with antimony atoms in an alternating empty-full pattern. The square voids are arranged with alternating degrees of tilt, and only the same-tilt channels are filled with antimony.

A noteworthy feature present in the  $CaRE_3SbO_4$  phases is an unusually high temperature factor for one of the oxygen atoms; a feature common to all *RE-Sb-O* phases studied by our group. The O atoms at the centre of the  $RE_4O$  tetrahedra are displaced from their ideal position towards the empty square voids, which likely results from the Coulomb repulsion between Sb and other O anions. The shortest Sb-Sb distances in  $CaRE_3SbO_4$  equal the *c* parameter (3.8-4.0 Å), which excludes any possible dimer formation between the Sb atoms. Furthermore, since there are no Sb-O interactions, the antimony atoms in the structure can be viewed as isolated  $Sb^{3-}$  anions. The overall formula of  $CaRE_3SbO_4$  can thus be written as  $(Ca^{2+})(RE^{3+})_3(Sb^{3-})(O^{2-})_4$  and is charge balanced.

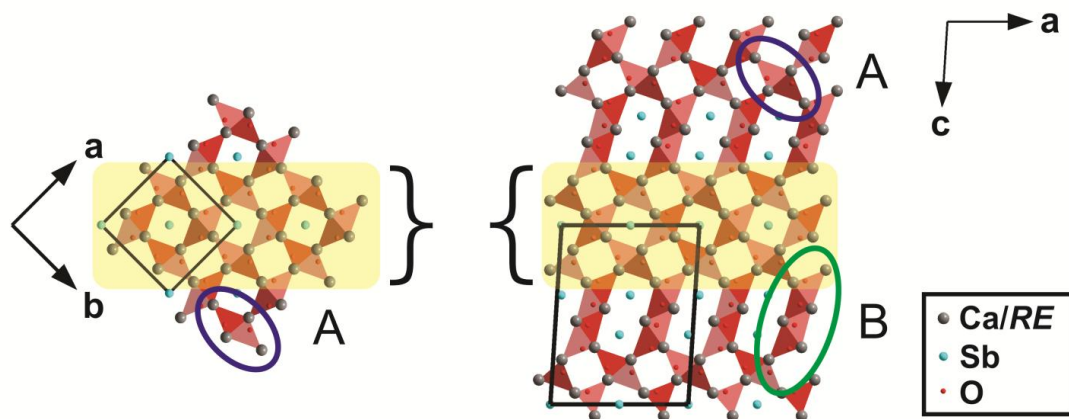


**Figure 4.2.** The  $\text{CaRE}_3\text{SbO}_4$  (left) and  $\text{Ca}_2\text{RE}_8\text{Sb}_3\text{O}_{10}$  (right) structures viewed along the  $c$  and  $b$  directions, respectively. The 2D slabs in each structure are composed of  $\text{RE}_4\text{O}$  tetrahedra. The  $\text{CaRE}_3\text{SbO}_4$  structure contains only one type of building block while the  $\text{Ca}_2\text{RE}_8\text{Sb}_3\text{O}_{10}$  structure contains two types. Only the  $\text{RE}$  sites are shown for  $\text{Ca}_2\text{RE}_8\text{Sb}_3\text{O}_{10}$ .

#### 4.3.5 Structural Features of $\text{Ca}_2\text{RE}_8\text{Sb}_3\text{O}_{10}$

The  $\text{Ca}_2\text{RE}_8\text{Sb}_3\text{O}_{10}$  and  $\text{Ca}_2\text{RE}^{\text{I}}_4\text{RE}^{\text{II}}_4\text{Sb}_3\text{O}_{10}$  structures are identical, and we will focus only on the  $\text{Ca}_2\text{RE}_8\text{Sb}_3\text{O}_{10}$  phases. Similar to  $\text{CaRE}_3\text{SbO}_4$  and other  $\text{RE-Sb-O}$  phases studied, the framework of the  $\text{Ca}_2\text{RE}_8\text{Sb}_3\text{O}_{10}$  structure is composed of  $\text{RE}_4\text{O}$  tetrahedra (Figure 4.2; only  $\text{RE}$  atoms are assumed on the  $\text{Ca/RE}$  sites). In contrast to  $\text{CaRE}_3\text{SbO}_4$ , the  $\text{RE}_4\text{O}$  tetrahedra form two different building blocks in  $\text{Ca}_2\text{RE}_8\text{Sb}_3\text{O}_{10}$ :  $\text{RE}_6\text{O}_2$  blocks formed from two edge-sharing  $\text{RE}_4\text{O}$  tetrahedra (block A) and  $\text{RE}_{10}\text{O}_4$  blocks formed from four edge-sharing  $\text{RE}_4\text{O}$  tetrahedra (block B). The  $\text{RE}_6\text{O}_2$  blocks are connected in the same way as in  $\text{CaRE}_3\text{SbO}_4$ , but they form only a 1D strip propagating along the  $a$  direction instead of a 2D layer. The 1D strips are stitched together by the  $\text{RE}_{10}\text{O}_4$  units, oriented almost along the  $c$  direction, to form a 2D slab. These 2D slabs are

stacked along the  $b$  direction and define the 3D framework of the structure. As mutual arrangement of the  $RE_6O_2$  blocks within the 1D strip is similar to that in  $CaRE_3SbO_4$ , we see the same square channels in  $Ca_2RE_8Sb_3O_{10}$ . Unlike  $CaRE_3SbO_4$ , only one third of the square voids are occupied by Sb atoms, in an empty-full-empty pattern along the  $c$  direction. Another notable difference is the splitting of Ca and  $RE$  into different atomic sites  $\sim 0.1 - 0.3 \text{ \AA}$  apart, with the Ca positions dislocated towards the centre of the square voids, as well as the gaps between Sb2 atoms (see Supporting Information). Due to the presence of longer  $RE_{10}O_4$  units, the rectangular channels that accommodate two Sb atoms are also created in the  $Ca_2RE_8Sb_3O_{10}$  structure. The presence of the  $CaRE_3SbO_4$  structural fragments in  $Ca_2RE_8Sb_3O_{10}$  may explain the systematic conversion of  $CaRE_3SbO_4$  into  $Ca_2RE_8Sb_3O_{10}$  with sufficient heat treatment.

The  $Ca_2RE_8Sb_3O_{10}$  structures contain an oxygen atom (O4) with an unusually high anisotropic displacement parameter that is dislocated from the ideal position at the centre of the tetrahedron and closer to the empty square voids. As in  $CaRE_3SbO_4$ , such shifts likely minimize anion-anion repulsion between the neighboring O atoms and O/Sb atoms. A unique feature of the  $Ca_2RE_8Sb_3O_{10}$  structure is the disorder of the Sb atoms (Sb2 site) in the larger channels. As discussed above, the Sb2 atoms have an unusually large  $U_{22}$  temperature factor along the  $b$  direction. This is verified by plotting an experimental electron density map (Figure 4.3, the electron density map of the Sb1 atoms is provided for comparison). This electron density distribution is best modeled by moving Sb2 off the mirror plane, from the special  $4i$  position  $(x, 0, z)$  to the general  $8j$  position  $(x, y, z)$ , and

reducing the site occupancy to 50%. The resulting shift also yields shorter and longer Sb-Sb distances (Table 4.6). While the shorter distances are still too long to constitute a typical  $\text{Sb}_2^{4-}$  dimer pair, such as in the case of  $\text{Ca}_5\text{Al}_2\text{Sb}_6^{141}$ , or a  $\text{Sb}_\infty^{1-}$  chain, as in the case of  $\text{KSb}^{142}$  and  $\text{Ba}_3\text{Sb}_4\text{O}^{143}$ , it does indicate an increased level of Sb orbital interaction that may influence the charge transport properties. Similar cases of Sb disorder and Sb-Sb interactions were observed in the  $\text{RE}_8\text{Sb}_3\text{O}_8$ ,  $\text{RE}_2\text{SbO}_2$ , and  $\text{Ho}_2(\text{Sb,Bi})\text{O}_2$  phases, which primarily owe their charge carrier transport to the unusual Sb behavior as the Sb  $p$  states are dominant near the Fermi level in each structure.<sup>99, 101, 127</sup>

**Table 4.6. Shortest and longest possible Sb2-Sb2 distances for the  $\text{Ca}_2\text{RE}_8\text{Sb}_3\text{O}_{10}$  phases.**

Phase	Model 1:	Model 2: Sb2 in the 8j site	
	Sb2 in the 4i site	Shortest Sb2-Sb2 distance	Longest Sb2-Sb2 distance
$\text{Ca}_2\text{Pr}_8\text{Sb}_3\text{O}_{10}$	3.923(1) Å	3.64(1) Å	4.21(1) Å
$\text{Ca}_2\text{Nd}_8\text{Sb}_3\text{O}_{10}$	3.888(1) Å	3.569(6) Å	4.208(6) Å
$\text{Ca}_2\text{Sm}_8\text{Sb}_3\text{O}_{10}$	3.843(1) Å	3.500(5) Å	4.186(5) Å
$\text{Ca}_2\text{Gd}_8\text{Sb}_3\text{O}_{10}$	3.799(1) Å	3.458(5) Å	4.139(5) Å
$\text{Ca}_2\text{Tb}_8\text{Sb}_3\text{O}_{10}$	3.779(1) Å	3.433(4) Å	4.125(4) Å

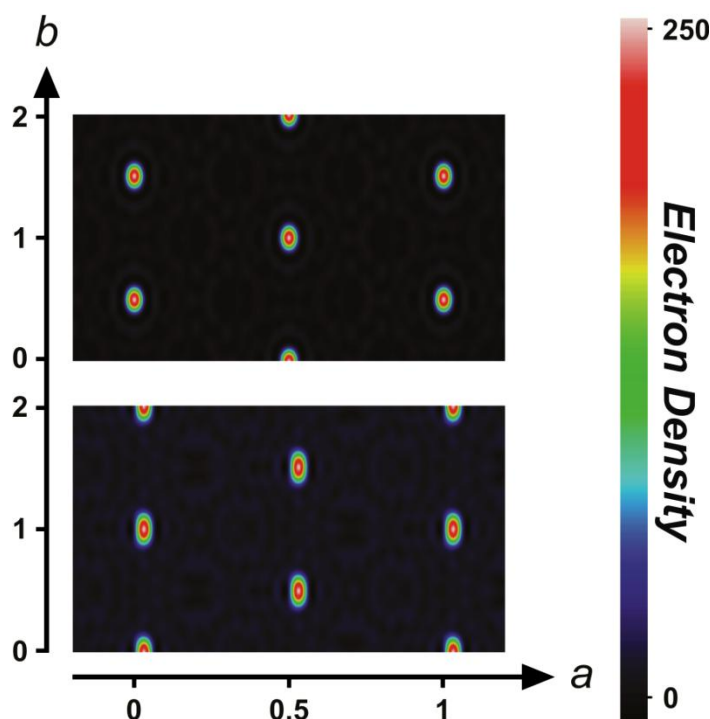


**Figure 4.3.** Electron density maps of the  $\text{Ca}_2\text{Sm}_8\text{Sb}_3\text{O}_{10}$  structure displaying the Sb1 atoms (upper map,  $z = 0$ ) and the Sb2 atoms (lower map,  $z = 0.389$ ). The oblong shape of the electron density for the Sb2 atoms suggests split positions.

#### 4.3.6 Electrical and Hall Resistivity

Electrical resistivities measured on a PPMS for the  $\text{CaRE}_3\text{SbO}_4$ ,  $\text{Ca}_2\text{RE}_8\text{Sb}_3\text{O}_{10}$ , and  $\text{Ca}_2\text{RE}^{\text{I}}_4\text{RE}^{\text{II}}_4\text{Sb}_3\text{O}_{10}$  samples decrease exponentially with temperature, displaying a typical Arrhenius-type behaviour for non-degenerate semiconductors (Figures 4.4 and 4.5). The lone exception was the  $\text{Ca}_2\text{Nd}_8\text{Sb}_3\text{O}_{10}$  sample, which was determined to be too resistive even at room temperature to obtain reliable data. In general, the  $\text{CaRE}_3\text{SbO}_4$  samples are less electrically resistive than the  $\text{Ca}_2\text{RE}_8\text{Sb}_3\text{O}_{10}$  and  $\text{Ca}_2\text{RE}^{\text{I}}_4\text{RE}^{\text{II}}_4\text{Sb}_3\text{O}_{10}$  samples at room temperature; the calculated activation energies are smaller and the

charge carrier concentrations are larger for the  $\text{CaRE}_3\text{SbO}_4$  samples. The room temperature electrical resistivities from the PPMS measurements also agree well with the values obtained from the Accent Hall system (Table 4.7), with more conductive samples having greater Hall mobility. The room temperature resistivity values of the  $\text{CaRE}_3\text{SbO}_4$ ,  $\text{Ca}_2\text{RE}_8\text{Sb}_3\text{O}_{10}$ , and  $\text{Ca}_2\text{RE}^{\text{I}}_4\text{RE}^{\text{II}}_4\text{Sb}_3\text{O}_{10}$  samples are also close to those of the  $\text{RE}_3\text{SbO}_3$  and  $\text{RE}_8\text{Sb}_3\text{O}_8$  phases.<sup>99</sup> The Hall data indicate that all  $\text{CaRE}_3\text{SbO}_4$  phases behave as *n*-type conductors with carrier concentrations of  $1.5\text{-}8.4\times 10^{16}/\text{cm}^3$ . The  $\text{Ca}_2\text{Sm}_8\text{Sb}_3\text{O}_{10}$  and  $\text{Ca}_2\text{Sm}_4\text{Gd}_4\text{Sb}_3\text{O}_{10}$  phases are *p*-type conductors and have lower carrier concentrations of  $2.08\times 10^{15}$  and  $8.45\times 10^{15}/\text{cm}^3$ , respectively. Since the structure type is preserved between members of the  $\text{CaRE}_3\text{SbO}_4$  and  $\text{Ca}_2\text{RE}_8\text{Sb}_3\text{O}_{10}$  series, we assume the difference in charge carrier concentrations between phases arises from minor deviations from the ideal stoichiometry with respect to calcium and rare earth, with at least one species either in deficiency or acting as a dopant. Unfortunately, our analytic techniques limit our ability to acquire more precise compositions to substantiate this claim.

**Table 4.7. Room temperature electrical and Hall resistivity data for selected  $\text{CaRE}_3\text{SbO}_4$ ,  $\text{Ca}_2\text{RE}_8\text{Sb}_3\text{O}_{10}$ , and  $\text{Ca}_2\text{RE}^{\text{I}}_4\text{RE}^{\text{II}}_4\text{Sb}_3\text{O}_{10}$  samples.**

Sample	Hall coefficient	Hall mobility	Resistivity (Hall data)	Resistivity (PPMS data)	Activation energy	Bulk carrier concentration
$\text{CaCe}_3\text{SbO}_4$	$-0.354 \text{ m}^2 \text{ C}^{-1}$	$12.1 \text{ cm}^2 \text{ V}^{-1} \text{ s}^{-1}$	$8.60 \text{ } \Omega \text{ cm}$	$18.4 \text{ } \Omega \text{ cm}$	0.22 eV	$8.40 \times 10^{16} \text{ cm}^{-3}$
$\text{CaPr}_3\text{SbO}_4$	$-0.161 \text{ m}^2 \text{ C}^{-1}$	$8.63 \text{ cm}^2 \text{ V}^{-1} \text{ s}^{-1}$	$28.0 \text{ } \Omega \text{ cm}$	$38.1 \text{ } \Omega \text{ cm}$	0.33 eV	$1.85 \times 10^{16} \text{ cm}^{-3}$
$\text{CaNd}_3\text{SbO}_4$	$-0.204 \text{ m}^2 \text{ C}^{-1}$	$26.0 \text{ cm}^2 \text{ V}^{-1} \text{ s}^{-1}$	$16.5 \text{ } \Omega \text{ cm}$	$23.1 \text{ } \Omega \text{ cm}$	0.31 eV	$1.45 \times 10^{16} \text{ cm}^{-3}$
$\text{CaSm}_3\text{SbO}_4$	$-0.116 \text{ m}^2 \text{ C}^{-1}$	$3.63 \text{ cm}^2 \text{ V}^{-1} \text{ s}^{-1}$	$67.2 \text{ } \Omega \text{ cm}$	$77.4 \text{ } \Omega \text{ cm}$	0.28 eV	$2.56 \times 10^{16} \text{ cm}^{-3}$
$\text{Ca}_2\text{Nd}_4\text{Sm}_4\text{Sb}_3\text{O}_{10}$	-	-	-	$910 \text{ } \Omega \text{ cm}$	0.44 eV	-
$\text{Ca}_2\text{Sm}_8\text{Sb}_3\text{O}_{10}$	$1.50 \text{ m}^2 \text{ C}^{-1}$	$98.1 \text{ cm}^2 \text{ V}^{-1} \text{ s}^{-1}$	$108 \text{ } \Omega \text{ cm}$	$73.4 \text{ } \Omega \text{ cm}$	0.26 eV	$2.08 \times 10^{15} \text{ cm}^{-3}$
$\text{Ca}_2\text{Sm}_4\text{Gd}_4\text{Sb}_3\text{O}_{10}$	$1.88 \text{ m}^2 \text{ C}^{-1}$	$135 \text{ cm}^2 \text{ V}^{-1} \text{ s}^{-1}$	$22.2 \text{ } \Omega \text{ cm}$	$11.0 \text{ } \Omega \text{ cm}$	0.32 eV	$8.45 \times 10^{15} \text{ cm}^{-3}$

The  $\text{Ca}_2\text{RE}_8\text{Sb}_3\text{O}_{10}$  and  $\text{Ca}_2\text{RE}_4^{\text{I}}\text{RE}_4^{\text{II}}\text{Sb}_3\text{O}_{10}$  samples show small resistivity anomalies at temperatures between 220 and 260 K. Such local behavior is unlikely to result from an impurity as a more conductive impurity should dominate the resistivity data below a certain temperature, rather than in the intermediate temperature range. Furthermore, X-ray powder diffraction data confirmed the purity of each sample. Another possibility we explored was a magnetic ordering. However, magnetization measurements (Appendix Figure A4-2) indicated that  $\text{Ca}_2\text{RE}_8\text{Sb}_3\text{O}_{10}$  and  $\text{Ca}_2\text{RE}_4^{\text{I}}\text{RE}_4^{\text{II}}\text{Sb}_3\text{O}_{10}$  are simple paramagnets between 2 and 350 K. X-ray single crystal diffraction data of a  $\text{Ca}_2\text{Sm}_8\text{Sb}_3\text{O}_{10}$  crystal was also collected at a series of temperatures between 240K and 150K in order to detect any structural changes. While some degree of atomic disorder was noticed at 220K after warming the crystal from lower temperatures, it does not appear to be a reason for the change in electrical resistivity. We believe this anomaly to be the result of an undetermined instrumental error.

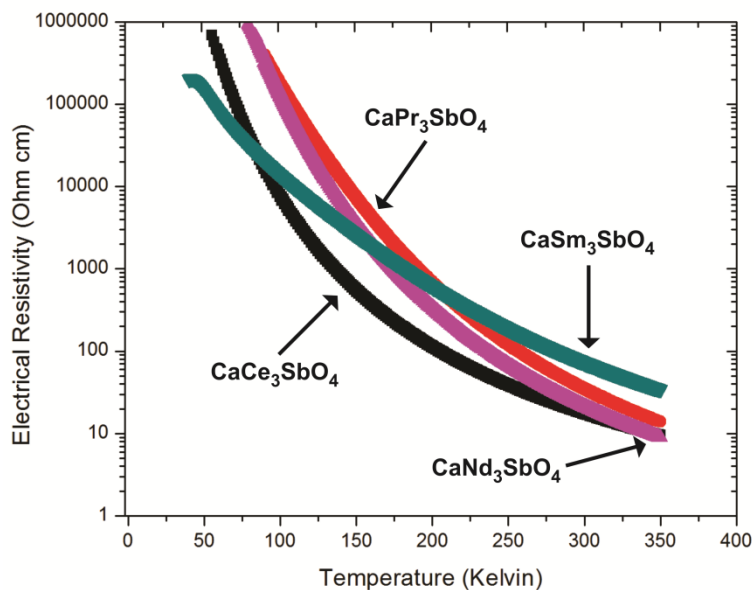


Figure 4.4. Electrical resistivities of the phase pure  $\text{CaRE}_3\text{SbO}_4$  samples.

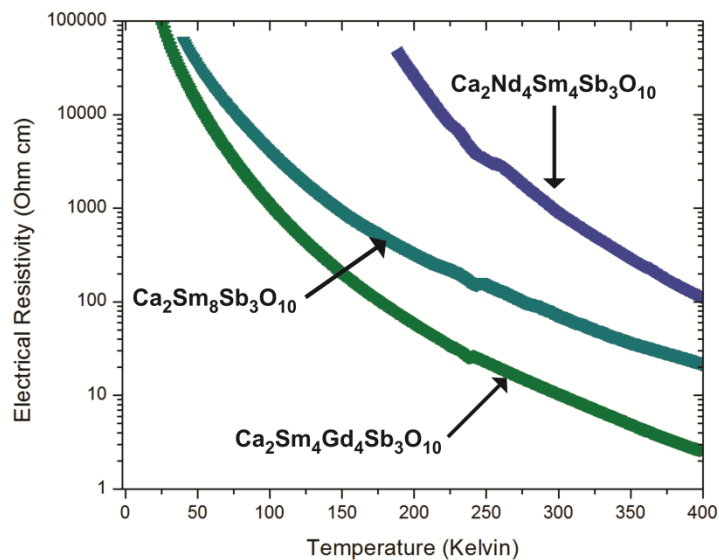


Figure 4.5. Electrical resistivities of the phase pure  $\text{Ca}_2\text{RE}_8\text{Sb}_3\text{O}_{10}$  and  $\text{Ca}_2\text{RE}^{\text{I}}_4\text{RE}^{\text{II}}_4\text{Sb}_3\text{O}_{10}$  samples.

While the semiconducting behavior of the  $\text{CaRE}_3\text{SbO}_4$  phases agrees with their charge balanced formula  $(\text{Ca}^{2+})(\text{RE}^{3+})_3(\text{Sb}^{3-})(\text{O}^{2-})_4$ ,  $\text{Ca}_2\text{RE}_8\text{Sb}_3\text{O}_{10}$  and  $\text{Ca}_2\text{RE}^{\text{I}}_4\text{RE}^{\text{II}}_4\text{Sb}_3\text{O}_{10}$  are expected to be metallic, if Sb atoms are treated as individual anions:  $(\text{Ca}^{2+})_2(\text{RE}^{3+})_8(\text{Sb}^{3-})_3(\text{O}^{2-})_{10}(\text{h}^+)$ . If we assume all Sb2 atoms to form dimers in  $\text{Ca}_2\text{RE}_8\text{Sb}_3\text{O}_{10}$  and  $\text{Ca}_2\text{RE}^{\text{I}}_4\text{RE}^{\text{II}}_4\text{Sb}_3\text{O}_{10}$ , the formula becomes electron rich  $(\text{Ca}^{2+})_2(\text{RE}^{3+})_8(\text{Sb}^{3-})(\text{Sb}^{2-})_2(\text{O}^{2-})_{10}(\text{e}^-)$ , and the phases should be metallic as well. To achieve a charge balance, we would have to presume that only half of the Sb2 atoms make dimers and half remain as isolated  $\text{Sb}^{3-}$  anions. The charge-balanced formula  $(\text{Ca}^{2+})_2(\text{RE}^{3+})_8(\text{Sb}^{3-})_2(\text{Sb}^{2-})(\text{O}^{2-})_{10}$  could then explain the semiconducting behavior. However, the experimental Sb2-Sb2 distances are too long ( $>3.4 \text{ \AA}$ ) to substantiate the existence of single bonds within the  $\text{Sb}_2^{4-}$  dimers and the presence of the band gap.

Most likely, the Sb2 disorder in  $\text{Ca}_2\text{RE}_8\text{Sb}_3\text{O}_{10}$  and  $\text{Ca}_2\text{RE}^{\text{I}}_4\text{RE}^{\text{II}}_4\text{Sb}_3\text{O}_{10}$  results in the Anderson localization<sup>144</sup> of the states within the pseudogap, created by the extended Sb2-Sb2 interactions. The formation of the pseudogap dominated by the Sb2 states is indeed supported by the electronic structure calculations (see below). As a result of the atomic disorder, highly localized states will form near the Fermi level within the pseudogap, resulting in activation energy of charge carriers and semiconducting properties. Thus, a distinctive trend emerges in which the phases with smaller rare earths display reduced Sb2 vibrations (supported by X-ray single crystal data), a more narrow range of localized states, and lower electrical resistivity, with approximately one order of magnitude in reduction along the rare earth series. This behavior has been previously

observed in the  $RE_2SbO_2$  and  $Ho_2(Sb,Bi)O_2$  series<sup>101, 127</sup> in the form of three separate electrical transport mechanisms, including variable range hopping ( $RE = Nd, Sm$ ), and thermal excitation to empty states below ( $RE = Gd$ ) and above ( $RE = Ho, Er$ ) the mobility of edge of the localized states.<sup>145</sup> Based on the electrical resistivity data for the  $Ca_2RE_8Sb_3O_{10}$  samples, it appears that the charge carriers are thermally promoted from the localized states over the mobility edge into higher energy excited states, yielding a regular semiconducting behaviour.

#### 4.3.7 Electronic Structure of $CaRE_3SbO_4$

Electronic structure calculations support the presence of a small band gap for all  $CaRE_3SbO_4$  phases, in agreement with resistivity data. These calculations also support our simple electron counting scheme, which predicted semiconducting properties. The band gap values obtained from the calculations cannot be completely reliable, as the  $8h$  site was assumed to be fully occupied by rare-earth atoms and not by the  $Ca/RE$  mixture. We will focus our analysis on the electronic structure of  $Sm_4SbO_4$  (Figure 4.6, the DOS for other structures are given in the Appendix as Figure A3-4). The valence band below the Fermi level is dominated by the  $Sb$   $p$  orbitals, while the conduction band above the Fermi level is dominated by the  $Sm$   $d$  states, in good agreement with the  $(Ca^{2+})(RE^{3+})_3(Sb^{3-})(O^{2-})_4$  formula. Interestingly, the  $Sb$   $p$  states near the Fermi level are spread out over a large energy range with a low density of states. This feature is common to other  $RE$ - $Sb$ - $O$  phases, but is more pronounced in  $CaRE_3SbO_4$ , which may be rationalized by the shorter than usual  $RE$ - $Sb$  bonds compared to other  $RE$ - $Sb$ - $O$  phases.

Such strong *RE-Sb* interactions would result in a greater energy separation between bonding and anti-bonding states, resulting in a “flattening” of the Sb states near the Fermi level.

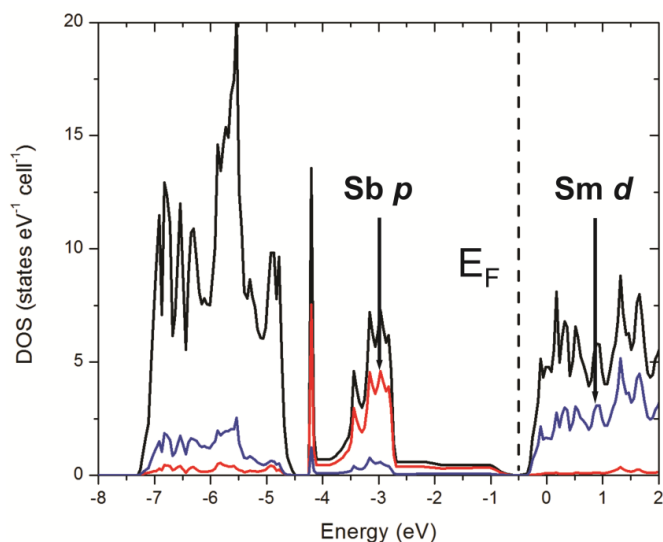


**Figure 4.6.** Calculated total and partial densities of states (DOS) for the  $\text{Sm}_4\text{SbO}_4$  structure. The Fermi level is placed at the energy corresponding to the electron count of the  $\text{CaSm}_3\text{SbO}_4$  composition.

#### 4.3.8 Electronic Structure of $\text{Ca}_2\text{RE}_8\text{Sb}_3\text{O}_{10}$

The results of the calculated electronic structure of each  $\text{RE}_{10}\text{Sb}_3\text{O}_{10}$  phase indicated that there should be no band gap at the Fermi level, and the structure should possess metallic type behaviour, in agreement with its non-charge balanced electron formula with only one type of the Sb2 anions (Figure 4.7). However, as was evidenced in the electrical resistivity data, the sample instead behaves like a semiconductor. While the X-ray single crystal data did not support an ordering of the Sb2 site, we generated a set of

hypothetical structures with the Sb2 ordering for the electronic structure calculations. This required the  $b$  parameter to be doubled and half of the Sb2 atoms to be moved off the mirror plane in order to form dimers, resulting in a  $(\text{Ca}^{2+})_2(\text{RE}^{3+})_8(\text{Sb}^{3-})_2(\text{Sb}^{2-})(\text{O}^{2-})_{10}$  charge balanced formula and ideally opening a band gap. Such arrangements of the Sb2 atoms gave four reduced symmetry supercells for  $\text{Sm}_{10}\text{Sb}_3\text{O}_{10}$ , presented in the Supporting Information as S1, S2, S3, and S4. However, each supercell yields a metallic-type electronic structure, regardless of the Sb2 arrangements, in contrast to the experimental semiconducting properties. The discrepancy between electronic structure and electrical resistivity data was also observed in the  $\text{RE}_8\text{Sb}_3\text{O}_8$  and  $\text{RE}_2\text{SbO}_2$  phases, and can be explained by the Anderson localization of the disordered Sb2 atoms.

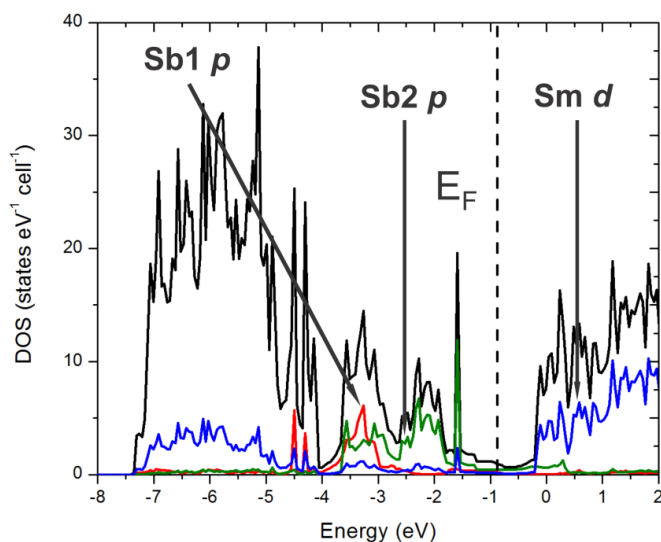


**Figure 4.7. Calculated electronic band structure of the  $\text{Sm}_{10}\text{Sb}_3\text{O}_{10}$  structure, including the total and partial densities of states. The Fermi level is placed at the energy level corresponding to the  $\text{Ca}_2\text{Sm}_8\text{Sb}_3\text{O}_{10}$  composition.**

For each calculated  $RE_{10}Sb_3O_{10}$  electronic structure, the valence band states are dominated by the Sb  $p$  orbitals, while the conduction band states are dominated by  $RE$   $d$  orbitals. Interestingly, however, the Sb1  $p$  states are mainly dispersed in the lower energy range, while the Sb2  $p$  states dominate near the Fermi level. This separation can be rationalized based on the shorter  $RE$ -Sb distances for the Sb1 atoms as compared to the Sb2 atoms, resulting in stronger bonding interactions and lower energy. Such a distribution of states near the Fermi level can potentially be exploited by substitution of antimony with other pnictogens or  $p$  elements such as tellurium, as was done for the  $RE_2(Sb/Bi)O_2$  series.<sup>101</sup> This substitution can allow for not only band structure modification, but also tuning of charge transport mechanisms by modifying the degree of the Sb2 disorder. Optimization of transport properties is theoretically more flexible for the  $Ca_2RE_8Sb_3O_{10}$  series than the  $RE_8Sb_3O_8$  series, as  $2/3$  of the Sb sites in the  $Ca_2RE_8Sb_3O_{10}$  structure are disordered, versus only  $1/3$  of the Sb atoms in  $RE_8Sb_3O_8$ , although both phases are still less flexible than the  $RE_2SbO_2$  phase, which has all of its Sb atoms disordered. This method of tuning the charge transport properties could potentially be used to improve the thermoelectric properties of other rare-earth suboxide phases.

#### 4.4 Conclusions

We have obtained two new families of the rare-earth antimonide oxides,  $CaRE_3SbO_4$  and  $Ca_2RE_8Sb_3O_{10}$  phases. In contrast to the  $RE_2SbO_2$ ,  $RE_3SbO_3$ , and

$RE_8Sb_3O_8$  structures previously prepared in our lab, the new phases require calcium to be stabilized and charge balanced. As demonstrated in this work and earlier works, high-temperature fusion of  $RESb$  and  $RE_2O_3$  into complex structures is a promising approach to discover new phases and prepare novel narrow band semiconductors.

While we were successful in obtaining new semiconducting phases,  $CaRE_3SbO_4$  and  $Ca_2RE_8Sb_3O_{10}$  are too resistive for any potential thermoelectric application. The  $Ca_2RE_8Sb_3O_{10}$  and  $Ca_2RE^I_4RE^{II}_4Sb_3O_{10}$  samples display promise for physical property tuning through the rare-earth substitution, which was shown to enhance the electrical properties while maintaining the same structure. We propose that semiconducting properties of  $Ca_2RE_8Sb_3O_{10}$  stem from the Sb2 atoms, which dominate the valence band states near the Fermi level and whose disorder leads to the Anderson localizations. As was the case for the  $RE_2SbO_2$  phases, this degree of disorder may be tuned by the size of the rare-earth, allowing for easy control of charge transport properties. We also propose that this strategy can involve substitution of antimony with other elements such as bismuth or tellurium, and may result in improved thermoelectric properties.

## **Chapter 5. Synthesis, Crystal Structure, and Physical Properties of the $\text{Gd}_3\text{BiO}_3$ and $\text{Gd}_8\text{Bi}_3\text{O}_8$ phases**

This chapter contains the material covered in the manuscript “Synthesis, Crystal Structure, and Physical Properties of the  $\text{Gd}_3\text{BiO}_3$  and  $\text{Gd}_8\text{Bi}_3\text{O}_8$  phases”, which is currently being revised for publication in the Journal of Solid State Chemistry. The experimental procedures, structure determinations, and data interpretations were performed by the candidate. Ms. Fang Yuan carried out magnetic susceptibility measurements, Dr. Taras Kolodiazhnyi performed physical property measurements on a bulk sample of  $\text{Gd}_8\text{Bi}_3\text{O}_8$ , and Dr. Kosuke Kosuda performed electron microprobe analyses on selected samples.

The second and third known rare-earth bismuthide oxides,  $\text{Gd}_3\text{BiO}_3$  and  $\text{Gd}_8\text{Bi}_3\text{O}_8$ , have been discovered via high temperature reactions at  $1300^\circ\text{C}$ . Like its Gd-Sb-O counterparts, the  $\text{Gd}_3\text{BiO}_3$  and  $\text{Gd}_8\text{Bi}_3\text{O}_8$  phases crystallize in the monoclinic  $C2/m$  space group, with the latter containing disordered Bi atoms along the  $b$  direction of the unit cell. Unlike the  $\text{RE}_8\text{Sb}_3\text{O}_8$  series, the formation of the  $\text{Gd}_3\text{BiO}_3$  phase does not necessarily precede the formation of  $\text{Gd}_8\text{Bi}_3\text{O}_8$ , which is likely due to the difficulty of accommodating bismuth in the  $\text{RE-O}$  framework due to its larger size. Physical property measurements performed on a pure  $\text{Gd}_8\text{Bi}_3\text{O}_8$  sample reveal semiconducting behavior. While electronic structure calculations predict metallic behavior due to an unbalanced electron count; the semiconducting behavior is attributed to the Anderson localization of the Bi  $p$  states near the Fermi level as a result of atomic disorder. Unfortunately, the experimentally determined physical properties render  $\text{Gd}_8\text{Bi}_3\text{O}_8$  unsuitable for thermoelectric applications.

## 5.1 Introduction

Thermoelectric materials are able to perform both power generation and heating/cooling functions<sup>1</sup>, and have found a use in niche applications for which flexibility and long operation lifetimes outweigh the efficiency. Nevertheless, the improvement of the physical properties of benchmark thermoelectrics is still a frequently explored area of research, and a variety of different techniques are commonly employed

to achieve this goal. Bulk nanostructuring<sup>61, 63, 146</sup>, mesostructuring<sup>45</sup>, and charge carrier filtering<sup>54</sup> are often used, but one such technique that is often overlooked is the perturbation of charge transport properties without structural modification. This method is based on the substitution of elements that preserve the overall structure type and charge carrier concentration, but heavily influence the physical properties of the system by modifying the atomic disorder. This strategy is most prominently featured in clathrates containing “rattling” atoms, such as  $\text{Sr}_8\text{Ga}_{16}\text{Ge}_{30}$ <sup>147, 148</sup>, in which the resulting reduction of the lattice thermal conductivity improves the thermoelectric efficiency. Of course, the practicality of this approach may vary considerably between different systems depending on the nature of the atomic disorder present.

An excellent example of this type of physical property modification has been performed in the  $RE_2\text{SbO}_2$  and  $RE_2\text{BiO}_2$  series of phases. These phases adopt the anti- $\text{ThCr}_2\text{Si}_2$  structure for all  $RE$ , and are ordered with alternate layers of  $RE$ -O tetrahedra and disordered antimony/bismuth atoms along the  $c$  direction.<sup>102, 149</sup> Previous literature has demonstrated that the physical properties of these phases can be significantly altered through a systematic adjustment of atomic disorder associated with localized electronic states.<sup>101, 127</sup> In the case of  $RE_2\text{SbO}_2$ , it is hypothesized that Anderson localization of disordered Sb  $p$  states is responsible for the observed semiconducting behavior, in contrast with its unbalanced electron formula  $(RE^{3+})_2(\text{Sb}^{3-})(\text{O}^{2-})_2(\text{h}^+)$ , which suggests a metallic character. As the size of  $RE$  decreases, atomic site disorder decreases, and different charge carrier transport mechanisms may occur which allow for a simultaneous

increase in electrical conductivity and Seebeck coefficient. Likewise, a semiconductor to metal transition is observed in the  $RE_2BiO_2$  series for members with increasingly small  $RE$ . The  $RE_2BiO_2$  phases with large  $RE$  are known to have poor bismuth-bismuth orbital overlap which inhibits charge carrier propagation and reduces electrical conductivity. This behavior does not occur for members of the series with small  $RE$  due to better orbital overlap which allows the predicted metallic behavior to occur. Further studies on the effects of atomic substitution on disorder and electrical resistivity were performed on the  $Ho_2Sb_{1-x}Bi_xO_2$  series, which displayed a semiconductor to metal transition with increasing bismuth substitution.<sup>101</sup> Thus, by simple substitution of one similar atom for another, the physical properties may be heavily modified, in spite of the unchanged charge carrier concentration. This phenomenon is possible due to the adjustment of antimony/bismuth disorder, which is systematically reduced through the unit cell contraction.

The versatility of the  $RE_2SbO_2$  and  $RE_2BiO_2$  phases has motivated us to explore the other  $RE$ -Sb-O and  $RE$ -Bi-O members of the series for similar physical property modifications. Likewise, these phases may display interesting thermoelectric properties, due to a potential separation of functions in different layers of the lattice, as is the case with  $Na_xCo_2O_4$ <sup>80</sup> and  $CaZn_2Sb_2$ .<sup>79</sup> It is by this design that we have successfully prepared the first members of the  $RE_3BiO_3$  and  $RE_8Bi_3O_8$  series: only the second and third known rare earth bismuthide oxide phases to date. We report the synthetic conditions, compositions, physical properties, and electronic structures of the  $Gd_3BiO_3$  and  $Gd_8Bi_3O_8$

phases, assess their relationships to the known *RE*-Sb-O and *RE*-Bi-O phases, and evaluate their potential as thermoelectrics.

## 5.2 Experimental

### 5.2.1 Synthesis

Samples were made using high-purity *RE* metal (99.9 wt.% or better, SmartElements), bismuth metal (99.998 wt.%, Alfa Aesar) and *RE*<sub>2</sub>O<sub>3</sub> powder (99.99 wt.%, Rhône-Poulenc). The rare earth bismuthides *RE*Bi (*RE* = Sm – Dy) were first prepared as precursors for all reactions to avoid the loss of elemental bismuth from heat treatments. These binaries were prepared by mixing rare earth filings and bismuth powder in a 1:1 molar ratio. Each sample was sealed in carbon coated, evacuated silica tubes of 10 to 15 cm in length under 10<sup>-4</sup> torr. Samples were heated by the following trend: heat to 235°C at 50°C/h, dwell for 12 h, heat to 350°C at 10°C/h, dwell for 12 h, heat to 850°C at 50°C/h, dwell for 48 h. This heating trend was specifically chosen to avoid unwanted explosive reactions that would otherwise take place. All binaries obtained by this method are in the form of a black powder with a slight purple hue. Analysis by X-ray powder diffraction reveals Bragg peaks in accordance with the literature data for the *RE*Bi series<sup>150</sup> albeit with very large peak widths, suggesting poor crystallite formation. This is not a concern, as the formation of a binary eliminates the necessity of elemental bismuth for the synthesis of *RE*<sub>3</sub>BiO<sub>3</sub> and *RE*<sub>8</sub>Bi<sub>3</sub>O<sub>8</sub>.

Several compositions were attempted in order to yield the phase pure  $RE_8Bi_3O_8$  samples, but ultimately, only the  $Gd_8Bi_3O_8$  phase was successfully prepared. In order to obtain pure samples of  $Gd_8Bi_3O_8$ , a loading composition of  $Gd_3BiO_3$  ( $GdBi + Gd_2O_3$ ) must be used; samples with a composition of  $Gd_8Bi_3O_8$  yield large  $Gd_2BiO_2$  impurities. This suggests that there is a change in composition due to impurities or losses during the reaction, even when using the  $GdBi$  binary. Samples with a loading composition of  $Gd_3BiO_3$  were prepared by mixing stoichiometric amounts of the  $GdBi$  binary with  $Gd_2O_3$  in an argon-filled glove box. Unlike  $Gd_8Bi_3O_8$ , the  $Gd_3BiO_3$  phase cannot be prepared in bulk. Instead, the  $Gd_3BiO_3$  phase can only be formed as a minor phase when an excess amount of  $GdBi$  is used. Samples with a composition of  $Gd_7Bi_{4.33}O_4$  ( $4.333 GdBi + 1.333 Gd_2O_3$ ) were shown to yield crystals of  $Gd_3BiO_3$  upon reaction.

All samples were pressed into pellets and sealed in tantalum ampoules using an arc melter. High-temperature reaction conditions were accomplished through the use of an induction furnace. The tantalum ampoules containing samples were placed in a molybdenum susceptor, which was heated under dynamic vacuum below  $10^{-4}$  torr by radio frequency induction from a water-chilled copper coil. The  $Gd_8Bi_3O_8$  phase was observed to only form in a very narrow range of temperatures between  $1300^\circ\text{C}$  and  $1350^\circ\text{C}$ . Lower temperatures did not yield any observable reaction while higher temperatures yield the  $Gd_2BiO_2$  phase exclusively. Pure samples of  $Gd_8Bi_3O_8$  could be prepared by heat treatment at  $1300^\circ\text{C}$  for 24 hours, yielding gray, solid chunks. Crystals of  $Gd_3BiO_3$  were isolated from a sample of  $Gd_7Bi_{4.33}O_4$  heated at  $1350^\circ\text{C}$  for 24 hours.

### 5.2.2 X-ray Single Crystal Diffraction

The single crystal of the  $\text{Gd}_3\text{BiO}_3$  was analyzed on a STOE IPDSII diffractometer at room temperature using  $\text{Mo K}_\alpha$  radiation in the whole reciprocal sphere. The  $\text{Gd}_8\text{Bi}_3\text{O}_8$  crystal was analyzed on a Bruker SMART Apex II diffractometer at room temperature and 100 K using  $\text{Mo K}_\alpha$  radiation in the whole reciprocal sphere. Intensity corrections for Lorentz and polarization effects were treated by the SAINT program. The temperature of the crystal was controlled by a dry stream of nitrogen. Crystal structures were determined and solved using the SHELX software.<sup>128</sup> A summary of the refinement results is presented in Tables 5.1 and 5.2. The  $\text{Gd}_3\text{BiO}_3$  and  $\text{Gd}_8\text{Bi}_3\text{O}_8$  phases crystallize in the monoclinic  $C2/m$  space group with the same structure type as the  $\text{RE}_3\text{SbO}_3$  and  $\text{RE}_8\text{Sb}_3\text{O}_8$  series. A considerable  $y$ -coordinate shift for the Bi2 atoms in  $\text{Gd}_8\text{Bi}_3\text{O}_8$  is observed in the low temperature data. Assuming an ordering of Bi2 atoms which yields the shortest Bi-Bi separation, a minimum distance of 3.59(1) Å is possible, although this is still too long to constitute a possible bismuth dimer pair (approximately 3.0Å).<sup>151, 152</sup> The reciprocal space maps for each data set were carefully inspected and no additional diffraction peaks indicative of a superstructure could be detected. Further information on the crystal structure of  $\text{Gd}_8\text{Bi}_3\text{O}_8$  can be obtained from the Fachinformationszentrum Karlsruhe, 76344 Eggenstein-Leopoldshafen, Germany (fax (49) 7247-808-666; email [crysdata@fiz.karlsruhe.de](mailto:crysdata@fiz.karlsruhe.de)), by quoting the CSD depository number 429459 ( $\text{Gd}_3\text{BiO}_3$ ), 428036 ( $\text{Gd}_8\text{Bi}_3\text{O}_8$  room temperature), and 428037 ( $\text{Gd}_8\text{Bi}_3\text{O}_8$  low temperature).

**Table 5.1. Crystallographic and refinement data for the Gd<sub>3</sub>BiO<sub>3</sub> and Gd<sub>8</sub>Bi<sub>3</sub>O<sub>8</sub> crystals.**

	Gd <sub>3</sub> BiO <sub>3</sub>	Gd <sub>8</sub> Bi <sub>3</sub> O <sub>8</sub> Room temperature	Gd <sub>8</sub> Bi <sub>3</sub> O <sub>8</sub> Low temperature
<b>Refined composition</b>	Gd <sub>3</sub> BiO <sub>3</sub>	Gd <sub>8</sub> Bi <sub>2.875(2)</sub> O <sub>8</sub>	Gd <sub>8</sub> Bi <sub>2.876(2)</sub> O <sub>8</sub>
<b>Space group</b>	<i>C2/m</i>	<i>C2/m</i>	<i>C2/m</i>
<b>Radiation</b>		Mo K <sub>α</sub> (0.71073 nm)	
<b>Scan mode</b>		Omega	
<b>Temperature</b>	293 K	293 K	100 K
<b>Crystal dimensions (mm)</b>	0.0777 x 0.0544 x 0.0257	0.0780 x 0.0406 x 0.0392	0.0780 x 0.0406 x 0.0392
<b><i>a</i> (Å)</b>	13.444(3)	13.3939(3)	13.394(3)
<b><i>b</i> (Å)</b>	3.8449(8)	3.8736(1)	3.8638(8)
<b><i>c</i> (Å)</b>	12.033(2)	15.1160(3)	15.120(3)
<b><i>β</i></b>	118.31(3)°	107.031(2)°	107.08(3)°
<b>Volume (Å<sup>3</sup>)</b>	547.6(2)	749.86(3)	748.8(3)
<b><i>p</i><sub>calc</sub> (g/cm<sup>3</sup>)</b>	8.839	8.799	8.812
<b><i>Z</i></b>	4	2	2
<b>Index ranges</b>	-21 ≤ <i>h</i> ≤ 21 -6 ≤ <i>k</i> ≤ 6 -19 ≤ <i>l</i> ≤ 19	-23 ≤ <i>h</i> ≤ 23 -7 ≤ <i>k</i> ≤ 6 -26 ≤ <i>l</i> ≤ 27	-25 ≤ <i>h</i> ≤ 25 -7 ≤ <i>k</i> ≤ 7 -18 ≤ <i>l</i> ≤ 29
<b>2θ max</b>	70.16°	80.38°	86.20°
<b>Measured reflections</b>	10930	9526	8884
<b>Unique reflections</b>	1352	2536	3003
<b>Reflections used</b>	9405	2167	2247
<b>Max/min transmission</b>	0.0342/0.2049	0.03791/0.26336	0.0269/0.2007
<b>Number of parameters</b>	44	62	62
<b>Max/min electron density</b>	4.148/-4.085	3.369/-2.960	3.336/-2.663
<b>Goodness-of-fit on  F<sup>2</sup> </b>	1.096	0.981	1.009
<b>R indices</b>	<i>R</i> <sub>1</sub> (>4σ) = 0.0482 <i>wR</i> <sub>2</sub> = 0.1078 <i>R</i> <sub>1</sub> (all data) = 0.0617	<i>R</i> <sub>1</sub> (>4σ) = 0.0419 <i>wR</i> <sub>2</sub> = 0.0784 <i>R</i> <sub>1</sub> (all data) = 0.0758	<i>R</i> <sub>1</sub> (>4σ) = 0.0449 <i>wR</i> <sub>2</sub> = 0.0890 <i>R</i> <sub>1</sub> (all data) = 0.0752

**Table 5.2. Atomic parameters for the Gd<sub>3</sub>BiO<sub>3</sub> and Gd<sub>8</sub>Bi<sub>3</sub>O<sub>8</sub> crystals.**

Atom	Site	Occupancy	x	y	z	U <sub>eq</sub>
Gd <sub>3</sub> BiO <sub>3</sub>						
<b>Gd1</b>	4 <i>i</i>	1	0.12244(7)	0	0.43981(8)	0.0114(2)
<b>Gd2</b>	4 <i>i</i>	1	0.34684(8)	0	0.79653(7)	0.0109(2)
<b>Gd3</b>	4 <i>i</i>	1	0.87098(8)	0	0.09492(9)	0.0140(2)
<b>Bi1</b>	4 <i>i</i>	1	0.88285(5)	0.5	0.32174(5)	0.0119(2)
<b>O1</b>	4 <i>i</i>	1	0.309(1)	0	0.594(1)	0.007(2)
<b>O2</b>	4 <i>i</i>	1	0.335(1)	0	0.983(1)	0.014(2)
<b>O3</b>	4 <i>i</i>	1	0.438(1)	0.5	0.805(1)	0.014(2)
Gd <sub>8</sub> Bi <sub>3</sub> O <sub>8</sub> at 293 K						
<b>Gd1</b>	4 <i>i</i>	1	0.72041(4)	0	0.08909(3)	0.0085(1)
<b>Gd2</b>	4 <i>i</i>	1	0.45553(4)	0	0.17134(4)	0.0129(1)
<b>Gd3</b>	4 <i>i</i>	1	0.87984(4)	0	0.34868(4)	0.0086(1)
<b>Gd4</b>	4 <i>i</i>	1	0.64335(4)	0	0.43164(4)	0.0104(1)
<b>Bi1</b>	4 <i>i</i>	1	0.17197(3)	0	0.26606(3)	0.0137(1)
<b>Bi2</b>	4 <i>g</i>	0.437(2)	0	0.026(9)	0	0.022(3)
<b>O1</b>	4 <i>i</i>	1	0.4702(7)	0	0.3663(7)	0.025(2)
<b>O2</b>	4 <i>i</i>	1	0.8832(6)	0	0.2007(5)	0.010(1)
<b>O3</b>	4 <i>i</i>	1	0.2969(5)	0	0.0668(5)	0.006(1)
<b>O4</b>	4 <i>i</i>	1	0.1637(6)	0	0.5134(6)	0.014(1)
Gd <sub>8</sub> Bi <sub>3</sub> O <sub>8</sub> at 100 K						
<b>Gd1</b>	4 <i>i</i>	1	0.72019(4)	0	0.08908(3)	0.00530(9)
<b>Gd2</b>	4 <i>i</i>	1	0.45569(4)	0	0.17153(4)	0.0086(1)
<b>Gd3</b>	4 <i>i</i>	1	0.88020(4)	0	0.34867(3)	0.00557(9)
<b>Gd4</b>	4 <i>i</i>	1	0.64414(4)	0	0.43051(4)	0.00603(9)
<b>Bi1</b>	4 <i>i</i>	1	0.17273(3)	0	0.26563(3)	0.00874(8)
<b>Bi2</b>	4 <i>g</i>	0.438(2)	0	0.036(2)	0	0.014(1)
<b>O1</b>	4 <i>i</i>	1	0.4714(6)	0	0.3657(6)	0.014(2)
<b>O2</b>	4 <i>i</i>	1	0.8835(6)	0	0.2006(5)	0.007(1)
<b>O3</b>	4 <i>i</i>	1	0.2965(6)	0	0.0669(5)	0.007(1)
<b>O4</b>	4 <i>i</i>	1	0.1640(6)	0	0.5131(5)	0.008(1)

### **5.2.3 X-ray Powder Diffraction**

All samples were analyzed by X-ray powder diffraction on a PANalytical X'Pert Pro instrument using Cu  $K_{\alpha 1}$  incident radiation and an X'Celerator detector. Approximately 50 mg of sample was ground using a mortar and pestle and then deposited on a zero background Si sample holder. The data were collected in the  $2\theta$  range between  $20^\circ$  and  $70^\circ$  and analyzed using the Rietveld refinement method (Rietica program<sup>114</sup>) to determine sample purity and lattice constants. The structural parameters obtained from the single crystal solution were used for the refinements.

### **5.2.4 Energy-Dispersive X-ray Spectroscopy**

The tantalum ampoules which contained samples of reacted  $Gd_8Bi_3O_8$  were analyzed by energy-dispersive X-ray spectroscopy (EDS) in order to detect impurities or side products as a result of synthesis. This was done as a means to explain the change in stoichiometry from  $Gd_3BiO_3$  to  $Gd_8Bi_3O_8$  upon heat treatments. The EDS experiments were conducted on a JEOL 7000F scanning electron microscope equipped with an X-Max detector. Nickel metal was used as a standard for calibration.

### **5.2.5 Electron Microprobe Analysis (EPMA)**

The samples of interest were mounted in discs of epoxy resin one inch in diameter and approximately 10 mm in thickness. Polishing was accomplished using a Struers Rotopol-31 unit with a Struers RotoForce-4 revolving sample holder. The final step of polishing used a solution of diamond dust of approximately  $0.05\mu\text{m}$  in size. Quantitative elemental analysis of the samples was performed by electron probe microanalysis

(EPMA) using wavelength-dispersive (WDS) X-ray spectroscopy (model JXA-8500F, JEOL).  $\text{Gd}_3\text{Ga}_5\text{O}_{12}$ , Bi metal, and  $\text{CaSiO}_3$  were used as standards for determining the quantities of Gd, Bi, and O, respectively.

### 5.2.6 Coordination Polyhedra Analysis

Coordination polyhedra of all respective crystal structures were analyzed with the Dido95 program.<sup>130</sup> For this purpose, we have calculated the volumes of Sb/Bi sites for a set of known *RE*-Sb/Bi-O phases, which are represented by the volumes of the Wigner-Seitz polyhedra. The atomic positions determined from the room temperature  $\text{Gd}_3\text{BiO}_3$  and  $\text{Gd}_8\text{Bi}_3\text{O}_8$  X-ray single crystal solution were used for calculations. Literature data for the  $\text{Gd}_3\text{SbO}_3$ ,  $\text{Gd}_8\text{Sb}_3\text{O}_8$ ,  $\text{CaGd}_3\text{SbO}_4$ ,  $\text{Ca}_2\text{Gd}_8\text{Sb}_3\text{O}_{10}$ ,  $\text{Gd}_2\text{SbO}_2$ , and  $\text{Gd}_2\text{BiO}_2$  phases<sup>99, 107, 127</sup> were used for calculations as a comparative study. All phases with disordered Sb and Bi atoms were treated as idealized structures with no displacement from the high symmetry positions (e.g. movement of Bi2 in  $\text{Gd}_8\text{Bi}_3\text{O}_8$  from a 2a site to a 4g site).

### 5.2.7 Thermoelectric Measurements

A pure sample of  $\text{Gd}_8\text{Bi}_3\text{O}_8$  was pressed into a pellet, sealed in a 15 cm evacuated quartz tube, and annealed at 700°C for 48 hours, achieving a density of approximately 80%. No decomposition or impurity formation was observed by X-ray powder diffraction experiments. Upon quenching and retrieval, the pellet was mounted in epoxy resin and cut into a 2 x 2 x 8 mm bar using an alumina blade with a kerosene lubricant.

The thermoelectric data was collected from a rectangular shaped sample with a two-probe technique using a press contact assembly produced by Wimbush Science &

Technology and on a PPMS instrument (Quantum Design, USA). During the electrical resistivity measurements, the samples were heated with a speed of 1 K/min to allow thermal equilibration with a cryostat. The thermal conductivity and Seebeck coefficient were measured using commercial thermal transport option of the Physical Properties Measurements System (Quantum Design, USA) by scanning the sample temperature from 380 K down to 2 K with a speed of 0.2 K/min. The thermal conductivity was measured by applying a heat pulse of ca. 10-20 mW to one end of the sample with the other end anchored to a heat sink. The heat pulse was automatically adjusted so that the resulting temperature gradient across the sample does not exceed 3 % of the average sample temperature. Commercial software from Quantum Design was used to model the evolution of the temperature gradient over time upon applying the heat pulse by nonlinear least-squares fitting routine with two time constants. Correction of the thermal conductivity for heat loss at  $T > 300$  K was done by adjusting the infrared emissivity value which itself is dependent on the electrical conductivity of the sample. The Seebeck coefficient was obtained using a similar fitting routine that also included corrections for linear drift and offset voltages.

### **5.2.8 Magnetic Measurements**

Magnetization of a sample of  $\text{Gd}_8\text{Bi}_3\text{O}_8$  was measured using a Quantum Design SQUID magnetometer with a magnetic field of 1000 Oe in the field-cooled mode. Approximately 100 mg of sample was used for measurement. A diamagnetic correction was applied to the extracted data. An experimental value of the effective magnetic

moment per formula unit of  $22.46 \mu_B$  was obtained from our data, which agrees well with the theoretical value of  $22.24 \mu_B$  based on the Curie-Weiss law.<sup>153</sup>

### **5.2.9 Electronic Band Structure Calculations**

The electronic structure of the  $Gd_3BiO_3$  and  $Gd_8Bi_3O_8$  phases were calculated using the tight-binding, linear-muffin tin orbital method<sup>117</sup> with the atomic sphere approximation (TB-LMTO-ASA) as implemented in the Stuttgart program.<sup>118</sup> All  $4f$  electrons were considered as core electrons. Exchange and correlation were treated by the local density approximation (LDA).<sup>119</sup> A scalar relativistic approximation<sup>120</sup> was employed to account for all relativistic effects except spin-orbit coupling. Overlapping Wigner-Seitz cells were constructed with radii determined by requiring the overlapping potential to be the best approximation to the full potential, according to the atomic sphere approximation (ASA). Automatic sphere generation<sup>121</sup> was performed to construct empty spheres to be included in the unit cell in order to satisfy the overlap criteria of the TB-LMTO-ASA model. The  $Gd_8Bi_3O_8$  X-ray single crystal solution with the Bi2 atoms placed on the  $2a$  site, including lattice parameters and atomic coordinates, was used as the model for calculations.

## 5.3 Results and Discussion

### 5.3.1 Structures

The  $\text{Gd}_3\text{BiO}_3$  and  $\text{Gd}_8\text{Bi}_3\text{O}_8$  phases crystallize in the same space group as the corresponding  $\text{RE}_3\text{SbO}_3$  and  $\text{RE}_8\text{Sb}_3\text{O}_8$  phases with the monoclinic  $C2/m$  symmetry. Lattice expansion for both phases in comparison to  $\text{RE}_3\text{SbO}_3$  and  $\text{RE}_8\text{Sb}_3\text{O}_8$  is also observed which is consistent with the larger size of bismuth. The  $\text{Gd}_3\text{BiO}_3$  structure is defined by  $\text{RE}_4\text{O}$  tetrahedra which connect to each other by edge sharing to form two distinct building blocks of two and four units (Figure 5.1). These two building blocks order along the  $b$  direction of the unit cell and are connected to each other by edge sharing, creating rectangular channels occupied by two bismuth atoms per layer. The  $\text{Gd}_8\text{Bi}_3\text{O}_8$  structure is quite similar, being defined by a  $\text{RE-O}$  framework with building blocks of two and six  $\text{RE}_4\text{O}$  units, as well as containing larger rectangular channels occupied by three bismuth atoms per layer. Additionally, the Bi2 atoms in  $\text{Gd}_8\text{Bi}_3\text{O}_8$  yield very large  $U_{22}$  thermal vibration parameters when placed on the  $2a$  site. To better understand this disorder, a crystal of  $\text{Gd}_8\text{Bi}_3\text{O}_8$  was collected at both room temperature and 100 K, and subsequently solved using two separate models: one with Bi2 atoms located on the  $2a$  site and another with the Bi2 atoms shifted off the mirror plane on to the  $4g$  site. The result of the second model is a reduction in the  $U_{22}$  thermal vibration parameter and an improvement in the  $R$  factors (Table 5.3).

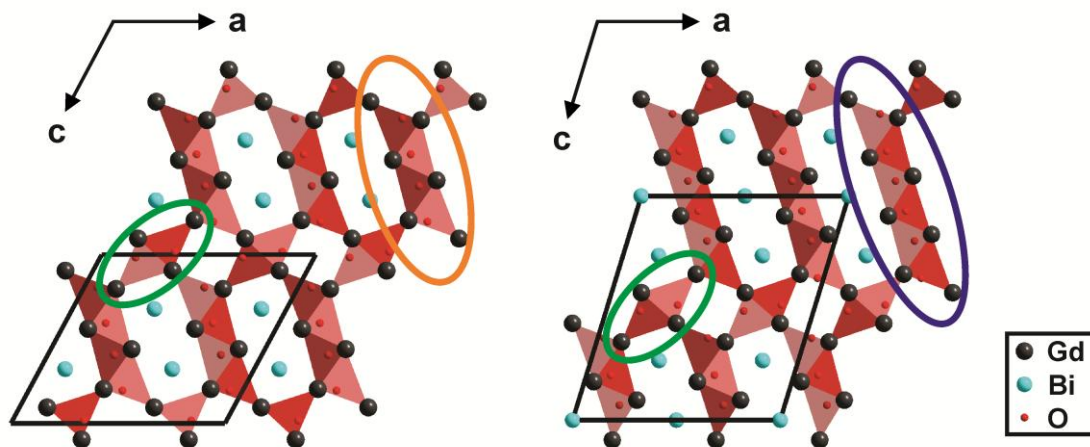


**Figure 5.1.** The  $\text{Gd}_3\text{BiO}_3$  (left) and  $\text{Gd}_8\text{Bi}_3\text{O}_8$  (right) structures viewed along the  $b$  directions of each unit cell. Both structures are defined by a framework of  $\text{Gd}_4\text{O}$  tetrahedra which stack together to form building blocks of composed of two, four, or six units (green, orange, and blue ellipses, respectively).

**Table 5.3.** Refinement results for the  $\text{Gd}_8\text{Bi}_3\text{O}_8$  crystal by placing Bi2 at the  $2a$  and  $4g$  sites.

Temperature	Site	Occupancy	$y$ coordinate	$U_{22}$	$U_{\text{eq}}$	$R_1$ value
293(2) K	2a	1	0	0.0679(8)	0.0324(6)	0.0474
	4g	0.437(2)	0.026(9)	0.047(8)	0.022(3)	0.0419
100(2) K	2a	1	0	0.0629(7)	0.0270(2)	0.0493
	4g	0.438(2)	0.036(2)	0.031(3)	0.014(1)	0.0449

### 5.3.2 Formation of $\text{Gd}_3\text{BiO}_3$ and $\text{Gd}_8\text{Bi}_3\text{O}_8$

Unlike the corresponding  $\text{Gd}_3\text{SbO}_3$  and  $\text{Gd}_8\text{Sb}_3\text{O}_8$  series, formation of  $\text{Gd}_3\text{BiO}_3$  does not necessarily precede  $\text{Gd}_8\text{Bi}_3\text{O}_8$ . The reaction of  $\text{GdBi}$  and  $\text{Gd}_2\text{O}_3$  was shown to form primarily  $\text{Gd}_8\text{Bi}_3\text{O}_8$  or  $\text{Gd}_2\text{BiO}_2$ , depending on the temperature used. Trace amounts of  $\text{Gd}_3\text{BiO}_3$  could be found in samples containing a large excess of  $\text{GdBi}$  when heated at

1300°C. Pure samples of  $Gd_8Bi_3O_8$ , however, can be successfully synthesized in a very narrow range of temperature between 1300°C and 1350°C. Lower temperatures do not yield any products, while higher temperatures yield  $Gd_2BiO_2$  and  $Gd_2O_3$  impurities. Substitution of bismuth with antimony in  $Gd_8Sb_xBi_{3-x}O_8$  was also attempted, with pure samples prepared for  $x \leq 0.5$ . Samples with greater antimony substitution were observed to form  $Gd_2Sb_xBi_{1-x}O_2$  impurities throughout the entire range of temperatures tested. We were unable to obtain  $RE_3BiO_3$  or  $RE_8Bi_3O_8$  for any  $RE$  other than gadolinium, although we believe they almost certainly do exist. The difficulty in preparing and isolating  $RE_3BiO_3$  and  $RE_8Bi_3O_8$  may be due to the fact that the corresponding  $RE_2BiO_2$  phases are significantly more thermodynamically stable.

Obtaining a pure phase of  $Gd_8Bi_3O_8$  is rather difficult to achieve, as the ideal loading composition does not equal the stoichiometry of the targeted structure, due in large part to the high thermodynamic stability of the  $Gd_2BiO_2$  phase (and  $RE_2BiO_2$  in general). Samples with loading compositions of  $RE_8Bi_3O_8$  will always yield  $RE_2BiO_2$  regardless of the heating trend used. Any efforts to compensate this by using less bismuth or adding additional  $RE$  or  $RE_2O_3$  invariably fail and/or lead to the formation of  $RE_2BiO_2$ . Furthermore, in the case of  $Gd_8Bi_3O_8$ , heating at temperatures of 1350°C or greater irreversibly converts any  $Gd_8Bi_3O_8$  present into  $Gd_2BiO_2$ . In order to yield  $Gd_8Bi_3O_8$ , a loading composition of  $Gd_3BiO_3$  was used, which is the same method used to exploit the formation of the  $RE_8Sb_3O_8$  phase from  $RE_3SbO_3$ .<sup>99</sup> This occurs by deposition of impurities onto the surface of the tantalum ampoules as confirmed by scanning electron

microscopy (SEM) experiments. Magnification of a tantalum ampoule which contained a reaction of  $\text{Gd}_3\text{BiO}_3$  reveals microcrystallites distributed throughout the entire ampoule interior (Figure 5.2). Subsequent analysis by energy dispersive X-ray spectroscopy (EDS) experiments reveal gadolinium and oxygen emission peaks, but none associated with bismuth, indicating that only  $\text{Gd}_2\text{O}_3$  (and possibly Gd metal) are expelled from the sample during reaction, which would shift the composition from  $\text{Gd}_3\text{BiO}_3$  to the more bismuth-rich  $\text{Gd}_8\text{Bi}_3\text{O}_8$ .

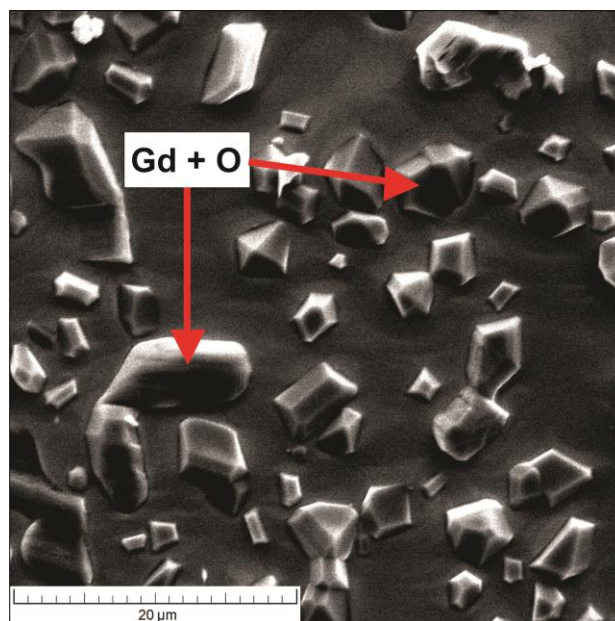


**Figure 5.2. The surface of a tantalum ampoule containing the reaction of  $\text{Gd}_3\text{BiO}_3$ . Only Gd and O signals are observed from the EDS data, indicating that  $\text{Gd}_2\text{O}_3$  and/or Gd may have been expelled during the reaction and deposited on the ampoule.**

The successful method to yield pure  $\text{Gd}_8\text{Bi}_3\text{O}_8$  as determined by our experiments is to use small sample sizes of 300 mg or less with heat treatments at  $1300^\circ\text{C}$  for 24 hours. This method was chosen since a small sample size is able to deposit all of its impurities onto the surface of the tantalum ampoule without additional heat treatments. The heating trend was optimized to allow complete reaction of the sample without allowing sufficient time for conversion into  $\text{Gd}_2\text{BiO}_2$ . However, single crystal X-ray diffraction experiments suggest a consistent deficiency in bismuth from the theoretical value of 50% occupancy. This would amount to a stoichiometry of approximately  $\text{Gd}_8\text{Bi}_{2.875(2)}\text{O}_8$ , which is considerably lower than the antimony deficiency observed from the  $\text{Gd}_8\text{Sb}_3\text{O}_8$  X-ray single crystal data ( $\text{Gd}_8\text{Sb}_{2.98(1)}\text{O}_8$ ).<sup>99</sup> To establish the true composition, we performed electron probe microanalysis (EPMA) on the  $\text{Gd}_8\text{Bi}_3\text{O}_8$  sample; the result yielded a stoichiometry of  $\text{Gd}_{8.00(5)}\text{Bi}_{2.80(8)}\text{O}_{9.63(7)}$ , with the gadolinium atoms being normalized to eight per formula unit (oxygen content is higher than expected due to surface oxidation during polishing). While these results support the X-ray single crystal data, the bismuth content is within three standard deviations from the targeted  $\text{Gd}_8\text{Bi}_3\text{O}_8$  composition. Thus, we cannot say for certain if the  $\text{Gd}_8\text{Bi}_3\text{O}_8$  phase indeed contains bismuth deficiency.

The potential bismuth deficiency in  $\text{Gd}_8\text{Bi}_3\text{O}_8$ , as well as the entire reason that rare-earth bismuthide oxide phases are limited to  $\text{RE}_2\text{BiO}_2$ ,  $\text{RE}_3\text{BiO}_3$ , and  $\text{RE}_8\text{Bi}_3\text{O}_8$ , can be explained by the large size of bismuth and the relative difficulty of its accommodation within the corresponding  $\text{RE-Sb-O}$  crystal structures. Calculations of the Wigner-Seitz

polyhedra of the antimony atoms for the Gd-containing phases (Table 5.4) reveal that the  $\text{Gd}_2\text{SbO}_2$ ,  $\text{Gd}_8\text{Sb}_3\text{O}_8$ , and  $\text{Gd}_3\text{SbO}_3$  phases contain the largest Sb site volumes of all the known Gd-Sb-O phases (tetragonal  $(RE^I RE^{II})_3\text{SbO}_3$  cannot be made with one rare earth<sup>100</sup> and  $RE_9\text{Sb}_5\text{O}_5$ <sup>103, 104</sup> has not been reported for gadolinium). Notably, the  $\text{Gd}_3\text{SbO}_3$  phase contains smaller Sb site polyhedra than both  $\text{Gd}_8\text{Sb}_3\text{O}_8$  and  $\text{Gd}_2\text{SbO}_2$ , which explains the considerable difficulty in forming  $\text{Gd}_3\text{BiO}_3$ . Since it was reported that  $\text{Ca}_2\text{RE}_8\text{Bi}_3\text{O}_{10}$  does not exist<sup>107</sup>, it can be assumed that the threshold for formation of a *RE*-Bi-O phase requires a Sb site volume of  $\sim 28 \text{ \AA}^3$  or greater for the corresponding *RE*-Sb-O phase. A notable increase in the Wigner-Seitz polyhedra size is also observed in the *RE*-Bi-O analogues, which agrees with the expected result.

**Table 5.4. Coordination polyhedra volumes of the Sb and Bi sites in selected Gd-Sb-O and Gd-Bi-O phases.**

Phase	Smallest Sb/Bi site volume	Largest Sb/Bi site volume
Gd-Sb-O phases		
$\text{CaGd}_3\text{SbO}_4^*$	$27.22(8) \text{ \AA}^3$	$27.22(8) \text{ \AA}^3$
$\text{Gd}_3\text{SbO}_3^*$	$28.39(5) \text{ \AA}^3$	$28.39(5) \text{ \AA}^3$
$\text{Gd}_8\text{Sb}_3\text{O}_8$	$29.01(4) \text{ \AA}^3$	$29.47(4) \text{ \AA}^3$
$\text{Ca}_2\text{Gd}_8\text{Sb}_3\text{O}_{10}$	$26.78(3) \text{ \AA}^3$	$28.26(3) \text{ \AA}^3$
$\text{Gd}_2\text{SbO}_2^*$	$33.3(2) \text{ \AA}^3$	$33.3(2) \text{ \AA}^3$
Gd-Bi-O phases		
$\text{Gd}_3\text{BiO}_3^*$	$29.50(5) \text{ \AA}^3$	$29.50(5) \text{ \AA}^3$
$\text{Gd}_8\text{Bi}_3\text{O}_8$	$29.68(4) \text{ \AA}^3$	$30.29(4) \text{ \AA}^3$
$\text{Gd}_2\text{BiO}_2^*$	$34.2(2) \text{ \AA}^3$	$34.2(2) \text{ \AA}^3$

\* Only one Sb/Bi site is present in the structure.

### 5.3.3 Physical Properties

The  $\text{Gd}_8\text{Bi}_3\text{O}_8$  phase was determined to have an Arrhenius-type decrease in electrical resistivity with increasing temperature (Figure 5.3), indicative of semiconducting behavior. A minimum value of  $24 \text{ } \Omega \text{ cm}$  is obtained at 365 K; approximately in-between  $\text{Sm}_8\text{Sb}_3\text{O}_8$  and  $\text{Ho}_8\text{Sb}_3\text{O}_8$ . Using the Arrhenius equation, an activation energy of  $0.046(1) \text{ eV}$  is calculated, which is similar in magnitude to the derived values from the  $\text{RE}_8\text{Sb}_3\text{O}_8$  phases ( $0.090 \text{ eV}$  for  $\text{Sm}_8\text{Sb}_3\text{O}_8$ ,  $0.12 \text{ eV}$  for  $\text{Ho}_8\text{Sb}_3\text{O}_8$ ). The Seebeck coefficient diverges at low temperature, which is characteristic for semiconductors, but switches from  $n$ -type to  $p$ -type around 110 K. The latter may be attributed to the changes in the band structure, during which the  $p$ -type carriers become dominant. Both data sets suggest that  $\text{Gd}_8\text{Bi}_3\text{O}_8$  would make a very poor thermoelectric material, however.

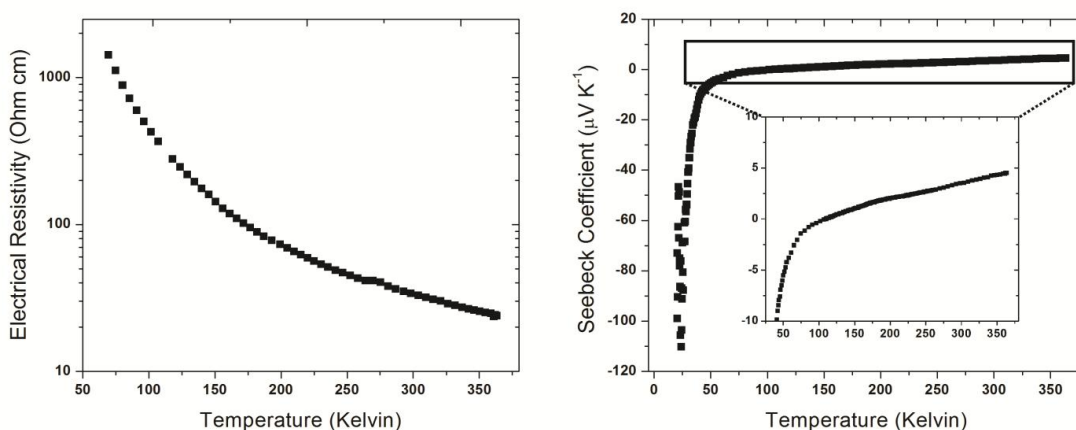


**Figure 5.3. Electrical resistivity data (left) and Seebeck coefficient data (right) of a sample of  $\text{Gd}_8\text{Bi}_3\text{O}_8$ .**

The thermal conductivity of  $\text{Gd}_8\text{Bi}_3\text{O}_8$  sharply increases with temperature to a maximum of about  $0.95 \text{ W m}^{-1} \text{ K}^{-1}$  at about 180 K, after which it steadily declines; most likely as a result of Umklapp scattering (Figure 5.4). Due to the poor electrical conductivity of the sample, the thermal conductivity of  $\text{Gd}_8\text{Bi}_3\text{O}_8$  is almost entirely attributed to lattice thermal conductivity. A small increase in thermal conductivity is noticed at approximately 10 K, which suggests a possible magnetic transition. Subsequent magnetization measurements revealed that while  $\text{Gd}_8\text{Bi}_3\text{O}_8$  shows paramagnetic behavior throughout most of its temperature range, an antiferromagnetic ordering of the sample at 10 K does indeed occur.

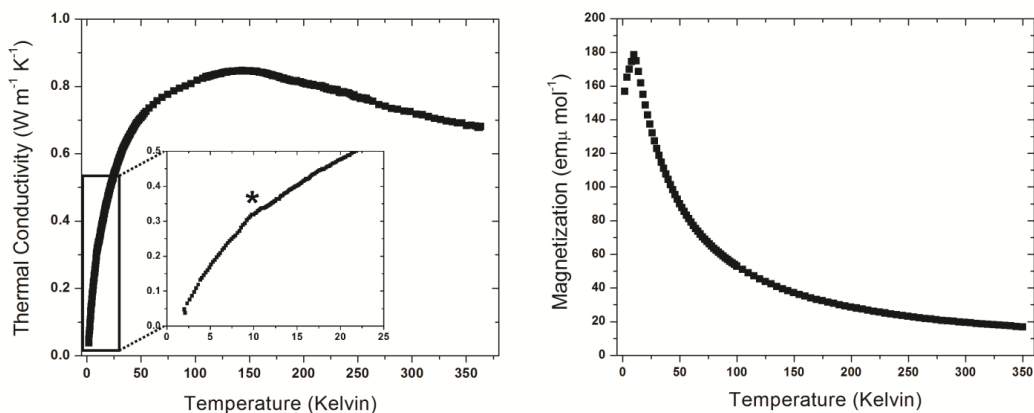


**Figure 5.4. Thermal conductivity data (left) and Magnetization data (right) of a sample of  $\text{Gd}_8\text{Bi}_3\text{O}_8$ .**

### 5.3.4 Electronic Structures

As is the case with  $\text{RE}_3\text{SbO}_3$ , the  $\text{Gd}_3\text{BiO}_3$  phase is charge balanced with a  $(\text{Gd}^{3+})_3(\text{Bi}^{3-})(\text{O}^{2-})_3$  formula. Conversely, the  $\text{Gd}_8\text{Bi}_3\text{O}_8$  phase is inherently non-charge

balanced if it is assumed that no bismuth dimers are present, yielding a  $(\text{Gd}^{3+})_8(\text{Bi}^{3-})_3(\text{O}^{2-})_8(\text{h}^+)$  formula. Furthermore, electronic structure calculations performed by the tight-binding, linear-muffin tin orbital method<sup>117</sup> have determined that both the  $\text{Gd}_3\text{BiO}_3$  and the  $\text{Gd}_8\text{Bi}_3\text{O}_8$  phase have a metallic type distribution of states: a feature also observed with the  $\text{RE}_8\text{Sb}_3\text{O}_8$  series, but not  $\text{RE}_3\text{SbO}_3$ . For both phases, the bonding states at the Fermi level are dominated by Bi  $p$  orbitals, while the conduction band states are dominated by empty Gd  $d$  orbitals (Figure 5.5), in good agreement with the  $(\text{Gd}^{3+})_3(\text{Bi}^{3-})(\text{O}^{2-})_3$  and  $(\text{Gd}^{3+})_8(\text{Bi}^{3-})_3(\text{O}^{2-})_8(\text{h}^+)$  proposed formulas. Since our calculations do not match the observed behavior in electrical resistivity of  $\text{Gd}_8\text{Bi}_3\text{O}_8$ , we argue that the observed semiconducting behavior in our data is due to the Anderson localization of bismuth states. This phenomenon may occur in a disordered structure where localized states are created near the Fermi level, resulting in an activation energy for charge carriers and semiconducting behavior. The origin of the semiconducting behavior in  $\text{Gd}_8\text{Bi}_3\text{O}_8$  can be traced to the highly disordered bismuth atoms, which form the localized states at the pseudogap. The metallic character of the  $\text{Gd}_3\text{BiO}_3$  electronic structure may be due to the electrical properties of the Gd-Bi framework being preserved from the binary phase.<sup>154</sup> Unfortunately, we could not measure the physical properties of  $\text{Gd}_3\text{BiO}_3$  to verify this.

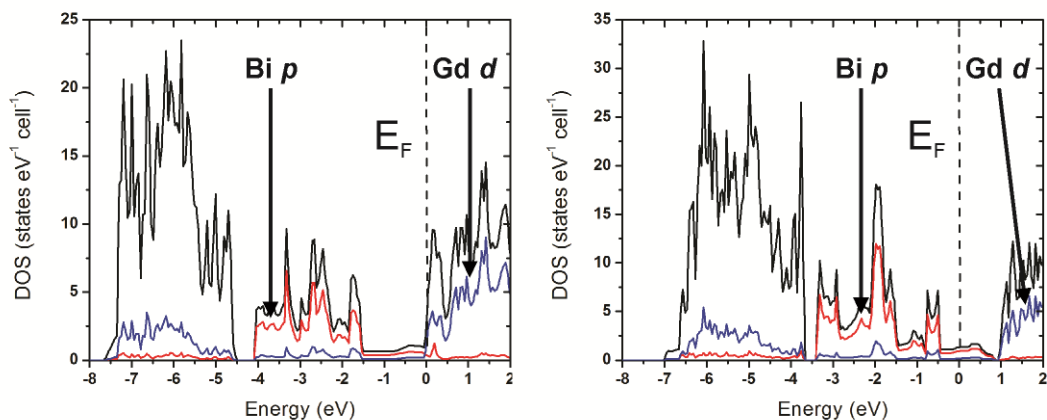


**Figure 5.5. Contribution of orbitals to bands near the Fermi level in the electronic band structure of  $Gd_3BiO_3$  (left) and  $Gd_8Bi_3O_8$  (right).**

## 5.4 Conclusions

The  $Gd_3BiO_3$  and  $Gd_8Bi_3O_8$  phases were both prepared and their crystal structures were solved. The  $Gd_8Bi_3O_8$  phase was successfully prepared via high temperature reactions, while  $Gd_3BiO_3$  is only observed as a minor impurity. Due to the existence of the significantly more stable  $RE_2BiO_2$  series, the  $RE_8Bi_3O_8$  series requires very specific conditions for formation, and may exist only in a narrow range of temperatures. A pure sample of  $Gd_8Bi_3O_8$  analyzed by physical property measurements confirmed semiconducting behavior with values similar to the analogous  $RE_8Sb_3O_8$  series. An antiferromagnetic transition is observed at 10 K, which coincides with a slight increase in thermal conductivity. Unfortunately, due to both high electrical resistivity and low

Seebeck coefficient,  $\text{Gd}_8\text{Bi}_3\text{O}_8$  does not seem to display any promise for thermoelectric applications.

## **Chapter 6. Investigation of the physical properties and compositions of the $\text{Ca}_2\text{RE}_7\text{Pn}_5\text{O}_5$ series ( $\text{RE}$ is a rare-earth metal, $\text{Pn} = \text{Sb, Bi}$ )**

This chapter contains the material covered in the manuscript “Investigation of the physical properties and compositions of the  $\text{Ca}_2\text{RE}_7\text{Pn}_5\text{O}_5$  series ( $\text{RE}$  is a rare-earth metal,  $\text{Pn} = \text{Sb, Bi}$ )”, which is currently unpublished, but will be submitted to a peer reviewed scientific journal. The experimental procedures, structure determinations, and data interpretations were performed by the candidate. Ms. Fang Yuan carried out magnetic susceptibility measurements, Dr. Taras Kolodiazhnyi performed physical property measurements on bulk  $\text{Ca}_2\text{RE}_7\text{Pn}_5\text{O}_5$  samples, and Dr. Kosuke Kosuda performed electron microprobe analyses on specially prepared  $\text{Ca}_2\text{RE}_7\text{Pn}_5\text{O}_5$  samples.

The  $\text{Ca}_2\text{RE}_7\text{Pn}_5\text{O}_5$  phases ( $\text{RE}$  = rare earth metal,  $\text{Pn}$  = Sb, Bi) were successfully prepared from high temperature reactions at 1225-1300°C. These phases maintain the same structure types as the parent  $\text{RE}_9\text{Pn}_5\text{O}_5$  phases, except with a site mixing of Ca/RE and some calcium presence on the normally vacant  $2a$  sites. The study and preparation of these phases was motivated by the desire to shift the metallic type properties of the parent  $\text{RE}_9\text{Pn}_5\text{O}_5$  phases to a level more suitable for thermoelectric applications. Electrical resistivity measurements performed on pure, bulk samples indicated all phases to be narrow band gap semiconductors or semimetals, supporting the charge balanced electron count of the  $\text{Ca}_2\text{RE}_7\text{Pn}_5\text{O}_5$  composition. Unfortunately, all samples are either too electrically resistive or suffer from low Seebeck voltages, negating any potential usage as thermoelectrics. Electronic band structure calculations performed on idealized  $\text{RE}_9\text{Pn}_5\text{O}_5$  structures revealed the presence of a pseudogap at the Fermi level, which is consistent with the observed electrical resistivity and Seebeck coefficient behavior.

## 6.1 Introduction

One of the reemerging areas of research in the development of alternate forms of energy is the study of new and more efficient thermoelectric materials. While most of the early thermoelectrics obtained efficiencies  $ZT \sim 1$ , theoretical studies performed in the 1990s suggested the decoupling of the electrical conductivity and Seebeck coefficient by forming quantum nanostructures with reduced dimensionality.<sup>46-48</sup> Although not intended,

the major advancements in thermoelectric efficiency have instead arisen from the reduction of thermal conductivity by nanostructuring.<sup>155</sup> Such notable gains in efficiency have ushered in a new age of research into thermoelectrics, and a doubling of efficiency ( $ZT \sim 2$ ) among the state of the art materials, such as PbTe-SrTe.<sup>45</sup>

Devices containing thermoelectric materials are capable of performing heating and cooling, depending on the direction of the applied current, as well as being able to convert waste heat into a usable form of electricity.<sup>2</sup> Thermoelectrics offer several advantages over other competing energy sources including long operation hours, scalability, quietness, and versatility. Unfortunately, thermoelectrics suffer from low efficiencies due to the tradeoffs between Seebeck coefficient  $\alpha$ , electrical conductivity  $\sigma$ , and charge carrier thermal conductivity. To obtain the most suitable balance of these properties in a single phase, narrow band gap semiconductors and semiconductors are targeted for thermoelectric applications as they possess electrical properties corresponding to an optimized power factor  $\alpha^2\sigma$ . The thermal conductivity  $\kappa$  of a thermoelectric material must also be kept as low as possible, so structures containing soft bonds, heavy atoms, and site disorder are popular choices. A myriad number of methods are then applied to reduce thermal conductivity further, mostly by doping and nanostructuring.

One of the more noteworthy strategies for the design of a good thermoelectric is the design of a natural superlattice structure, in which electrically conductive and phonon scattering properties are accomplished in separate portions of the lattice. Such an

approach is advantageous since it allows for the tuning of one property without affecting the other, and may yield a structure with a phonon-glass electron-crystal (PGEC) type behavior, as postulated by Slack.<sup>20</sup> Several successful thermoelectric materials, such as  $\text{Ca}_{1-x}\text{Yb}_x\text{Zn}_2\text{Sb}_2$ <sup>79</sup> and  $\text{Na}_x\text{Co}_2\text{O}_4$ <sup>80</sup> display natural superlattice type structures, and have been shown to achieve good  $ZT$  values.

As per the natural superlattice approach, we have turned our attention on rare-earth pnictide oxide phases. Ideally, we may achieve good thermoelectric properties from a natural superlattice type structure containing the electrically conductive and thermally insulating frameworks of rare-earth pnictides and rare-earth oxides, respectively. The presence of heavy rare-earth and pnictogen elements and the added structural complexity introduced by chemical fusion of different sublattices would also serve to heavily reduce thermal conductivity. In particular, the  $\text{RE}_9\text{Pn}_5\text{O}_5$  series is of special interest, since it displays natural superlattice-type structures, with alternating slabs of  $\text{RE}_5\text{Pn}_5$  and  $\text{RE}_4\text{O}_5$  stacked along the  $c$ -direction.<sup>103, 104</sup> The pristine  $\text{RE}_9\text{Pn}_5\text{O}_5$  phases have been shown to behave as metals, owing to their unbalanced electron counts, which renders them unsuitable as thermoelectrics. Additionally, these phases are very air sensitive, requiring great precautions for usage and handling. Our group has studied the incorporation of carbon into these phases in the past in an effort to stabilize their structures and form charge balanced phases for the purpose of thermoelectricity, but we were unable to achieve a pure, stable sample.<sup>106</sup>

Our studies on the  $\text{CaRE}_3\text{SbO}_4$  and  $\text{Ca}_2\text{RE}_8\text{Sb}_3\text{O}_{10}$  phases<sup>107</sup> motivated us to explore calcium substitution in the  $\text{RE}_9\text{Pn}_5\text{O}_5$  phases. By a simple electron counting scheme, a charge balanced  $\text{Ca}_2\text{RE}_7\text{Pn}_5\text{O}_5$  formula would exist if the  $\text{RE}_9\text{Pn}_5\text{O}_5$  structure would tolerate calcium/rare-earth mixing. Verily, we have demonstrated that the  $\text{Ca}_2\text{RE}_7\text{Pn}_5\text{O}_5$  phases do in fact exist, demonstrating that calcium substitution simultaneously improves the stability and maintains the structure of the parent  $\text{RE}_9\text{Pn}_5\text{O}_5$  phase while also eliminating its metallic-type conduction. In this work, we present the details of the synthetic approach, structural and compositional analyses, physical property measurements, and electronic structure calculations of the  $\text{Ca}_2\text{RE}_7\text{Pn}_5\text{O}_5$  phases.

## 6.2 Experimental

### 6.2.1 Synthesis

Samples were made using high-purity *RE* metals ( $RE = \text{Pr, Sm, Gd, Dy}$ ; 99.9 wt.% or better, SmartElements), calcium metal (99.98 wt.% Alfa Aesar), antimony metal (99.999 wt.%, CERAC Inc.),  $\text{RE}_2\text{O}_3$ , (99.99 wt.%, Rhône-Poulenc for  $RE = \text{Sm, Gd, Dy}$ ; 99.9 wt.% Alfa Aesar for  $RE = \text{Pr}$ ), and calcium oxide (99.99 wt. %, CERAC). The  $\text{RESb}$  and  $\text{REBi}$  binary phases were first prepared as precursors to avoid the use of elemental antimony and bismuth, which are volatile at high temperatures. These samples were prepared in an argon-filled glove box by mixing stoichiometric amounts of *RE* and Sb/Bi. The  $\text{RESb}$  samples were pressed into pellets while the  $\text{REBi}$  samples were not. All

samples were sealed below  $10^{-4}$  torr in evacuated quartz ampoules of 10 to 15 cm in length. These samples were sealed in carbon coated silica tubes to avoid reaction between *RE* and silica. The *RESb* samples were heated in a box furnace at 600°C for 12 hours, then at 850°C for 48 hours. The *REBi* samples were heated at 235°C for 12 hours, then at 350°C for 12 hours, and finally at 850°C for 48 hours. The resulting powder was ground and pressed into a pellet within an argon-filled glove box. The pellets were then sealed in silica tubes and heated at 850°C for 48 hours. Black, solid chunks of rare-earth antimonides and rare-earth bismuthides were obtained in this manner, and the purity of each sample was confirmed by X-ray powder diffraction experiments.

Preparation of the  $\text{Ca}_2\text{RE}_7\text{Sb}_5\text{O}_5$  and  $\text{Ca}_2\text{RE}_7\text{Bi}_5\text{O}_5$  samples (*RE* = Pr, Sm, Gd, Dy) was accomplished by mixing stoichiometric amounts of calcium oxide, rare-earth sesquioxide ( $\text{RE}_2\text{O}_3$ ), and *RESb/REBi* precursors in an argon-filled glove box. All samples were consolidated with the use of a hydraulic press, and were subsequently sealed in tantalum ampoules with the use of an arc melter. This method allows for high temperature reactions with no oxidation, sample loss, or reaction with the container. High-temperature reaction conditions were accomplished through the use of an induction furnace. The tantalum ampoules containing samples were placed in a molybdenum susceptor, which was heated under dynamic vacuum below  $10^{-4}$  torr by radio frequency induction from a water-chilled copper coil. The  $\text{Ca}_2\text{RE}_7\text{Sb}_5\text{O}_5$  and  $\text{Ca}_2\text{RE}_7\text{Bi}_5\text{O}_5$  samples were heated for 18 hours at 1300°C and 1225°C, respectively. Upon completion of heat treatments, samples were allowed to cool for one hour before removal. The  $\text{Ca}_2\text{RE}_7\text{Sb}_5\text{O}_5$

and  $\text{Ca}_2\text{RE}_7\text{Bi}_5\text{O}_5$  samples were obtained as shiny, molten chunks. Decomposition of the  $\text{Ca}_2\text{RE}_7\text{Sb}_5\text{O}_5$  and  $\text{Ca}_2\text{RE}_7\text{Bi}_5\text{O}_5$  samples due to moisture after at least 48 hours was confirmed by X-ray powder diffraction. Thus, all samples were stored in a vacuum sealed dessicator filled with drierite, which was observed to maintain sample purity for several months. A summary of all samples prepared is presented in Table 6.1.

**Table 6.1.  $\text{Ca}_2\text{RE}_7\text{Pn}_5\text{O}_5$  samples prepared by high-temperature synthesis in an induction furnace ( $\text{Pn} = \text{Sb, Bi}$ ).**

System	RE used	Loading composition	Temperature used	State
$\text{Ca}_2\text{RE}_7\text{Sb}_5\text{O}_5$	Pr, Sm, Gd	$2\text{CaO} + 5\text{RESb} + \text{RE}_2\text{O}_3$	1300°C	Light gray, molten
$\text{Ca}_2\text{RE}_7\text{Bi}_5\text{O}_5$	Gd, Dy	$2\text{CaO} + 5\text{REBi} + \text{RE}_2\text{O}_3$	1225°C	Dark gray, molten

## 6.2.2 X-ray Single Crystal Diffraction

Single crystals picked up from the samples were analyzed on a Bruker SMART Apex II diffractometer using Mo  $K_\alpha$  radiation. Intensity corrections for Lorentz and polarization effects were performed with the SAINT program.<sup>113</sup> A multi-scan absorption correction was applied based on the crystal shape determined by optical face indexing. Each structure contained commensurate satellite peaks in the  $ab$  plane, resulting in a supercell with a fivefold increase in volume. All data sets except  $\text{Ca}_2\text{Dy}_7\text{Sb}_5\text{O}_5$  were detwinned using the TWINABS program to eliminate intensity bias due to overlapping reflections. Crystal structures were determined and solved using the SHELX software.<sup>128</sup>

A summary of the refinement results is presented in Tables 6.2 and 6.3. All  $\text{Ca}_2\text{RE}_7\text{Pn}_5\text{O}_5$  phases crystallize in the  $P4/n$  space group, much like the analogous  $\text{RE}_9\text{Sb}_5\text{O}_5$  phases. Upon inspection, it was observed that there was an unusually large amount of electron density on the normally vacant  $2a$  sites in each structure (except  $\text{Ca}_2\text{Dy}_7\text{Bi}_5\text{O}_5$ ). As such, these phases were refined with calcium occupation on the  $2a$  site, which served to reduce the residual electron density and yielded improved  $R$  factors. Further information on the crystal structures can be found in the Supporting information and may be obtained from the Fachinformationszentrum Karlsruhe, 76344 Eggenstein-Leopoldshafen, Germany (fax (49) 7247-808-666; email [crysdata@fiz.karlsruhe.de](mailto:crysdata@fiz.karlsruhe.de)), by quoting the CSD depository numbers 429690 – 429692 for  $\text{Ca}_2\text{RE}_7\text{Sb}_5\text{O}_5$  and 429693 – 429694 for  $\text{Ca}_2\text{RE}_7\text{Bi}_5\text{O}_5$ .

**Table 6.2. Crystallographic and refinement data for the  $\text{Ca}_2\text{RE}_7\text{Pn}_5\text{O}_5$  crystals.**

	$\text{Ca}_2\text{Pr}_7\text{Sb}_5\text{O}_5$	$\text{Ca}_2\text{Sm}_7\text{Sb}_5\text{O}_5$	$\text{Ca}_2\text{Gd}_7\text{Sb}_5\text{O}_5$	$\text{Ca}_2\text{Gd}_7\text{Bi}_5\text{O}_5$	$\text{Ca}_2\text{Dy}_7\text{Bi}_5\text{O}_5$
<b>Refined composition</b>	$\text{Ca}_{2.16(1)}\text{Pr}_{7.00(1)}\text{Sb}_5\text{O}_5$	$\text{Ca}_{2.122(8)}\text{Sm}_{7.000(8)}\text{Sb}_5\text{O}_5$	$\text{Ca}_{2.045(6)}\text{Gd}_{7.000(6)}\text{Sb}_5\text{O}_5$	$\text{Ca}_{2.28(1)}\text{Gd}_{7.00(1)}\text{Bi}_5\text{O}_5$	$\text{Ca}_{2.00(1)}\text{Dy}_{7.00(1)}\text{Bi}_5\text{O}_5$
<b>Space group</b>	<i>P4/n</i>	<i>P4/n</i>	<i>P4/n</i>	<i>P4/n</i>	<i>P4/n</i>
<b>Radiation</b>	Mo $\text{K}_\alpha$ (0.71073 nm)				
<b>Scan mode</b>	$\omega$ and $\phi$				
<b>Temperature</b>	296(2) K				
<b>Crystal dimensions (mm)</b>	0.080 x 0.066 x 0.053	0.072 x 0.064 x 0.058	0.077 x 0.070 x 0.062	0.083 x 0.068 x 0.061	0.115 x 0.094 x 0.049
<b><i>a</i> (Å)</b>	10.223(1)	10.067(1)	9.992(1)	10.102(1)	9.9996(1)
<b><i>c</i> (Å)</b>	9.138(2)	9.011 (2)	8.976(2)	9.027(2)	8.9341(2)
<b>Volume (Å<sup>3</sup>)</b>	955.1(3)	913.2(3)	896.2(3)	921.2(3)	893.34(2)
<b>Twin fractions</b>	0.513/0.487(4)	0.515/0.485(2)	0.511/0.489(2)	0.521/0.479(2)	N/A
<b><math>\rho_{\text{calc}}</math> (g/cm<sup>3</sup>)</b>	6.126	6.641	6.935	8.353	8.708
<b><i>Z</i></b>	2	2	2	2	2
<b>Index ranges</b>	$-13 \leq h \leq 14$ $0 \leq k \leq 20$ $0 \leq l \leq 18$	$0 \leq h \leq 20$ $-13 \leq k \leq 14$ $-18 \leq l \leq 0$	$0 \leq h \leq 20$ $-13 \leq k \leq 14$ $-17 \leq l \leq 0$	$0 \leq h \leq 20$ $-13 \leq k \leq 14$ $-18 \leq l \leq 0$	$-19 \leq h \leq 17$ $-20 \leq k \leq 19$ $-17 \leq l \leq 17$
<b><math>2\theta</math> max</b>	90.80°	90.76°	90.82°	90.90°	90.64°
<b>Measured reflections</b>	23235	44532	28980	35183	36098
<b>Unique reflections</b>	3314	3850	3786	3896	3757

<b>Reflections used</b>	3918	9464	5120	6235	1848
<b>Max/min transmission</b>	0.748926/0.543945	0.748926/0.543945	0.748927/0.474572	0.748927/0.504498	0.758275/0.528576
<b>Number of parameters</b>	54	55	55	55	53
<b>Max/min electron density</b>	4.182/-3.249	3.752/-3.947	3.994/-2.720	3.928/-3.596	4.352/-2.836
<b>Goodness-of-fit on <math> F^2 </math></b>	1.013	1.024	1.047	1.109	1.019
<b>R indices</b>	$R_1 (>4\sigma) = 0.0542$	$R_1 (>4\sigma) = 0.0467$	$R_1 (>4\sigma) = 0.0325$	$R_1 (>4\sigma) = 0.0529$	$R_1 (>4\sigma) = 0.0383$
	$wR_2 = 0.1217$	$wR_2 = 0.0881$	$wR_2 = 0.0630$	$wR_2 = 0.0891$	$wR_2 = 0.0824$
	$R_1$ (all data) = 0.1537	$R_1$ (all data) = 0.0938	$R_1$ (all data) = 0.0709	$R_1$ (all data) = 0.1162	$R_1$ (all data) = 0.0682

**Table 6.3. Refinement results for the  $\text{Ca}_2\text{RE}_7\text{Pn}_5\text{O}_5$  crystals based on the occupation of the  $2a$  site by calcium.**

Crystal <sup>a</sup>	Ca4 site occupancy	Largest peak	Largest hole	R <sub>1</sub> value
$\text{Ca}_2\text{Pr}_7\text{Sb}_5\text{O}_5$	0	15.446	-6.321	0.0552
	0.16(1)	4.182	-3.249	0.0542
$\text{Ca}_2\text{Sm}_7\text{Sb}_5\text{O}_5$	0	11.474	-4.129	0.0477
	0.122(8)	3.752	-3.947	0.0467
$\text{Ca}_2\text{Gd}_7\text{Sb}_5\text{O}_5$	0	5.222	-2.820	0.0326
	0.045(5)	3.994	-2.740	0.0325
$\text{Ca}_2\text{Gd}_7\text{Bi}_5\text{O}_5$	0	31.496	-8.469	0.0550
	0.28(1)	3.928	-3.596	0.0529

<sup>a</sup> The  $\text{Ca}_2\text{Dy}_7\text{Bi}_5\text{O}_5$  crystal did not show any significant electron density on the  $2a$  site, which was thus left unoccupied.

### 6.2.3 X-ray Powder Diffraction

Each sample under study was analyzed by X-ray powder diffraction on a PANalytical X'Pert Pro instrument using Cu  $K_{\alpha 1}$  incident radiation and an X'Celerator detector. Approximately 50 mg of sample was ground up using a mortar and pestle and deposited on a zero-background Si holder. The data was collected in the  $2\theta$  range between  $20^\circ$  and  $70^\circ$  and analyzed using the Rietveld refinement method (Rietica program<sup>114</sup>) to determine sample purity and lattice constants. The structural parameters obtained from the single crystal solutions were used for the refinements, and site occupancies for calcium and rare-earth were fixed.

#### **6.2.4 Electron Microprobe Analysis (EPMA)**

The samples of interest were mounted in discs of epoxy resin one inch in diameter and approximately 10 mm in thickness. Polishing was accomplished using a Struers Rotopol-31 unit with a Struers RotoForce-4 revolving sample holder. The final step of polishing used a solution of diamond dust of approximately 1  $\mu\text{m}$  in size. Quantitative elemental analysis of the samples was performed by electron probe microanalysis (EPMA) using wavelength-dispersive (WDS) X-ray spectroscopy (model JXA-8500F, JEOL).  $\text{CaSiO}_3$ ,  $\text{PrB}_6$ ,  $\text{SmB}_6$ ,  $\text{Gd}_3\text{Ga}_5\text{O}_{12}$ ,  $\text{DyP}_5\text{O}_{14}$ , antimony metal, and bismuth metal were used as standards to determine the concentration of oxygen, Ca, Pr, Sm, Gd, Dy, Sb, and Bi in the samples, respectively.

#### **6.2.5 Electrical Resistivity Measurements**

Pure samples of  $\text{Ca}_2\text{RE}_7\text{Sb}_5\text{O}_5$  ( $\text{RE} = \text{Pr, Sm, Gd, Dy}$ ) were prepared, pressed, sealed in evacuated quartz ampoules, and annealed at  $500^\circ\text{C}$  for three days. Powder X-ray diffraction analysis confirmed no decomposition or generation of impurities by these methods. Once annealed, samples were cut into bars of approximately  $8 \times 2 \times 2$  mm in dimensions using a kerosene lubricant to avoid sample oxidation, and were subsequently stored in an argon atmosphere. Four-probe electrical resistivity measurements were carried out on a Quantum Design Physical Property Measurement System (PPMS). Platinum leads were attached on the rectangular bars using Epo-Tek H20E silver epoxy. The contacts for all samples were cured under a stream of ultra-high purity Ar inside a tube furnace.

### 6.2.6 Electronic Band Structure Calculations

The electronic structures of all samples for which a crystal could be obtained and solved were calculated using the tight-binding, linear-muffin tin orbital method<sup>117</sup> with the atomic sphere approximation (TB-LMTO-ASA) as implemented in the Stuttgart program.<sup>118</sup> All 4*f* electrons were considered as core electrons. Exchange and correlation were treated by the local density approximation (LDA).<sup>119</sup> A scalar relativistic approximation<sup>120</sup> was employed to account for all relativistic effects except spin-orbit coupling. Overlapping Wigner-Seitz cells were constructed with radii determined by requiring the overlapping potential to be the best approximation to the full potential, according to the atomic sphere approximation (ASA). Automatic sphere generation<sup>121</sup> was performed to construct empty spheres to be included in the unit cell in order to satisfy the overlap criteria of the TB-LMTO-ASA model. The X-ray single crystal data, including lattice parameters and atomic coordinates, were used as the model for calculations. The Ca/*RE* sites in Ca<sub>2</sub>RE<sub>7</sub>Sb<sub>5</sub>O<sub>5</sub> and Ca<sub>2</sub>RE<sub>7</sub>Bi<sub>5</sub>O<sub>5</sub> were set to be fully occupied by rare-earth atoms, resulting in idealized RE<sub>9</sub>Sb<sub>5</sub>O<sub>5</sub> structures with no changes in atomic parameters (such approach neglects a size difference<sup>131</sup> between Ca<sup>2+</sup> and RE<sup>3+</sup>). The Ca4 site was also left vacant due to its low occupancy.

## 6.3 Results and Discussion

### 6.3.1 Phase Formation and Stability

In a previous study by our group, the  $RE_9Sb_5O_5$  phases were reacted with carbon in an effort to yield a charge balanced, stable phase (assuming  $C^{4+}$  was present). In most cases, however, a pure sample could not be obtained, and all samples were observed to be highly air sensitive.<sup>106</sup> Instead, we have determined that stabilization by calcium addition is more practical. Our experiments revealed that sample compositions of  $Ca_2RE_7Pn_5O_5$  may yield air stable, pure phases through high temperature reaction conditions. Site mixing of calcium and rare-earth is accomplished in all  $Ca_2RE_7Pn_5O_5$  phases due to similar atomic radii<sup>131</sup>; this strategy was also employed in the discovery of the  $CaRE_3SbO_4$  and  $Ca_2RE_8Sb_3O_{10}$  phases.<sup>107</sup>

The stable nature of the  $Ca_2RE_7Pn_5O_5$  phases most likely results from the charge balanced electron formula achieved by substitution of trivalent  $RE^{3+}$  with divalent  $Ca^{2+}$ . Due to the mixing of calcium and rare-earth, as well as the potential for site deficiency, a  $Ca_{5-x}RE_{5+0.667x}Sb_5O_5$  compositional series with varying amounts of calcium and rare-earth may exist. However, our studies concluded that all samples of this series share the same Bragg peak positions in their powder X-ray diffraction data, suggesting that there is an optimal composition of calcium + rare-earth that is most stable. We then determined that the  $Ca_2RE_7Pn_5O_5$  stoichiometry yielded the most pure samples, indicating this system is thermodynamically driven to a charge balanced phase. Thus, our synthetic approach was

able to yield pure  $\text{Ca}_2\text{RE}_7\text{Sb}_5\text{O}_5$  phases for the  $\text{RE} = \text{La} - \text{Dy}$ , and pure  $\text{Ca}_2\text{RE}_7\text{Bi}_5\text{O}_5$  samples for late members of the  $\text{RE} = \text{Gd} - \text{Dy}$  series ( $\text{Ca}_2\text{RE}_7\text{Bi}_5\text{O}_5$  samples containing early  $\text{RE}$  were observed to form  $(\text{Ca},\text{RE})_2\text{BiO}_2$ ).

High temperature reactions in an induction furnace are necessary to form pure  $\text{Ca}_2\text{RE}_7\text{Pn}_5\text{O}_5$  samples. Phase formation was observed to occur for all temperatures between  $1200^\circ\text{C}$  and  $1600^\circ\text{C}$ , although temperatures of  $1300^\circ\text{C}$  and  $1225^\circ\text{C}$  were determined to be the most suitable for obtaining pure samples of  $\text{Ca}_2\text{RE}_7\text{Sb}_5\text{O}_5$  and  $\text{Ca}_2\text{RE}_7\text{Bi}_5\text{O}_5$ , respectively. Gray, molten products are obtained for the  $\text{Ca}_2\text{RE}_7\text{Pn}_5\text{O}_5$  samples, with the  $\text{Ca}_2\text{RE}_7\text{Bi}_5\text{O}_5$  samples being slightly darker in tone. A set of experiments performed on the pristine  $\text{RE}_9\text{Pn}_5\text{O}_5$  samples confirmed their instability, with samples tarnishing in air after a few minutes and full decomposition in air after 24-48 hours. In contrast, the  $\text{Ca}_2\text{RE}_7\text{Pn}_5\text{O}_5$  phases were observed to be stable in dry air or argon, although still reactive in moist air, with noticeable decomposition occurring after 48 hours. Thus, storage in an argon-filled glovebox was deemed to be necessary in order to prevent the loss of sample integrity.

### 6.3.2 Structural Determination and Analysis

The basic frameworks of the  $\text{Ca}_2\text{RE}_7\text{Pn}_5\text{O}_5$  phases are identical to the  $\text{RE}_9\text{Pn}_5\text{O}_5$  series. Based on the single crystal data, all  $\text{Ca}_2\text{RE}_7\text{Pn}_5\text{O}_5$  phases adopt the tetragonal  $P4/n$  symmetry, assuming an oxygen-stuffed, rare-earth deficient derivative of the  $\text{Sc}_2\text{Sb}$ -type structure.<sup>156, 157</sup> Each  $\text{Ca}_2\text{RE}_7\text{Pn}_5\text{O}_5$  phase contains site mixing of calcium and rare-earth. These phases contain NaCl-type  $(\text{Ca}/\text{RE})_5\text{Pn}_5$  slabs stacked along the  $c$ -direction which

are separated by  $(Ca/RE)_4O_5$  layers containing  $(Ca/RE)_4O$  and  $(Ca/RE)_5O$  polyhedra (Figure 6.1). One fifth of all calcium/rare-earth sites with respect to the  $Sc_2Sb$  structure are vacant in the parent  $RE_9Pn_5O_5$  phases; these ordered vacancies form the basis of the superstructure with respect to the original  $P4/nmm$  cell and occur in the  $(Ca/RE)_4O_5$  layers, forming ordered, empty channels along the  $c$ -direction.<sup>104</sup> The existence of the  $P4/n$  phase was also confirmed by X-ray powder diffraction experiments based on the presence of characteristic weak (220) and (221) reflections which are observed for the  $P4/n$  superstructure, but not the  $P4/nmm$  structure.

According to the single crystal diffraction data, each phase (except  $Ca_2Dy_7Bi_5O_5$ ) displays pseudomerohedral twinning with  $1/5$  of all reflections shared between domains. In order to obtain reliable diffraction intensities, each data set (except for  $Ca_2Dy_7Bi_5O_5$ ) had to be detwinned with the TWINABS program, yielding corrected intensities that could be used to solve the crystal structure of one twin component. The resulting data sets were solved with good  $R$  factors and yielded atomic parameters comparable to those in the original  $RE_9Pn_5O_5$  structures. However, one major difference was observed: each of the crystal solutions, apart from  $Ca_2Dy_7Bi_5O_5$ , had residual electron density on the normally vacant  $2a$  site. Since the pristine  $RE_9Pn_5O_5$  phases do not contain rare earth atoms on these sites, we assume calcium on the  $2a$  site.

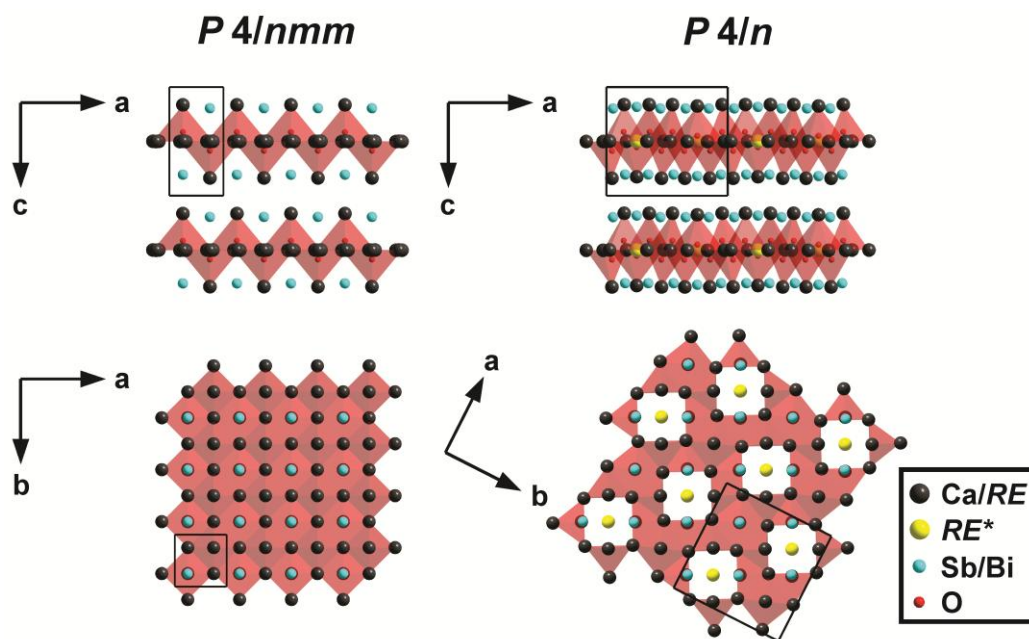


**Figure 6.1. Structural comparison of the  $P4/nmm$  and  $P4/n$  structures. The normally vacant sites in the  $P4/n$  structure are hereto assigned to be occupied by calcium in  $\text{Ca}_2\text{RE}_7\text{Pn}_5\text{O}_5$  (yellow atoms).**

### 6.3.3 Compositional Analysis

Unfortunately, our crystallographic models of the  $\text{Ca}_2\text{RE}_7\text{Pn}_5\text{O}_5$  phases make it difficult to obtain an accurate composition, not only due to the site mixing of calcium and rare-earth, but the presence of calcium on the  $2a$  site. Since we are unable to refine two atoms and a vacancy on the same site, and since a crystal may not represent a sample as a whole, we cannot determine the true composition from X-ray single crystal data alone. Thus, we performed electron microprobe analysis on all samples in order to verify their compositions and purities. The results are presented below in Table 6.4, along with a comparison to the X-ray single crystal data.

**Table 6.4. Comparison of experimentally determined compositions of  $\text{Ca}_2\text{RE}_7\text{Sb}_5\text{O}_5$  and  $\text{Ca}_2\text{RE}_7\text{Bi}_5\text{O}_5$  samples derived from EPMA and X-ray single crystal diffraction experiments.**

Loading composition	EPMA results <sup>a</sup>	X-ray single crystal data
$\text{Ca}_2\text{Pr}_7\text{Sb}_5\text{O}_5$	$\text{Ca}_{2.13(6)}\text{Pr}_{6.89(4)}\text{Sb}_{5.00(4)}\text{O}_{6.92(6)}$	$\text{Ca}_{2.16(1)}\text{Pr}_{7.00(1)}\text{Sb}_5\text{O}_5$
$\text{Ca}_2\text{Sm}_7\text{Sb}_5\text{O}_5$	$\text{Ca}_{2.03(5)}\text{Sm}_{7.00(3)}\text{Sb}_{5.00(3)}\text{O}_{6.47(5)}$	$\text{Ca}_{2.122(8)}\text{Sm}_{7.000(8)}\text{Sb}_5\text{O}_5$
$\text{Ca}_2\text{Gd}_7\text{Sb}_5\text{O}_5$	$\text{Ca}_{2.16(6)}\text{Gd}_{6.92(3)}\text{Sb}_{5.00(3)}\text{O}_{5.75(6)}$	$\text{Ca}_{2.045(6)}\text{Gd}_{7.000(6)}\text{Sb}_5\text{O}_5$
$\text{Ca}_2\text{Gd}_7\text{Bi}_5\text{O}_5$	$\text{Ca}_{2.07(5)}\text{Gd}_{6.95(3)}\text{Bi}_{5.00(3)}\text{O}_{5.99(6)}$	$\text{Ca}_{2.28(3)}\text{Gd}_{7.00(2)}\text{Bi}_5\text{O}_5$
$\text{Ca}_2\text{Dy}_7\text{Bi}_5\text{O}_5$	$\text{Ca}_{2.11(6)}\text{Dy}_{6.93(4)}\text{Bi}_{5.00(3)}\text{O}_{5.75(6)}$	$\text{Ca}_{2.00(2)}\text{Dy}_{7.00(2)}\text{Bi}_5\text{O}_5$

<sup>a</sup> The  $\text{Ca}_2\text{RE}_7\text{Sb}_5\text{O}_5$  and  $\text{Ca}_2\text{RE}_7\text{Bi}_5\text{O}_5$  samples were normalized to compositions containing five antimony/bismuth atoms.

Each of the structures determined from the X-ray single crystal data that contain calcium on the  $2a$  site were refined to have an excess of calcium with respect to rare earth. However, the EPMA data for all samples revealed atomic amounts no greater than three standard deviations from the loading compositions. The calcium amounts were consistently higher than expected, which is perhaps due to the fact that the  $\text{K}_\alpha/\text{K}_\beta$  peaks of calcium and the  $\text{L}_\alpha/\text{L}_\beta$  peaks of antimony overlap. The oxygen amounts were also well above the expected values, which can be attributed to oxidation from surface polishing. No tantalum signals were observed in any of the data sets. Based on the EPMA, we believe that all samples under study maintain the loading compositions without any significant fluctuations.

### 6.3.4 Electrical Properties and Electronic Structure

The pure  $\text{Ca}_2\text{RE}_7\text{Sb}_5\text{O}_5$  and samples displayed an Arrhenius-type decrease in electrical resistivity with temperature, suggesting that these phases are semiconductors (a bump in the  $\text{Ca}_2\text{Pr}_7\text{Sb}_5\text{O}_5$  data at lower temperatures occurs due to an antiferromagnetic transition). Conversely, the  $\text{Ca}_2\text{RE}_7\text{Bi}_5\text{O}_5$  phases displayed a linear decrease in electrical resistivity with temperature (Figure 6.2). These types of behavior directly contrast with the parent  $\text{RE}_9\text{Pn}_5\text{O}_5$  phases, which were reported to have metallic-type conduction.<sup>103</sup> Thus, by reducing the electron count, we did succeed in removing the metallic-type electrical resistivity behavior with respect to the parent  $\text{RE}_9\text{Pn}_5\text{O}_5$  structures and achieved activation energies on the order of about 0.04-0.06 eV in  $\text{Ca}_2\text{RE}_7\text{Sb}_5\text{O}_5$  (Table 6.5). Furthermore, the  $\text{Ca}_2\text{RE}_7\text{Pn}_5\text{O}_5$  phases display similar or lower electrical resistivity than most other rare-earth pnictide oxide phases studied by our group so far. However, these electrical resistivities (around 0.1-2  $\Omega$  cm at room temperature) are still too great for any thermoelectric applications.

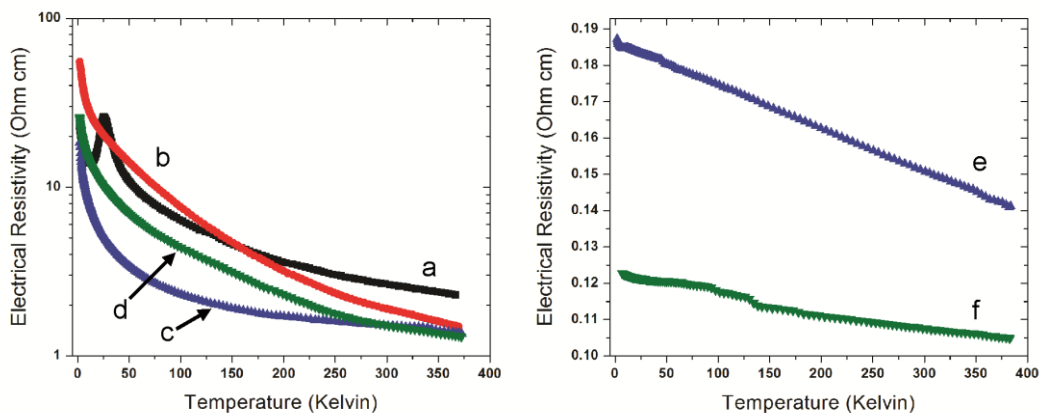


**Figure 6.2.** Electrical resistivity data for the  $\text{Ca}_2\text{RE}_7\text{Pn}_5\text{O}_5$  samples: a)  $\text{Ca}_2\text{Pr}_7\text{Sb}_5\text{O}_5$ , b)  $\text{Ca}_2\text{Sm}_7\text{Sb}_5\text{O}_5$ , c)  $\text{Ca}_2\text{Gd}_7\text{Sb}_5\text{O}_5$ , d)  $\text{Ca}_2\text{Dy}_7\text{Sb}_5\text{O}_5$ , e)  $\text{Ca}_2\text{Gd}_7\text{Bi}_5\text{O}_5$ , and f)  $\text{Ca}_2\text{Dy}_7\text{Bi}_5\text{O}_5$ .

**Table 6.5.** Room temperature electrical and activation energy data for selected  $\text{Ca}_2\text{RE}_7\text{Pn}_5\text{O}_5$  samples.

Sample	Room temperature electrical resistivity	Activation energy
$\text{Ca}_2\text{Pr}_7\text{Sb}_5\text{O}_5$	1.92 $\Omega$ cm	0.058 eV
$\text{Ca}_2\text{Sm}_7\text{Sb}_5\text{O}_5$	1.51 $\Omega$ cm	0.048 eV
$\text{Ca}_2\text{Gd}_7\text{Sb}_5\text{O}_5$	1.52 $\Omega$ cm	0.042 eV
$\text{Ca}_2\text{Gd}_7\text{Bi}_5\text{O}_5$	0.151 $\Omega$ cm	~0 eV
$\text{Ca}_2\text{Dy}_7\text{Bi}_5\text{O}_5$	0.108 $\Omega$ cm	~0 eV

Seebeck coefficient measurements ( $\alpha$ ) on the  $\text{Ca}_2\text{RE}_7\text{Sb}_5\text{O}_5$  and  $\text{Ca}_2\text{RE}_7\text{Bi}_5\text{O}_5$  samples revealed a near-linear dependence of  $\alpha$  on temperature, with  $\alpha$  approaching zero as  $T \rightarrow 0$  for all samples (Figure 6.3), suggesting that some order of metallic character is yet conserved. The  $\text{Ca}_2\text{RE}_7\text{Sb}_5\text{O}_5$  samples display larger Seebeck coefficients than the

$\text{Ca}_2\text{RE}_7\text{Bi}_5\text{O}_5$  samples, most likely due to their more semiconductor-like behavior in electrical resistivity. The  $\text{Ca}_2\text{Pr}_7\text{Sb}_5\text{O}_5$  and  $\text{Ca}_2\text{Sm}_7\text{Sb}_5\text{O}_5$  phases also display a curvature in their Seebeck coefficient data with increasing temperature, which could arise from contributions from electrons and holes in a complex multiband structure. The nature of this type of conduction may also explain why  $\text{Ca}_2\text{Gd}_7\text{Sb}_5\text{O}_5$  is *p*-type while  $\text{Ca}_2\text{Gd}_7\text{Bi}_5\text{O}_5$  is *n*-type (albeit weakly). Unfortunately, the Seebeck values obtained from our experiments are far lower than those observed from benchmark materials ( $\alpha \geq 150 \mu\text{V K}^{-1}$ ), making thermoelectric applications unlikely.

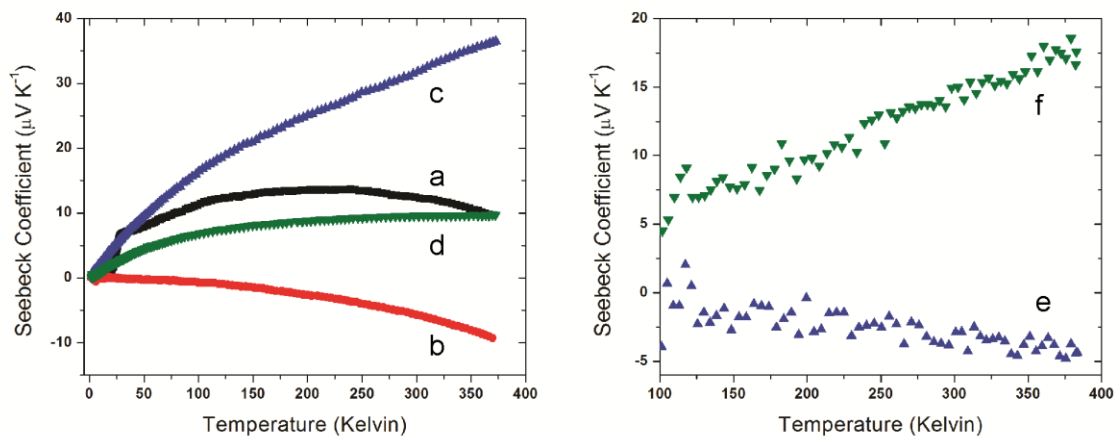


**Figure 6.3. Seebeck coefficient data for the  $\text{Ca}_2\text{RE}_7\text{Pn}_5\text{O}_5$  samples: a)  $\text{Ca}_2\text{Pr}_7\text{Sb}_5\text{O}_5$ , b)  $\text{Ca}_2\text{Sm}_7\text{Sb}_5\text{O}_5$ , c)  $\text{Ca}_2\text{Gd}_7\text{Sb}_5\text{O}_5$ , d)  $\text{Ca}_2\text{Dy}_7\text{Sb}_5\text{O}_5$ , e)  $\text{Ca}_2\text{Gd}_7\text{Bi}_5\text{O}_5$ , and f)  $\text{Ca}_2\text{Dy}_7\text{Bi}_5\text{O}_5$ .**

Electronic band structure calculations performed on the idealized  $\text{RE}_9\text{Pn}_5\text{O}_5$  structures reveal the presence of a noticeable pseudogap (density of states  $\neq 0$ ) at the Fermi level, corresponding to a charge balanced electron formula. Such a distribution of

states would be expected to yield semiconducting or semimetallic-like behavior, in agreement with our electrical resistivity and Seebeck coefficient data. As such, we argue the system is thermodynamically driven to a  $\text{Ca}_2\text{RE}_7\text{Pn}_5\text{O}_5$  formula when calcium is introduced. We acknowledge, however, that the calculated band gaps contain a certain level of error, due to the assumption of full site occupation by  $\text{RE}$  coupled with constant unit cell parameters. For all phases, the valence band is dominated by  $\text{Pn } p$  states immediately below the Fermi level, and the states in the conduction band are dominated by  $\text{RE } d$  states. As with many other rare-earth pnictide oxide structures, the density of states approaching the Fermi level becomes quite small, which may explain the relatively high electrical resistivity values. No significant differences are noticed between any of the calculated electronic structures, which agree with the similar values in electrical resistivities obtained by our experiments.

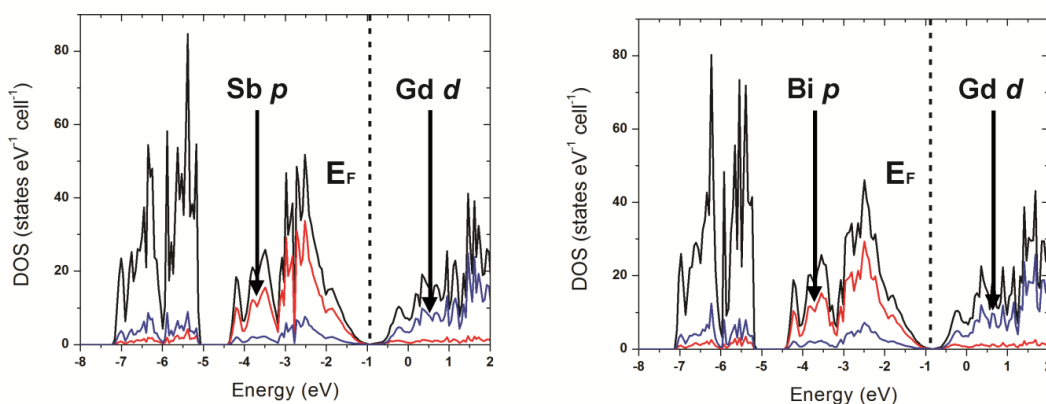


**Figure 6.4.** Calculated electronic band structures for the  $\text{Ca}_2\text{Gd}_7\text{Sb}_5\text{O}_5$  structure (left) and  $\text{Ca}_2\text{Gd}_7\text{Bi}_5\text{O}_5$  structure (right).

## 6.4 Conclusions

Substituting rare earth with calcium in  $RE_9Pn_5O_5$  was shown to yield pure, charge-balanced  $Ca_2RE_7Pn_5O_5$  phases upon high temperature reactions. Samples of  $Ca_2RE_7Pn_5O_5$  were observed to be much more stable versus the corresponding  $RE_9Pn_5O_5$  phases when prepared by similar methods, although the former are still moisture sensitive. X-ray powder and single crystal diffraction experiments confirmed that the  $Ca_2RE_7Pn_5O_5$  phases crystallize in the same  $P4/n$  structure type as the parent  $RE_9Pn_5O_5$  phases, and in most cases display the same twinning laws. The acquired X-ray single crystal data suggested residual electron density on the  $2a$  site, which was assigned to be partially filled with calcium.

Electrical resistivity and Seebeck coefficient measurements performed on pure  $Ca_2RE_7Pn_5O_5$  samples yielded semiconducting behavior for  $Ca_2RE_7Sb_5O_5$  phases and semimetallic behavior for  $Ca_2RE_7Bi_5O_5$  phases, in contrast to the metallic nature of the parent  $RE_9Pn_5O_5$  structures. Unfortunately, the electrical resistivity and Seebeck coefficient values are not ideal for thermoelectric applications. The calculated electronic structures seem to agree with the observed semiconducting and semimetallic behavior, although our ability to verify the nature of the pseudogaps by this method is limited by the precision of our calculations.

## Chapter 7. Conclusions and Future Work

This dissertation covers the syntheses, structural features, and physical properties of the  $(RE^I RE^{II})_3SbO_3$ ,  $CaRE_3SbO_4$ ,  $Ca_2RE_8Sb_3O_{10}$ ,  $RE_3BiO_3$ ,  $RE_8Bi_3O_8$ ,  $Ca_2RE_7Sb_5O_5$ , and  $Ca_2RE_7Bi_5O_5$  phases, where applicable. The goal of these projects was to design a material that would combine the electrical properties of a  $RE$ -Sb/Bi framework with the thermally insulating properties of a  $RE$ -O framework, resulting in a structurally complex phase that could potentially perform well as a thermoelectric. Our studies concluded that most of these phases have electrical resistivities a few orders of magnitude too great for use in thermoelectric devices, by comparison to other commonly used materials such as  $Bi_2Te_3$  and  $Zn_4Sb_3$ . However, these materials may be potentially useful if optimized due to their good thermal stabilities and tunable electrical properties, as is the case with  $Ca_2RE_8Sb_3O_{10}$ . Furthermore, our studies may also help characterize the  $RE$ -Sb/Bi-O system collectively with respect to both a chemical and physical perspective. By understanding the relationships between these phases, we may be able to discover and characterize future materials.

### 7.1 Structural Features

The  $RE$ -Sb/Bi-O phases discussed in this dissertation adopt a wide variety of crystal structures, but are all related by a fundamental theme. Most phases are defined by

building blocks consisting of  $RE_4O$  tetrahedra stitched together as repeating units. These building blocks may consist of two, three, four, or six  $RE_4O$  units, depending on the phase. In the case of  $(RE^I RE^{II})_3SbO_3$ ,  $CaRE_3SbO_4$ ,  $Ca_2RE_8Sb_3O_{10}$ ,  $RE_3BiO_3$ , and  $RE_8Bi_3O_8$ , the tetrahedra in the same building blocks are connected by edge sharing while the different building blocks themselves are connected by corner sharing. These building blocks form a 3D network that extends in the direction of the primary symmetry axis ( $b$ -axis for the monoclinic phases,  $c$ -axis for the tetragonal phases). Alternatively, in the case of  $RE_2PnO_2$ , the  $RE_4O$  tetrahedra are instead stitched together in a single unit by edge sharing, forming a two dimensional  $RE$ -O framework that extends indefinitely. For each of these structures, the  $RE$ -O framework defines empty channels or planes that are occupied by Sb and Bi atoms. Since each phase contains Sb and Bi coordinated around the electropositive rare earth atoms, we can conclude that each of these species are anionic, thus preserving the original  $RE$ -Sb/Bi framework at least to some extent.

## 7.2 Chemistry and Structural Modification

In order for the physical properties of potential  $RE$ - $Pn$ -O phases to be ideal for thermoelectric applications, each phase must exist as a suboxide, containing anionic antimony or bismuth. The reactions between  $RE Pn$  and  $RE_2O_3$  (and other species) must be carried out in a safe, controlled, and inert atmosphere at high temperatures. Our synthetic approaches were designed in such a way as to provide enough energy to

rearrange  $RE-Pn$  and  $RE-O$  bonds, but also avoid unwanted oxidation or losses of antimony/bismuth.

The chemistry behind the  $RE-Pn-O$  phases is both diverse and complex, with most of the phases explored in this dissertation requiring very specific heating trends and conditions to produce. For instance, the tetragonal  $(RE^I RE^{II})_3 SbO_3$  phase can only be formed using very high temperatures of 1550°C or greater, as well as two rare earth of sufficiently different size in order to stabilize its arrangement of  $RE-O$  building blocks. Likewise, the  $Gd_3 BiO_3$  and  $Gd_8 Bi_3 O_8$  phases could only be formed in a very narrow range of temperatures (~1300°C) with very precise compositions. The difficulty in preparing these phases originates from the difficulty of introducing bismuth atoms into their  $RE-O$  framework due to size constraints: a problem easily circumvented in  $Gd_2 BiO_2$  due to the stacking of Gd-O and Bi layers in its crystal structure. As such,  $RE_2 BiO_2$  is by far the most thermodynamically stable  $RE-Bi-O$  phase studied to date and is the product of nearly every other experiment performed in this system to date.

The  $CaRE_3 SbO_4$  and  $Ca_2 RE_8 Sb_3 O_{10}$  phases share a trait with the  $RE_3 SbO_3$  and  $RE_8 Sb_3 O_8$  phases in the sense that excessive heat treatments of one phase will yield the other. As such,  $CaRE_3 SbO_4$  could be obtained via short reaction times at 1600°C as a kinetic product, while  $Ca_2 RE_8 Sb_3 O_{10}$  would gradually form over time as a thermodynamic product. However, pure samples of  $Ca_2 RE_8 Sb_3 O_{10}$  could not be obtained in this way due to large differences in stoichiometry, and instead, reactions at 1300°C using of elemental calcium and antimony were required. Interestingly, the Sb atoms in  $Ca_2 RE_8 Sb_3 O_{10}$  were

observed to be disordered along the b-direction in their respective unit cells, and the degree of disorder could be modified by the substitution of one rare earth for another. This feature was determined to influence its physical properties, as discussed in Chapter 4.

Finally, the  $\text{Ca}_2\text{RE}_7\text{Pn}_5\text{O}_5$  phases can also be prepared as charge balanced, calcium-mixed derivatives of the parent  $\text{RE}_9\text{Pn}_5\text{O}_5$  phases. Much like the  $\text{RE}_2\text{PnO}_2$  series, these phases contain alternating stacks of  $\text{RE-Pn}$  and  $\text{RE-O}$  layers, which allows the lattice to relax and accommodate both antimony and bismuth easily. As such, these phases are significantly easier to prepare than other  $\text{RE-Pn-O}$  phases, but were shown to convert to  $\text{RE}_2\text{PnO}_2$  at medium temperatures, indicating that  $\text{RE}_2\text{PnO}_2$  is likely the most thermodynamically stable  $\text{RE-Pn-O}$  phase currently known.

### 7.3 Physical Properties

Despite the interesting properties of the  $\text{RE-Pn-O}$  phases from a structural perspective, none of the phases discussed in this dissertation pose any immediate use as thermoelectric materials as a result of their high electrical resistivities or low Seebeck voltages. However, we were successful in each case by creating an activation energy and introducing structural complexity in the  $\text{RE-Pn}$  framework. The  $\text{Ca}_2\text{RE}_8\text{Sb}_3\text{O}_{10}$  phases in particular may show promise for future modification. As demonstrated from our experiments in Chapter 4, the electrical resistivity sharply decreases when shifting from

left to right in the rare earth series. This unexpected behavior is the result of modifying the extent of Sb disorder and the subsequent range of Anderson localized states. If later members of the series, such as  $\text{Ca}_2\text{Dy}_7\text{Sb}_3\text{O}_{10}$  or  $\text{Ca}_2\text{Er}_7\text{Sb}_3\text{O}_{10}$  could be prepared in high purity, they may attain values of electrical resistivity that would be suitable for thermoelectric materials, assuming that the trend observed for the earlier members of the series is preserved. A summary of room temperature electrical resistivity and calculated activation energy values for the *RE-Pn-O* phases is summarized in Table 7.1.

**Table 7.1. Room temperature electrical resistivity values and electronic band gaps of selected *RE-Pn-O* phases.**

Series	Phase	Room temperature electrical resistivity ( $\Omega$ cm)	Activation energy (eV)
<b>(<i>RE<sup>I</sup>RE<sup>II</sup></i>)<sub>3</sub>SbO<sub>3</sub></b>	La <sub>1.5</sub> Dy <sub>1.5</sub> SbO <sub>3</sub>	1.05	0.11
	La <sub>1.5</sub> Ho <sub>1.5</sub> SbO <sub>3</sub>	1.05	0.093
	Ce <sub>1.5</sub> Ho <sub>1.5</sub> SbO <sub>3</sub>	0.223	0.044
<b>Ca<i>RE</i><sub>3</sub>SbO<sub>4</sub></b>	CaCe <sub>3</sub> SbO <sub>4</sub>	18.4	0.22
	CaPr <sub>3</sub> SbO <sub>4</sub>	38.1	0.33
	CaSm <sub>3</sub> SbO <sub>4</sub>	23.1	0.31
	CaGd <sub>3</sub> SbO <sub>4</sub>	77.4	0.28
<b>Ca<sub>2</sub><i>RE</i><sub>8</sub>Sb<sub>3</sub>O<sub>10</sub></b>	Ca <sub>2</sub> Nd <sub>8</sub> Sb <sub>3</sub> O <sub>10</sub> <sup>a</sup>	10340	-
	Ca <sub>2</sub> Nd <sub>4</sub> Sm <sub>4</sub> Sb <sub>3</sub> O <sub>10</sub>	910	0.44
	Ca <sub>2</sub> Sm <sub>8</sub> Sb <sub>3</sub> O <sub>10</sub>	73.4	0.26
	Ca <sub>2</sub> Sm <sub>4</sub> Gd <sub>4</sub> Sb <sub>3</sub> O <sub>10</sub>	11.0	0.32
<b>Gd<sub>8</sub>Bi<sub>3</sub>O<sub>8</sub></b>	Gd <sub>8</sub> Bi <sub>3</sub> O <sub>8</sub>	33.9	0.046
<b>Ca<sub>2</sub><i>RE</i><sub>7</sub>Sb<sub>5</sub>O<sub>5</sub></b>	Ca <sub>2</sub> Pr <sub>7</sub> Sb <sub>5</sub> O <sub>5</sub> <sup>a</sup>	2.65	0.033
	Ca <sub>2</sub> Sm <sub>7</sub> Sb <sub>5</sub> O <sub>5</sub> <sup>a</sup>	1.92	0.058
	Ca <sub>2</sub> Gd <sub>7</sub> Sb <sub>5</sub> O <sub>5</sub> <sup>a</sup>	1.52	0.048
	Ca <sub>2</sub> Dy <sub>7</sub> Sb <sub>5</sub> O <sub>5</sub> <sup>a</sup>	1.52	0.042
<b>Ca<sub>2</sub><i>RE</i><sub>7</sub>Bi<sub>5</sub>O<sub>5</sub></b>	Ca <sub>2</sub> Gd <sub>7</sub> Bi <sub>5</sub> O <sub>5</sub> <sup>a</sup>	0.151	-
	Ca <sub>2</sub> Dy <sub>7</sub> Bi <sub>5</sub> O <sub>5</sub> <sup>a</sup>	0.108	-

<sup>a</sup> Currently unpublished data.

## 7.4 Further Exploration of the *RE-Pn-O* System

The discovery of the  $\text{CaRE}_3\text{SbO}_4$  and  $\text{Ca}_2\text{RE}_8\text{Sb}_3\text{O}_{10}$  phases was the result of altering the electron count of the system by the introduction of divalent calcium. Due to their similar size, calcium and rare earth atoms function similarly in terms of the structural features of these phases. The aforementioned phases cannot be prepared without calcium, as it is not possible to achieve the correct electron count in either case when using only rare earth atoms. Thus, it may be possible to discover new phases as a result of heteroatom substitution in *RE-Pn-O*. The most obvious approach would be to select atoms that maintain a similar atomic radius when compared to rare earth. Based on this criterion, two elements immediately gain interest: sodium and thorium. When comparing six coordinate atomic radii, monovalent sodium displays an atomic radius nearly identical to  $\text{Ce}^{3+}$ , while tetravalent thorium displays an atomic radius nearly identical to  $\text{Gd}^{3+}$ .<sup>131</sup> A novel structure that contains these elements mixed with calcium or rare earth may be possible as a result of previously unobtainable electron counts. While sodium and thorium can be difficult to handle due to reactivity and radioactivity, respectively, they present an exciting exploratory synthetic approach that may yield new phases.

Preliminary studies conducted on introducing other species into the *RE-Pn-O* framework have yielded some interesting results. The reaction of a Na-Ca-Sm-Sb-O system at 1375°C have yielded X-ray powder data that cannot be indexed as any known

phase, although our efforts to obtain a single crystal for analysis have been unsuccessful to this point. More interestingly, our experiments have led to an interesting breakthrough as a result of further exploring the Ca-RE-Bi-O system. A crystal of  $\text{Ca}_4\text{REBi}_3\text{O}$  has been successfully isolated, collected, and solved in the orthorhombic  $Pnma$  space group (Figure 7.1).

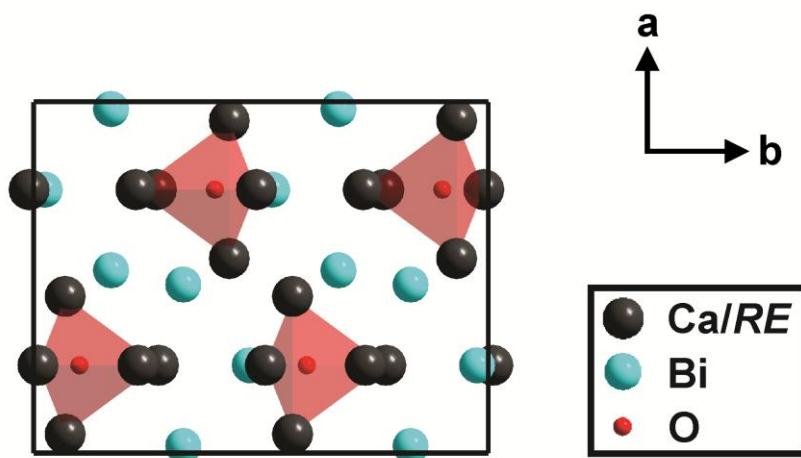


**Figure 7.1.** The  $\text{Ca}_4\text{REBi}_3\text{O}$  structure, viewed along the c-direction. This structure features isolated  $(\text{Ca},\text{RE})_4\text{O}$  tetrahedra and a three dimensional RE-Bi framework.

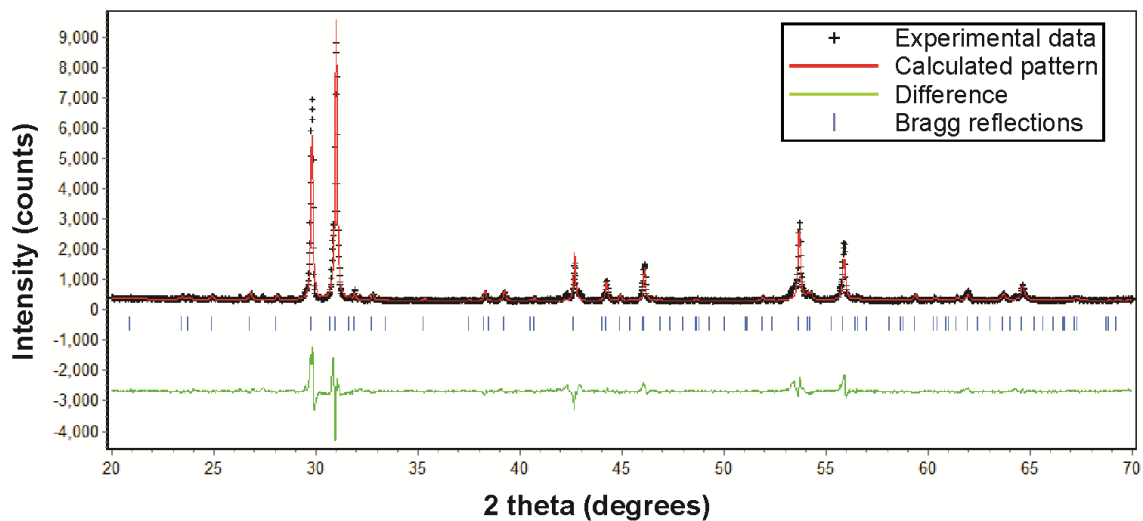
The  $\text{Ca}_4\text{REBi}_3\text{O}$  phase crystallizes in the  $\text{Ca}_5\text{Bi}_3\text{F}$  structure type<sup>158</sup>, which is itself a halogen-stuffed variant of the  $\text{Mn}_5\text{Si}_3$  structure type. Unlike other RE-Sb-O phases before it, the  $\text{Ca}_4\text{REBi}_3\text{O}$  phase is unique in the sense that it contains isolated  $\text{RE}_4\text{O}$  tetrahedra which do not form extended building blocks. These  $\text{RE}_4\text{O}$  tetrahedra are distributed between a RE-Bi framework that extends in three dimensions. The bismuth atoms only bond to rare-earth atoms, and do not appear to form dimer pairs, suggesting

the presence of  $\text{Bi}^{3-}$ . The analogous antimonide phases are also known for  $\text{Ca}_5\text{Sb}_3\text{Cl}$ ,  $\text{Ca}_5\text{Sb}_3\text{F}$ , and  $\text{Ba}_5\text{Sb}_3\text{Cl}$ , and adopt the hexagonal  $P6_3/mcm$  space group.<sup>158</sup> This new type of atomic arrangement may yield better thermoelectric properties on account of an extended *RE-Pn* network, and may also lead to the discovery of new *RE-Pn-O* phases.

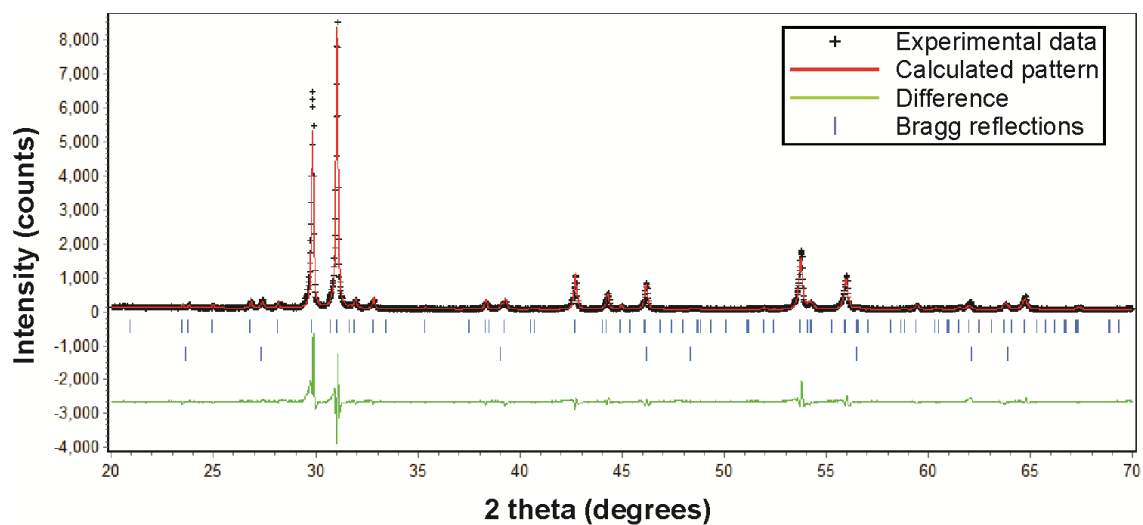
## **Appendix.**

### **A1. X-ray Powder Diffraction Data**

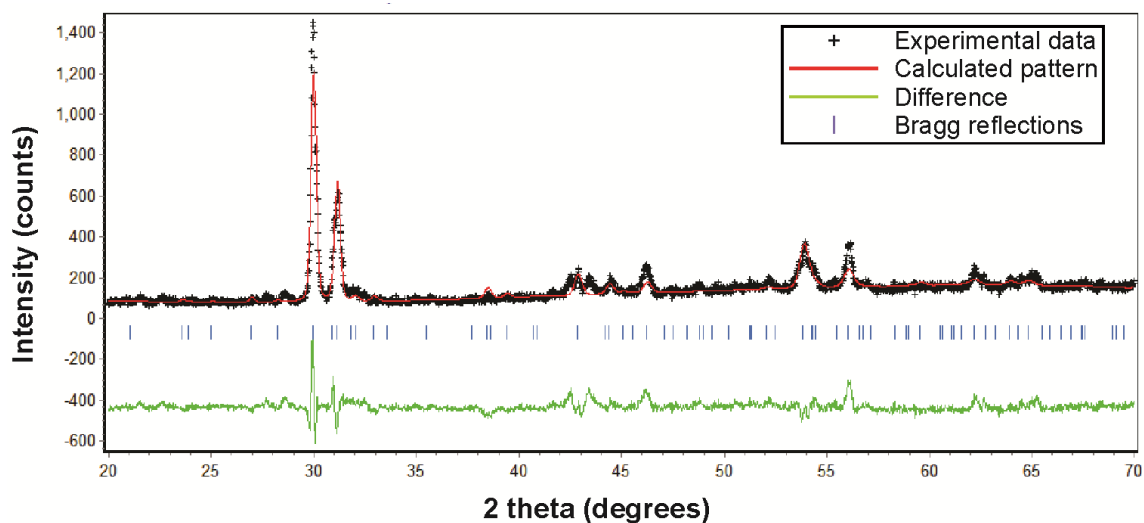
This section includes the Rietveld refinements of the X-ray powder data collected for the pure samples used for physical property measurements of each respective phase, as well as impure samples used to confirm the existence of related phases. The Rietica program<sup>114</sup> was used to refine background contributions, peak shapes, lattice parameters, and impurity concentrations. The data obtained from X-ray single crystal experiments was used as a starting model, where applicable. The site occupancies of the atoms in each structure were not refined, and were instead fixed to the values obtained from the X-ray single crystal solutions.

**A1.1 Tetragonal ( $RE^I RE^{II}$ ) $_3$ SbO $_3$** 

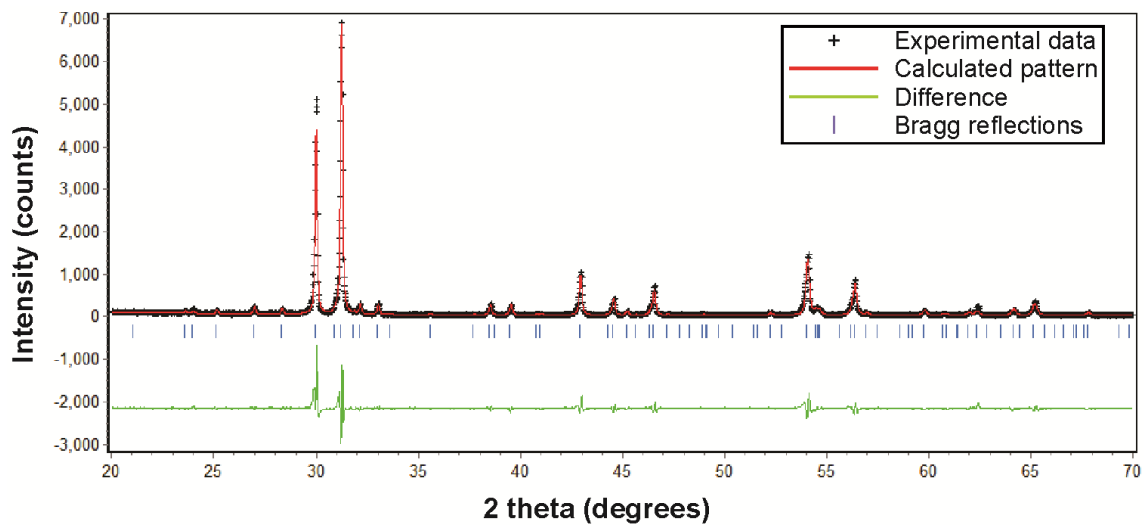
**Figure A1-1. Rietveld refinement of the X-ray powder data collected for a  $La_{1.5}Dy_{1.5}SbO_3$  sample.**



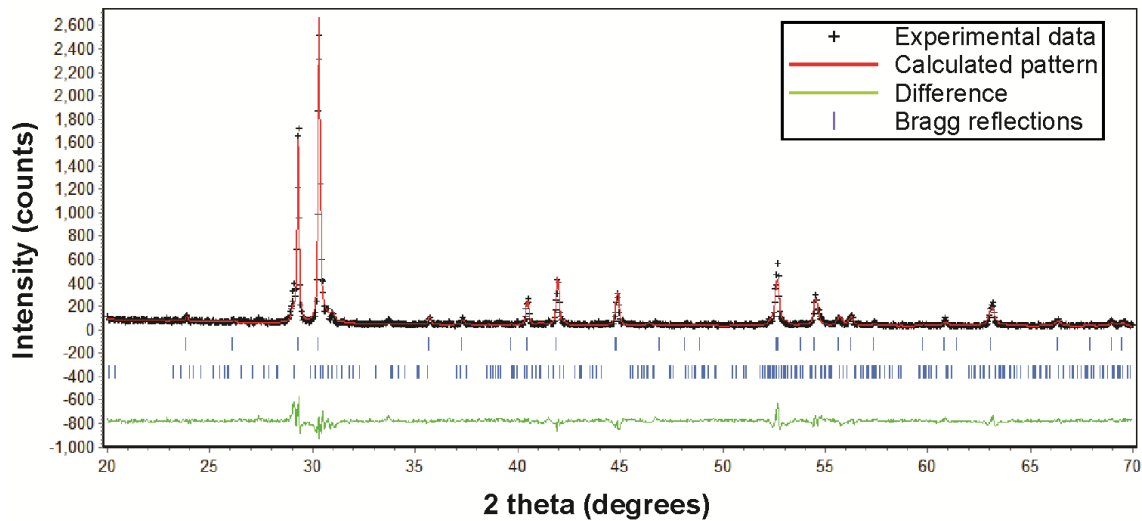
**Figure A1-2. Rietveld refinement of the X-ray powder data collected for a  $La_{1.5}Ho_{1.5}SbO_3$  sample.**



**Figure A1-3.** Rietveld refinement of the X-ray powder data collected for a  $\text{Ce}_{1.5}\text{Dy}_{1.5}\text{SbO}_3$  sample. This sample was not measured for physical properties, but can confirm the existence of the  $\text{Ce}_{1.5}\text{Dy}_{1.5}\text{SbO}_3$  phase.



**Figure A1-4.** Rietveld refinement of the X-ray powder data collected for a  $\text{Ce}_{1.5}\text{Ho}_{1.5}\text{SbO}_3$  sample.

**A1.2  $\text{CaRE}_3\text{SbO}_4$  and  $\text{Ca}_2\text{RE}_8\text{Sb}_3\text{O}_{10}$** 

**Figure A1-5. Rietveld refinement of the X-ray powder data collected for a  $\text{CaCe}_3\text{SbO}_4$  sample.**

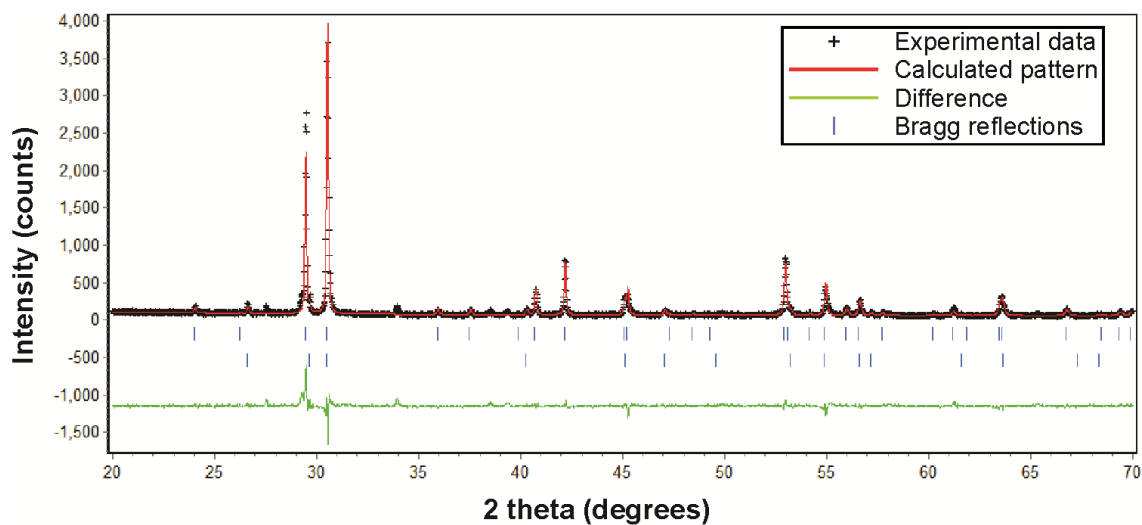


**Figure A1-6. Rietveld refinement of the X-ray powder data collected for a  $\text{CaPr}_3\text{SbO}_4$  sample.**

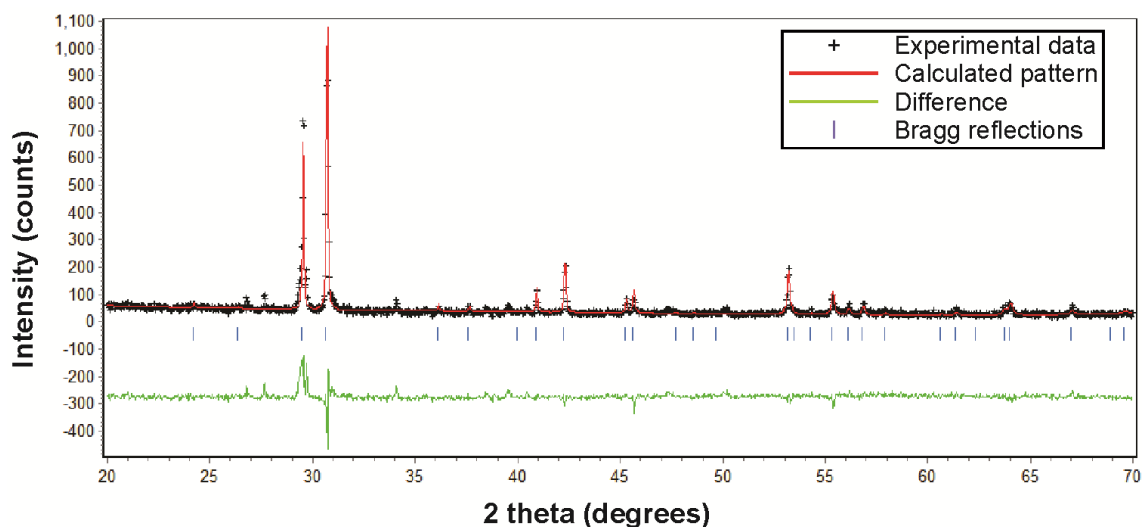


Figure A1-7. Rietveld refinement of the X-ray powder data collected for a  $\text{CaNd}_3\text{SbO}_4$  sample.

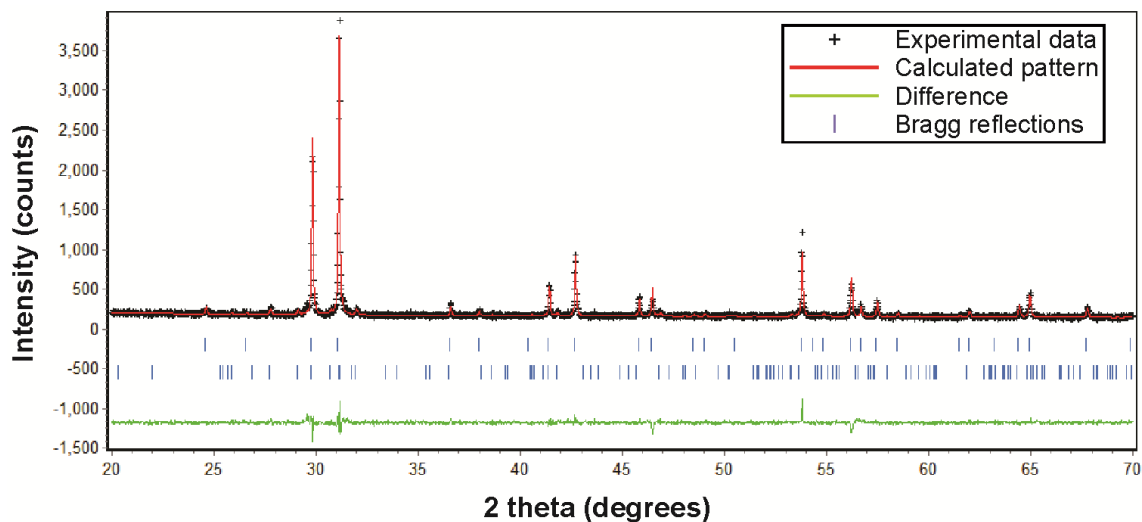
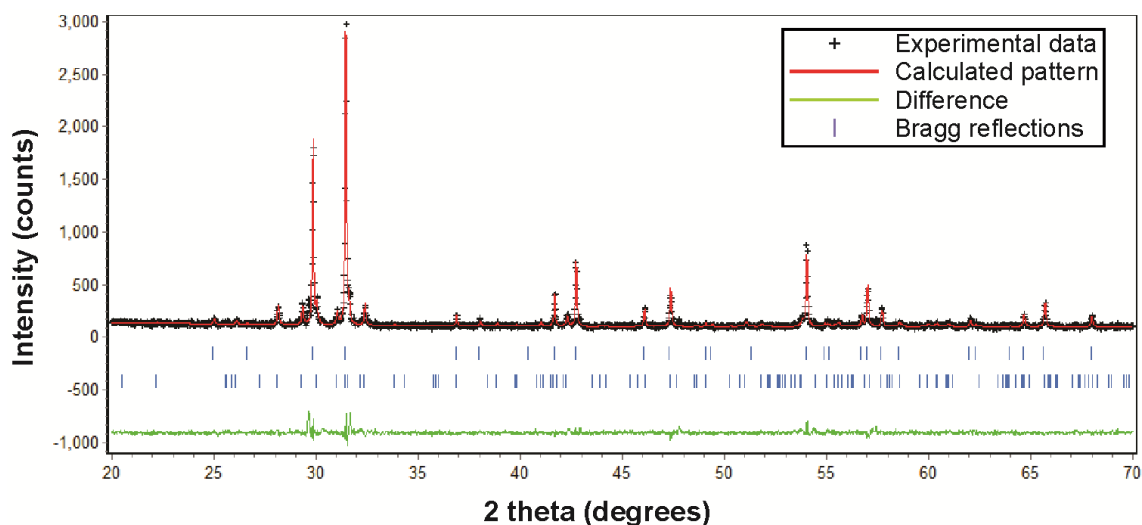
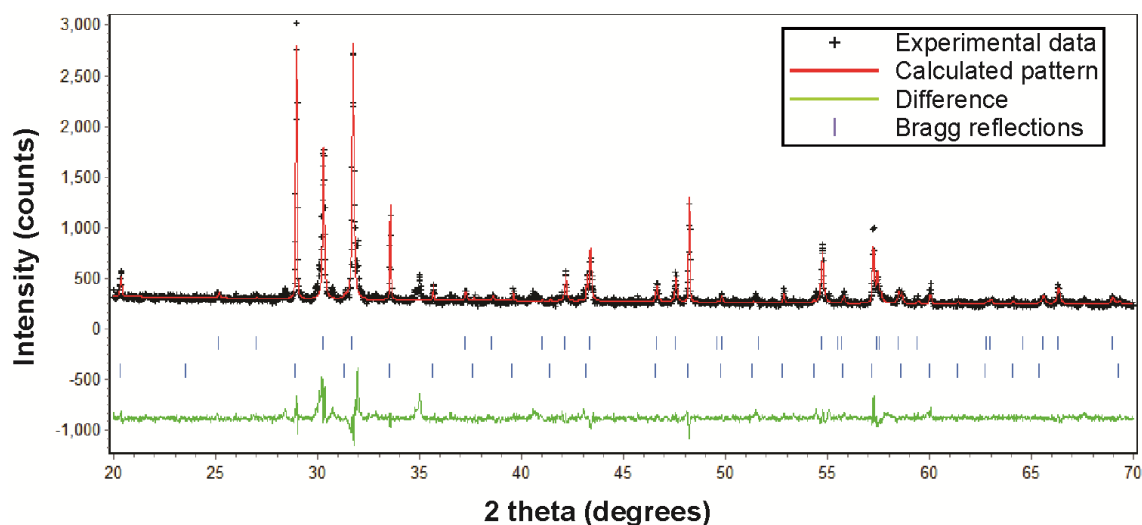


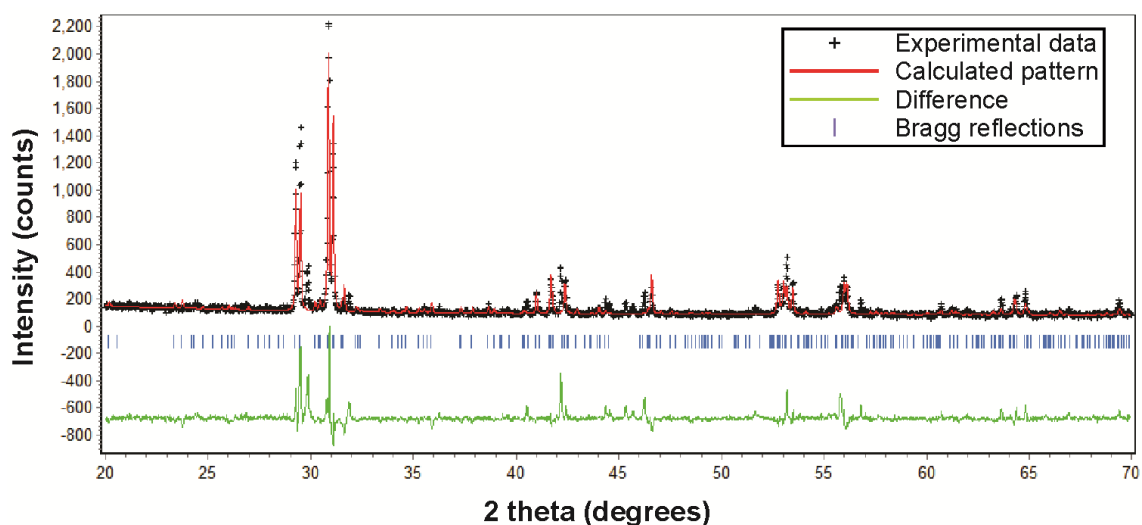
Figure A1-8. Rietveld refinement of the X-ray powder data collected for a  $\text{CaSm}_3\text{SbO}_4$  sample.



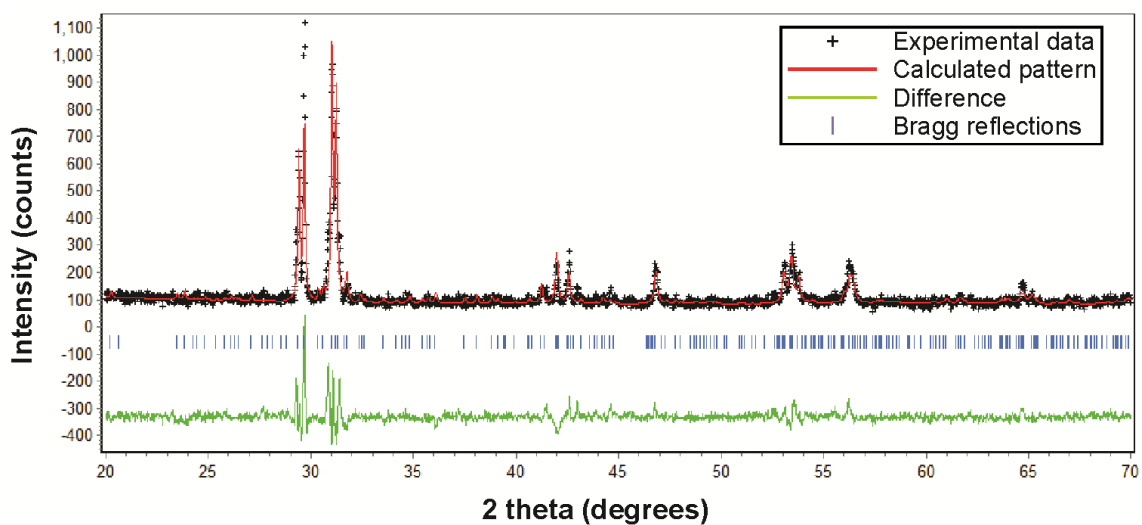
**Figure A1-9. Rietveld refinement of the X-ray powder data collected for a  $\text{CaGd}_3\text{SbO}_4$  sample.**



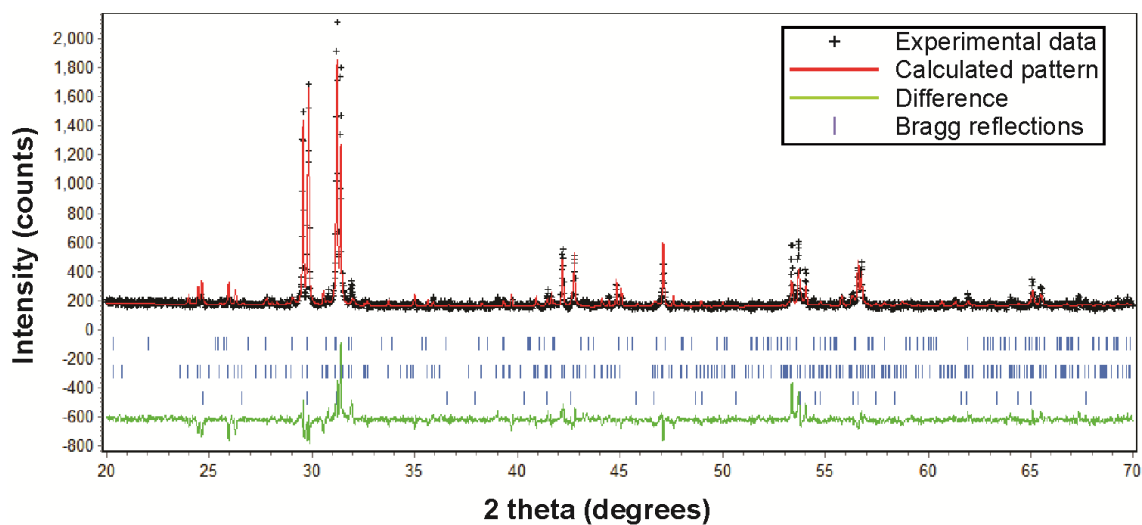
**Figure A1-10. Rietveld refinement of the X-ray powder data collected for a  $\text{CaDy}_3\text{SbO}_4$  sample. This sample was not measured for physical properties, but can confirm the existence of the  $\text{CaDy}_3\text{SbO}_4$  phase.**



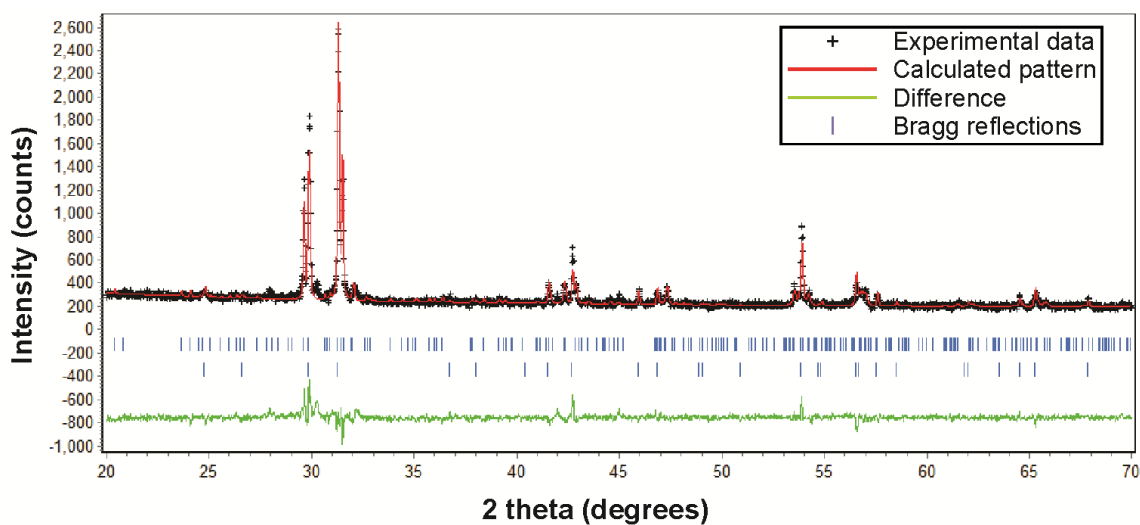
**Figure A1-11. Rietveld refinement of the X-ray powder data collected for a  $\text{Ca}_2\text{Nd}_8\text{Sb}_3\text{O}_{10}$  sample.**



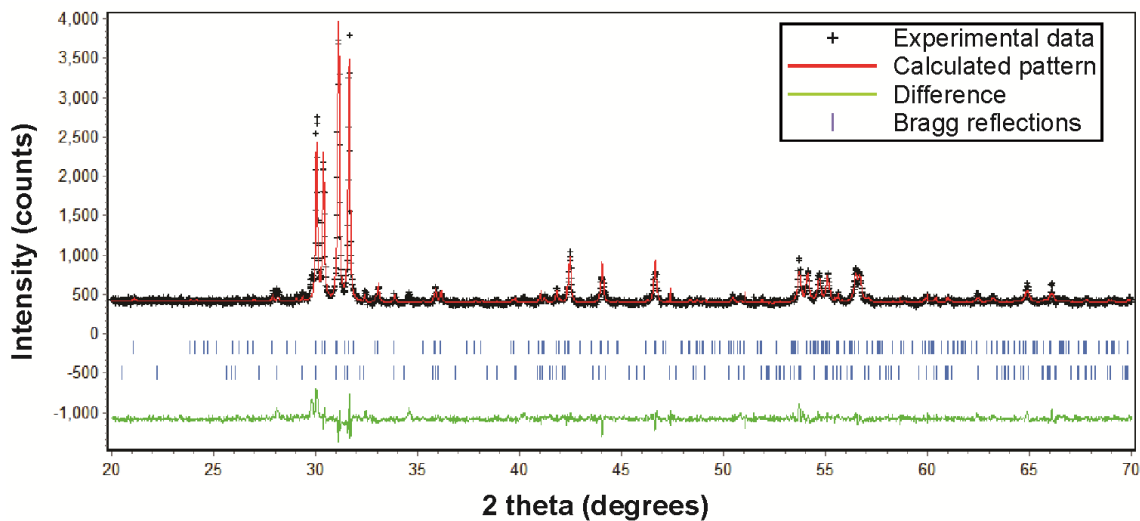
**Figure A1-12. Rietveld refinement of the X-ray powder data collected for a  $\text{Ca}_2\text{Nd}_4\text{Sm}_4\text{Sb}_3\text{O}_{10}$  sample.**



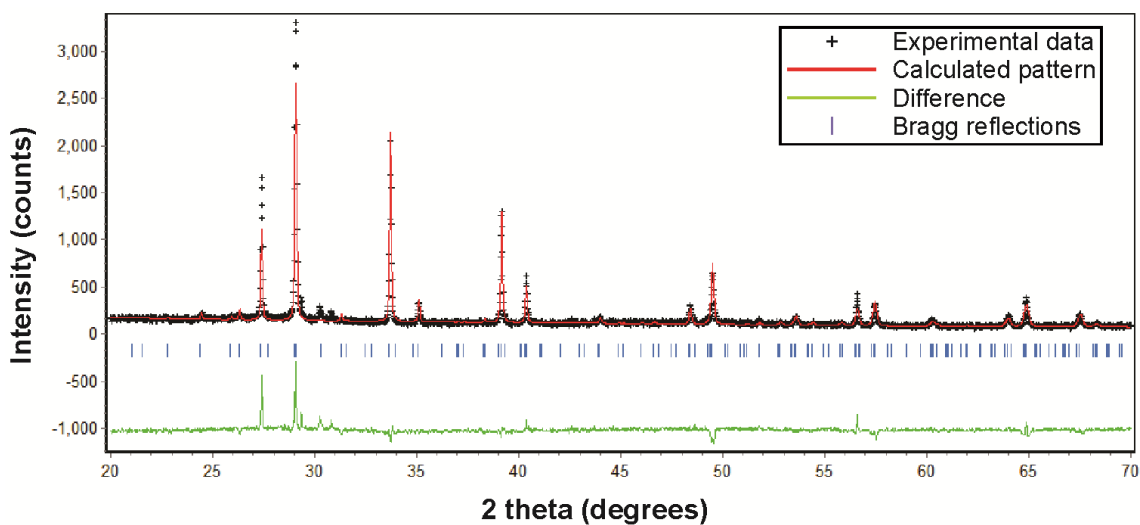
**Figure A1-13. Rietveld refinement of the X-ray powder data collected for a  $\text{Ca}_2\text{Sm}_8\text{Sb}_3\text{O}_{10}$  sample.**



**Figure A1-14. Rietveld refinement of the X-ray powder data collected for a  $\text{Ca}_2\text{Sm}_4\text{Gd}_4\text{Sb}_3\text{O}_{10}$  sample.**

**A1.3 Gd<sub>8</sub>Bi<sub>3</sub>O<sub>8</sub>**

**Figure A1-15. Rietveld refinement of the X-ray powder data collected for a Gd<sub>8</sub>Bi<sub>3</sub>O<sub>8</sub> sample.**

**A1.4 Ca<sub>2</sub>RE<sub>7</sub>Pn<sub>5</sub>O<sub>5</sub>**

**Figure A1-16. Rietveld refinement of the X-ray powder data collected for a Ca<sub>2</sub>Ce<sub>7</sub>Sb<sub>5</sub>O<sub>5</sub> sample.**

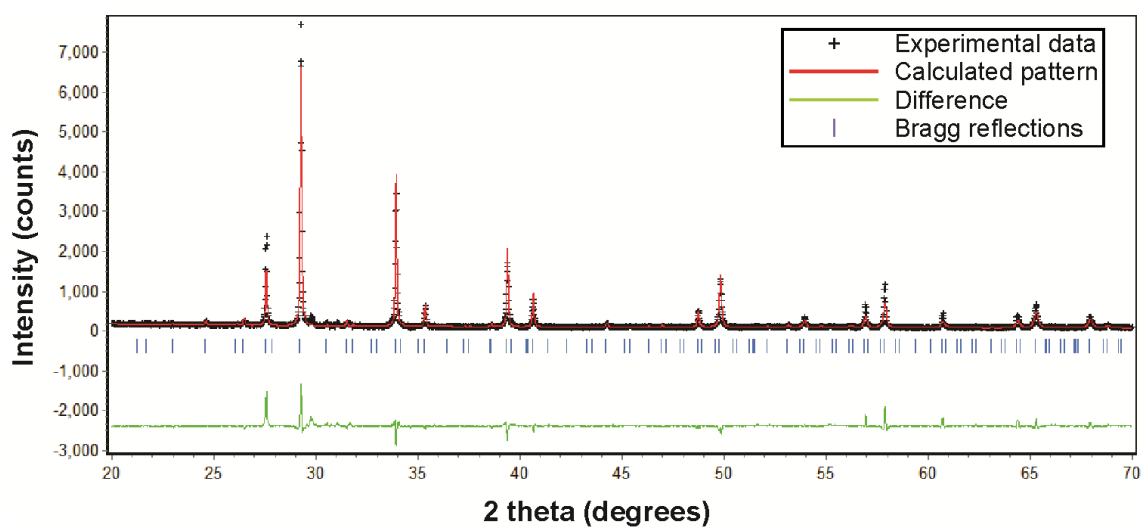


**Figure A1-17. Rietveld refinement of the X-ray powder data collected for a  $\text{Ca}_2\text{Pr}_7\text{Sb}_5\text{O}_5$  sample.**

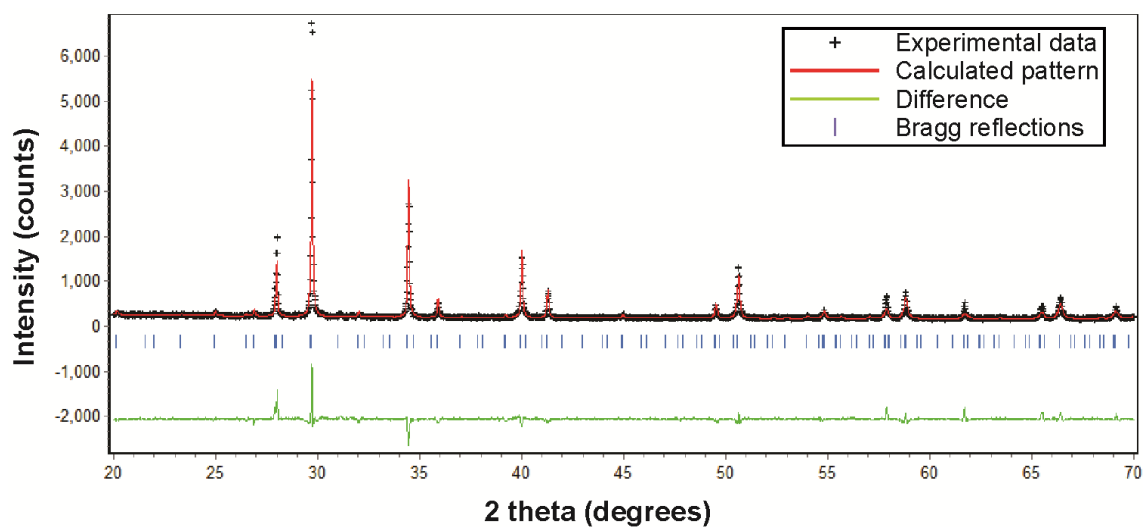


**Figure A1-18. Rietveld refinement of the X-ray powder data collected for a  $\text{Ca}_2\text{Sm}_7\text{Sb}_5\text{O}_5$  sample.**

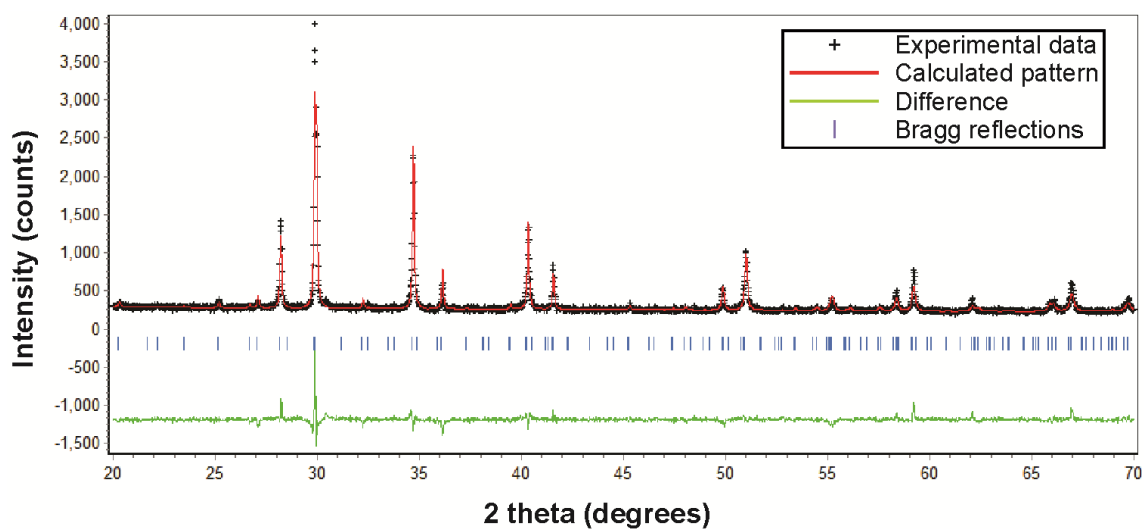


**Figure A1-19. Rietveld refinement of the X-ray powder data collected for a  $\text{Ca}_2\text{Gd}_7\text{Sb}_5\text{O}_5$  sample.**

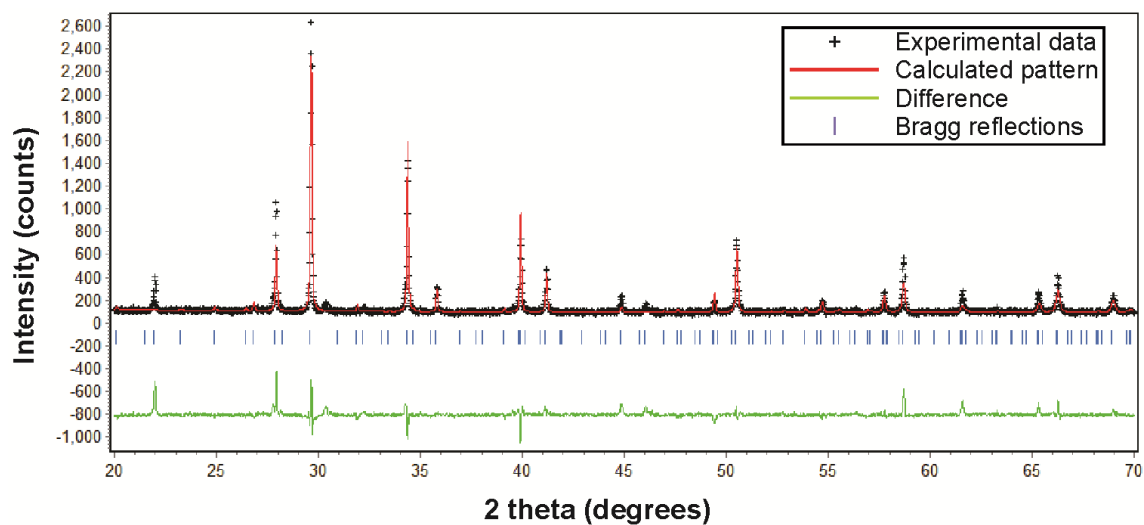


**Figure A1-20. Rietveld refinement of the X-ray powder data collected for a  $\text{Ca}_2\text{Gd}_7\text{Bi}_5\text{O}_5$  sample.**

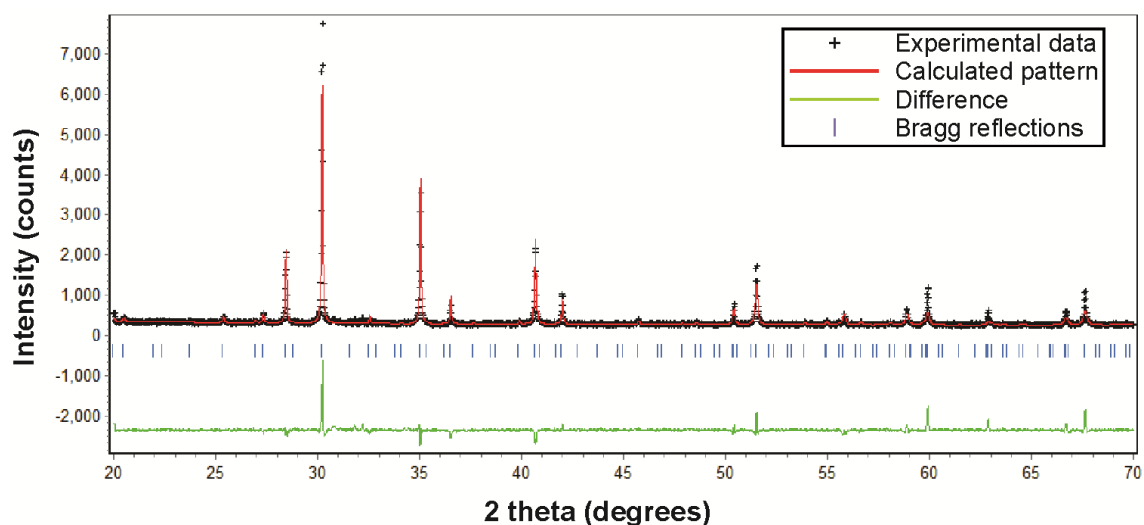


**Figure A1-21. Rietveld refinement of the X-ray powder data collected for a  $\text{Ca}_2\text{Dy}_7\text{Sb}_5\text{O}_5$  sample.**

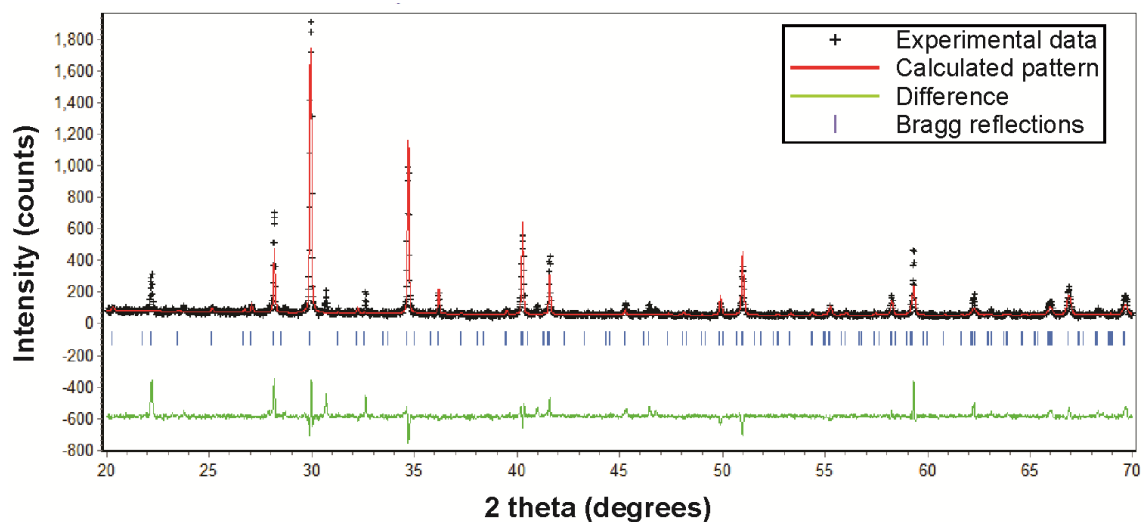


**Figure A1-22. Rietveld refinement of the X-ray powder data collected for a  $\text{Ca}_2\text{Dy}_7\text{Bi}_5\text{O}_5$  sample.**

## A2. Additional X-ray Single Crystal Data

This section includes X-ray single crystal data collected for phases not presented in the main body of the thesis.

**Table A2-1. Crystallographic and refinement data for a Dy<sub>3</sub>SbO<sub>3</sub> crystal.**

Dy <sub>3</sub> SbO <sub>3</sub>	
<b>Refined composition</b>	Dy <sub>3</sub> SbO <sub>3</sub>
<b>Space group</b>	<i>C2/m</i>
<b>a</b>	13.051(3) Å
<b>b</b>	3.8395(8) Å
<b>c</b>	11.683(2) Å
<b>β</b>	118.06(3)°
<b>Cell Volume</b>	516.6(2) Å <sup>3</sup>
<b>Z</b>	4
<b>Index ranges</b>	-20 ≤ h ≤ 19 -5 ≤ k ≤ 6 -18 ≤ l ≤ 18
<b>2θ range</b>	7.08° - 68.94°
<b>Total reflections</b>	4614
<b>Goodness-of-fit on F<sup>2</sup></b>	2.464
<b>R-indices</b>	R <sub>1</sub> = 0.0441 wR <sub>2</sub> = 0.0535 R <sub>1</sub> (all data) = 0.0511
<b>Extinction coefficient</b>	0.00059(4)

**Table A2-2. Atomic parameters for the Dy<sub>3</sub>SbO<sub>3</sub> crystal.**

<b>Atom</b>	<b>Site symmetry</b>	<b>Occupancy</b>	<b>x</b>	<b>y</b>	<b>z</b>	<b>U<sub>eq</sub></b>
<b>Dy1</b>	4i	1	0.11911(8)	0	0.44372(9)	0.0089(2)
<b>Dy2</b>	4i	1	0.34276(9)	0	0.7933(1)	0.0084(2)
<b>Dy3</b>	4i	1	0.87288(8)	0	0.09836(9)	0.0099(2)
<b>Sb1</b>	4i	1	0.8834(2)	0.5	0.3198(2)	0.0121(4)
<b>O1</b>	4i	1	0.3116(9)	0	0.591(1)	0.010(2)
<b>O2</b>	4i	1	0.334(1)	0	0.982(1)	0.016(2)
<b>O3</b>	4i	1	0.435(1)	0.5	0.806(1)	0.015(2)

**Table A2-3. Atomic parameters for the  $\text{CaRE}_3\text{SbO}_4$  crystals.**

Atom	Site	Occupancy	x	y	z	$U_{\text{eq}}$
<b><math>\text{Ca}_{0.95(4)}\text{Ce}_{2.95(4)}\text{SbO}_4</math></b>						
<b>Ca/Ce</b>	8h	0.24/0.76(1)	0.40665(6)	0.23601(7)	0	0.0114(2)
<b>Sb</b>	2a	1	0	0	0	0.0109(4)
<b>O</b>	8h	1	0.1756(7)	0.3588(7)	0	0.013(1)
<b><math>\text{Ca}_{1.01(2)}\text{Pr}_{2.99(2)}\text{SbO}_4</math></b>						
<b>Ca/Pr</b>	8h	0.253/0.747(4)	0.40633(3)	0.23640(3)	0	0.01033(9)
<b>Sb</b>	2a	1	0	0	0	0.0107(2)
<b>O</b>	8h	1	0.1760(3)	0.3600(3)	0	0.0126(6)
<b><math>\text{Ca}_{1.01(4)}\text{Nd}_{2.99(4)}\text{SbO}_4</math></b>						
<b>Ca/Nd</b>	8h	0.25/0.75(1)	0.40630(7)	0.23552(7)	0	0.0114(2)
<b>Sb</b>	2a	1	0	0	0	0.0109(4)
<b>O</b>	8h	1	0.1766(8)	0.3589(7)	0	0.014(1)
<b><math>\text{Ca}_{1.15(2)}\text{Sm}_{2.85(2)}\text{SbO}_4</math></b>						
<b>Ca/Sm</b>	8h	0.288/0.712(5)	0.40550(3)	0.23770(4)	0	0.0088(1)
<b>Sb</b>	2a	1	0	0	0	0.0102(2)
<b>O</b>	8h	1	0.1761(4)	0.3605(4)	0	0.0126(7)
<b><math>\text{Ca}_{1.17(2)}\text{Gd}_{2.83(2)}\text{SbO}_4</math></b>						
<b>Ca/Gd</b>	8h	0.293/0.707(4)	0.40504(3)	0.23824(3)	0	0.00868(8)
<b>Sb</b>	2a	1	0	0	0	0.0101(2)
<b>O</b>	8h	1	0.1765(3)	0.3613(3)	0	0.0126(6)

**Table A2-4. Atomic parameters for the  $\text{Ca}_2\text{RE}_8\text{Sb}_3\text{O}_{10}$  crystals.**

Atom	Site	Occupancy	x	y	z	$U_{\text{eq}}$
<b><math>\text{Ca}_{2.03(4)}\text{Pr}_{7.97(4)}\text{Sb}_{2.96(3)}\text{O}_{10}</math></b>						
<b>Ca1</b>	4i	0.331(7)	0.814(1)	0	0.0797(7)	0.0108(3)
<b>Pr1</b>	4i	0.669(7)	0.8271(1)	0	0.06432(8)	0.0108(3)
<b>Ca2</b>	4i	0.122(1)	0.09547(7)	0	0.1518(8)	0.0117(3)
<b>Pr2</b>	4i	0.724(8)	0.0942(1)	0	0.13618(7)	0.0117(3)
<b>Ca3</b>	4i	0.231(7)	0.418(1)	0	0.235(1)	0.0133(3)
<b>Pr3</b>	4i	0.769(7)	0.43739(9)	0	0.25062(8)	0.0133(3)
<b>Ca4</b>	4i	0.120(7)	0.265(2)	0	0.692(1)	0.0111(2)
<b>Pr4</b>	4i	0.880(7)	0.29385(7)	0	0.68150(4)	0.0111(2)
<b>Ca5</b>	4i	0.059(7)	0.364(3)	0	0.495(3)	0.0113(2)
<b>Pr5</b>	4i	0.941(7)	0.35313(5)	0	0.46466(6)	0.0113(2)
<b>Sb1</b>	2b	1	0	0.5	0	0.0195(4)
<b>Sb2</b>	8j	0.491(4)	0.03143(7)	0.036(2)	0.38820(6)	0.024(1)
<b>O1</b>	4i	1	0.2356(6)	0	0.0691(4)	0.017(2)
<b>O2</b>	4i	1	0.6060(5)	0	0.2062(4)	0.016(1)
<b>O3</b>	4i	1	0.0772(6)	0	0.8215(4)	0.019(1)
<b>O4</b>	4i	1	0.2959(6)	0	0.3154(5)	0.028(2)
<b>O5</b>	4i	1	0.2326(5)	0	0.5566(3)	0.013(1)
<b><math>\text{Ca}_{2.23(3)}\text{Nd}_{7.77(3)}\text{Sb}_{2.97(2)}\text{O}_{10}</math></b>						
<b>Ca1</b>	4i	0.341(5)	0.8134(7)	0	0.0776(5)	0.0109(2)
<b>Nd1</b>	4i	0.659(5)	0.82729(7)	0	0.06416(6)	0.0109(2)
<b>Ca2</b>	4i	0.289(5)	0.1212(6)	0	0.1527(5)	0.0114(2)
<b>Nd2</b>	4i	0.711(5)	0.09385(6)	0	0.13615(5)	0.0114(2)
<b>Ca3</b>	4i	0.261(5)	0.4188(7)	0	0.2358(6)	0.0117(2)
<b>Nd3</b>	4i	0.739(5)	0.43762(5)	0	0.25073(5)	0.0117(2)
<b>Ca4</b>	4i	0.146(5)	0.271(1)	0	0.693(1)	0.0110(2)
<b>Nd4</b>	4i	0.854(5)	0.29404(5)	0	0.68018(3)	0.0110(2)
<b>Ca5</b>	4i	0.080(6)	0.362(2)	0	0.493(2)	0.0122(2)

<b>Nd5</b>	4i	0.920(6)	0.35244(3)	0	0.46445(4)	0.0122(2)
<b>Sb1</b>	2b	1	0	0.5	0	0.0200(2)
<b>Sb2</b>	8j	0.491(3)	0.03118(5)	0.041(1)	0.38847(4)	0.0217(7)
<b>O1</b>	4i	1	0.2366(4)	0	0.0700(3)	0.015(1)
<b>O2</b>	4i	1	0.6064(4)	0	0.2061(3)	0.017(1)
<b>O3</b>	4i	1	0.0778(4)	0	0.8212(3)	0.019(1)
<b>O4</b>	4i	1	0.2955(5)	0	0.3146(5)	0.028(1)
<b>O5</b>	4i	1	0.2334(4)	0	0.5564(3)	0.0114(9)

**Ca<sub>2.11(4)</sub>Sm<sub>7.89(4)</sub>Sb<sub>2.99(3)</sub>O<sub>10</sub>**

<b>Ca1</b>	4i	0.341(6)	0.815(1)	0	0.0758(7)	0.0090(3)
<b>Sm1</b>	4i	0.659(6)	0.8277(1)	0	0.06362(8)	0.0090(3)
<b>Ca2</b>	4i	0.278(7)	0.119(1)	0	0.1523(7)	0.0105(3)
<b>Sm2</b>	4i	0.722(7)	0.09405(8)	0	0.13665(6)	0.0105(3)
<b>Ca3</b>	4i	0.232(6)	0.421(1)	0	0.237(1)	0.0115(2)
<b>Sm3</b>	4i	0.768(6)	0.43688(8)	0	0.24996(7)	0.0115(2)
<b>Ca4</b>	4i	0.115(6)	0.306(5)	0	0.686(4)	0.0101(2)
<b>Sm4</b>	4i	0.885(6)	0.2937(1)	0	0.6812(1)	0.0101(2)
<b>Ca5</b>	4i	0.091(7)	0.363(2)	0	0.491(2)	0.0120(2)
<b>Sm5</b>	4i	0.909(7)	0.35172(5)	0	0.46477(6)	0.0120(2)
<b>Sb1</b>	2b	1	0	0.5	0	0.0164(3)
<b>Sb2</b>	8j	0.497(4)	0.03026(7)	0.0446(9)	0.38877(5)	0.0174(6)
<b>O1</b>	4i	1	0.2364(5)	0	0.0705(3)	0.013(1)
<b>O2</b>	4i	1	0.6062(5)	0	0.2067(4)	0.018(2)
<b>O3</b>	4i	1	0.0767(5)	0	0.8210(3)	0.015(1)
<b>O4</b>	4i	1	0.2933(6)	0	0.3124(6)	0.034(2)
<b>O5</b>	4i	1	0.2333(5)	0	0.5565(3)	0.012(1)

**Ca<sub>2.08(4)</sub>Gd<sub>7.92(4)</sub>Sb<sub>2.97(3)</sub>O<sub>10</sub>**

<b>Ca1</b>	4i	0.339(7)	0.821(2)	0	0.075(1)	0.0091(3)
<b>Gd1</b>	4i	0.661(7)	0.8276(2)	0	0.0632(1)	0.0091(3)
<b>Ca2</b>	4i	0.279(8)	0.114(1)	0	0.1529(9)	0.0098(3)

<b>Gd2</b>	4i	0.721(8)	0.09345(9)	0	0.13639(7)	0.0098(3)
<b>Ca3</b>	4i	0.221(7)	0.421(1)	0	0.240(2)	0.0110(3)
<b>Gd3</b>	4i	0.779(7)	0.4371(1)	0	0.2500(1)	0.0110(3)
<b>Ca4</b>	4i	0.096(8)	0.277(4)	0	0.692(3)	0.0093(2)
<b>Gd4</b>	4i	0.904(8)	0.29492(7)	0	0.68085(5)	0.0093(2)
<b>Ca5</b>	4i	0.106(8)	0.360(2)	0	0.491(2)	0.0123(2)
<b>Gd5</b>	4i	0.894(8)	0.35106(5)	0	0.46438(7)	0.0123(2)
<b>Sb1</b>	2b	1	0	0.5	0	0.0141(3)
<b>Sb2</b>	8j	0.492(4)	0.03010(8)	0.045(1)	0.38925(6)	0.0143(7)
<b>O1</b>	4i	1	0.2360(6)	0	0.0705(4)	0.014(2)
<b>O2</b>	4i	1	0.6057(6)	0	0.2071(4)	0.015(2)
<b>O3</b>	4i	1	0.0773(6)	0	0.8214(4)	0.017(2)
<b>O4</b>	4i	1	0.2917(8)	0	0.3102(7)	0.035(3)
<b>O5</b>	4i	1	0.2343(5)	0	0.5571(4)	0.011(1)

**Ca<sub>1.91(5)</sub>Tb<sub>8.09(5)</sub>Sb<sub>3.01(2)</sub>O<sub>10</sub>**

<b>Ca1</b>	4i	0.321(5)	0.815(1)	0	0.0732(9)	0.0077(3)
<b>Tb1</b>	4i	0.679(5)	0.8283(1)	0	0.06483(9)	0.0077(3)
<b>Ca2</b>	4i	0.246(6)	0.122(1)	0	0.1540(8)	0.0095(2)
<b>Tb2</b>	4i	0.754(6)	0.09425(7)	0	0.13702(5)	0.0095(2)
<b>Ca3</b>	4i	0.218(5)	0.424(2)	0	0.240(2)	0.0100(2)
<b>Tb3</b>	4i	0.782(5)	0.4366(1)	0	0.24971(9)	0.0100(2)
<b>Ca4</b>	4i	0.050(4)	0.268(3)	0	0.729(2)	0.0088(1)
<b>Tb4</b>	4i	0.950(4)	0.29476(4)	0	0.68117(3)	0.0088(1)
<b>Ca5</b>	4i	0.118(6)	0.364(2)	0	0.491(2)	0.0112(2)
<b>Tb5</b>	4i	0.882(6)	0.35143(5)	0	0.46528(5)	0.0112(2)
<b>Sb1</b>	2b	1	0	0.5	0	0.0124(3)
<b>Sb2</b>	8j	0.504(3)	0.02978(6)	0.0458(7)	0.38877(5)	0.0120(5)
<b>O1</b>	4i	1	0.2362(5)	0	0.0702(3)	0.014(1)
<b>O2</b>	4i	1	0.6053(5)	0	0.2075(3)	0.013(1)
<b>O3</b>	4i	1	0.0775(5)	0	0.8214(4)	0.015(1)
<b>O4</b>	4i	1	0.2907(7)	0	0.3083(6)	0.040(2)
<b>O5</b>	4i	1	0.2343(5)	0	0.5573(3)	0.010(1)

---

**Table A2-5. Atomic parameters for the  $\text{Ca}_2\text{RE}_7\text{Pn}_5\text{O}_5$  crystals.**

Atom	Site	Occupancy	x	y	z	$U_{\text{eq}}$
<b><math>\text{Ca}_{2.16(1)}\text{Pr}_{7.00(1)}\text{Sb}_5\text{O}_5</math></b>						
<b>Ca1/Pr1</b>	2c	0.159/0.841(2)	0.25	0.25	0.3272(1)	0.0092(2)
<b>Ca2/Pr2</b>	8g	0.208/0.792(2)	0.14712(5)	0.95233(5)	0.66184(4)	0.01008(8)
<b>Ca3/Pr3</b>	8g	0.252/0.748(2)	0.33263(5)	0.02493(5)	0.99766(7)	0.0127(1)
<b>Ca4</b>	2a	0.16(1)	0.25	0.75	0	0.0127(1)
<b>Sb1</b>	2c	1	0.25	0.25	0.6852(1)	0.0102(2)
<b>Sb2</b>	8g	1	0.15255(5)	0.94805(5)	0.30200(4)	0.00934(7)
<b>O1</b>	2c	1	0.25	0.25	0.076(1)	0.013(2)
<b>O2</b>	8g	1	0.1319(6)	0.9733(6)	0.9088(6)	0.0122(9)
<b><math>\text{Ca}_{2.122(8)}\text{Sm}_{7.000(8)}\text{Sb}_5\text{O}_5</math></b>						
<b>Ca1/Sm1</b>	2c	0.187/0.813(2)	0.25	0.25	0.32703(8)	0.0089(1)
<b>Ca2/Sm2</b>	8g	0.204/0.796(2)	0.14691(4)	0.95282(3)	0.66118(3)	0.00946(6)
<b>Ca3/Sm3</b>	8g	0.249/0.751(2)	0.33286(3)	0.02470(3)	0.99806(6)	0.01011(7)
<b>Ca4</b>	2a	0.122(8)	0.25	0.75	0	0.01011(7)
<b>Sb1</b>	2c	1	0.25	0.25	0.6826(1)	0.0100(1)
<b>Sb2</b>	8g	1	0.15303(3)	0.94753(4)	0.30252(4)	0.00961(5)
<b>O1</b>	2c	1	0.25	0.25	0.069(1)	0.012(1)
<b>O2</b>	8g	1	0.1310(4)	0.9738(4)	0.9103(5)	0.0106(7)
<b><math>\text{Ca}_{2.045(6)}\text{Gd}_{7.000(6)}\text{Sb}_5\text{O}_5</math></b>						
<b>Ca1/Gd1</b>	2c	0.232/0.768(1)	0.25	0.25	0.32628(5)	0.00823(8)
<b>Ca2/Gd2</b>	8g	0.2407/0.7593(9)	0.14688(2)	0.95313(2)	0.66136(2)	0.00858(5)
<b>Ca3/Gd3</b>	8g	0.201/0.799(1)	0.33320(2)	0.02480(2)	0.99828(2)	0.00887(5)
<b>Ca4</b>	2a	0.045(5)	0.25	0.75	0	0.00887(5)
<b>Sb1</b>	2c	1	0.25	0.25	0.68040(5)	0.00920(8)
<b>Sb2</b>	8g	1	0.15325(2)	0.94739(2)	0.30252(2)	0.00873(4)
<b>O1</b>	2c	1	0.25	0.25	0.0680(6)	0.0126(9)

<b>O2</b>	8g	1	0.1312(2)	0.9744(3)	0.9103(3)	0.0097(4)
-----------	----	---	-----------	-----------	-----------	-----------

**Ca<sub>2.28(1)</sub>Gd<sub>7.00(1)</sub>Bi<sub>5</sub>O<sub>5</sub>**

<b>Ca1/Gd1</b>	2c	0.251/0.749(2)	0.25	0.25	0.3236(1)	0.0067(2)
<b>Ca2/Gd2</b>	8g	0.248/0.752(2)	0.14660(6)	0.95330(6)	0.66520(6)	0.00740(8)
<b>Ca3/Gd3</b>	8g	0.190/0.810(2)	0.33419(5)	0.02624(5)	0.99817(7)	0.0094(1)
<b>Ca4</b>	2a	0.28(1)	0.25	0.75	0	0.0094(1)
<b>Bi1</b>	2c	1	0.25	0.25	0.68274(8)	0.0072(1)
<b>Bi2</b>	8g	1	0.15318(4)	0.94695(4)	0.30312(3)	0.00674(5)
<b>O1</b>	2c	1	0.25	0.25	0.070(1)	0.008(2)
<b>O2</b>	8g	1	0.1320(7)	0.9729(7)	0.9137(7)	0.011(1)

**Ca<sub>2.00(1)</sub>Dy<sub>7.00(1)</sub>Bi<sub>5</sub>O<sub>5</sub>**

<b>Ca1/Dy1</b>	2c	0.257/0.743(2)	0.25	0.25	0.32031(6)	0.0124(1)
<b>Ca2/Dy2</b>	8g	0.279/0.721(2)	0.14545(3)	0.95450(3)	0.66505(3)	0.01225(8)
<b>Ca3/Dy3</b>	8g	0.157/0.843(2)	0.33300(3)	0.02432(5)	0.99757(3)	0.01197(6)
<b>Ca4*</b>	2a	0	-	-	-	-
<b>Bi1</b>	2c	1	0.25	0.25	0.67926(4)	0.01288(7)
<b>Bi2</b>	8g	1	0.15415(2)	0.94593(2)	0.30300(2)	0.01238(5)
<b>O1</b>	2c	1	0.25	0.25	0.0676(8)	0.019(2)
<b>O2</b>	8g	1	0.1301(4)	0.9757(4)	0.9120(4)	0.0131(6)

---

### A3. Additional Electronic Structures

This section includes the calculated electronic structures of phases for which X-ray single crystal solutions were obtained, but were not included in the content discussed in each chapter.

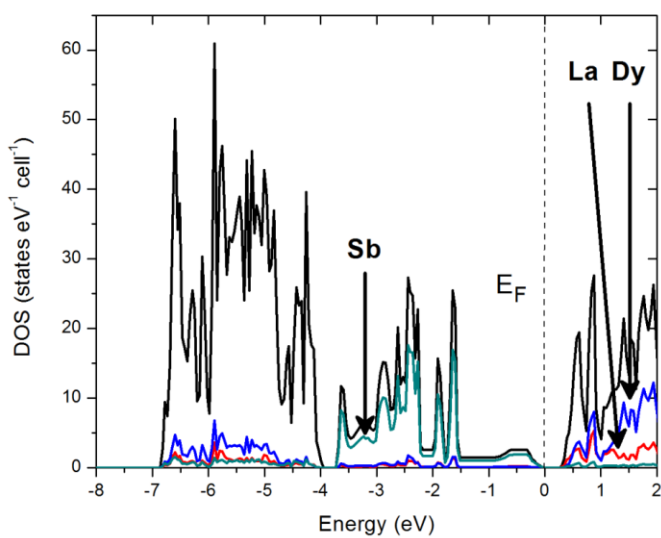


**Figure A3-1.** Calculated electronic structure of  $\text{La}_{1.5}\text{Dy}_{1.5}\text{SbO}_3$ .

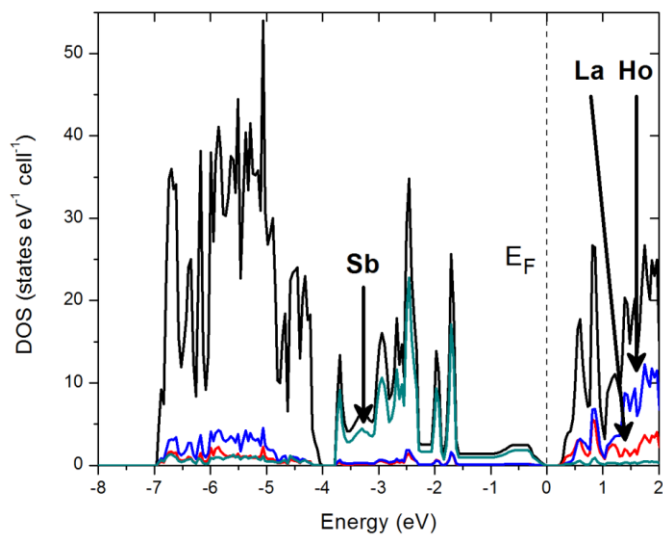


**Figure A3-2.** Calculated electronic structure of  $\text{La}_{1.5}\text{Ho}_{1.5}\text{SbO}_3$ .

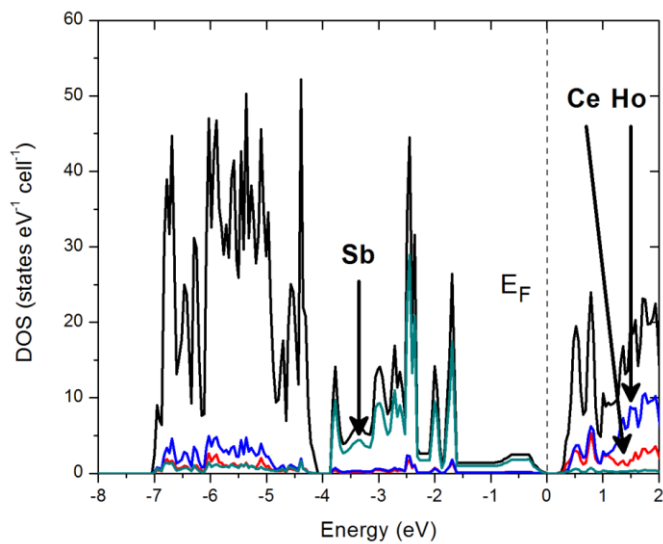


**Figure A3-3.** Calculated electronic structure of  $\text{Ce}_{1.5}\text{Ho}_{1.5}\text{SbO}_3$ .

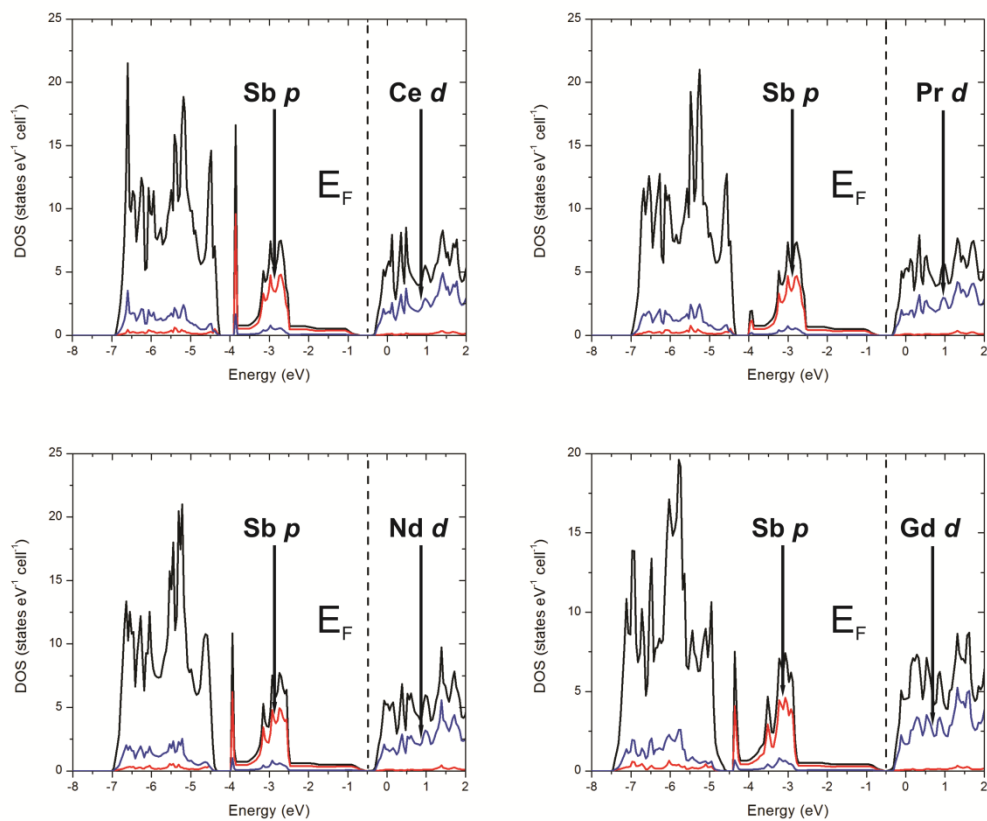


**Figure A3-4.** Calculated total and partial densities of states (DOS) for Ce<sub>4</sub>SbO<sub>4</sub> (top left), Pr<sub>4</sub>SbO<sub>4</sub> (top right), Nd<sub>4</sub>SbO<sub>4</sub> (bottom left), and Gd<sub>4</sub>SbO<sub>4</sub> (bottom right). The Ca/RE site is assumed to be occupied by RE atoms. The Fermi levels are placed at the energies corresponding to the electron count of the CaRE<sub>3</sub>SbO<sub>4</sub> composition.

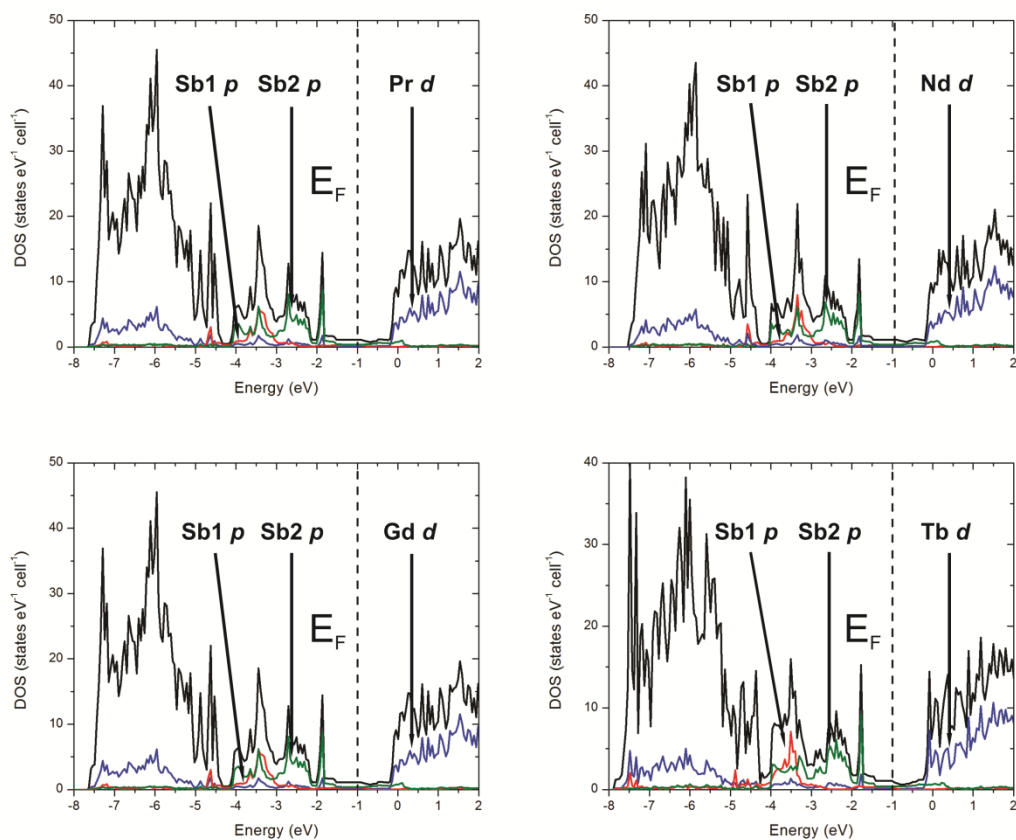


**Figure A3-5. Calculated total and partial densities of states (DOS) for Pr<sub>10</sub>Sb<sub>3</sub>O<sub>10</sub> (top left), Nd<sub>10</sub>Sb<sub>3</sub>O<sub>10</sub> (top right), Gd<sub>10</sub>Sb<sub>3</sub>O<sub>10</sub> (bottom left), and Tb<sub>10</sub>Sb<sub>3</sub>O<sub>10</sub> (bottom right). All Ca/RE sites are assumed to be occupied by RE atoms only. The Fermi levels are placed at the energies corresponding to the electron count of the Ca<sub>2</sub>RE<sub>8</sub>Sb<sub>3</sub>O<sub>10</sub> composition.**

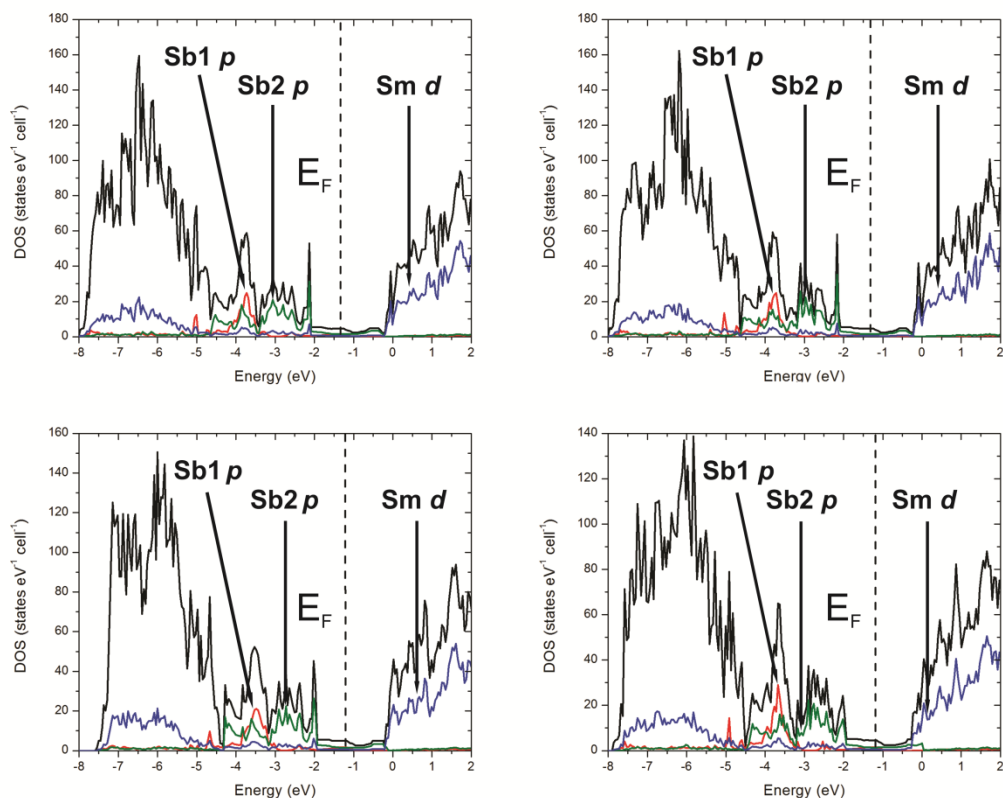


**Figure A3-6.** Calculated total and partial densities of states (DOS) for  $\text{Sm}_{10}\text{Sb}_3\text{O}_{10}$  superstructures S1 (top left), S2 (top right), S3 (bottom left), and S4 (bottom right). Each electronic structure corresponds to a different structural model presented in Figure 4.4. All Ca/RE sites are assumed to be occupied by RE atoms only. The Sb1 *p* states and the Sb2 *p* states correspond to the ordered and disordered antimony atoms, respectively, in the parent  $\text{Ca}_2\text{RE}_8\text{Sb}_3\text{O}_{10}$  structure. The Fermi levels are placed at the energies corresponding to the electron count of the  $\text{Ca}_2\text{RE}_8\text{Sb}_3\text{O}_{10}$  composition.

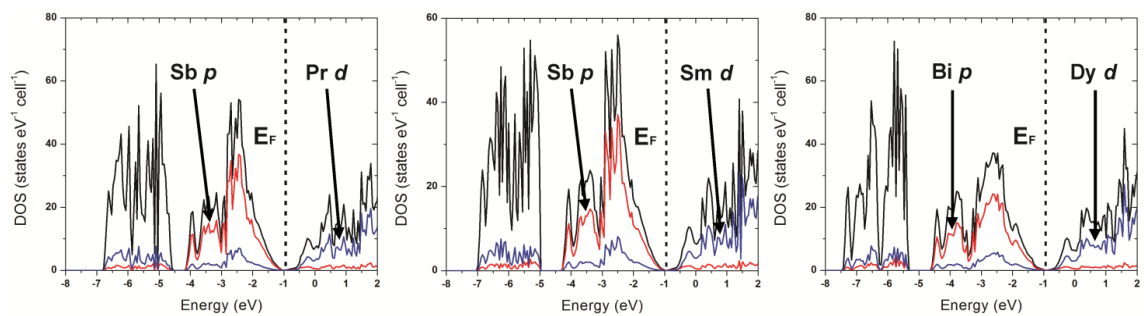


**Figure A3-7. Calculated electronic band structures for  $\text{Ca}_2\text{Pr}_7\text{Sb}_5\text{O}_5$  (left),  $\text{Ca}_2\text{Sm}_7\text{Sb}_5\text{O}_5$  (middle) and  $\text{Ca}_2\text{Dy}_7\text{Bi}_5\text{O}_5$  (right).**

## A4. Additional Physical Property Data

This section includes physical property data collected for the relevant pure samples discussed above, but were not included in the main text of this dissertation.

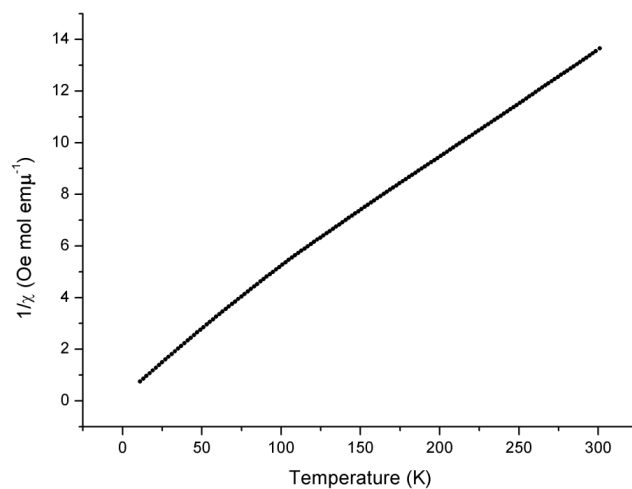


**Figure A4-1. Inverse magnetic susceptibility for  $\text{Ce}_{1.5}\text{Ho}_{1.5}\text{SbO}_3$ . A change in slope is observed at lower temperatures, corresponding to the ground state splitting of  $\text{Ce}^{3+}$ .**

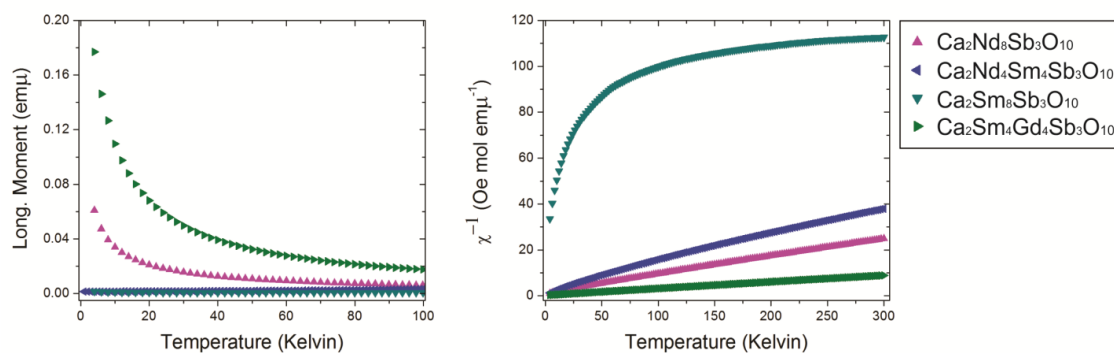


**Figure A4-2. Magnetization (left) and inverse susceptibility (right) data for the  $\text{Ca}_2\text{RE}_8\text{Sb}_3\text{O}_{10}$  and  $\text{Ca}_2\text{RE}^{\text{I}}_4\text{RE}^{\text{II}}_4\text{Sb}_3\text{O}_{10}$  samples.**

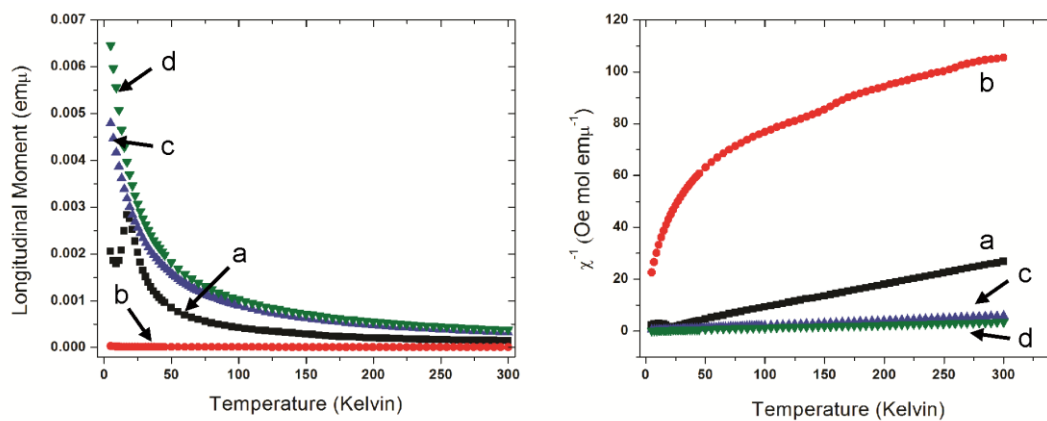


**Figure A4-3. Magnetization data for the  $\text{Ca}_2\text{RE}_7\text{Sb}_5\text{O}_5$  samples: a)  $\text{Ca}_2\text{Pr}_7\text{Sb}_5\text{O}_5$ , b)  $\text{Ca}_2\text{Sm}_7\text{Sb}_5\text{O}_5$ , c)  $\text{Ca}_2\text{Gd}_7\text{Sb}_5\text{O}_5$ , and d)  $\text{Ca}_2\text{Dy}_7\text{Sb}_5\text{O}_5$ .**

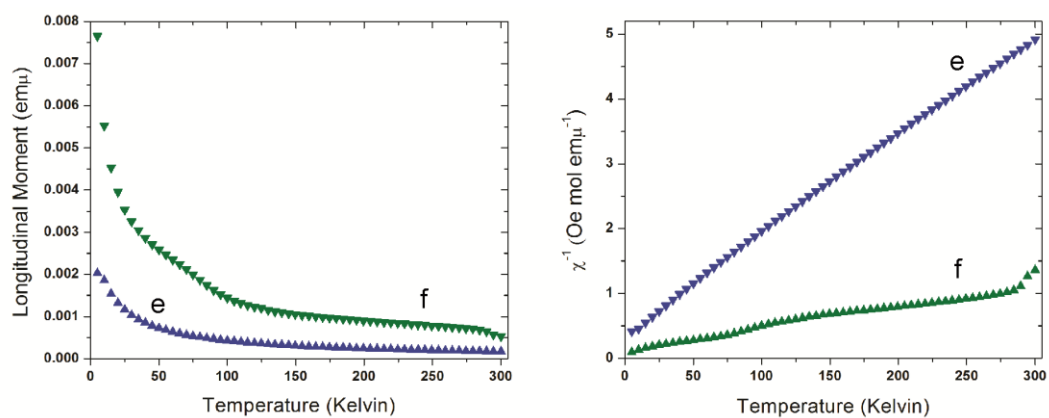


**Figure A4-4. Magnetization data for the  $\text{Ca}_2\text{RE}_7\text{Bi}_5\text{O}_5$  samples: e)  $\text{Ca}_2\text{Gd}_7\text{Bi}_5\text{O}_5$  and f)  $\text{Ca}_2\text{Dy}_7\text{Bi}_5\text{O}_5$ .**

## References

1. Disalvo, F. J., *Science (Washington, D. C.)* **1999**, 285 (5428), 703-706.
2. Tritt, T. M., *Science (Washington, D. C.)* **1996**, 272 (5266), 1276-1277.
3. Seebeck, T. J., *Treatises of the Royal Academy of Sciences in Berlin* **1825**, 265-373.
4. Ørsted, H. C., *Annales de Chimie et Physique* **22** **1823**, 375–389.
5. Lasance, C. J. M., *Electronics Cooling* **2006**, (November).
6. Winder, E. J.; Ellis, A. B.; Lisensky, G. C., *J. Chem. Educ.* **1996**, 73 (10), 940-946.
7. Fermi, E., *Rendiconti Lincei* **1926**, 3, 145-149.
8. Dirac, P. A. M., *Proceedings of the Royal Society, Series A* **1926**, 112 (762), 661-677.
9. Bloch, F., *Z. Physik* **1928**, 52, 555-600.
10. Drude, P., *Annalen der Physik* **1900**, 306 (3), 566.
11. Drude, P., *Annalen der Physik* **1900**, 308 (11), 369.
12. Kittel, C., *Introduction to Solid State Physics* **2005**, 8th Ed., 194-196.
13. Rowe, D. M., *CRC Handbook of Thermoelectrics: Macro to Nano* **2005**, CRC Press.
14. Lenz, H. F. E., *Ann. Electr. II.* **1839**, 380-384.
15. Sittig, M., *Thermoelectric materials* **1970**, Noyes Data Corp.
16. William, T., *R. Soc. Edinburgh: Earth Sci.* **1851**, 3, 91–98.
17. Altenkirch, E., *Phys. Z.* **1909**, 10, 560.
18. Altenkirch, E.; Gehlhoff, G., *Phys. Z.* **1911**, 12, 920.
19. Ioffe, A. F., *Semiconductor Thermoelements and Thermoelectric Cooling* **1957**, London, Infosearch.
20. Rowe, D. M., *CRC Handbook of Thermoelectrics* **1995**, CRC Press.
21. Heikes, R. R.; Ur, R. W., *Interscience Publishers* **1961**.
22. Cadoff, I. B.; Miller, E., *Materials Technology Series. Reinhold Publishing Cooperation* **1960**.
23. Egli, P. H., *John Wiley & Sons* **1960**.
24. Snyder, G. J., *Appl. Phys. Lett.* **2004**, 84 (13), 2436-2438.
25. Snyder, G. J.; Ursell, T. S., *Phys. Rev. Lett.* **2003**, 91 (14), 148301:1-148301:4.
26. Vining, C. B., *Nat Mater* **2009**, 8 (2), 83-85.
27. Perpetua, <http://www.perpetuapower.com/index.htm>.
28. Caframo, <http://www.caframolifestylesolutions.com/>.
29. Powerpractical, <http://powerpractical.com/>.
30. Yang, J.; Caillat, T., *MRS Bull.* **2006**, 31 (3), 224-229.
31. Clark, S., *Spaceflight Now* **2011**.
32. Cook, J. C.; Agle, D. C.; D., B., *NASA Voyager mission, NASA* **2013**.
33. Peat, C., *Heavens Above* **2014**.

34. Bennett, G. L.; Lombardo, J. J.; Hemler, R. J.; Silverman, G.; Whitmore, C. W.; Amos, W. R.; Johnson, E. W.; Zocher, R. W.; Hagan, J. C.; Englehart, R. W., *AIP Conf. Proc.* **2008**, *969*, 663-671.
35. NASA/JPL, *Voyager Bulletin* **1978**, *13*, 1-4.
36. Stabler, F. R., *Mater. Res. Soc. Symp. Proc.* **2006**, *886*, 13-21.
37. Sootsman, J. R.; Chung, D. Y.; Kanatzidis, M. G., *Angew. Chem., Int. Ed.* **2009**, *48* (46), 8616-8639.
38. MacDonald, D. K. C., *Thermoelectricity: An Introduction to the Principles* **1962**, John Wiley & Sons, Inc.
39. Omar, M. A., *Elementary Solid State Physics: Principles and Applications* **1999**, Pearson Education, Inc.
40. Cutler, M.; Mott, N. F., *Phys. Rev.* **1969**, *181* (3), 1336-1340.
41. Snyder, G. J.; Toberer, E. S., *Nat. Mater.* **2008**, *7* (2), 105-114.
42. Jonson, M.; Mahan, G. D., *Phys. Rev. B* **1980**, *21* (10), 4223-9.
43. White, M. A., *Properties of Materials* **1999**, Oxford University Press: New York.
44. Petit, A.-T.; Dulong, P.-L., *Annales de Chimie et de Physique* **1819**, *10*, 395-413.
45. Biswas, K.; He, J.; Blum, I. D.; Wu, C.-I.; Hogan, T. P.; Seidman, D. N.; Dravid, V. P.; Kanatzidis, M. G., *Nature (London, U. K.)* **2012**, *489* (7416), 414-418.
46. Balandin, A.; Wang, K. L., *J. Appl. Phys.* **1998**, *84* (11), 6149-6153.
47. Hicks, L. D.; Dresselhaus, M. S., *Phys. Rev. B* **1993**, *47* (19), 12727-12731.
48. Hicks, L. D.; Harman, T. C.; Dresselhaus, T. C., *Appl. Phys. Lett.* **1993**, *63* (23), 3230-3232.
49. Minnich, A. J.; Dresselhaus, M. S.; Ren, Z. F.; Chen, G., *Energy Environ. Sci.* **2009**, *2* (5), 466-479.
50. Heinrich, H.; Lischka, K.; Sitter, H.; Kriechbaum, M., *Phys. Rev. Lett.* **1975**, *35* (16), 1107-1110.
51. Zhao, L.-D.; Hao, S.; Lo, S.-H.; Wu, C.-I.; Zhou, X.; Lee, Y.; Li, H.; Biswas, K.; Hogan, T. P.; Uher, C.; Wolverton, C.; Dravid, V. P.; Kanatzidis, M. G., *J. Am. Chem. Soc.* **2013**, *135* (19), 7364-7370.
52. Zhao, L.-D.; He, J.; Hao, S.; Wu, C.-I.; Hogan, T. P.; Wolverton, C.; Dravid, V. P.; Kanatzidis, M. G., *J. Am. Chem. Soc.* **2012**, *134* (39), 16327-16336.
53. Bulat, L. P.; Drabkin, I. A.; Karataev, V. V.; Osvenskii, V. B.; Parkhomenko, Y. N.; Pshenai-Severin, D. A.; Pivovarov, G. I.; Tabachkova, N. Y., *Phys. Solid State* **2011**, *53* (1), 29-34.
54. Zide, J. M. O.; Vashaee, D.; Bian, Z. X.; Zeng, G.; Bowers, J. E.; Shakouri, A.; Gossard, A. C., *Phys. Rev. B* **2006**, *74* (20), 205335:1-205335:5.
55. Zide, J. M. O.; Vashaee, D.; Zeng, G.; Bowers, J. E.; Shakouri, A.; Gossard, A. C., *Los Alamos Natl. Lab., Prepr. Arch.* **2005**, 1-18.
56. Appleyard, N. J.; Nicholls, J. T.; Pepper, M.; Tribe, W. R.; Simmons, M. Y.; Ritchie, D. A., *Phys. Rev. B* **2000**, *62* (24), R16 275-R16 278.
57. Appleyard, N. J.; Nicholls, J. T.; Simmons, M. Y.; Tribe, W. R.; Pepper, M., *Phys. Rev. Lett.* **1998**, *81* (16), 3491-3494.

58. Cao, Y. Q.; Zhu, T. J.; Zhao, X. B.; Zhang, X. B.; Tu, J. P., *Appl. Phys. A: Mater. Sci. Process.* **2008**, *92* (2), 321-324.
59. Saleemi, M.; Toprak, M. S.; Li, S.; Johnsson, M.; Muhammed, M., *J. Mater. Chem.* **2012**, *22* (2), 725-730.
60. Son, J. S.; Choi, M. K.; Han, M.-K.; Park, K.; Kim, J.-Y.; Lim, S. J.; Oh, M.; Kuk, Y.; Park, C.; Kim, S.-J.; Hyeon, T., *Nano Lett.* **2012**, *12* (2), 640-647.
61. Quarez, E.; Hsu, K.-F.; Pcionek, R.; Frangis, N.; Polychroniadis, E. K.; Kanatzidis, M. G., *J. Am. Chem. Soc.* **2005**, *127* (25), 9177-9190.
62. Androulakis, J.; Pcionek, R.; Quarez, E.; Palchik, O.; Kong, H.; Uher, C.; Dangelo, J. J.; Hogan, T.; Tang, X.; Tritt, T.; Kanatzidis, M. G., *Mater. Res. Soc. Symp. Proc.* **2006**, *886* (Materials and Technologies for Direct Thermal-to-Electric Energy Conversion), 187-194.
63. Poudeu, P. F. P.; D'Angelo, J.; Downey, A. D.; Short, J. L.; Hogan, T. P.; Kanatzidis, M. G., *Angew. Chem., Int. Ed.* **2006**, *45* (23), 3835-3839.
64. Cook, B. A.; Kramer, M. J.; Haringa, J. L.; Han, M.-K.; Chung, D.-Y.; Kanatzidis, M. G., *Advanced Functional Materials* **2009**, *19* (8), 1254-1259.
65. Hsu, K. F.; Loo, S.; Guo, F.; Chen, W.; Dyck, J. S.; Uher, C.; Hogan, T.; Polychroniadis, E. K.; Kanatzidis, M. G., *Science (Washington, DC, U. S.)* **2004**, *303* (5659), 818-821.
66. Tobola, J.; Pierre, J.; Kaprzyk, S.; Skolozdra, R. V.; Kouacou, M. A., *J. Phys.: Condens. Matter* **1998**, *10* (5), 1013-1032.
67. Uher, C.; Yang, J.; Hu, S.; Morelli, D. T.; Meisner, G. P., *Phys. Rev. B* **1999**, *59* (13), 8615-8621.
68. Shen, Q.; Chen, L.; Goto, T.; Hirai, T.; Yang, J.; Meisner, G. P.; Uher, C., *Appl. Phys. Lett.* **2001**, *79* (25), 4165-4167.
69. Culp, S. R.; Poon, S. J.; Hickman, N.; Tritt, T. M.; Blumm, J., *Appl. Phys. Lett.* **2006**, *88* (4), 042106:1-042106:3.
70. Brown, S. R.; Kauzlarich, S. M.; Gascoin, F.; Snyder, G. J., *Chem. Mater.* **2006**, *18* (7), 1873-1877.
71. Wood, C., *Energy Convers. Manage.* **1984**, *24* (4), 317-329.
72. Yamashita, O.; Sadatomi, N., *J. Appl. Phys.* **2000**, *88* (1), 245-251.
73. Caillat, T.; Fleurial, J. P.; Borshchevsky, A., *J. Phys. Chem. Solids* **1997**, *58* (7), 1119-1125.
74. Mozharivskyj, Y.; Pecharsky, A. O.; Bud'ko, S.; Miller, G. J., *Chem. Mater.* **2004**, *16* (8), 1580-1589.
75. Snyder, G. J.; Christensen, M.; Nishibori, E.; Caillat, T.; Iversen, B. B., *Nat. Mater.* **2004**, *3* (7), 458-463.
76. Nolas, G. S.; Poon, J.; Kanatzidis, M., *MRS Bull.* **2006**, *31* (3), 199-205.
77. Christensen, M.; Snyder, G. J.; Iversen, B. B., *Int. Conf. Thermoelectr.* **2006**, *Part 1*, 40-43.
78. Fulmer, J.; Lebedev, O. I.; Roddatis, V. V.; Kaseman, D. C.; Sen, S.; Dolyniuk, J.-A.; Lee, K.; Olenov, A. V.; Kovnir, K., *J. Am. Chem. Soc.* **2013**, *135* (33), 12313-12323.

79. Gascoin, F.; Ottensmann, S.; Stark, D.; Haile, S. M.; Snyder, G. J., *Adv. Funct. Mater.* **2005**, *15* (11), 1860-1864.
80. Terasaki, I.; Sasago, Y.; Uchinokura, K., *Phys. Rev. B* **1997**, *56* (20), R12 685-R12 687.
81. Fujita, K.; Mochida, T.; Nakamura, K., *Jpn. J. Appl. Phys., Part 1* **2001**, *40* (7), 4644-4647.
82. Terasaki, I., *Int. Conf. Thermoelectr.* **2002**, 185-191.
83. Fouassier, C.; Matejka, G.; Reau, J.; Hagenmuller, P. J., *J. Solid State Chem.* **1973**, *6*, 532.
84. Funahashi, R.; Matsuhara, I.; Ikuta, T.; Takeuchi, T.; Mizutani, U.; Sodeoka, S., *Jpn. J. Appl. Phys., Part 1* **2000**, (39), L1127.
85. Yamamoto, T.; Uchinokura, K.; Tsukada, I., *Phys. Rev. B.* **2002**, (65), 184434.
86. Itoh, T.; Terasaki, I., *Jpn. J. Appl. Phys.* **2000**, (39), 6658.
87. Okuda, T.; Nakanishi, S.; Miyasaki, S.; Tokura, Y., *Phys. Rev. B.* **2001**, *63*, 113104.
88. Ohta, S.; Nomura, T.; Ohta, H.; Hirano, M.; Hosono, H.; Koumoto, K., *Jpn. Soc. Appl. Phys. Related Soc.* **2005**, 254.
89. Muta, H.; Kurosaki, K.; Yamanaka, S., *J. Alloys Compd.* **2003**, *350*, 292.
90. Muta, H.; Kurosaki, K.; Yamanaka, S., *J. Alloys Compd.* **2004**, *368*, 22.
91. Hebert, S.; Lambert, S.; Pelloquin, D.; Maignan, A., *Phys. Rev. B* **2001**, *64* (17), 172101:1-172101:4.
92. Koumoto, K.; Terasaki, I.; Funahashi, R., *MRS Bull.* **2006**, *31* (3), 206-210.
93. Brixner, L. H., *J. Inorg. Nucl. Chem.* **1960**, *15*, 199-201.
94. Abdusalyamova, M. N.; Shokirov, H. S.; Rakhmatov, O. I., *J. Less-Common Met.* **1990**, *166* (2), 221-227.
95. Ok, K. M.; Gittens, A.; Zhang, L.; Halasyamani, P. S., *J. Mater. Chem.* **2004**, *14* (1), 116-120.
96. Varfolomeev, M. B.; Narnov, B. A., *Zh. Neorg. Khim.* **1978**, *23* (7), 1737-1740.
97. Varfolomeev, M. B.; Toporenskaya, T. A.; Narnov, B. A., *Zh. Neorg. Khim.* **1979**, *24* (1), 244-247.
98. Michel, C.; Caignaert, V.; Raveau, B., *J. Solid State Chem.* **1991**, *90* (2), 296-301.
99. Wang, P.; Forbes, S.; Kolodiaznyi, T.; Kosuda, K.; Mozharivskyj, Y., *J. Am. Chem. Soc.* **2010**, *132* (25), 8795-8803.
100. Forbes, S.; Wang, P.; Yao, J.; Kolodiaznyi, T.; Mozharivskyj, Y., *Inorg. Chem.* **2013**, *52* (2), 1025-1031.
101. Wang, P. L.; Kolodiaznyi, T.; Yao, J.; Mozharivskyj, Y., *Chem. Mater.* **2013**, *25* (5), 699-703.
102. Benz, B., *Acta Cryst.* **1971**, *B27*, 853-854.
103. Nuss, J.; Georg von Schnering, H.; Grin, Y., *Z. Anorg. Allg. Chem.* **2004**, (630), 2287-2291.
104. Nuss, J.; Jansen, M., *Acta Cryst.* **2007**, *B63*, 843-849.

105. Cook, B. A.; Kramer, M. J.; Wei, X.; Harringa, J. L.; Levin, E. M., *J. Appl. Phys.* **2007**, *101* (5), 053715:1-053715:6.
106. Wang, P.; Forbes, S.; Svitlyk, V.; Aushana, A.; Mozharivskyj, Y., *Eur. J. Inorg. Chem.* **2011**, (26), 3887-3895.
107. Forbes, S.; Yuan, F.; Saporov, B.; Sefat, A. S.; Kosuda, K.; Kolodiazhnyi, T.; Mozharivskyj, Y., *Chem. Mater.* **2014**, *26* (7), 2289-2298.
108. Ewald, P. P., *Acta Cryst.* **1969**, *25*, 103.
109. Cullity, B. D., *Elements of X-Ray Diffraction* **1967**, Addison-Wesley Publishing Company, Inc.
110. Palmer, M. F. C., *Structure Determination by X-ray Crystallography 3rd ed.* **1993**, Pleum Press.
111. Pecharsky, V.; Zavaliji, P., *Fundamentals of Powder Diffraction and Structural Characterization of Materials* **2003**, Springer-Verlag.
112. *STOE X-Shape* **2004**, STOE & Cie GmbH.
113. *Bruker Analytical X-Ray Systems* **2002**.
114. Hunter, B. A.; Howard, C. J., **2000**, Rietica Australian Nuclear Science and Technology Organization.
115. Egerton, R. F., *Physical Principles of Electron Microscopy: an Introduction to TEM, SEM, and AEM* **2005**, Springer Science & Business Media.
116. Hall, E., *American Journal of Mathematics* **1879**, *2* (3), 287-292.
117. Andersen, O. K.; Pawlowska, Z.; Jepsen, O., *Phys. Rev. B* **1986**, *34*, 5253-5269.
118. Jepsen, O.; Burkhardt, A.; Andersen, O. K., *The TB-LMTO-ASA Program, version 4.7* **1999**, Max-Planck-Institut für Festkörperforschung.
119. Andersen, O. K.; Jepsen, O., *Phys. Rev. Lett.* **1984**, *53*, 2571-2574.
120. Andersen, O. K.; Jepsen, O.; Glotzel, D., *Highlights of Condensed Matter Theory* **1985**, Elsevier.
121. Jepsen, O.; Andersen, O. K., *Phys. Rev. B* **1995**, *97*, 35-47.
122. Bell, L. E., *Science* **2008**, *321* (5895), 1457-1461.
123. LaGrandeur, J.; Crane, D.; Hung, S.; Mazar, B.; Eder, A., *Int. Conf. Thermoelectr.* **2006**, *Part 1*, 343-348.
124. Watanabe, S., *Manufacture of thermoelectric generator* **1994**, JP06338636A.
125. Beyer, H.; Nurnus, J.; Bottner, H.; Lambrecht, A.; Roch, T.; Bauer, G., *Appl. Phys. Lett.* **2002**, *80* (7), 1216-1218.
126. Harman, T. C.; Spears, D. L.; Calawa, D. R.; Groves, S. H.; Walsh, M. P., *Int. Conf. Thermoelectr.* **1997**, 416-423.
127. Wang, P. L.; Kolodiazhnyi, T.; Yao, J.; Mozharivskyj, Y., *J. Am. Chem. Soc.* **2012**, *134* (3), 1426-1429.
128. Sheldrick, G. M., *SHELXL* **1997**, University of Gottingen.
129. Hamilton, W. C., *Acta Cryst.* **1965**, *18* (3), 502-510.
130. Koch, E.; Fischer, W., *Z. Kristallogr.* **1996**, *211*, 251-253.
131. Shannon, R. D., *Acta Cryst.* **1976**, *A32* (5), 751-767.
132. Papoian, G. A.; Hoffmann, R., *Angew. Chem., Int. Ed.* **2000**, *39* (14), 2409-2448.

133. Dughaish, Z. H., *Physica B* **2002**, 322 (1-2), 205-223.
134. Mahan, G.; Sales, B.; Sharp, J., *Phys. Today* **1997**, 50 (3), 42-47.
135. Kuznetsov, V. L.; Kuznetsova, L. A.; Kaliazin, A. E.; Rowe, D. M., *J. Appl. Phys.* **2000**, 87 (11), 7871-7875.
136. Saramat, A.; Svensson, G.; Palmqvist, A. E. C.; Stiewe, C.; Mueller, E.; Platzek, D.; Williams, S. G. K.; Rowe, D. M.; Bryan, J. D.; Stucky, G. D., *J. Appl. Phys.* **2006**, 99 (2), 023708:1-023708:5.
137. Fu, L.; Yang, J.; Xiao, Y.; Peng, J.; Liu, M.; Luo, Y.; Li, G., *Intermetallics* **2013**, 43, 79-84.
138. Nolas, G. S.; Kaeser, M.; Littleton, R. T. I.; Tritt, T. M., *Appl. Phys. Lett.* **2000**, 77 (12), 1855-1857.
139. Eisenmann, B.; Limartha, H.; Schaefer, H.; Graf, H. A., *Z. Naturforsch., B: Anorg. Chem., Org. Chem.* **1980**, 35B (12), 1518-1524.
140. Furusest, S.; Selte, K.; Kjekshus, A., *Acta Chem. Scand.* **1965**, 19 (1), 95-106.
141. Cordier, G.; Czech, E.; Jakowski, M.; Schaefer, H., *Rev. Chim. Miner.* **1981**, 18 (1), 9-18.
142. Hoenle, W.; Von Schnering, H. G., *Z. Kristallogr.* **1981**, 155 (3-4), 307-314.
143. Boss, M.; Petri, D.; Pickhard, F.; Zoennchen, P.; Roehr, C., *Z. Anorg. Allg. Chem.* **2005**, 631 (6-7), 1181-1190.
144. Anderson, P. W., *Phys. Rev.* **1958**, 109, 1492-1505.
145. Hill, R. M., *Phys. Status Solidi A* **1976**, 35 (1), K29-K34.
146. Poudel, B.; Hao, Q.; Ma, Y.; Lan, Y.; Minnich, A.; Yu, B.; Yan, X.; Wang, D.; Muto, A.; Vashae, D.; Chen, X.; Liu, J.; Dresselhaus, M. S.; Chen, G.; Ren, Z., *Science (Washington, DC, U. S.)* **2008**, 320 (5876), 634-638.
147. Keppens, V.; Sales, B. C.; Mandrus, D.; Chakoumakos, B. C.; Laermans, C., *Philos. Mag. Lett.* **2000**, 80 (12), 807-812.
148. Nolas, G. S.; Cohn, J. L.; Slack, G. A.; Schujman, S. B., *Appl. Phys. Lett.* **1998**, 73 (2), 178-180.
149. Nuss, J.; Jansen, M., *J. Alloys Compd.* **2009**, 480 (1), 57-59.
150. Kuzmin, R. N.; Nikitina, S. V., *Kristallografiya* **1963**, 8 (3), 453-454.
151. Calderazzo, F.; Morvillo, A.; Pelizzi, G.; Poli, R., *Journal of the Chemical Society, Chemical Communications* **1983**, (9), 507-508.
152. Gascoin, F.; Sevov, S. C., *J. Am. Chem. Soc.* **2000**, 122 (41), 10251-10252.
153. Haynes, W. M., *CRC Handbook of Chemistry and Physics 92nd ed.* **2012**, CRC Press: Boca Raton, FL, USA. 2640.
154. Li, D. X.; Haga, Y.; Shida, H.; Suzuki, T.; Kwon, Y. S., *Phys. Rev. B* **1996**, 54 (15), 10483-10491.
155. Li, J. F.; Liu, W. S.; Zhao, L. D.; Zhou, M., *NPG Asia Mater.* **2010**, 2, 152-158.
156. Berger, R., *Acta Chem. Scand., Ser. A* **1977**, A31 (6), 514-516.
157. Nuss, J.; Jansen, M., *Z. Kristallogr. - New Cryst. Struct.* **2002**, 217 (1), 19-20.
158. Hurng, W. M.; Corbett, J. D., *Chem. Mater.* **1989**, 1 (3), 311-319.